

# **Model Studies of Methanol Selective Oxidation over Copper Catalysts**

Von der Naturwissenschaftlichen Fakultät der Universität Hannover  
zur Erlangung des Grades  
Doktor der Naturwissenschaften  
Dr. rer. nat.  
genehmigte Dissertation

von  
M. Eng. Ling Zhou  
geboren am 16. Juli 1974 in Hubei, China

2005



# **Model Studies of Methanol Selective Oxidation over Copper Catalysts**

Von der Naturwissenschaftlichen Fakultät der Universität Hannover  
zur Erlangung des Grades  
Doktor der Naturwissenschaften  
Dr. rer. nat.  
genehmigte Dissertation

von  
M. Eng. Ling Zhou  
geboren am 16. Juli 1974 in Hubei, China

2005

Referent: Prof. Dr. R. Imbihl

Korreferent: Prof. Dr. J. Caro

Tag der Promotion: 15. Juni 2005

# Kurzzusammenfassung

Die Drucklücke in der Partialoxidation von Methanol an Kupfer sollte überbrückt werden indem der Druckbereich von UHV bis zu Atmosphärendruck variiert wird und indem in-situ-Methoden zur Charakterisierung der Oberfläche unter Reaktionsbedingungen Anwendung finden. Das Problem der Materiallücke kann nicht von dem der Drucklücke separiert werden, weil bei höheren Drücken durch die Reaktion die Kupferoberfläche stark modifiziert wird.

In dieser Arbeit wurde die Kinetik der Methanoxidation an einer Cu(110)-Oberfläche im Druckbereich von  $10^{-7}$  bis  $10^{-3}$  mbar untersucht. Um einen Zusammenhang herzustellen zwischen der Struktur und der Bedeckung der Oberfläche und der katalytischen Aktivität wurden als in-situ Techniken die niederenergetische Beugung von Elektronen (LEED), die Auger-Elektronenspektroskopie (AES), und die Photoelektronenemissionsmikroskopie (PEEM) eingesetzt. Darüber hinaus wurde die am Elektronenspeicherring BESSY vorhandene Möglichkeit, in-situ Röntgen-Photoelektronenspektroskopie (XPS) bei Drücken bis zu 1 mbar zu betreiben, genutzt, um die Adsorbatbedeckungen unter Reaktionsbedingungen quantitativ zu bestimmen.

Neben Formaldehyd als Hauptreaktionsprodukt wurden  $H_2$ ,  $H_2O$ , und  $CO_2$  als Produkte gemessen. Der reaktive Haftkoeffizient von Methanol ist hoch und erreicht 0.2. Es treten Reaktivitätsmaxima bei zwei Temperaturen auf: einem unteren Maximum bei 400 – 520 K, das oberhalb von Drücken von  $10^{-3}$  mbar verschwindet, und einen Hochtemperaturreaktionspeak bei 900 K, der auch bei hohen Drücken weiterbesteht. Großer Sauerstoffüberschuss führt zu einer Vergiftung der Reaktion. Als reaktive Zentren der O-bedeckten Cu(110)-Oberfläche waren zuvor die endständigen O-Atome der O-Cu-O-Ketten der  $(2\times 1)$ -O-Struktur identifiziert worden. Die dominanten Zwischenproduktspezies auf der Oberfläche sind die Methoxy- und die Formate-Spezies. Bei zyklischer Variation der Temperatur beobachtet man eine sehr

ausgeprägte Hysterese der Reaktionsrate, die auf unterschiedlichen Adsorbatbedeckungen in den beiden Zweigen der Ratenhysterese zurückzuführen ist.

In einer eigens konstruierten Hochdruckreaktionszelle, die über ein Transfersystem mit einer UHV-Kammer verbunden ist, wurde die Reaktion im  $10^{-2}$  mbar-Bereich über metallischen und anoxidierten Kupferoberflächen durchgeführt. Übergänge zwischen der metallischen Cu-Oberfläche und den beiden Oxiden  $\text{Cu}_2\text{O}$  und  $\text{CuO}$  wurden über den damit verbundenen Farbwechsel der Proben und über ellipsometrische Messungen beobachtet. Verglichen mit einer metallischen Cu-Oberfläche weist eine anoxidierte Cu-Oberfläche eine höhere Aktivität zur Formaldehydbildung auf wohingegen die stark oxidierte Probe ( $\text{CuO}$ ) eine erhöhte Tendenz zur Totaloxidation von Methanol zu  $\text{CO}_2$  zeigt. Offensichtlich ist der aktive Zustand der Oberfläche nicht rein metallisch, sondern weist eine erhöhte Konzentration von Volumensauerstoff im oberflächennahen Bereich auf Oxidation und Reduktion der Cu-Oberfläche unter den Bedingungen der katalytischen Methanoloxidation sind mit drastischen Aufrauungsvorgängen und der Ausbildung räumlicher Inhomogenitäten verbunden, was mit photographischen Abbildungen und mittels ellipsometrischer Mikroskopie gezeigt wurde.

Die raumzeitliche Dynamik der katalytischen Methanol-Oxidation wurde an  $\text{Cu}(110)$  und an zwei mikrostrukturierten Proben,  $\text{Pd}/\text{Cu}(110)$  und  $\text{Cu}/\text{ZnO}/\text{Al}_2\text{O}_3$  mittels PEEM studiert. Bei kleinen Drücken lief die Reaktion räumlich homogen auf  $\text{Cu}(110)$  und auf  $\text{Pd}/\text{Cu}(110)$  ab. Domänengrößenabhängige Effekte und Struktur-bildungen an den Metall/Metalloxid-Grenzflächen wurden hingegen auf  $\text{Cu}/\text{ZnO}/\text{Al}_2\text{O}_3$  gefunden, was möglicherweise auf einen synergetischen Effekt von  $\text{ZnO}$  auf die Aktivität von  $\text{Cu}$  hindeutet.

**Schlüsselwörter:** Kupfer; Kupferoxide; Modellkatalysatoren;  $\text{Cu}(110)$ ;  $\text{Pd}/\text{Cu}(110)$ ;  $\text{Cu}/\text{ZnO}/\text{Al}_2\text{O}_3$ ; Methanoloxidation; Formaldehyd; Kinetik; Hysterese; Methoxy; Format; Phasenübergänge; Drucklücke; Materiallücke

# Abstract

The pressure gap in the selective methanol oxidation over copper catalysts has been bridged by systematically increasing the pressure and utilizing the *in situ* techniques to monitor the state of the surface. The pressure gap problem cannot be separated from the material gap problem because at higher pressure the catalyst is strongly modified. Various model copper catalysts have been constructed in this work in order to bridge the material gap.

The kinetics of methanol oxidation over Cu(110) have been studied under low pressure conditions from  $10^{-7}$  to  $10^{-3}$  mbar in a UHV system. *In situ* low energy electron diffraction (LEED), Auger electron spectroscopy (AES), and photoelectron emission microscopy (PEEM) have been used to relate the presence of certain adsorbate phases to the catalytic activity. Moreover, with the help of the *in situ* high-pressure X-ray photoelectron spectroscopy (XPS) facility at BESSY, the variation of the adsorbate coverages during the reaction has been quantitatively investigated.  $H_2$ ,  $H_2O$ , and  $CO_2$  are found in addition to the main product formaldehyde. The reactive sticking coefficient of methanol reaches 0.2. Two rate maxima exist: one at around 400 – 520 K, which disappears when the total pressure exceeds  $10^{-3}$  mbar and the other at around 900 K that persists at high pressure. High oxygen partial pressures lead to a poisoning of the reaction. The terminal oxygen atoms of the (2×1)-O islands act as the active sites for methanol oxidation at low pressures. The (5×2)-methoxy and c(2×2)-formate are the important intermediates in the reaction. A pronounced rate hysteresis is observed when the temperature is cycled, which can be attributed to a hysteresis in the adsorbate coverages.

In a high-pressure reaction cell which is connected to a UHV chamber, the kinetics of methanol oxidation over metallic and oxidized copper surfaces have been studied in the  $10^{-2}$  mbar range. Transitions between the metallic surface and the two copper oxides,  $Cu_2O$  and  $CuO$ , are followed by the colour changes of the sample and

by *in situ* ellipsometric measurements. Compared with a metallic copper surface, a partially oxidized copper surface has higher reactivity to produce formaldehyde whereas the deeply oxidized surface (CuO) shows a higher activity towards total oxidation to CO<sub>2</sub>. Apparently, at high pressure the active state of the surface is not a completely reduced copper surface but a surface which contains some oxygen in the near surface region of the sample. Oxidation and reduction of the Cu surface are associated with a drastic change in the roughness and with spatial inhomogeneities as demonstrated by photographic imaging and ellipsometric microscopy.

The spatiotemporal dynamics of methanol oxidation over Cu(110) and two microstructured bimetallic samples, Pd/Cu(110) and Cu/ZnO/Al<sub>2</sub>O<sub>3</sub>, have been studied by PEEM in the UHV system. At low pressures, the reaction proceeds spatially homogeneous over Cu(110) and Pd/Cu(110), whereas both size effects and boundary effects have been observed over Cu/ZnO/Al<sub>2</sub>O<sub>3</sub>, which indicates a possible synergetic effect of ZnO on the activity of Cu.

**Keywords:** Copper; Copper oxide; Model catalysts; Cu(110); Pd/Cu(110); Cu/ZnO/Al<sub>2</sub>O<sub>3</sub>; Methanol oxidation; Formaldehyde; Kinetics; Hysteresis; Methoxy; Formate; Phase transition; Pressure gap; Material gap



# Contents

<b>1</b>	<b>Introduction</b>	<b>1</b>
<b>2</b>	<b>Experimental techniques</b>	<b>7</b>
2.1	Introduction . . . . .	7
2.2	Nomenclature in surface science . . . . .	8
2.3	Temperature-programmed techniques: TPD and TPRS . . . . .	8
2.4	Auger Electron Spectroscopy: AES . . . . .	10
2.4.1	The Auger process . . . . .	10
2.4.2	The Auger instrumentation . . . . .	12
2.4.3	Quantitative analysis . . . . .	14
2.5	Low Energy Electron Diffraction: LEED . . . . .	15
2.5.1	Experimental setup of LEED . . . . .	15
2.5.2	The theory behind LEED . . . . .	16
2.5.3	Diffraction and reciprocal space . . . . .	17
2.6	Photoelectron Emission Microscopy: PEEM . . . . .	18
2.6.1	PEEM instrumentation . . . . .	19
2.6.2	Applications of PEEM . . . . .	21
2.7	X-ray Photoelectron Spectroscopy: XPS . . . . .	22
2.7.1	Physical basis of XPS . . . . .	22
2.7.2	Experimental setup . . . . .	24
2.7.3	Study of adsorbates with XPS . . . . .	25
2.8	Ellipsometry . . . . .	26
2.8.1	Polarized light . . . . .	26

2.8.2	Basic equations of Ellipsometry . . . . .	27
2.8.3	Ellipsometer . . . . .	28
2.8.2	Principle of imaging Ellipsometry . . . . .	30
<b>3</b>	<b>Experimental setups</b>	<b>33</b>
3.1	Introduction . . . . .	33
3.2	The UHV system . . . . .	33
3.2.1	Ultrahigh vacuum . . . . .	35
3.2.2	Sample preparation . . . . .	35
3.2.3	Gas calibration . . . . .	37
3.2.4	Rate measurement . . . . .	39
3.3	The HP-UHV system . . . . .	39
3.3.1	Sample holder . . . . .	41
3.3.2	High pressure reaction cell . . . . .	42
3.3.2	Alignment of the Multiskop ellipsometer . . . . .	43
3.4	The HP-XPS setup at BESSY . . . . .	45
<b>4</b>	<b>Unstationary reaction kinetics</b>	<b>47</b>
4.1	Introduction . . . . .	47
4.2	LEED . . . . .	48
4.2.1	Oxygen reconstructions . . . . .	48
4.2.2	Surface structures formed during the surface reactions . . . . .	51
4.3	PEEM . . . . .	54
4.4	TPD . . . . .	57
4.5	Reaction mechanism . . . . .	61
4.6	Conclusions . . . . .	63
<b>5</b>	<b>Stationary reaction under low pressure conditions</b>	<b>65</b>
5.1	Introduction . . . . .	65
5.2	Stationary reaction kinetics . . . . .	66
5.2.1	Temperature dependence . . . . .	66
5.2.2	Total pressure dependence . . . . .	72

5.2.3	Oxygen partial pressure dependence . . . . .	74
5.3	Adsorbate coverages and reactivity . . . . .	78
5.3.1	LEED and AES . . . . .	78
5.3.2	PEEM . . . . .	80
5.3.3	XPS . . . . .	83
5.4	Reaction mechanism . . . . .	91
5.5	Conclusions . . . . .	96
<b>6</b>	<b>Methanol oxidation in an intermediate pressure range</b>	<b>99</b>
6.1	Introduction . . . . .	99
6.2	Reaction kinetics . . . . .	101
6.2.1	Effect of the gas flow and the pump speed . . . . .	101
6.2.2	Effect of the sample pretreatment . . . . .	104
6.2.3	Dependence on the surface phases . . . . .	107
6.2.4	Effect of the gas mixing ratio . . . . .	109
6.3	Reduction of the oxidized copper sample . . . . .	112
6.3.1	Phase transition observed by optical microscopy . . . . .	112
6.3.2	Phase transition determined by ellipsometry . . . . .	114
6.3.2.1	Integrating ellipsometry . . . . .	114
6.3.2.2	Imaging ellipsometry . . . . .	120
6.4	Surface phases and reactivity . . . . .	122
6.5	Surface morphology and reactivity . . . . .	125
6.6	Conclusions . . . . .	128
<b>7</b>	<b>Pressure and material gap</b>	<b>131</b>
7.1	Introduction . . . . .	131
7.2	Pressure gap . . . . .	132
7.2.1	UHV studies below $10^{-2}$ mbar . . . . .	133
7.2.2	Studies under technical conditions . . . . .	134
7.2.3	Bridging the pressure gap . . . . .	135
7.3	Material gap . . . . .	137
7.3.1	Copper . . . . .	138

7.3.2	Copper oxides. . . . .	138
7.3.3	Microstructured bimetallic copper catalysts . . . . .	141
7.3.3.1	Pd/Cu(110) . . . . .	142
7.3.3.2	Cu/ZnO/Al <sub>2</sub> O <sub>3</sub> . . . . .	145
7.4	Conclusions and outlook . . . . .	148
<b>9</b>	<b>Summary</b>	<b>151</b>
	<b>Bibliography</b>	<b>157</b>
	<b>List of abbreviations</b>	<b>169</b>
	<b>List of Figures</b>	<b>171</b>
	<b>List of Tables</b>	<b>180</b>
	<b>List of publications</b>	
	<b>Curriculum Vitae</b>	
	<b>Acknowledgements</b>	

# Chapter 1

## Introduction

The mechanism of a chemical reaction can be described as a sequence of elementary steps resulting in the transformation of reactants into reaction products. In the case of heterogeneous catalytic reactions, such a sequence of elementary steps is filled by the steps of reactants adsorption on the catalyst surface, surface reactions and finally products desorption from the surface. Indeed, all these steps favor the occurrence of a chemical reaction in the presence of a catalyst. The question then arises as to how these single steps occurring on the catalyst surfaces can be disentangled. To probe the issue, over the past century many electron spectroscopies and microscopies appeared and have been developed that permit the studies, on the molecular or atomic level, of surfaces and adsorbates under ultrahigh vacuum (UHV) conditions. These studies have furthered our understanding of a broad range of phenomena that occur on metal or metal oxide surfaces: adsorbate bonding, coverage effects, coadsorption effects and reactions [1-5].

Apparently, the UHV approach has many advantages in that not only well-defined structural conditions are provided, but also a whole variety of optical and particle impact (mostly electron) spectroscopies can easily be applied. However, there is a serious disadvantage with the UHV model approach and this is why many practical chemists still have objections to this more “physical” treatment of the catalytic problem. They argue that the UHV model is too far removed from the reality, since catalytic reactions are typically carried out under quite different conditions, namely, at atmospheric (or even higher) pressures and with much less well-defined surfaces, namely, large area samples consisting of powders, pellets, thin films,

polycrystalline foils, or even multi-component catalysts with a whole variety of additives (promoters) which are common in the industrial technology. The existence of these famous “pressure gap” and “material gap” problems separates the UHV single crystal model studies, which is powerfully used to explore the elementary steps of catalytic reactions, from the technical chemical or catalytic investigations [6]. Since the 1980s, many researchers have devoted more attention to solving the problems in order to efficiently use the results of model studies to explain or even predict specific features of the catalytic action of certain systems [7, 8].

The content of this PhD thesis work is part of the effort to bridge the pressure and material gap in methanol selective oxidation over copper catalysts, which is a sub-project in DFG (German Research Foundation) priority program SPP 1091 “From Ideal to Real Systems: Bridging the Pressure and Material Gap in Heterogeneous Catalysis”.

The mechanism of methanol oxidation over copper surfaces has been extensively studied because of its relevance to the industrially important catalytic synthesis of formaldehyde [9, 10]. High yields of partial oxidation of methanol to formaldehyde have been obtained with copper catalysts in UHV conditions although in industry silver is still mainly used for that purpose. In addition, the interaction of methanol with copper surfaces is a key mechanistic step in several technologically important catalytic processes, i.e., methanol synthesis from “syngas” over Cu/ZnO catalysts, and methanol steam reforming over Al<sub>2</sub>O<sub>3</sub> supported Cu/ZnO [11-15].

A significant number of both high pressure studies [16-22] and low pressure single crystal investigations [23-43] have been published focusing on various aspects of methanol oxidation over copper surfaces.

For the product formation the following reactions can be formulated, in which formaldehyde is produced via dehydrogenation (1.1) or oxidative dehydrogenation (1.2); alternatively, the total combustion to CO<sub>2</sub> may occur (1.3) [20, 31].



Here reaction (1.1) is purely formula because this reaction is known not to take place on a clean copper surface and requires oxygen to proceed [31].

Single crystal studies with Cu (110), (111), (100) surfaces as catalysts, especially with the Cu(110) surface, have been conducted with temperature programmed desorption (TPD), molecular beam techniques, scanning tunnelling microscopy (STM), etc. [23-43]. These techniques were typically applied under unstationary conditions and carried out in UHV system.

Wachs and Madix [23] used thermal desorption spectroscopy (TDS) with selective isotopic substitutions to deduce many details of the mechanism on the Cu(110) surface and to infer the presence of several intermediates. Their work and that of many others clearly show that the oxygen free surface has a very low reactivity for the dissociative adsorption of methanol. Consequently, their reaction studies were largely confined to oxygen precovered surface. They concluded that methoxy,  $\text{CH}_3\text{O}$ , was the most abundant intermediate, whereas formate,  $\text{OOCH}$ , was identified as a less abundant but more stable intermediate.

While numerous studies have confirmed the prominent role of methoxy in the methanol oxidation mechanism, the role of the formate intermediate has been less clear. Bowker and Madix [24] concluded that formaldehyde desorption is the only significant pathway in methanol oxidation on the Cu(110) surface and the earlier report [23] of a formate intermediate was due to formaldehyde contamination in the methanol used. Sexton et al. dismissed their own observations of  $\text{CO}_2$  desorption as due to adventitious formaldehyde present during methanol exposures [42]. In a study of methanol oxidation on the Cu(111) surface using scanning kinetic spectroscopy, Russell et al. [43] also observed a small amount of  $\text{CO}_2$  desorption, and concluded that formate formation was an intrinsic feature of methanol oxidation on copper surfaces. A more recent TPD study on the Cu(110) surface indicated that formate was indeed a significant intermediate in methanol oxidation and that the amount of formate on the surface could be increased by altering the methanol dosing conditions [32]. Recent density functional calculations based on a  $\text{Cu}_{22}$  cluster [44] showed that formate formation from the reaction of methanol with oxygen on the Cu(111) surface is exothermic by 406 kJ/mol compared to only 74.8 kJ/mol for methoxy.

The microscopic details of the reaction on the Cu(110) surface have been mainly investigated with STM by Bowker et al and more recently by Leibsle *et al.*, with some studies reporting only methoxy and oxygen [26, 27], whereas others report observing methoxy, oxygen and formate [28, 41]. The difficulties associated with reproducibly identifying formate on Cu(110) in the course of methanol oxidation evidently originate from the detailed arrangements of the two-dimensional overlayer structures formed by both oxygen and methoxy, and that these structures are influenced by such factors as the rate of dosing, the order of dosing, the rate of heating and the time between dosing and surface analysis. From the observation of ordered adlayers of reactive intermediates with STM, a number of detailed insights into the reaction mechanism could be obtained [26-29], even though distinguishing between methoxy and formate adlayers with STM requires great care [39] since it is still in debate whether an ordered  $c(2\times 2)$  structure formed during the coadsorption of methanol and oxygen contains methoxy or formate species.

The main topics in high pressure studies of methanol oxidation over polycrystalline copper and copper foil can be summarized: (i) the identification of active phases and surface species using high pressure *in situ* techniques [16-22], and (ii) establishing the role of strain in determining the catalytic activity of copper under conditions of the real catalysis [14]. It was reported that the initial copper catalyst has to be activated by a pretreatment procedure with oxidation/reduction cycles. A complex scenario of a rate oscillation was discovered and related to the framework of a phase transition between metallic copper and copper oxides [19]. A novel sub-surface oxygen species was detected using *in situ* near-edge X-ray absorption fine structure (NEXAFS) spectroscopy and X-ray photoelectron spectroscopy (XPS). It exists during the reaction under high pressure conditions, and the presence of this new oxygen species could be correlated to the yield of formaldehyde [16, 20, 21, 22]. Furthermore, it was mentioned that the copper suboxide is formed by atomic oxygen penetrating the copper matrix which causes strain in the lattice of the copper crystal. However it is still under discussion how the strain affects the catalytic reactivity in real catalytic conditions [45].



Compiling previous UHV single crystal and high pressure polycrystal studies, it still remains unclear to what extent the adsorbates (oxygen, methoxy or formate) really determine the reactivity of the Cu(110) surface. Especially, the engraving contradictions existing due to the variation of measurement conditions (i.e., pressure and material) are not understood well yet. One way to tackle the problems is to measure the reaction kinetics under stationary conditions and to utilize the *in situ* techniques for probing the adsorbates variation on the surface, because any detailed mechanism has of course to be consistent with the macroscopic kinetics.

In this thesis, after a short introduction of the applied experimental techniques in chapter 2 and a description of the experimental setups in chapter 3, the unstationary reaction kinetics of methanol oxidation over a Cu(110) surface are firstly presented in chapter 4.

The steady state kinetics of methanol oxidation over a Cu(110) surface in the low pressure range from  $10^{-7}$  –  $10^{-3}$  mbar were systematically studied in a UHV system equipped with Auger electron spectroscopy (AES), low energy electron diffraction (LEED) and photoelectron emission microscopy (PEEM). Here, *in situ* AES, LEED and PEEM measurements permit us to relate the presence of certain adsorbate phases to the catalytic activity. Moreover, with the help of the *in situ* high-pressure XPS facility at BESSY (Berlin electron storage ring company for synchrotron radiation), the variation of the adsorbate layers during the reactions could be quantitatively determined using the very bright and tunable synchrotron X-ray source. These contents are presented in chapter 5.

Beyond  $10^{-3}$  mbar, the activities of different surface phases over a copper sample, which is originally a flat, well ordered and clean Cu(110) single crystal, were measured in a home-built high pressure reaction cell which is connected to a UHV chamber equipped with a quadrupole mass spectrometer (QMS) for gas analysis. In this system, ellipsometry is applied as a new *in situ* technique to revealing the variation of both surface and subsurface phases during the reaction. In chapter 6, some preliminary but promising results will be shown to explain the reaction kinetics under intermediate pressure conditions.

---

Finally, the efforts to bridge the pressure gap and material gap in methanol oxidation reaction are briefly summarized in chapter 7. As an important attempt to bridge the material gap in this thesis work, two well defined bimetallic model catalysts, Pd/Cu(110) and Cu/ZnO/Al<sub>2</sub>O<sub>3</sub>, were used to study the spatiotemporal dynamics of the reaction.

## Chapter 2

# Experimental techniques

### 2.1 Introduction

The investigation of the nature of adsorbed species and the kinetics and dynamics of surface processes represents a major research area in heterogeneous catalysis, which must be bolstered by a comprehensive characterization of the reaction mechanism with various spectroscopies, microscopies and other techniques. This is the reason that an experimental system is normally equipped with more than one technique, to obtain as much information as possible in order to achieve a general understanding of the catalytic reactions. A number of surface-sensitive techniques can be applied for providing different information of the surface catalytic reactions, for example, to define the structure, morphology and composition of the surface, and to determine the intermediates involving in the elementary steps that constitute the catalytic reaction.

In this work several techniques were used to study the reaction mechanism of methanol oxidation over copper model catalysts: traditional temperature-programmed techniques for adsorbates studies and rate measurements, Auger electron spectroscopy (AES) determining the elemental composition of the surface, low energy electron diffraction (LEED) determining the geometrical surface structure, photoelectron emission microscopy (PEEM) for spatio-temporal dynamics studies, X-ray photoelectron spectroscopy (XPS) providing quantitative analysis of the surface adsorbate layers, and Ellipsometry giving the information about the surface and

subsurface phases. A brief introduction to the principles of the above techniques and their applications in this thesis is presented in this chapter.

## 2.2 Nomenclature in surface science

Before describing the techniques, a brief summary of the notation used in surface science studies is given since in this thesis a single crystal sample is mainly used as the catalyst and surface structures are often discussed.

Each crystal surface has a specific crystallographic orientation identified by the plane along which the sample is cut. This plane is specified by the so called Miller indices, which are equal to the coordinates of the shortest reciprocal lattice vectors. Thus a plane with Miller indices  $h, k, l$  is normal to the reciprocal lattice vector  $h \mathbf{a}_1 + k \mathbf{a}_2 + l \mathbf{a}_3$ , where  $\mathbf{a}_i$  are the unit cell vectors [46]. To give an example, the Cu(110) surface is the copper substrate (face-centred cubic) cut along the plane orthogonal to the direction given by the vector  $\mathbf{a} = \mathbf{a}_1 + \mathbf{a}_2$  (here,  $|\mathbf{a}_1| = |\mathbf{a}_2|$ ).

Once an adsorbate presents on the surface, a notation to describe the overlayer is also necessary. Most of the so-called adsorbate superstructures can be assigned in Wood's nomenclature [47]. Firstly the adsorbate lattice vectors  $\mathbf{b}_1, \mathbf{b}_2$ , and the substrate unit cell vectors  $\mathbf{a}_1, \mathbf{a}_2$  should be defined. The relation between the adsorbate lattice and the substrate surface lattice is expressed by the ratios of the lengths of the vectors of the unit cell, i.e.,  $|\mathbf{b}_1| / |\mathbf{a}_1|$  and  $|\mathbf{b}_2| / |\mathbf{a}_2|$ . If the adsorbate lattice is rotated by an angle  $\alpha$  with respect to the substrate lattice, the value of  $\alpha$  is also indicated. Primitive (p) and centred (c) unit cells are indicated by p and c, respectively. Taken together, we may write for the surface structure of an overlayer of adsorbate species on the  $\{h, k, l\}$  plane of a crystal M:

$$M \{h, k, l\} - (|\mathbf{b}_1| / |\mathbf{a}_1| \times |\mathbf{b}_2| / |\mathbf{a}_2|) - R \cdot \alpha .$$

## 2.3 Temperature-programmed techniques: TPD and TPRS

There are a range of techniques for studying surface reactions and molecular adsorptions on surfaces which utilize temperature-programming to discriminate the processes with different activation parameters. Of these, the most useful ones for

single crystal studies are temperature-programmed desorption (TPD) and temperature-programmed reaction spectroscopy (TPRS), which have not substantive differences in the operation. The basic experiments are very simple, involving

1. For TPD: adsorption of one or more molecular species onto the sample surface at low temperature (frequently 300 K, but sometimes sub-ambient); For TPRS: inletting a stable reactant gas flow into the vacuum chamber so that the gases continuously react on the sample surface.
2. Heating of the sample in a controlled manner (preferably so as to give a linear temperature ramp) whilst monitoring the evolution of species from the surface into the gas phase. Comparing with a fast heating rate in a TPD experiment (0.5 K/sec up to 20 K/sec), a slow heating rate (lower than 10 K/min) is normally applied in the TPR experiment to ensure that the reaction is close to steady state conditions.

Normally the detector of choice is a quadrupole mass spectrometer (QMS), and the sample is very close to the QMS cone. The whole process is computer controlled with quasi-simultaneous monitoring of a large number of possible products (Fig. 2.1) [48]. Data obtained from such an experiment consist of the intensity variation of each recorded mass fragment as a function of time or temperature. The sensitivity of the technique is good with attainable detection limits below 0.1 ML (monolayer) of adsorbate in TPD.

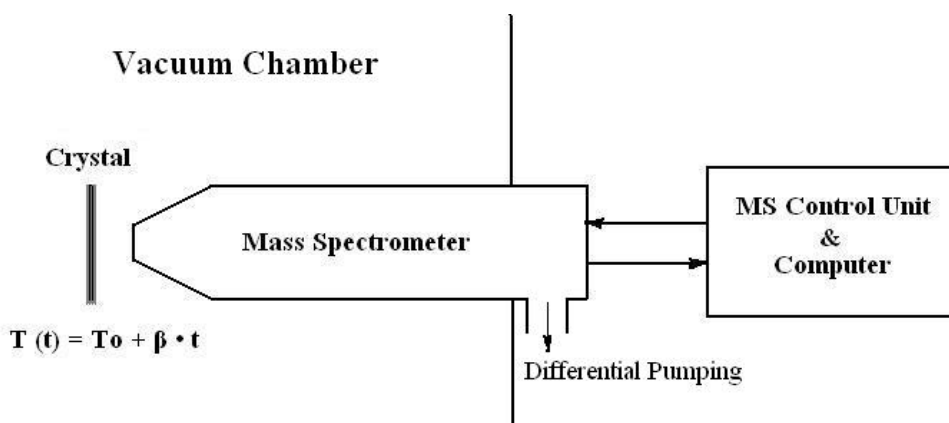


**Figure 2.1** Scheme of the experimental setup for temperature-programmed techniques.

From TPD experiment, the following points are worth noting:

1. The area under a peak is proportional to the amount originally adsorbed, i.e., proportional to the surface coverage.
2. The kinetics of desorption (obtained from the peak profile and the coverage dependence of the desorption characteristics) give information on the state of aggregation of the adsorbed species, e.g., molecular vs. dissociative.
3. The position of the peak (the peak temperature) is related to the enthalpy of adsorption, i.e., to the strength of binding to the surface.

In general, TPD offers plentiful information of the surface intermediates involved in the elementary reactions [49, 50], so that it was applied for adsorbate investigation and providing the information for unstationary reaction kinetics in this thesis. Whereas TPRS gives the most important information to describe the rate equation of the reaction, i.e., the way in which reaction rates depend on the temperature and the partial pressure of the gases [49]. In this work, TPR experiments were used to determine the stationary reaction kinetics in different pressure ranges.

## 2.4 Auger Electron Spectroscopy: AES

Auger Electron Spectroscopy was developed in the late 1960's, deriving its name from the effect first observed in 1925 by Pierre Auger, a French Physicist [48]. It is a surface specific technique utilising the emission of electrons in the Auger process, and is one of the most commonly employed surface analytical techniques for determining the composition of the surface layers of a sample. In this work, the technique has been used daily to check the cleanliness of the surface, and more importantly it was applied to providing the quantitative elemental information for *in situ* adsorbates analysis during the reactions.

### 2.4.1 The Auger process

If a solid is irradiated with a beam of electrons of medium or higher energy (1 keV ~ 10 keV), outer and inner electronic shells of the atoms are ionized. Relaxation

of the primary electron hole can occur in two different ways, which are illustrated in Fig. 2.2: [6]

1. The core hole is filled by an energetically higher electron of the same atom, and the resulting energy is emitted via electromagnetic radiation (X-ray), according to  $\Delta E = h\nu$ .
2. As before, the core hole is filled by an outer electron, but the energy equivalent is, in a radiationless manner, transferred to a second electron of the atom, namely, the Auger electron, which is ejected and leaves the atom with a characteristic kinetic energy  $E_{kin}$ .

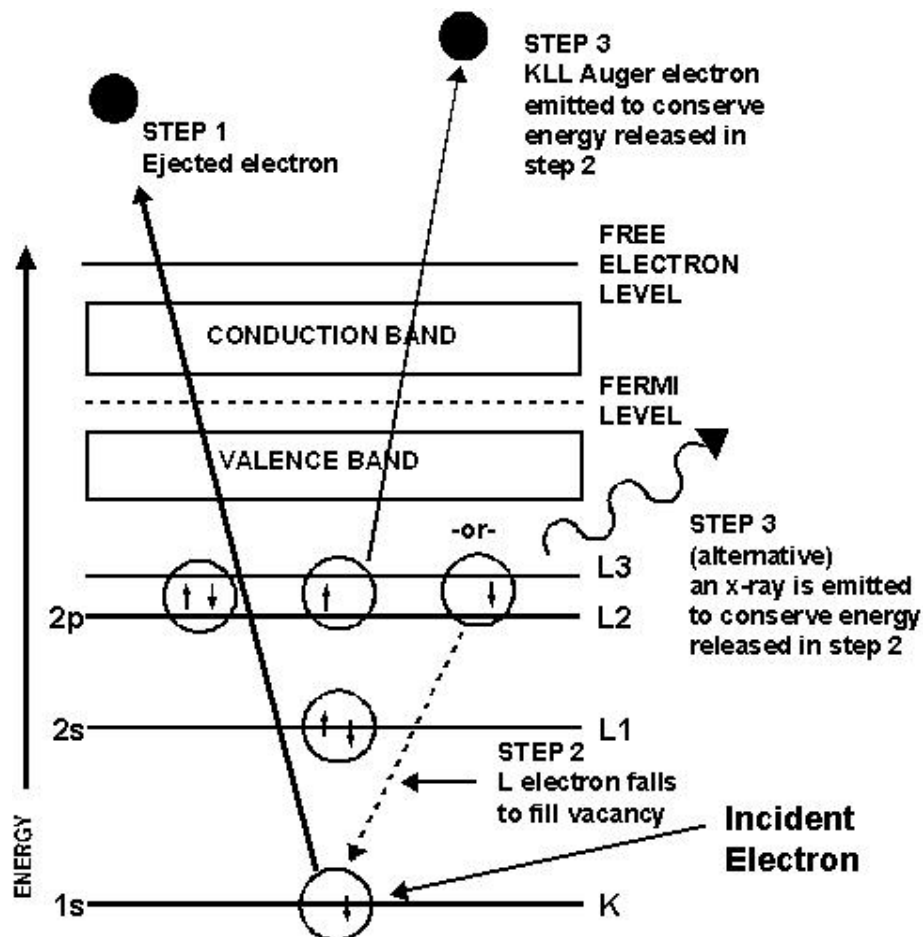


**Figure 2.2** Energy-level diagram illustrating the two possible filling mechanisms of a K-shell core hole generated by electron-impact ionization.

The most prominent property of an Auger electron is its kinetic energy, which is characteristic for a given atom. This can be clarified by explaining the three

processes that occur in Fig. 2.2. The first process is the ionization of an inner shell, say, a K shell (1s electron). The second process is the internal transition of an outer electron, for example, an L<sub>2</sub> electron (2p<sub>1/2</sub>), to the K shell to fill the hole. Apparently, a second electronic level becomes involved here. The third process is the energy transfer to a third electron (the Auger electron), often of the same shell (L<sub>2</sub> or L<sub>3</sub> = 2p<sub>1/2</sub>, 2p<sub>3/2</sub>), but of course, also from an outer (M) shell. No matter from where the Auger electron is emitted, three electronic states participate in the process, and with relaxation phenomena neglected, the kinetic energy (KE) of the Auger electron can be written by

$$KE = E_1 - E_2 - E_3, \quad (2.1)$$

where E<sub>1</sub> denotes the binding energy of the initial core electron prior to ionization, E<sub>2</sub> that of the electron that fills the core hole, and E<sub>3</sub> the binding energy of the ejected electron. The essence of using Auger electron spectroscopy as an element-specific analytical tool is that in each case the emitted electron carries a characteristic energy, which arises from the combination of energetically well-defined atomic levels unique for a given atom.

For atoms with many electron states, there are many possible different Auger transitions. According to the above process, Auger transitions are assigned by capital letters denoting the shells, whereby sub-figures indicate the participating sub-shells. The sequence of these capitals is chosen according to Eq. 2.1. For example, in Fig. 2.2, the Auger process can be named as KL<sub>2</sub>L<sub>3</sub> transition. Likewise, KLM, LMM, MNN, and NOO transitions can occur and lead to a wealth of Auger emission features for high Z elements.

## 2.4.2 The AES instrumentation

AES setup in its simplest form involves an electron gun with an up to 10 keV adjustable beam energy for a target excitation, and an electron spectrometer for energy analysis of the emitted Auger electrons. In the development of AES as a practical tool for surface analysis, several types of electron energy analyzers have been employed, including the 127° cylindrical analyzer, the retarding field analyzer used in the LEED-Auger apparatus, and the cylindrical mirror analyzer. Because of its



superior signal-to-noise capability, the cylindrical mirror analyzer (CMA) is used almost exclusively for modern AES apparatus. A schematic diagram of a CMA for obtaining Auger spectra is shown in Fig. 2.3.

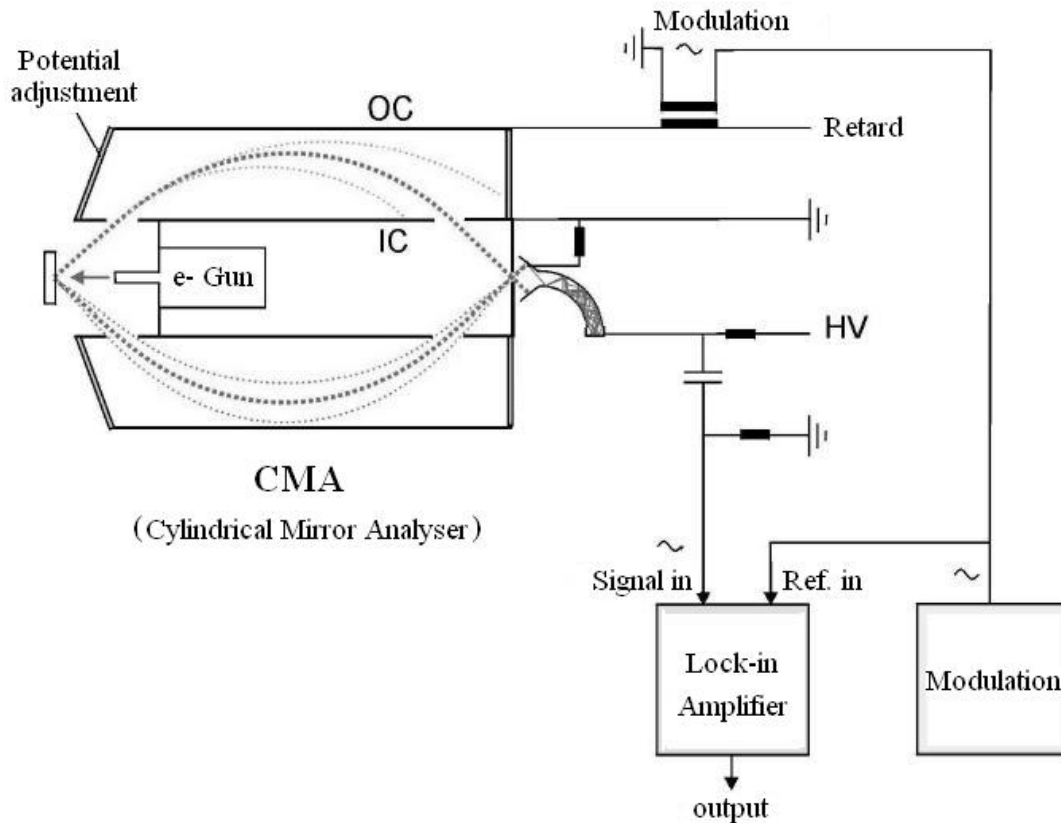


**Figure 2.3** Operation of the cylindrical mirror analyzer as an Auger Electron Spectrometer.

The CMA contains an internal electron gun mounted with its optical axis coincident with the CMA symmetry axis. The electron beam is focused on a point on the surface of the sample, which is positioned at the source point of the CMA. Auger electrons ejected from the point of excitation move radially outwards until they pass through a grid-covered aperture on the inner cylinder. A negative potential applied to the outer cylinder directs electrons with specific energy back through a second aperture on the inner cylinder and finally through a small exit aperture on the CMA symmetry axis. The pass energy,  $E$ , of the CMA is proportional to the potential applied to the outer cylinder. The range of electron energies,  $\Delta E$ , which are

transmitted, is determined by the resolution  $R$  given by  $R = \Delta E / E$ . For commercial AES,  $R$  is typically 0.5 %. [51]

The Auger electron energy distribution,  $N(E)$ , is generated by plotting the output of the electron multiplier vs. the negative voltage applied to the outer cylinder. The  $dN(E) / dE$  function is generated by superimposing a small a.c. voltage on the outer cylinder voltage and synchronously detecting the in-phase signal from the electron multiplier with a lock-in amplifier. The output signal is recorded: the Y-axis is proportional to  $dN(E) / dE$ , and the X-axis is proportional to the kinetic energy of Auger electrons emitted from the specimen.

### 2.4.3 Quantitative analysis

AES is a surface-sensitive spectroscopic technique used for an elemental analysis of surfaces. It offers a high sensitivity (typically ca. 0.01 ML) for all elements except H and He [48, 51, 53]. The intensity of a given Auger line deserves most attention because there is a direct proportionality between the number of excited atoms and the Auger intensity. Unfortunately, the actual situation in a quantitative determination of elements present on the surface is rather more complicated, because Auger electrons also can be excited in deeper layers of the solid. According to the electrons mean free path curve in solids as a function of their kinetic energy [52], at least three, sometimes up to five, atomic layers can contribute to an Auger electron spectrum. This makes an absolute quantitative AES measurement rather difficult.

In practical application of AES, a semiquantitative determination of the elemental composition is often sufficient. One approach is to compare the measured intensity from an unknown specimen with that from a standard with known composition under equal conditions. This method works quite well as long as matrix effects can be neglected, i.e., as long as pure elements can be used as standards [53]. Another approach is simpler but less accurate, that is, atomic concentrations can be calculated by first measuring elemental peak-to-peak heights in a spectrum and then applying sensitivity factors based on standard spectra of pure elements or selected compounds [51].

## 2.5 Low Energy Electron Diffraction: LEED

The name says everything: it's a technique based on the diffraction effect of low energy electrons scattered from the atoms of the surface. The obtained information is about the geometry of the surface and the existence of the ordered overlayers. This technique is often used due to the fact that it gives a wealth of information even without complicated analysis. In this work, it is also used as a daily fast check of the surface preparation.

### 2.5.1 Experimental setup of LEED

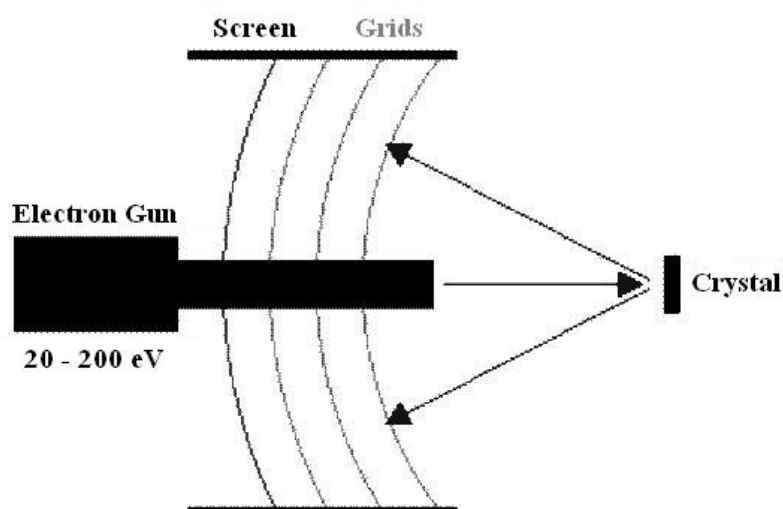


*Figure 2.4 Scheme of the experimental setup for LEED.*

A LEED experiment uses a beam of a well-defined low energy electrons (typically in the range 20 - 200 eV) incident on the sample. The sample itself must be an atomic periodical crystal with a well-ordered surface structure in order to generate a back-scattered electron diffraction pattern. A typical experimental setup is shown in Fig. 2.4 [48].

Only the elastically-scattered electrons contribute to the diffraction pattern; the lower energy (secondary) electrons are removed by energy-filtering grids placed in front of the fluorescent screen that is employed to display the pattern.

## 2.5.2 The theory behind LEED

Based on the principles of the wave-particle duality, a beam of electrons may be equally regarded as a succession of electron waves incident on the sample. These waves will be scattered by regions of high localised electron density, i.e., the surface atoms, which can therefore be considered to act as point scatterers. From de Broglie relation ( $\lambda = h / p$ , in which  $\lambda$  is the wavelength of the electrons,  $p$  is the electron momentum, and  $h$  is the Planck constant,  $6.626 \times 10^{-34}$  J s) the range of wavelengths of electrons employed in LEED experiments is comparable with atomic spacing, which is the necessary condition for diffraction effects associated with the atomic structure to be observed [48]. Furthermore the technique is sensitive just to the first few layers of the surface since the mean free path of the low energy electron interaction with the material is only  $\sim 5 - 10$  Å.

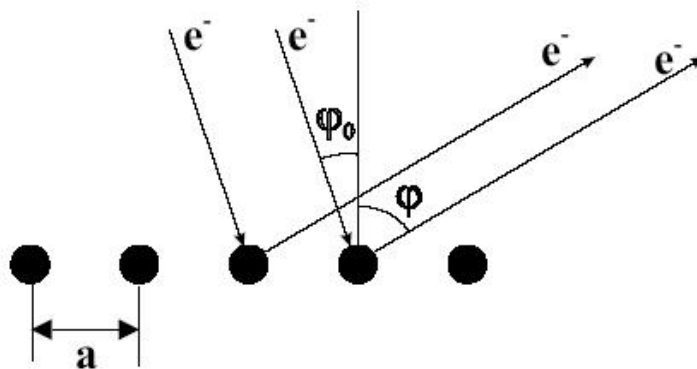


*Figure 2.5 Scheme of the diffraction process.*

The waves associated with the scattered electrons can have a constructive interference if they satisfy the Bragg diffraction condition: [3]

$$a (\sin \theta - \sin \theta_0) = n \lambda \quad (2.2)$$

in which  $a$  is the mutual distance between the scatterers,  $\lambda$  is the wavelength of the electrons,  $\theta$  and  $\theta_0$  are the incident and the reflected angles of the electrons, and  $n$  is the diffraction order (see Fig. 2.5). The diffraction condition can give origin to a good LEED pattern when a long range order of atoms is present ( $a$  should be constant to give sharp diffraction spots).

### 2.5.3 Diffraction and reciprocal space

In order to discuss the details of the information in a LEED experiment, the two-dimensional surface should now be considered, which can be regarded as an array of parallel rows of atoms along  $[h, k]$  direction with a distance  $d_{h,k}$ . The corresponding diffracted beam will appear in the same plane as the incoming beam, perpendicular to the direction  $[h, k]$ .

Again, in close analogy to Eq. 2.2, there will be interference maxima at angles  $\varphi$  given by

$$d_{h,k} (\sin \mathbf{j} - \sin \mathbf{j}_0) = n \mathbf{l} . \quad (2.3)$$

Most often, the LEED experiment is carried out under normal incidence conditions ( $\varphi_0 = 0$ ), and Eq. 2.3 simplifies to

$$\sin \mathbf{j} = n \mathbf{l} / d_{h,k} . \quad (2.4)$$

It is now quite important that the formation of a surface layer with a new or altered periodicity will give rise to additional or altered interference maxima, since the sensitivity of LEED is not restricted to the outermost layer; also, the second and third layers are imaged. It means the LEED pattern contains both the substrate maxima and additional spots caused by the overlayer. If the “grating” distance here is denoted by  $d'_{h,k}$ , one obtains

$$\sin \mathbf{j}' = n \mathbf{l} / d'_{h,k} , \quad (2.5)$$

a condition which is fulfilled simultaneously to Eq. 2.4, and additional diffraction spots appear on the LEED screen. These “extra” spots can be easily associated with ordered adsorbate layers or (in some cases), also with reconstructed surfaces; they help to identify adsorbate periodicities and coverages.

A more elegant description of the diffraction physics can be obtained using the Laue formalism in two dimensions, based on the concept of reciprocal space. If  $\mathbf{s}$  and  $\mathbf{s}_0$  denote the unit vectors for the directions of the scattered and incident beam, respectively, the interference conditions on a two-dimensional lattice (distance  $\mathbf{a}_1$ , of scatterers in  $h$ -direction, distance  $\mathbf{a}_2$  in  $k$ -direction) read:

$$\mathbf{a}_1 (\mathbf{s} - \mathbf{s}_0) = h \mathbf{l} \quad (2.6a)$$

$$\mathbf{a}_2 (\mathbf{s} - \mathbf{s}_0) = k \mathbf{l} \quad (2.6b)$$

The two equations 2.6 must be solved simultaneously for all possible  $\mathbf{s}$  at given  $\mathbf{s}_0$ ; the solution is found as

$$(\mathbf{s} - \mathbf{s}_0) / I = h \mathbf{a}_1^* + k \mathbf{a}_2^* = \mathbf{g}, \quad (2.7)$$

where the  $\mathbf{a}_1^*$  and  $\mathbf{a}_2^*$  are the unit mesh vectors, and  $\mathbf{g}$  is a translation vector of the so-called reciprocal lattice which is related with the real space lattice via the conditions:

$$\mathbf{a}_1 \cdot \mathbf{a}_1^* = 1 \quad (2.8a)$$

$$\mathbf{a}_1 \cdot \mathbf{a}_2^* = 0 \quad (2.8b)$$

$$\mathbf{a}_2 \cdot \mathbf{a}_2^* = 1 \quad (2.8c)$$

$$\mathbf{a}_2 \cdot \mathbf{a}_1^* = 0 \quad (2.8d)$$

This means that  $\mathbf{a}_1^*$  is always perpendicular to  $\mathbf{a}_2$  and has the length

$$|\mathbf{a}_1^*| = 1 / (|\mathbf{a}_1| \sin \mathbf{a}), \quad (2.9a)$$

correspondingly,  $\mathbf{a}_2^* \perp \mathbf{a}_1$ , and

$$|\mathbf{a}_2^*| = 1 / (|\mathbf{a}_2| \sin \mathbf{a}), \quad (2.9b)$$

whereby  $\mathbf{a}$  denotes the angle between the real space lattice vectors  $\mathbf{a}_1$  and  $\mathbf{a}_2$ . These relations can be used to construct the reciprocal lattice from the real space lattice and vice versa [6].

In a LEED experiment, one determines the direction of the diffracted beams (vector  $\mathbf{s}$ ) as points of intersection with the hemispheres of the LEED optics which are made visible as bright spots on the fluorescent screen. The well-known Ewald construction can serve to illustrate the interference conditions. Here it suffices to say that the LEED pattern obtained is a direct representation of the reciprocal lattice [54]. Since it is possible to relate the reciprocal space to the real space through equations 2.9, from a LEED pattern we can obtain the information about the geometry of the surface and the adsorbates layer.

## 2.6 Photoelectron Emission Microscopy: PEEM

Photoelectron microscopy uses electron lenses to directly image the photo-emitted electrons from the surface region of the specimen onto a screen, converting the electron image into visible light. The microscopy dates from the early 1930s, when electron lenses and so-called emission microscopes were developed [55-57].

Using PEEM, the different grey scales of the work function patterns can be imaged which give the spatio-temporal dynamic information of the surface adlayer variation in the catalytic surface reactions [58]. As a less destructive technique, in this work, PEEM grey intensities were used to *in situ* monitor the changes of the surface work function during the reactions. In addition, PEEM was also applied to studying the dynamic behaviour of the bimetallic model surfaces.

### 2.6.1 PEEM instrumentation

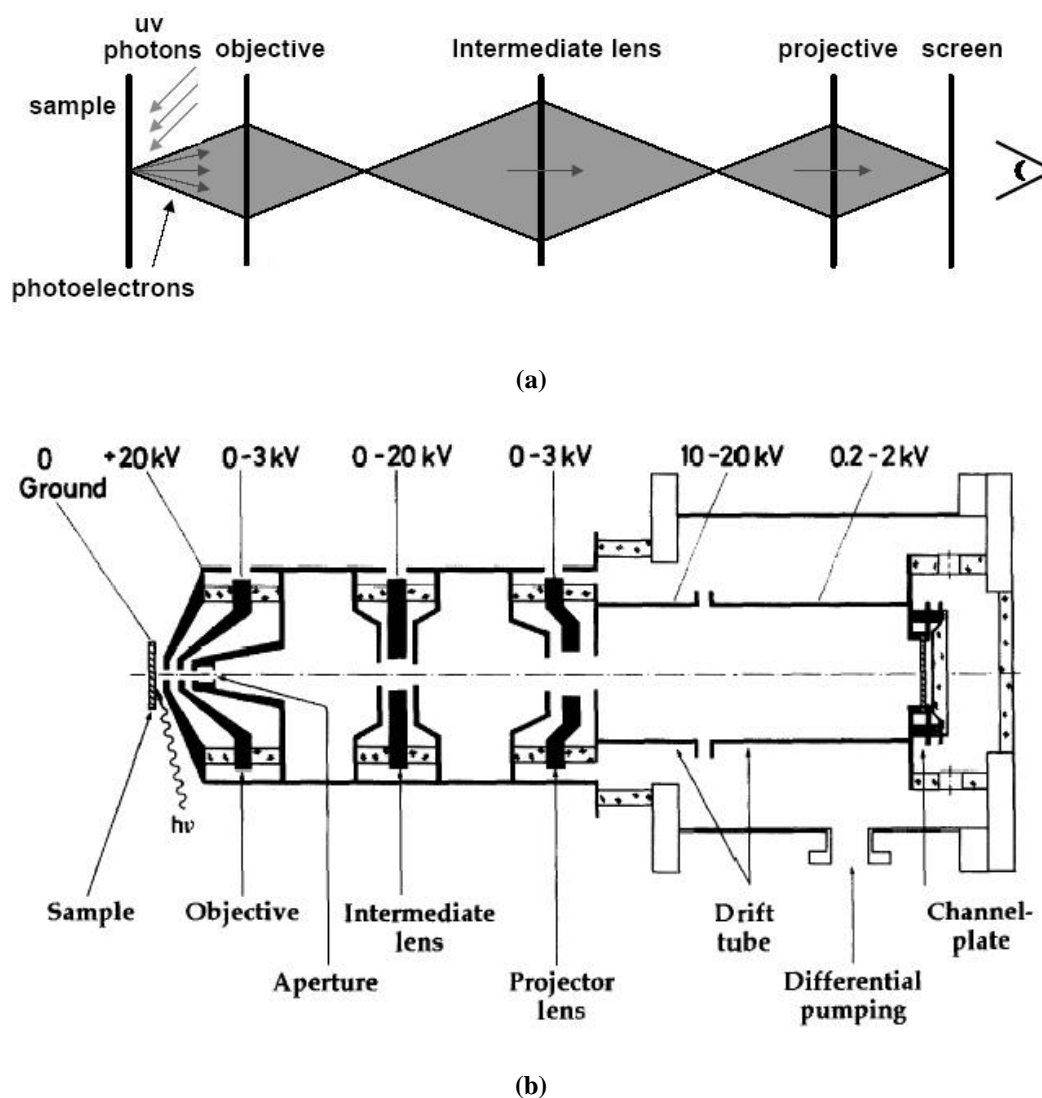


Figure 2.6 Schematic drawing of the Photoelectron Emission Microscope (PEEM).

The schematic drawing of the lens system in a PEEM is shown in Fig. 2.6 [58, 59]. It is a parallel imaging instrument, which uses the complete distribution of the emitted photoelectrons to image the surface region. The viewed area of the sample must therefore be illuminated homogeneously with appropriate UV-light.

As illustrated in Fig. 2.6 (a), the PEEM usually consists of an objective (cathode) lens, an intermediate lens and a projective lens.

In any emission electron microscope, the objective lens determines the lateral resolution. For the PEEM, the resolution  $r$  is approximately:

$$r \approx d \Delta E / e U$$

(2.10) with  $d$  being the distance between the sample and the objective,  $\Delta E$  being the distribution width of the initial electron energies and  $U$  the accelerating voltage. Using typical values of  $d = 4$  mm,  $\Delta E = 0.5$  eV and  $U = 20$  kV results in a theoretical resolution of  $r = 100$  nm [60]. For compensating lens aberrations a stigmator can be introduced between the objective and the intermediate lens. The stigmator / deflector can also be used for limited displacements of the imaged area without physically moving the sample in front of the objective [61]. Two different apertures, the so-called contrast- and the field-aperture, are used to cut certain electron trajectories in the imaging column. The contrast aperture is positioned in the back focal plane of the objective and is used to manipulate the angular distribution of the emitted photoelectrons. The field aperture is placed at the first real image inside the column. Here, only the central part of the image is transmitted, while the rest is cut by the field aperture. This option is of particular importance if information only of a selected area is required [58].

Next to the objective lens, the intermediate lens is used to vary the total magnification between  $100\times$  if the lens is deactivated, and up to  $1000\times$  when needed [60]; the projective lens combined with a two-element deceleration lens is applied to matching the electron velocity to the highest sensitivity of a multichannel plate (MCP) acting as the image intensifier. Finally, a screen is situated after the MCP to convert the electron image into visible light.

An additional problem for investigating surface reactions with a PEEM is the restriction of pressure below  $10^{-6}$  mbar. This is in part circumvented by the



differential pumping of PEEM which allows its operation up to pressure of  $10^{-3}$  mbar even in the presence of oxygen around the sample. To maintain three orders of magnitude pressure difference, an aperture of 300  $\mu\text{m}$  diameter has to be incorporated at the focus of the objective lens, as shown in Fig. 2.6 (b) [59].

## 2.6.2 Applications of PEEM

In a PEEM, the surface adsorbates can be studied using UV-light source, with the photon energy below 6.5 eV which is close to the work function  $\mathbf{f}$  of the surface. Due to the low excitation energy it constitutes probably the softest probe capable of sampling the electronic structure of the sample [59]. It is well known that adsorbates change the local work function of the substrate due to their dipole moment [62]. And the change of the local work function results in a contrast of the photoemission image, as long as the areas with a different work function are large enough to be resolved laterally by the instrument.

According to Fowler's theory [63],

$$Y \propto (\mathbf{h}\mathbf{n} - \mathbf{f})^2, \quad (2.11)$$

where  $Y$  is the photoelectron yield,  $\mathbf{h}\mathbf{n}$  is the photon energy and  $\mathbf{f}$  is the work function, it is possible to determine the absolute work function of the surface, clean or covered, to an accuracy of several meV, by plotting the square root of the total yield of photoelectrons versus the photon energy when the photon energy is varied from values 0.5 eV below  $\mathbf{f}$  to about 1 eV above the threshold. In a practical application of PEEM, since the grey scale intensity of the image is proportional to the photoelectron yield, the square root of the intensity value is shown to follow linearly the negative work function change, that is to say, high work function areas are imaged as dark, low work function areas as bright in PEEM. By plotting the PEEM intensity versus time or temperature, one can *in situ* study the surface work function change during the reaction. Furthermore, if the intensity of certain adsorbates could be determined, one can follow the change of the surface adlayers.

Heterogeneous catalysis is based on reactions between particles adsorbed on a surface. Even with a single-crystal surface and under steady state conditions, the

lateral distribution of adsorbates may be non-uniform. Such situations may be associated, for example, with temporal oscillations of the reaction rate, giving rise to spatio-temporal pattern formation. PEEM with the high enough lateral ( $\sim 0.1 \text{ }\mu\text{m}$ ) and temporal ( $\sim 20 \text{ ms}$ ) resolution is a unique tool for the investigation of “real time” spatio-temporal dynamics, especially for examining adsorbates diffusion in very small areas or on heterogeneous surfaces [64].

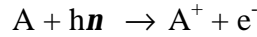
## 2.7 X-ray Photoelectron Spectroscopy: XPS

X-ray Photoelectron Spectroscopy was developed in the mid-1960' by Kai Siegbahn and his research group based on the photoelectron effect [65]. It is a widely used technique utilising the X-ray photo-ionization and energy-dispersive analysis of emitted photoelectrons to study the chemical composition of the surface region of a sample. Because it is often used for chemical analysis, the technique is sometimes also known as an alternative acronym, ESCA (Electron Spectroscopy for Chemical Analysis). In this work, XPS was applied to quantitative *in situ* analysis of the variation of the adsorbate layers during the reactions using a very bright and tunable synchrotron X-ray source.

### 2.7.1 Physical basis of XPS

Photoelectron spectroscopy is based upon a single photon in/electron out process. From many points of view this underlying process is a much simpler phenomenon than the Auger process. Monochromatic X-ray photons, with an energy  $E = h\nu$ , where  $h$  is the Planck constant and  $\nu$  is the frequency (Hz) of the radiation, illuminate the sample. The photon is absorbed by the sample atom, leading to ionization and the emission of a core (inner shell) electron. The kinetic energy distribution of the emitted photoelectrons (i.e. the number of emitted photoelectrons as a function of their kinetic energy) can be measured using any appropriate electron energy analyser and a photoelectron spectrum can thus be recorded [51].

The process of photoionization can be considered as looking an overall process as follows: [48]



The conservation of energy then requires that:

$$E(A) + h\nu = E(A^+) + E(e^-) \quad (2.12)$$

Since the electron's energy is present solely as the kinetic energy (KE) this can be rearranged to give the following expression for the KE of the photoelectron:

$$KE = h\nu - (E(A^+) - E(A)). \quad (2.13)$$

The final term in brackets, representing the difference in energy between the ionized and neutral atoms, is generally called the binding energy (BE) of the electron - this then leads to the following commonly quoted equation:

$$KE = h\nu - BE. \quad (2.14)$$

Note that the binding energies (BE) of energy levels in solids are conventionally measured with respect to the Fermi-level of the solid, rather than the vacuum level. This involves a small correction to the equation (2.14) in order to account for the work function ( $\phi$ ) of the solid,

$$KE = h\nu - BE - \phi. \quad (2.15)$$

For each element, a characteristic binding energy is associated with each core atomic orbital i.e. each element gives rise to a characteristic set of peaks in the XP spectrum at kinetic energies determined by the photon energy and the respective binding energies. The presence of peaks at particular energies therefore indicates the presence of a specific element in the sample under study.

Furthermore, different binding states of a given element, due to changes in the chemical structure and oxidation state, can be recognized by a systematic shift in peak positions in the XP spectrum which is so-called chemical shifts. Atoms of a higher positive oxidation state exhibit a higher binding energy due to the extra coulombic interaction between the photo-emitted electron and the ion core. This capability to discriminate between different oxidation states and chemical environments is one of the major strengths of the XPS technique. In practice, the resolution of atoms with slightly different chemical shifts is limited by the corresponding peak widths which are governed by a combination of factors [51]: the intrinsic width of the initial level and the lifetime of the final state; the line-width of the incident radiation which for traditional x-ray sources can only be improved by using x-ray monochromators; and

the resolving power of the electron-energy analyser, etc. In most cases, the second factor is the major contribution to the overall line width and the XPS resolution can be improved by using synchrotron X-ray radiation sources.

### 2.7.2 Experimental setup

The basic elements of an X-ray photoelectron spectrometer are depicted in Fig. 2.7.

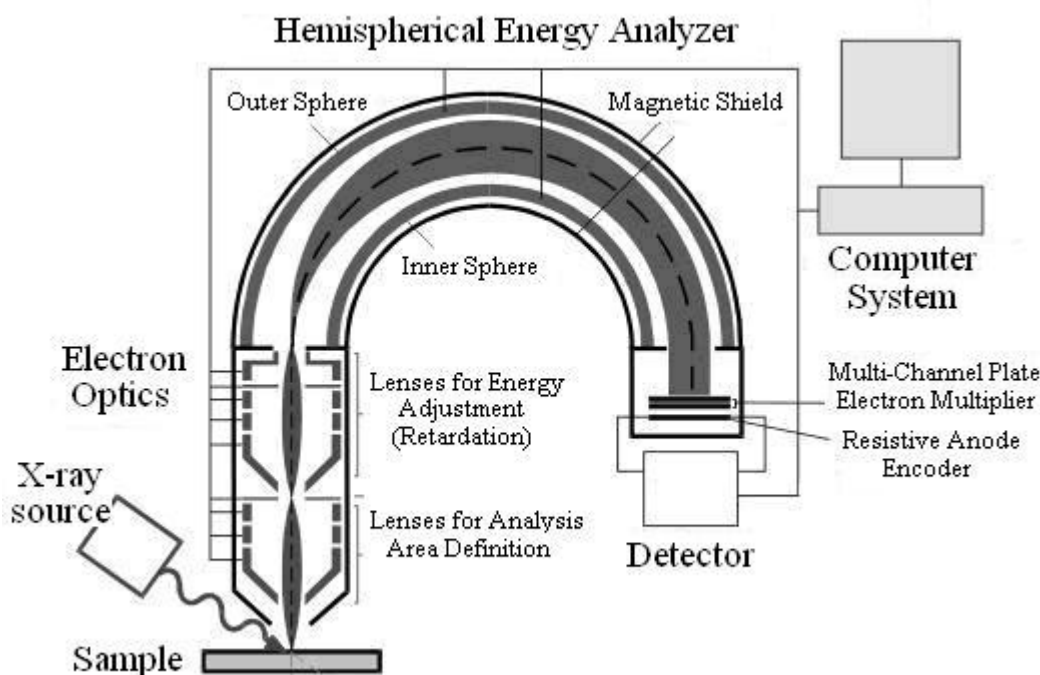


*Figure 2.7* The basic elements of an X-ray photoelectron spectrometer.

The X-ray source of a XP spectrometer produces intense X-radiation, which irradiates the sample and causes photon-ejection of the core electrons. The electron optics introduces the ejected electrons into an energy analyzer, where they are energy-analyzed and detected with the help of an electron multiplier in order to provide suitable signal intensity as a function of the electron kinetic energy or binding energy.

The most commonly employed laboratory X-ray sources are: Mg  $K_{\alpha}$  radiation ( $h\nu = 1253.6$  eV) and Al  $K_{\alpha}$  radiation ( $h\nu = 1486.6$  eV). Thus the emitted photoelectrons have kinetic energies in the range of ca. 0 - 1250 eV or 0 - 1480 eV.

Since such electrons have very short inelastic mean free paths (IMFP) in solids, the technique is very surface sensitive. The development of synchrotron radiation sources has enabled high resolution studies to be carried out with radiation spanning a much wider and more complete energy range (5 - 5000 eV). [48]

There are many different designs of electron energy analysers, but the preferred option for photoemission experiments is a concentric hemispherical analyser (CHA), which uses an electric field between two hemispherical surfaces to disperse the electron trajectories according to their kinetic energy. The detector commonly used is a multi-channel electron multiplier. The output of the multiplier is a series of pulses that are fed into a pulse amplifier / discriminator and finally into the computer system. [51]

### 2.7.3 Study of adsorbates with XPS

As mentioned in section 2.6, photoemission is a particularly useful tool for the study of adsorbed species on surfaces since it is intrinsically surface sensitive and much less destructive than electron impact spectroscopies. Even for high energy X-ray photons, the cross sections of photodesorption and photodissociation are small compared to the respective cross sections of the electron impact [53]. So XPS has the advantage of avoiding beam-induced effects to a large extent comparing with AES measurements.

For a given element, the line intensity is usually proportional to the number of excitable atoms and hence to its concentration, because the excitation probability of a core level is independent of the valence state of the atom. This allows exploiting XPS for quantitative determination of surface-adsorbate coverages. The height of the core level peaks is a relative measure of the adsorbate coverages. Calibration in absolute terms is also possible, e.g., at a known saturation coverage [53]. Therefore, sticking coefficients or adsorption and desorption kinetics can be observed by XPS. Furthermore, the energetic position of core lines yields the surface chemical shift. This surface chemical shift is composed of a relaxation and a bonding contribution, and if one of those can be calculated or is available from other data, the other can be derived.

## 2.8 Ellipsometry

Ellipsometry refers to a class of optical experiments which measure changes in the state of light polarization upon reflection from or transmission through a sample of interest. It is a powerful technique for the characterization of thin films on surfaces, which allows the determination of optical constants and thickness of a layer system [66]. It provides the information not only in the surface region but also in the subsurface layer. Furthermore it is a light in / light out technique and therefore has no pressure limitation. In this work, it was applied to *in situ* detection of the variation of the surface and subsurface phases during the reactions under intermediate pressure conditions.

### 2.8.1 Polarized light

Light is an electromagnetic wave consisting of an electric field  $\mathbf{E}$  and a magnetic field  $\mathbf{B}$ . Its features relevant for Ellipsometry can be described within the framework of Maxwell's theory [67]. The field vectors are mutually perpendicular and also perpendicular to the propagation direction as given by the wave vector  $\mathbf{k}$ .

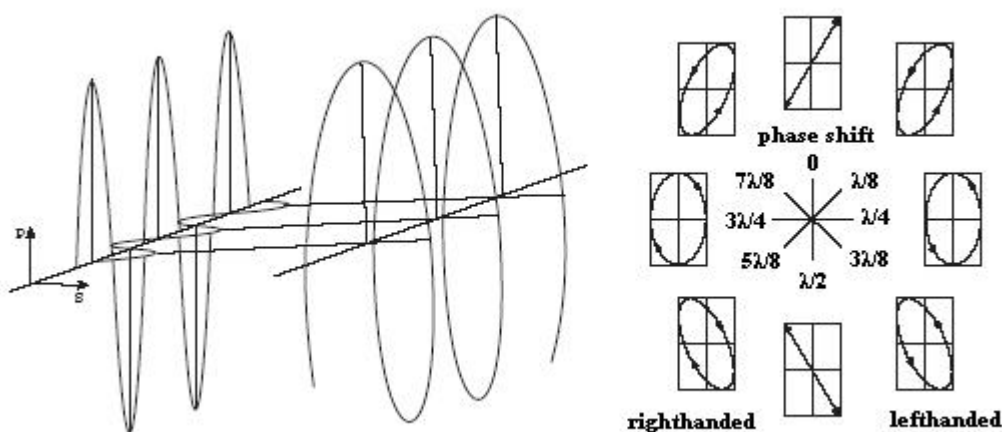


**Figure 2.8** The Jones representation of polarized light represents any state of polarization as a linear combination of two orthogonal linearly polarized light waves.

All states of polarization are classified according to the trace of the electrical

field vector during one period. A conventional mathematical representation of a given state of polarization is so called Jones vector [68]:

$$\mathbf{E} = \begin{pmatrix} |\mathbf{E}_p| e^{id_p} \\ |\mathbf{E}_s| e^{id_s} \end{pmatrix} = \begin{pmatrix} \mathbf{E}_p \\ \mathbf{E}_s \end{pmatrix} \quad (2.16)$$

where  $\mathbf{E}_p$  is the parallel component of the electric field  $\mathbf{E}$  lying within the plane of incidence,  $\mathbf{E}_s$  is the component of the electric field  $\mathbf{E}$  perpendicular to the plane of incidence (s for the German word “senkrecht”),  $|\mathbf{E}_p|$  and  $|\mathbf{E}_s|$  are the amplitudes,  $d_p$  and  $d_s$  are the phases.

Different states of polarization are depicted in Fig. 2.8. The state of polarization is

- linear, if  $d_p - d_s = 0$  or  $d_p - d_s = \pi$ ;
- elliptical, if  $d_p \neq d_s$  and  $|\mathbf{E}_p| \neq |\mathbf{E}_s|$ ;
- circular for the special case  $d_p - d_s = \pi/2$  and  $|\mathbf{E}_p| = |\mathbf{E}_s|$ .

Linear polarized light can be generated upon reflection from a surface at the Brewster angle  $\Phi_p$ , which is defined by the formula

$$\tan \Phi_p = n_2 / n_1 \quad (2.17)$$

where  $n_i$  are the refractive indexes of the materials involved [68].

## 2.8.2 Basic equations of Ellipsometry

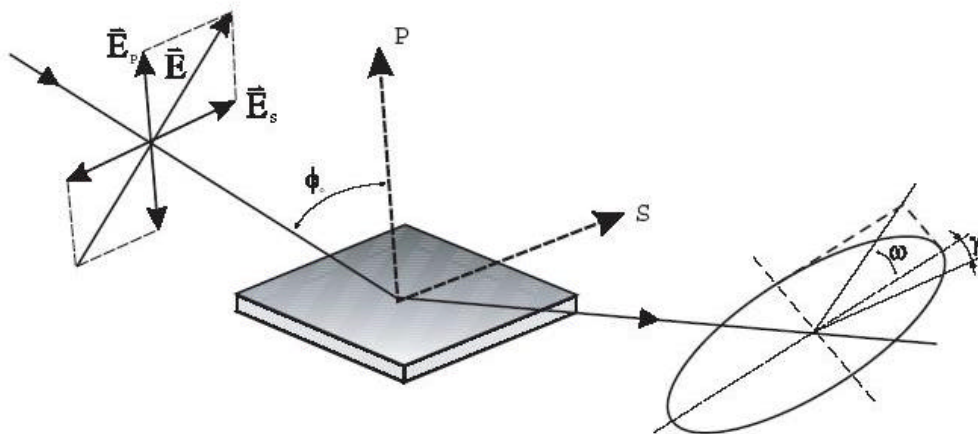


**Figure 2.9** Schematic drawing of the principle components of the electric field vector involved in a reflection experiment using linearly polarized light.

A schematic drawing of the principle components involved in a reflection experiment using linearly polarized light is shown in Fig. 2.9.

The incident linearly polarized light becomes elliptically polarized after reflection. The incident and reflected beam can be described by their corresponding Jones vector:

$$\mathbf{E}_{\text{inc}} = \begin{pmatrix} |\mathbf{E}_p^i| e^{id_p^i} \\ |\mathbf{E}_s^i| e^{id_s^i} \end{pmatrix} \quad \mathbf{E}_{\text{refl}} = \begin{pmatrix} |\mathbf{E}_p^r| e^{id_p^r} \\ |\mathbf{E}_s^r| e^{id_s^r} \end{pmatrix} \quad (2.18)$$

Two quantities, the relative change in phase difference  $\Delta$  and the change of the ratio of reflected to incident amplitudes  $\Psi$ , can be introduced to describe the changes in the state of polarization.

$$\Delta = (d_p^r - d_s^r) - (d_p^i - d_s^i) \quad (2.19)$$

$$\tan \Psi = \frac{|\mathbf{E}_p^r|/|\mathbf{E}_p^i|}{|\mathbf{E}_s^r|/|\mathbf{E}_s^i|} \quad (2.20)$$

With these definitions the basic equation of Ellipsometry is obtained

$$\tan \Psi \cdot e^{i\Delta} = \frac{r_p}{r_s} = \mathbf{r} = f(\text{wavelength } \mathbf{I}, \text{ layer parameters}), \quad (2.21)$$

to relate the measurable quantities  $\Delta$  and  $\Psi$  with the reflectivity properties of the sample [66], which are given by the corresponding Fresnel reflection coefficients  $r_p$  and  $r_s$  for p- and s- polarized light respectively. Their ratio  $\mathbf{r}$  is a complex quantity depending on the wavelength  $\mathbf{I}$  and the layer parameters of the sample (optical coefficients and layer thicknesses).

### 2.8.3 Ellipsometer

The basic setup of a typical ellipsometer is illustrated in Fig. 2.10 [66]. The main components are a laser light source, a polarizer (P) which produces linearly polarized light, a compensator (C) which introduces a defined phase retardation of one field component with respect to the orthogonal one, the sample (S), the analyzer (A) and a detector. Therefore, this setup is usually called the PCSA arrangement. With such a configuration, it is much easier to directly evaluate  $\Delta$  and  $\Psi$  from the



measured angle settings of polarizer and analyzer than with all other configurations, e.g. PSCA, PSA [68].

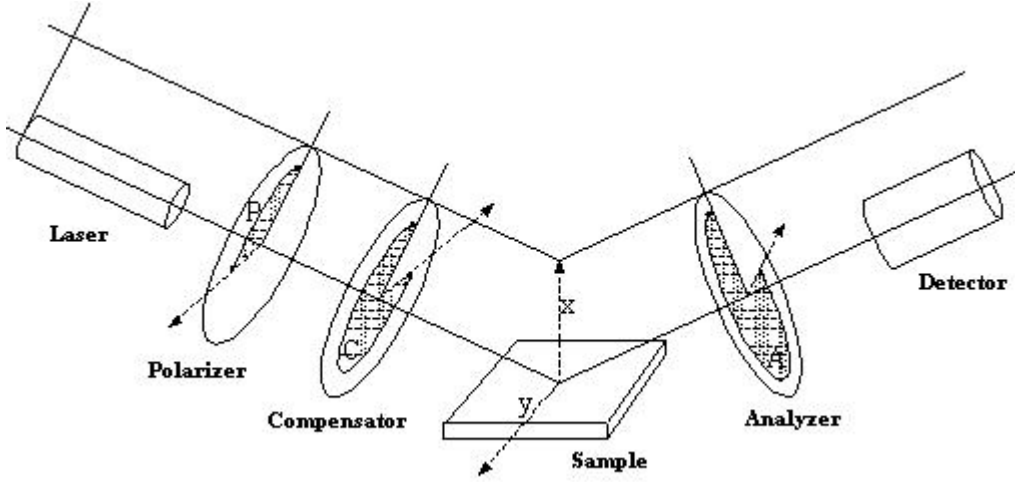


Figure 2.10 Ellipsometer in a PCSA-configuration.

We can describe the  $\mathbf{E}$ -vector at the detector as a function of the setting of all components including the unknown reflectivity properties of the sample:

$$\mathbf{E}_{\text{Detector}} = \mathbf{T}^A \mathbf{R}(A) \mathbf{T}^S \mathbf{R}(-C) \mathbf{T}^C \mathbf{R}(C - P) \mathbf{T}^P \mathbf{R}(P) \mathbf{E}_{\text{Laser}} \quad (2.22)$$

where  $\mathbf{T}$  is the Jones-matrix for the effect of each optical component,  $\mathbf{R}$  is the matrix to transform the vector between the coordinate systems of adjacent components [68]. One must understand equation (2.22) from right to left: the laser is linearly polarized by the polarizer with the matrix operator  $\mathbf{T}^P \mathbf{R}(P)$ , then the linear polarized light is rotated to the coordinate system of the compensator by the matrix operator  $\mathbf{R}(C - P)$ , then the compensator acts on the state of polarization as given by  $\mathbf{T}^C$ , then the existing light from the compensator is rotated to the coordinate system of the sample by the matrix operator  $\mathbf{R}(-C)$  and so on.

A particular implementation to simply measure the values of  $\Delta$  and  $\Psi$  is so-called Nullellipsometry, within which the setting of the optical components is chosen such that the light at the detector vanishes [66]. A given elliptical state of polarization of the incident light is generated with the help of the polarizer and compensator. It is adjusted in such a way that it leads to linear polarized light after reflection from the

sample. And then the linear polarized light can be completely extinguished with the help of the analyzer. The fast axis of the compensator is normally set to an angle of  $\pm 45^\circ$  with respect to the plane of incidence. With these requirements and conditions, the equation (2.22) can be simplified as

$$\tan \Psi \cdot e^{i\Delta} = \frac{\mathbf{r}_P}{\mathbf{r}_S} = -\tan \mathbf{A}_0 \exp\left(i\left(\frac{\mathbf{P}}{2} - 2\mathbf{P}_0\right)\right) \text{ if } C = 45^\circ \quad (2.23)$$

$$\tan \Psi \cdot e^{i\Delta} = \frac{\mathbf{r}_P}{\mathbf{r}_S} = \tan \mathbf{A}_0 \exp\left(i\left(2\mathbf{P}_0 + \frac{\mathbf{P}}{2}\right)\right) \text{ if } C = -45^\circ \quad (2.24)$$

which links the quantities  $\Delta$  and  $\Psi$  to the null settings of the polarized  $\mathbf{P}_0$  and analyzer  $\mathbf{A}_0$ . Once a setting  $(\mathbf{P}_0, \mathbf{A}_0)$  has been determined which provides a complete cancellation of the light, then the same holds for the pair  $(\mathbf{P}_0', \mathbf{A}_0')$ :

$$(\mathbf{P}_0', \mathbf{A}_0') = (\mathbf{P}_0 + 90^\circ, 180^\circ - \mathbf{A}_0) \quad (2.25)$$

These nontrivial pairs of nullsettings are referred as ellipsometric zones. Measurements in various zones lead to a high accuracy in the determination of absolute values for  $\Delta$  and  $\Psi$  [66].

It should be noted here, although accurate values for  $\Delta$  and  $\Psi$  have been directly measured, the calculated optical properties of a film or the film thickness might be completely incorrect if no appropriate model for the composition of the investigated system had been deduced first. Therefore, to extract useful information about a sample, it is necessary to perform a model dependent analysis of the ellipsometric  $\Delta$  and  $\Psi$  data. This simulation can be very difficult at times.

#### 2.8.4 Principle of imaging Ellipsometry

Ellipsometry can also be extended to an imaging technique which offers a wider field of applications [69]. Some surfaces under investigation are laterally inhomogeneous on a micrometer scale due to variations in the thickness or surface composition or due to changes in the orientational order of the molecules at the interface. In this case the lateral inhomogeneity is imparted to the properties of the reflected light. The most well-known imaging technique for a visualization of these features is Brewster Angle Microscopy (BAM) [70] which has been successfully

employed for characterizing the phase diagrams and the morphology of Langmuir films. BAM is based on the principle that the reflectivity of the P-polarized light is zero at the Brewster angle. Any modification of the Brewster conditions, as for instance the presence of a single monolayer, modifies the reflectivity. In contrast to BAM, imaging Ellipsometry is not bound to the existence of a Brewster angle and can even be employed for the investigation of monolayers on highly reflecting supports.

The changes in the setup of imaging Ellipsometry are fairly simple placing a magnifying objective lens between the sample and the analyser, and using a monochrom CCD-camera instead of the detector [66]. If one has succeeded to establish a uniform blank image of the surface, the “null” image, any local change of the reactant coverage results in a local change of  $\Delta$  and  $\Psi$ . These additional changes are not compensated for and give rise to a locally brighter image of the sample at the CCD-camera. So, in principle, it is possible to use Ellipsometry to image dynamic processes of adsorbates on a surface and to image surface reactions which normally occur between submonolayer coverages of the reactants on the catalytic surface.

Imaging Ellipsometry works under an oblique angle of incidence which imposes certain restrictions on the diameter and working distance of the objective. As a result the resolution is limited to about 1 – 3  $\mu\text{m}$  [71]. Another problem arises from the limitation of the so-called depth-of-field at a high magnification. While imaging, depending on the angle of incidence and the numerical aperture [72], only a region of the order of 1 – 50  $\mu\text{m}$  of the illuminated part of the sample is in focus.



# Chapter 3

## Experimental Setups

### 3.1 Introduction

The general intention of the thesis work is to bridge the pressure gap and material gap in the study of methanol selective oxidation over copper model catalysts. That is to say, the studies of the reaction under both ultrahigh vacuum conditions and relatively high pressure conditions are included in this thesis. A Cu(110) single crystal is mainly used as catalyst. Therefore a UHV system and a high pressure reaction cell combined with a UHV chamber (simply we call it the HP-UHV system below) are the main setups for this thesis work. In addition, a high pressure XPS setup (simply we call it the HP-XPS setup below) at BESSY was used to quantitatively study the adsorbate variation during the reactions. In this chapter, a detailed description of these experimental setups is given, some of the important operation methods of the instruments and experiments are presented as well.

### 3.2 The UHV system

Fig. 3.1 shows a schematic drawing of the UHV system which is equipped with various scientific instruments: Auger electron spectroscope (AES), low energy electron diffraction (LEED), quadrupole mass spectrometer (QMS), and photoelectron emission microscope (PEEM). A standard ion gun is used for the sample cleaning via ion etching. A highly precision, high rigid UHV specimen manipulator (OMNIAX) supports sample movements in the chamber in all directions (x-, y-, z-, turning in 360°,

and tilt). All the instruments were well calibrated to make sure the measurements are reliable.

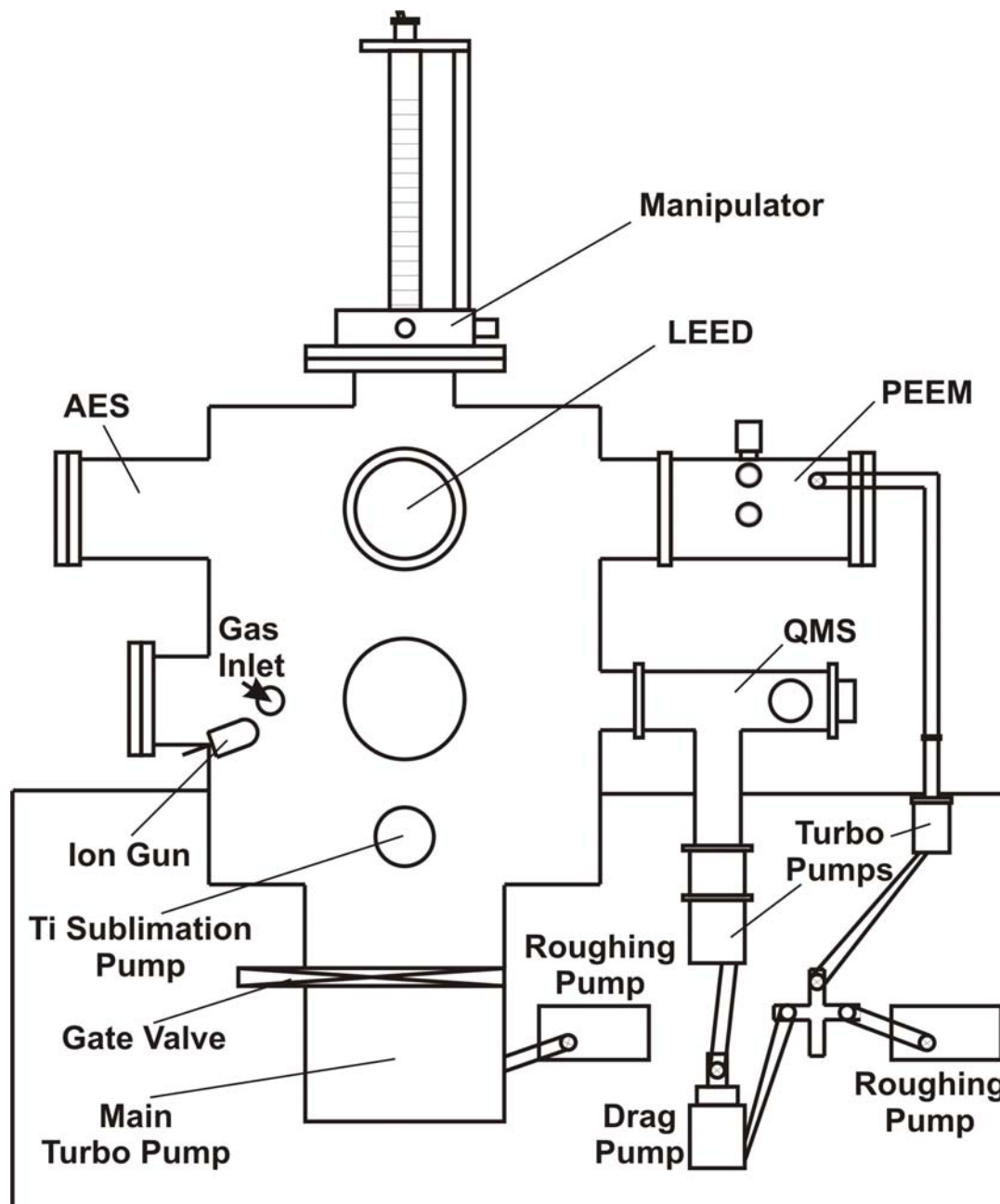


*Figure 3.1* Schematic drawing of the UHV system equipped with AES, LEED, QMS, and PEEM.

In PEEM the sample was illuminated with UV photons from a D<sub>2</sub> discharge lamp (photon energy  $\approx 6$  eV). The grey scale of the PEEM intensity was determined from digitization of the recorded PEEM images.

### 3.2.1 Ultrahigh vacuum

Ultrahigh vacuum is necessary mainly because it provides the condition to work with a clean sample and since the used techniques rely on electrons as probes [73]. To get such a low pressure condition ( $10^{-10}$  –  $10^{-9}$  mbar), the system is equipped with several kinds of pumps: roughing pump (above  $10^{-3}$  mbar), a turbo molecular pump ( $10^{-10}$  –  $10^{-3}$  mbar) and titanium sublimation pump (Fig. 3.1). QMS and PEEM are differentially pumped according to the requirement of their operations. The titanium sublimation pump is used to rapidly achieve a good background pressure. Normally after the sample cleaning procedure, a 10 second running of the titanium sublimation pump is necessary to get a  $10^{-9}$  mbar background pressure back soon. And after the long time reaction experiments, an overnight timed (each 0.5 – 1 hour depending on the pressure of the rest gases) running of the titanium sublimation pump is a feasible way to recover the UHV condition in the next day.

When the system is pumped after the venting, a procedure, called bake-out, has to be applied for days (chamber 150 – 180 °C, tubes above turbo pumps 120 – 150 °C, gas inlet system 100 – 120 °C), with the main purpose of pumping out the water adsorbed on the walls of the chamber. After the bake-out, all the filaments should be degassed to clean them from all impurities while the chamber is still hot.

### 3.2.2 Sample preparation

Four samples have been used and mounted into the UHV system: two Cu(110) single crystal samples, a Pd/Cu(110) microstructured sample and a Cu/ZnO/Al<sub>2</sub>O<sub>3</sub> microstructured sample.

Considered the design of the sample holder, all samples were mounted in the following way: the sample was fixed in a small tantalum frame, which was mounted on the sample holder by two tantalum wires serving for resistive heating. The sample temperature was monitored by means of a chromel-alumel thermocouple normally attached to the edge of the sample.

The dimensions of two Cu(110) single crystal samples are approximately 9 mm × 11 mm with a thickness of approximately 1.5 mm. They were cut to within 0.5°

of the (110) plane and polished mechanically down to 0.25  $\mu\text{m}$ . In the UHV chamber, the Cu(110) surfaces were cleaned by repeated cycles of  $\text{Ar}^+$  ion bombardment ( $P_{\text{Ar}} = 5 \times 10^{-5}$  mbar, 600 eV, and sample current 1.2 – 1.5  $\mu\text{A}$ ) followed by annealing to 800 K until no traces of S, C and O were detected by AES and a sharp (1 $\times$ 1) LEED pattern was observed. *In situ* AES (see chapter 5) showed that no impurities other than C and O containing adsorbates were present under reaction conditions. The reproducibility of the hysteresis measurements without additional cleaning cycles between two measurements (see chapter 5) ruled out the build-up of a significant amount of coke deposits.

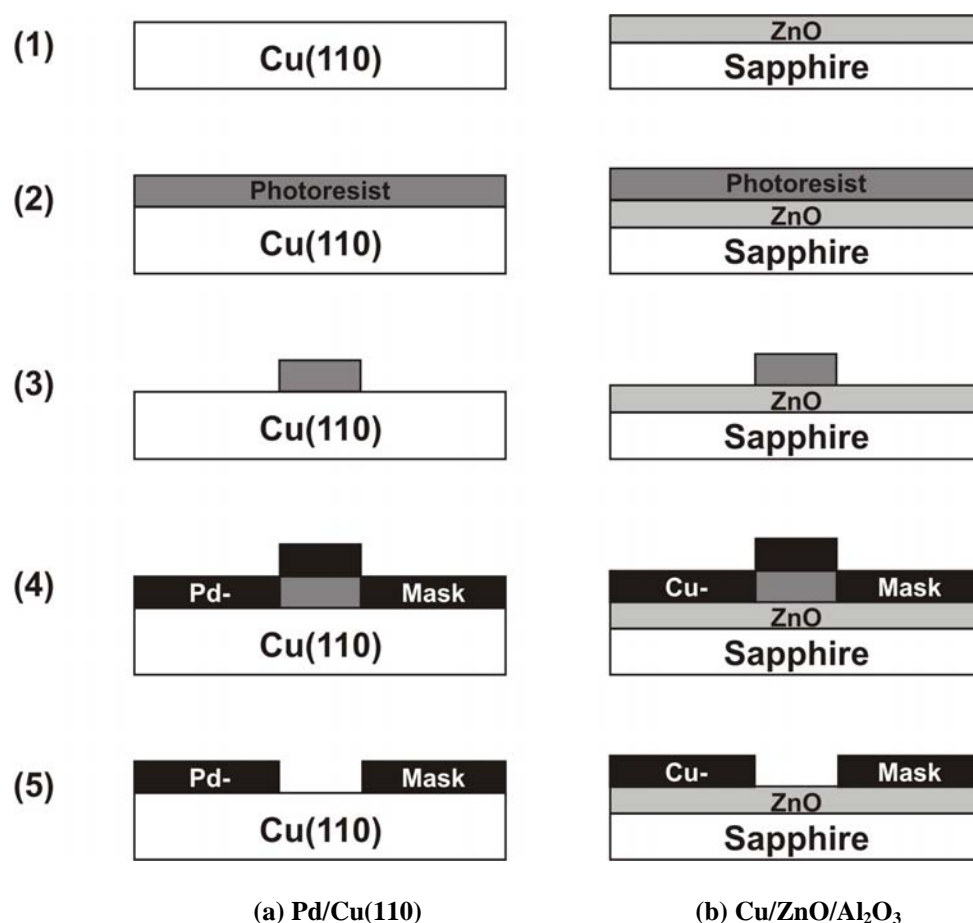


**Figure 3.2** Schematic drawing of the photolithography processes to prepare the microstructured Pd/Cu(110) sample (a), which has an approximate 1500 Å palladium layer on Cu(110); and Cu/ZnO/Al<sub>2</sub>O<sub>3</sub> sample (b), which has an approximate 1500 Å copper layer and a few micrometers ZnO layer on top of sapphire (Al<sub>2</sub>O<sub>3</sub>).



Both the microstructured copper samples were produced by photolithography at Institute of Physics, University of Hannover. As shown in Fig. 3.2, the standard steps involved in the photolithographic process are:

(1). Cleaning the crystal (Cu(110) or ZnO/Al<sub>2</sub>O<sub>3</sub>) with acetone, methanol and isopropanol; drying in the nitrogen stream.

(2). Laying on the photoresist (ARK 4040) on the crystal surfaces in a centrifuge with 3000 U/min for 60 s; baking at 90 °C for 5 min.

(3). Exposing the photoresist with UV light through the mask; development of the photoresist in the developer solution (AR 300-49) for 65 s; rinsing with distilled water and drying in the nitrogen stream; baking at 115 °C for 5 min.

(4). Evaporating the palladium layer on Cu(110) substrate (a) or the copper layer on ZnO/Al<sub>2</sub>O<sub>3</sub> substrate (b) by means of an electron beam evaporator with a pressure of  $2 \times 10^{-6}$  mbar (10 kV, 40 mA, approximately 1 Å/s); the thickness of the evaporated layer is about 1500 Å.

(5). Removing of the remaining photoresist by rinsing with acetone and isopropanol; drying in the nitrogen stream.

In order to avoid the formation of alloys on the well defined surfaces, a soft cleaning procedure was applied for the two microstructured samples: Ar<sup>+</sup> ion bombardment ( $P_{Ar} = 1 \times 10^{-5}$  mbar, 600 e V, and sample current 0.5 – 0.8 μA) followed by annealing to 600 K until no impurities can be detected by AES.

### 3.2.3 Gas calibration

The gas inlet system is connected to the UHV chamber by an all-metal valve. The gas line can be differentially pumped in order to change or pump the gases. All gases were introduced via leak valves, and for oxygen a feedback-stabilized gas inlet system (MKS) served for the control of the gas in pressure ramping experiments. Liquid methanol was filled in the clean glass tube (especially water free), which then was mounted into the gas line. The methanol vapour was purified by freeze-pump cycles using liquid nitrogen. Oxygen of purity 5.0 and methanol of purity 2.8 were used.

Calibration gases ( $H_2$ ,  $H_2O$ ,  $CO$ , formaldehyde, methanol,  $O_2$ ,  $CO_2$ ) were applied in order to relate the QMS signal to the partial pressures in the chamber. For water and methanol the vapour pressure over the liquid phase proved to be sufficient. In order to calibrate formaldehyde, the vapour pressure of solid para-formaldehyde was taken. From the detected mass intensities ( $m/e = 2, 18, 28, 30, 31, 32, 44$ ) by QMS, the true partial pressure were calculated by

$$\begin{bmatrix} P_{H_2} \\ P_{H_2O} \\ P_{CO} \\ P_{CH_2O} \\ P_{CH_3OH} \\ P_{O_2} \\ P_{CO_2} \end{bmatrix} = \mathbf{T}_{7 \times 7} \begin{bmatrix} I_2 \\ I_{18} \\ I_{28} \\ I_{30} \\ I_{31} \\ I_{32} \\ I_{44} \end{bmatrix}, \quad (3.1)$$

where  $\mathbf{T}_{7 \times 7}$  is the inverse matrix of  $\mathbf{S}_{7 \times 7}$  determined by

$$\begin{bmatrix} I_2 \\ I_{18} \\ I_{28} \\ I_{30} \\ I_{31} \\ I_{32} \\ I_{44} \end{bmatrix} = \mathbf{S}_{7 \times 7} \begin{bmatrix} P_{H_2, set} \\ P_{H_2O, set} \\ P_{CO, set} \\ P_{CH_2O, set} \\ P_{CH_3OH, set} \\ P_{O_2, set} \\ P_{CO_2, set} \end{bmatrix}. \quad (3.2)$$

From the pumping rates for the different gases, the flow rates also could be determined for each gas by

$$F \left[ molecule \cdot s^{-1} \cdot cm^{-2} \right] = P [mbar] \times 2.83 \times 10^{20} \times \sqrt{\frac{29}{m}}, \quad (3.3)$$

where  $m$  is the molecular weight of each gas.

Since the absolute partial pressures and the gas flows were obtained, the H-, O- and C-mass balance could be checked for all TPR-spectra presented in the thesis. Mass conservation for carbon checked by comparing the total consumption and total production is better than 5 %, for oxygen and hydrogen the corresponding numbers are below 20 %.

### 3.2.4 Rate measurement

For kinetic measurements, the system was operated as a continuous-flow reactor in the pressure range of  $10^{-7}$  mbar to  $10^{-3}$  mbar. The sample was moved close to a cone so that only gas molecules which were reflected from the sample could enter the cone and be detected by the QMS. We can therefore determine the reactive sticking coefficient  $s_{\text{reac}}$  *in situ* from the measured partial pressure variation of methanol and oxygen. Denoting the signal of a gas without reaction by  $I_0$  we calculate the reactive sticking coefficient  $s_{\text{reac}}$  as

$$s_{\text{reac}} = \frac{I_0 - I}{I_0}. \quad (3.4)$$

In our case the signal at 300 K is used as  $I_0$  since a reaction rate of practically zero has been measured at this temperature.

One notes that the ion source in our QMS system is in line-of-sight to the sample (see Fig. 2.1 in chapter 2). In principle, with this setup, the signal  $I$  should be corrected for the molecular velocity, which varies with surface temperature at  $T^{1/2}$ . However, in our measurements, since a cone positioned close to the sample separates the UHV chamber from the differentially pumped QMS system, nearly all particles leaving the sample (ejected into an angle of  $2\pi$ ) enter the QMS chamber where they hit the chamber walls several times and are equilibrated at 300 K before being detected by the QMS. We can nevertheless calculate that, if the QMS with an active area of about  $1 \text{ cm}^2$  ionization cage is positioned in line-of-sight at a distance of about 40 cm away from the sample, the fraction of ejected particles reaching the ionization chamber without hitting the chamber walls amounts about  $1 \text{ cm}^2 / (40 \text{ cm})^2 / 2\pi \approx 1 \times 10^{-4}$  which can be completely neglected. Therefore, no influence of the sample temperature has been considered in the calculation of the absolute reaction flow rate. Furthermore, this temperature factor would, however, cancel out because it would appear both in the denominator and in the numerator of the formula (3.4).

## 3.3 The HP-UHV system

Fig. 3.3 shows the arrangement of the HP-UHV system which was used to conduct the experiments under relative high pressure conditions ( $10^{-3}$  – 1 mbar).

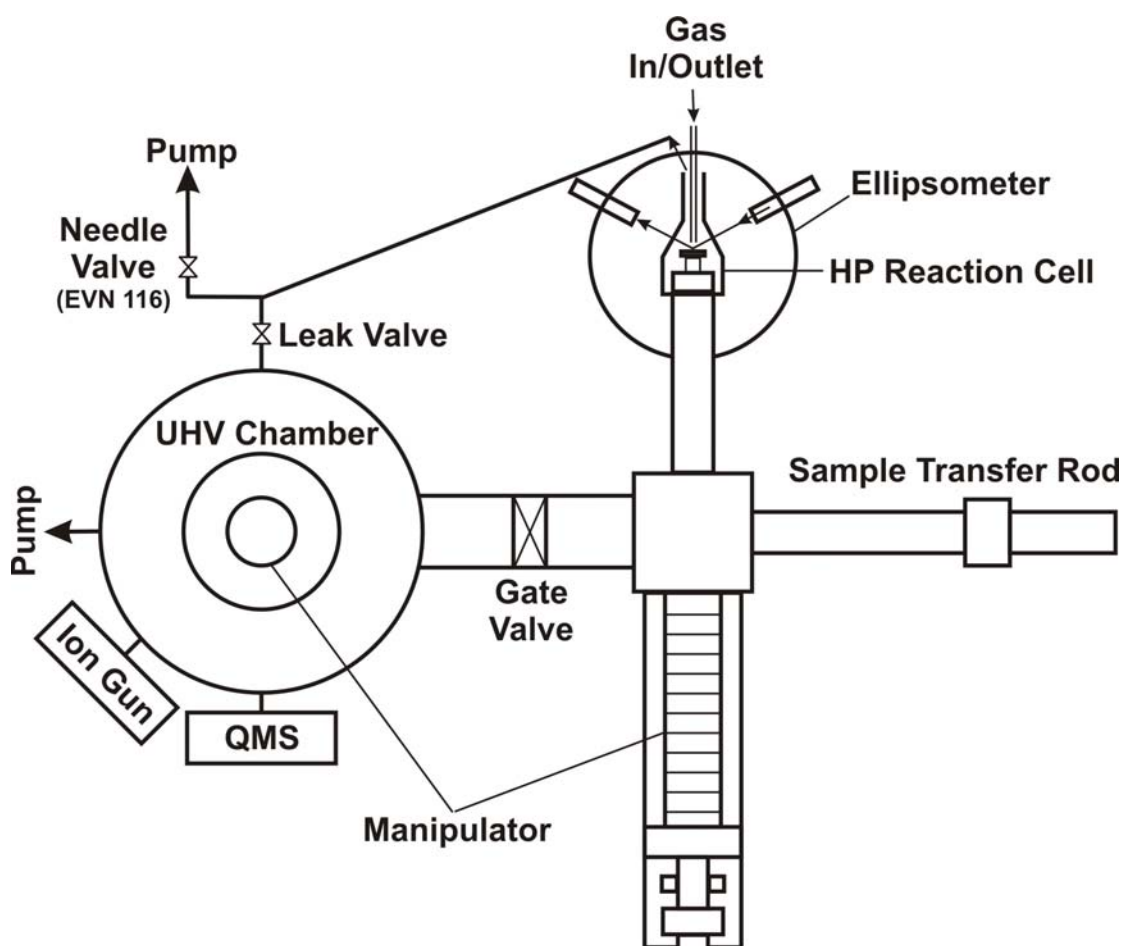


*Figure 3.3 Schematic drawing of the HP-UHV system equipped with ellipsometer.*

The high pressure reaction cell was separately pumped and connected to the UHV chamber by a gate valve, where the sample transfer rod can pass through. The UHV chamber, which has the background pressure at  $10^{-10}$  mbar, is equipped with an ion gun and a Hiden HALO 201 quadrupole mass spectrometer. The gases in the high pressure reaction cell can be leaked into the UHV chamber by means of a leak valve and analyzed by QMS. In principle, the sample can be cleaned in the UHV chamber, and then transferred to the high pressure reaction cell for *in situ* ellipsometry measurement. The pump speed in the high-pressure line can be varied by using an

adjustable needle valve (Pfeiffer EVN116) in front of the turbo molecular pump. And the full pump speed was calculated as about 0.4 L/s for gases.

### 3.3.1 Sample holder

A copper sample ( $9 \times 11 \text{ mm}^2$ , 1.5 mm thick), which is originally a flat and atomically well ordered Cu(110) single crystal, was used as the catalyst in the relative high pressure reaction experiments. As shown in Fig. 3.4, the sample was firmly mounted on a specially designed button-heater (SINTEC Ceramics GmbH) which enabled temperature programmed experiments in the 290 K – 750 K range. Heating ramps were adjusted by a PID controller (Eurotherm 2416) which controlled a programmable power supply (DELTA ES 030-10) feeding the button-heater. The sample temperature was monitored by means of a chromel-alumel thermocouple attached to the edge of the sample. The whole pieces were held on top of a sapphire, which can be conveniently slipped in and out of a support for smoothly sample transfer.

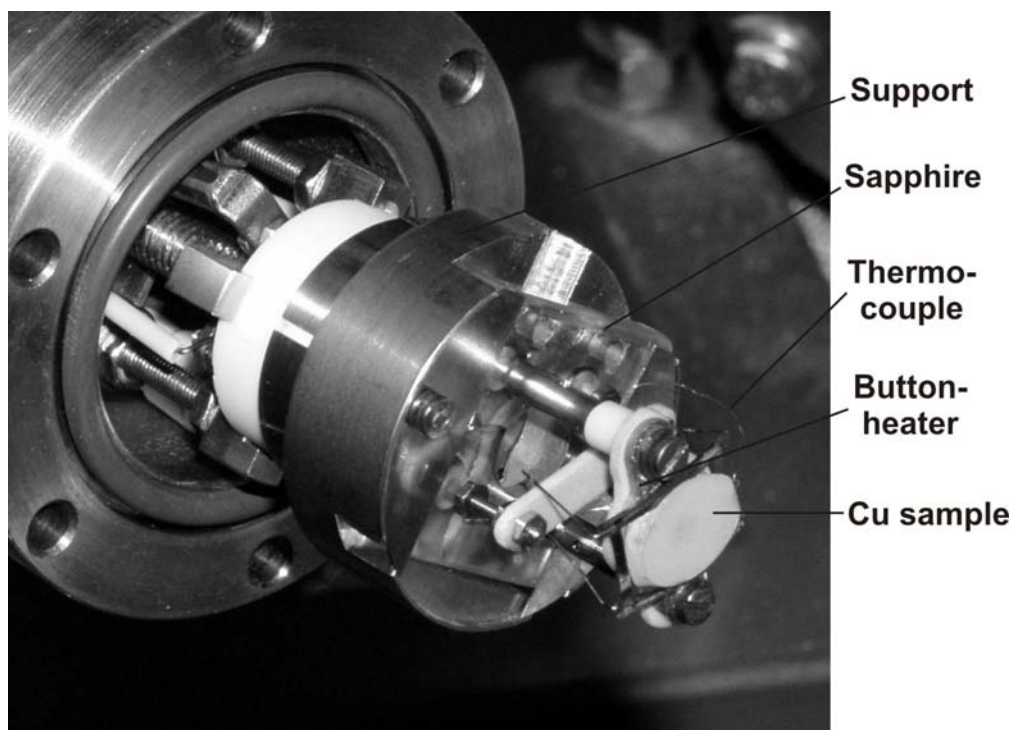


*Figure 3.4* The home-built sample holder for ellipsometer application.

### 3.3.2 High pressure reaction cell

The high pressure reaction cell was home-built and specially designed for the application of a commercial ellipsometer (Multiskop, Optrel GbR). As shown in Fig. 3.5, two quartz windows for the in and outgoing laser beam were used giving a reflection angle of  $70^\circ$  with respect to the surface normal. The reaction cell has a volume of approximate 0.1 liters.

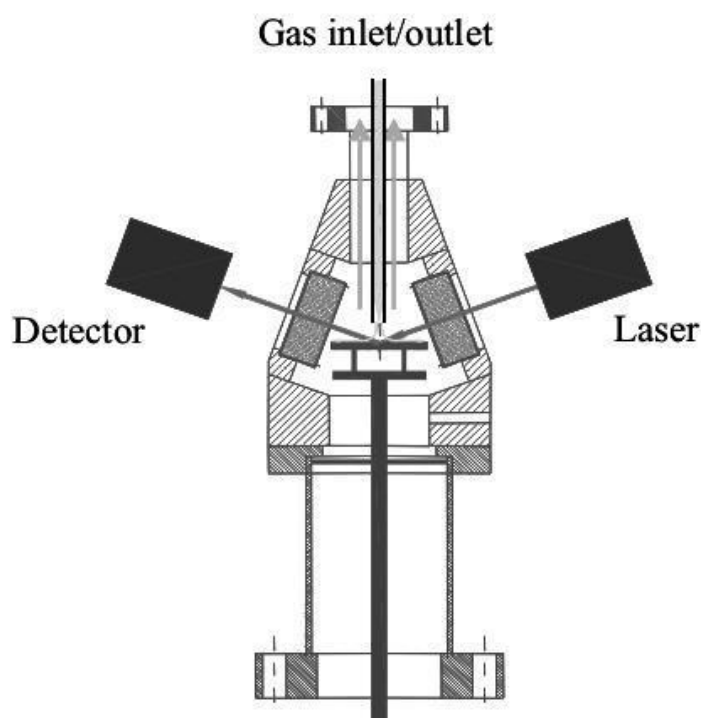


*Figure 3.5 Schematic drawing of the high pressure reaction cell for ellipsometer application.*

For kinetics measurements, the reaction cell was operated as a continuous-flow reactor. All gases were introduced via MKS flow controllers and reached the sample surface through a stainless steel pipe which faced the sample at a distance of  $\approx 2$  mm normal to the sample surface, as indicated in Fig. 3.5. The gases were then pumped out of the reactor through an exhaust concentrically mounted around the gas inlet pipe. The pressure in the reaction cell was measured by a Baratron pressure gauge (MKS 622A) and could be adjusted by setting a stable gas flow or choosing the desired pump speed. A small part of the exhaust stream was leaked into the UHV

chamber by means of a leak valve and monitored by QMS. The leakage of the leak valve and the pump speed were kept stable during all experiments.

Calibration gases ( $\text{H}_2$ ,  $\text{H}_2\text{O}$ ,  $\text{CO}$ , formaldehyde, methanol,  $\text{O}_2$ ,  $\text{CO}_2$ ) were also applied in this system in order to relate the QMS signal to the real partial pressures in the reaction cell. From the detected masses ( $m/e = 2, 18, 28, 30, 31, 32, 44$ ) and the total pressure in the reaction cell, the true partial pressure were calculated by a matrix inversion technique. From the obtained absolute partial pressures and the known gas flows, the H-, O- and C-mass balance can be checked for all presented TPR-spectra. Mass conservation for carbon checked by comparing the total consumption and total production is better than 5 %.

### 3.3.3 Alignment of the Multiskop ellipsometer

Fig. 3.6 shows the arrangement of the Multiskop ellipsometer and the high pressure reaction cell.

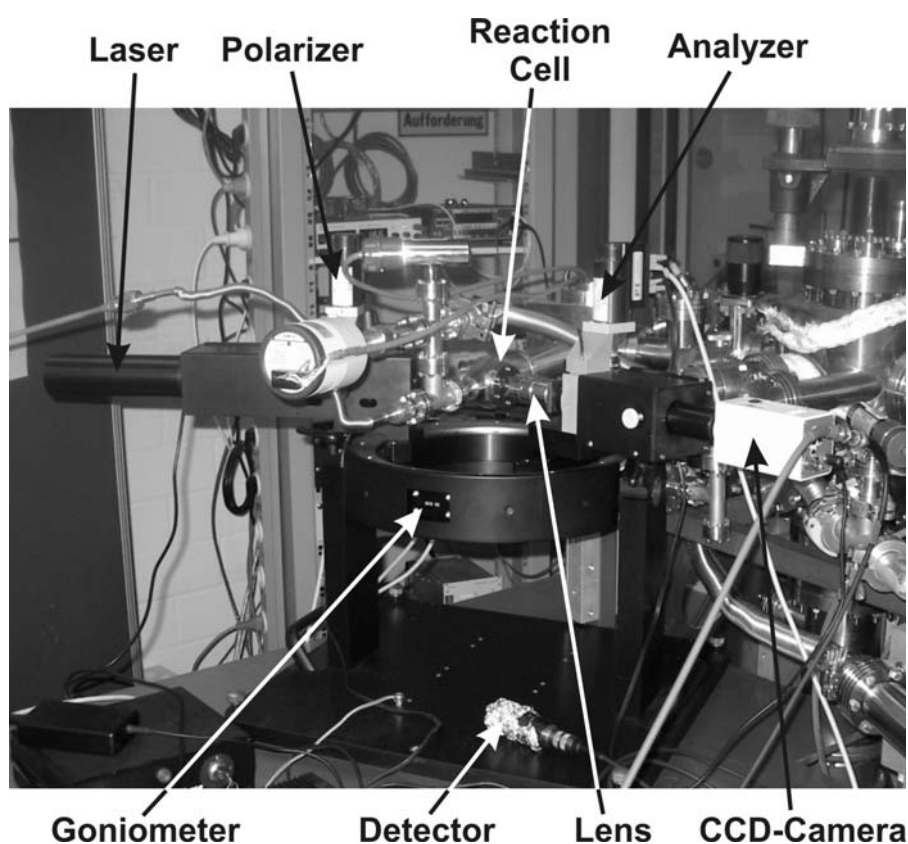


*Figure 3.6 Arrangement of the Multiskop Ellipsometer and the reaction cell.*

Before the measurement, a careful alignment of the position and the optical components of the Multiskop ellipsometer had to be conducted according to a defined procedure [66].

The optical components of the ellipsometer were pre-aligned externally with a standard layer material, for example, the oxidized Si-wafers. The alignment steps include obtaining circularly polarized light, defining angular position of Polarizer and Analyzer, defining angular position of compensator, and finally checking the angle of incidence.

Then as indicated in Fig. 3.6, the ellipsometer was moved to the reaction cell and the relative position of the ellipsometer to the reaction cell was carefully aligned. For alignment, the cover of the reaction cell had to be removed, and the sample surface was exposed directly to the laser beam.

1. Definition of the plane of incidence: The plane of incidence, which all angles of the polarization optics refer to, is defined by the laser beam and the normal of the sample. The laser beam should be firstly aligned parallel to the laser and detector arms. And then the relative position of the laser arm and the sample had to be carefully adjusted until the incident point on the sample surface did not move while the angular position of laser arm (the angle of the incident beam) was changed.

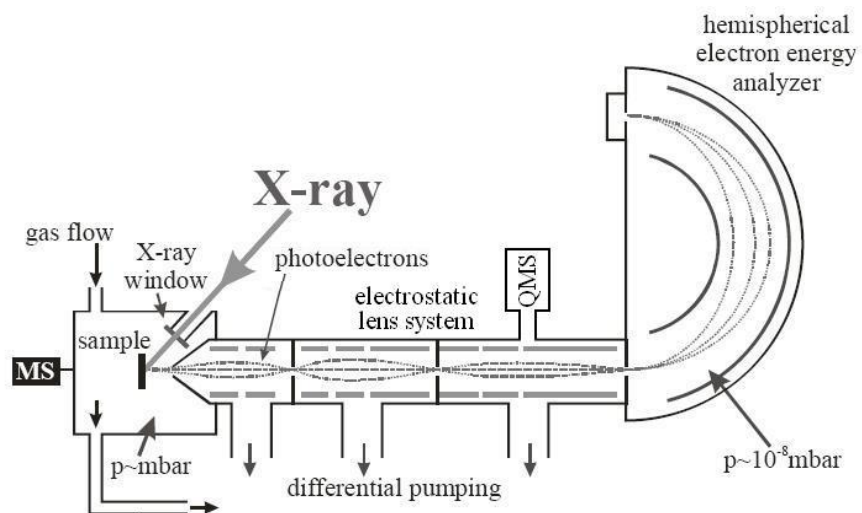
2. Definition of the angular positions of the laser arm and the detector arm: The easiest way to define the angular position of laser and detector arms is to first define the zero degree position of the laser arm and then the 90 degree position of the detector arm.

Here, the step 1 and step 2 may be necessary to be operated cyclically until the plane and the angles of incidence and reflection are well defined.

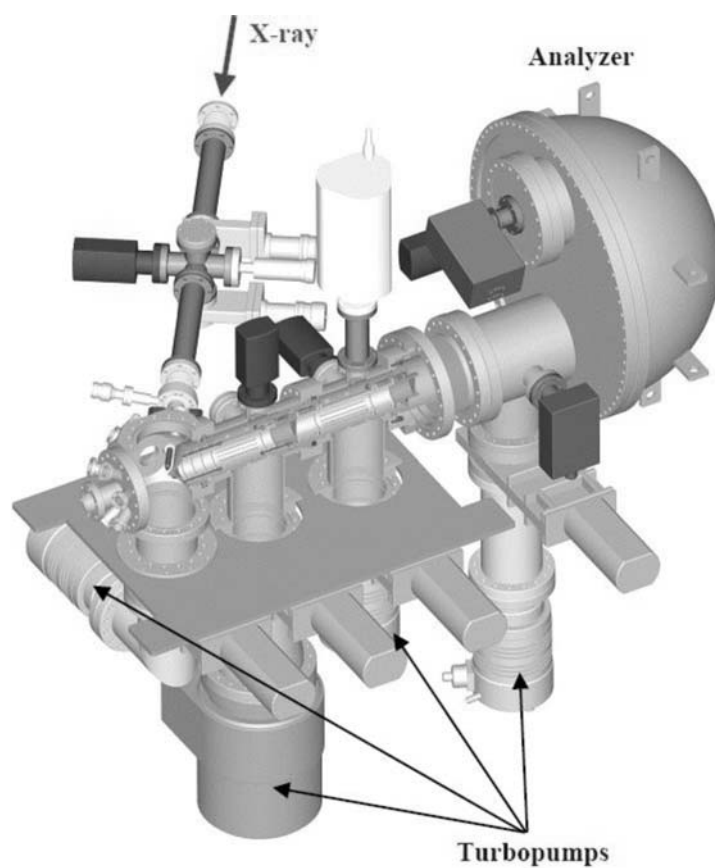
For the kinetic ellipsometry measurement, two parameters ( $\delta$  and  $\psi$ ) were determined in the so called 1/3-zone scheme measuring the reflected light intensity over a  $1 \times 2 \text{ mm}^2$  large illuminated sample area using a photodiode in the detector. For imaging ellipsometry, as shown in Fig. 3.6, a 5 × lens and a 1/2" monochrom CCD-camera instead of the detector provide a serial of surface images in ellipsometric contrast.



### 3.4 The HP-XPS setup at BESSY



(a)



(b)

Figure 3.7 Schematic drawings of the in situ HP-XPS setup at BESSY.

Fig. 3.7 shows the schematic drawings of the HP-XPS setup using synchrotron X-ray source at BESSY.

X-rays are admitted to the experimental cell through a 100 nm thick SiN<sub>x</sub> window, where they illuminate the sample surface. The emitted photoelectrons enter a differentially pumped electrostatic lens system and are focused on the entrance slit of a standard electron energy analyser, where high vacuum conditions are maintained by another pumping stage.

As shown in Fig. 3.7, the application of the differential pumping stages allows minimizing the travel path of photoelectrons in the gas phase so that a high pressure gas atmosphere can be introduced into the sample cell instead of the obligatory UHV conditions in the conventional XPS system. The maximum gas pressure in the sample cell during *in situ* analysis is limited by several factors, like the distance between sample and the first aperture, the intensity of the X-ray light, the photoelectron collection and the detection efficiencies, the kinetic energy of photoelectrons and the type of the gas. In practice, the setup allows tuning the total pressure in the reaction cell between 10<sup>-7</sup> mbar and 1 mbar.

A Cu(110) single crystal was mounted onto a temperature-controlled sample stage in the experimental cell. The sample temperature was varied with the help of an infrared laser heating system in the range from 300 K - 800 K. The Cu(110) surface was cleaned by repeated cycles of Ar<sup>+</sup> ion bombardment ( $P_{Ar} = 5 \times 10^{-5}$  mbar, 600 e V, and sample current 1.2 – 1.5 μA) followed by annealing to 800 K until no trace of contamination was detected by XPS.

The gases in the reaction cell can be monitored by two QMS systems shown in Fig. 3.7 (a): a BALZERS PRISMA<sup>TM</sup> QMS which connected to the reaction cell by means of a leak valve, and a Hiden HALO 201 QMS which is located in the differential pumping stage in front of the analyzer. In our experiments, the kinetics measurements were mainly conducted with the Hiden QMS system. In order to control the gas flow reaching the Hiden QMS detector, the pump speed of the differential pumping stages had to be adjusted accordingly.

# Chapter 4

## Unstationary reaction kinetics

### 4.1 Introduction

The study of the reaction mechanism on a surface can be broken down into three distinct questions [27]: how does the reaction occur on the surface, what do the reaction products do while they are on the surface, and how do they leave the surface? Even though these questions are to some degree coupled, it is still the most intuitive way to separately investigate the processes occurring on the surface and to present the data and interpretation pertinent to each of the above questions. These investigations are typically carried out under unstationary reaction conditions in a UHV system and can yield detailed insight into the reaction mechanism.

The adsorption and partial oxidation of methanol on the oxygen precovered Cu(110) surface have been studied with a variety of surface sensitive techniques [23-27]: TPD and molecular beam reaction measurements have been used to determine the chemical nature of the adsorbed species and the formed products; LEED and STM have been employed to determine the surface structure of the oxygen covered surface and the structures formed by reaction with methanol. However, there still exist some contradictive points: i) under which condition formate forms on the surface and ii) what is its ordered surface structure.

In this chapter, the unstationary reaction kinetics of methanol oxidation over Cu(110) surface are presented by combining our TPD, LEED and PEEM experimental results with the former STM studies mainly conducted by the group of

M. Bowker. The detailed reaction pathways are summarized so that the following studies under stationary reaction conditions can be better understood.

## 4.2 LEED

All the adsorbate-induced ordered structures observed in the former studies with LEED and STM in connection with the system Cu(110) / CH<sub>3</sub>OH + O<sub>2</sub> were obtained in our experiments as sharp LEED patterns as demonstrated in Fig. 4.1.

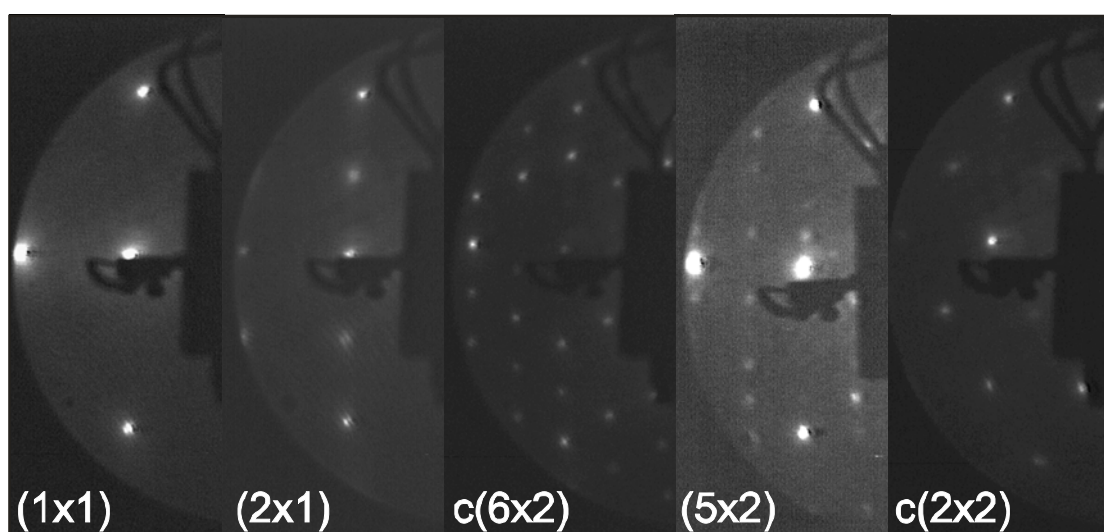


*Figure 4.1* LEED structures observed in methanol oxidation over Cu(110) (see text).

The clean Cu(110) substrate shows a sharp (1×1) LEED pattern. The (2×1) and c(6×2) LEED patterns represent the oxygen reconstructions on Cu(110) substrate with different oxygen coverages. The (5×2) and c(2×2) LEED patterns can be observed under certain adsorption conditions dosing with oxygen and methanol and relate to the stable and ordered intermediates surface structures.

### 4.2.1 Oxygen reconstructions

The adsorption of oxygen onto the Cu(110) surface has been extensively studied for many years and a comprehensive review can be found in Ref. [74]. The structural details for two oxygen-induced reconstructions, Cu(110)-(2×1)-O and

Cu(110)-c(6×2)-O, are now quite well established by a range of structure investigations [75-86], including LEED, STM, surface X-ray diffraction (SXRD), low energy ion scattering (LEIS), and quantum chemical simulation, etc. Fig. 4.2 indicates schematically these two structures.

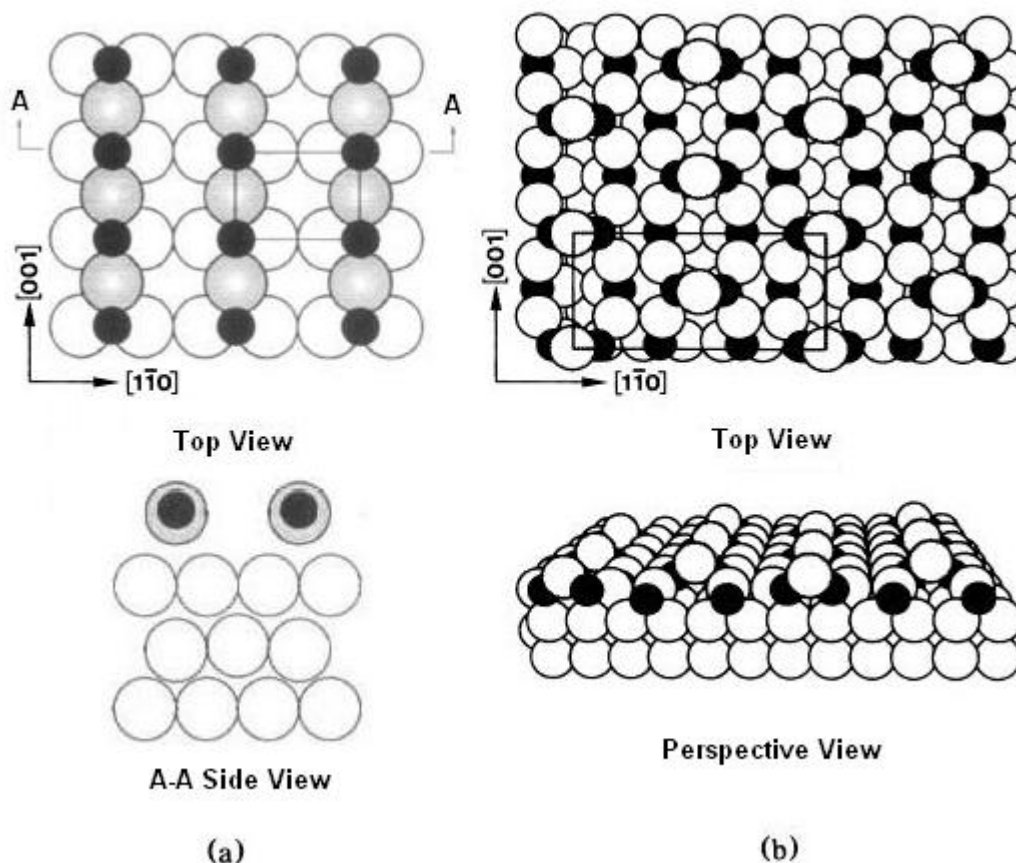


**Figure 4.2** Schematic drawings for two equilibrium oxygen reconstructions: (a) Cu(110)-(2×1)-O [79], (b) Cu(110)-c(6×2)-O [76]. The small black circles represent the O atoms, whereas the grey and white circles represent super Cu atoms and Cu atoms in the layers below, respectively. Unit cells are shown.

Oxygen adsorption on the Cu(110) surface at room temperature generates a (2×1) added row structure in which oxygen molecules dissociatively adsorb, diffuse and capture Cu adatoms which are thermally generated by evaporation from the Cu surface step edges (a solid / vapour equilibrium in two dimensions) [87]. These units form long chains of alternating O-Cu atoms which lie along the [001] direction with attractive lateral forces between the chains. As shown in Fig. 4.2 (a), a fully (2×1)-O

covered Cu(110) surface consists of 1/2 ML oxygen (1 monolayer =  $1.08 \times 10^{15}$  atoms/cm<sup>2</sup>) and 1/2 ML added copper atoms.

The sticking probability of oxygen on the clean Cu(110) surface at room temperature is initially high, e.g. exposure of 10 L oxygen (1 langmuir =  $1 \times 10^{-6}$  Torr · s) already leads to a fully (2×1)-O covered Cu(110) surface. But it decreases precipitously after an oxygen coverage of 1/2 ML is reached. A much higher oxygen exposure above  $10^4$  L and the elevated temperature above 100 °C are necessary to form the higher coverage c(6×2) structure.

As shown in Fig. 4.2 (b), the equilibrium structure for the Cu(110)-c(6×2)-O reconstructions consists of two Cu-O-Cu chains for each three (1×1) lattice spacings in the  $[1\bar{1}0]$  direction, as compared to the (2×1) structure with only one Cu-O-Cu chain per two (1×1) lattice spacings in the  $[1\bar{1}0]$  direction; i.e. the oxygen coverage and the added copper coverage associated with the chains are increased from 1/2 to 2/3 ML. The Cu-O-Cu chains are connected by Cu atoms (1/6 ML), coordinated to every second O atom along the chain. These copper atoms, which are gliding on top of the structure, constitute the c(6×2) “superstructure” with respect to the underlying bare (1×1) copper surface. In total, a fully c(6×2)-O covered Cu(110) surface consists of 2/3 ML oxygen and 5/6 ML added copper atoms [76] which may be considered to be a precursor to oxidation of the copper.

It was reported [81] that the oxygen reconstruction of the surface implies not only a morphological change, but also a decrease of the reactivity of the oxygen atoms involved. This was proved by monitoring reactions of the oxygen reconstructed Cu(110) surface with STM for methanol oxidation [26], ammonia dehydrogenation [88] or CO oxidation [89]. It was found that both the fully (2×1)-O and c(6×2)-O covered Cu(110) surfaces are very inert to the reactions.

It should be mentioned that, compared with the Cu(110)-(2×1)-O surface, the Cu(110)-c(6×2)-O reconstructed surface is less important in UHV studies since the appearance of the structure requires high oxygen exposure and usually this structure does not show up during the stationary reactions under UHV conditions.

### 4.2.2 Surface structures formed during the surface reactions

The variations of the surface adsorbate structures during the sequential and co-dosing of oxygen and methanol at room temperature ( $\sim 300$  K) were monitored by LEED.

A clean Cu(110) surface exposure of methanol up to  $10^4$  L showed no obvious changes of a sharp (1 $\times$ 1) LEED pattern. This is in agreement with the former molecular beam reaction and STM results [90] that the clean Cu(110) surface has a very low adsorption probability for methanol at room temperature.

The sequential dosing starting with a Cu(110) surface half filled with a (2 $\times$ 1)-O ( $\theta_{\text{O}} = 0.25$  ML, 5 L O<sub>2</sub> exposure) followed by exposure to methanol created a well ordered (5 $\times$ 2) structure. Whereas the same dosing process starting with a Cu(110) surface fully filled with a (2 $\times$ 1)-O ( $\theta_{\text{O}} = 0.5$  ML, 10 L O<sub>2</sub> exposure) showed no changes of a sharp (2 $\times$ 1)-O LEED pattern. These LEED observations indicate that the 0.5 ML oxygen reconstructed surface is very unreactive compared with the 0.25 ML oxygen reconstructed surface. In fact it has been already reported in a very early paper [23] that a pronounced maximum in oxidation activity with surface oxygen coverage exists.

The well ordered (5 $\times$ 2) structure was detected by LEED and STM in 1994 [26] and it was reported that this structure can be related to methoxy adsorbed on the Cu(110) surface. Fig. 4.3 (a) shows a tentative model for the Cu(110)-(5 $\times$ 2)-methoxy structures, which is closest to the observations in the STM experiments, proposed by the group of M. Bowker [27, 41]. It is visible that a unit cell contains 0.6 ML added copper atoms, to which 0.4 ML methoxy molecules are bonded. It was also suggested [27] that the presence of added copper atoms in the (5 $\times$ 2) structure creates additional adsorption sites that can be occupied by other gases, for example, oxygen.

Co-dosing with methanol and oxygen under low pressure ( $p(\text{CH}_3\text{OH}) = 1 \times 10^{-7}$  mbar,  $p(\text{O}_2) = 0.5 \times 10^{-7}$  mbar) at room temperature leads also to a sharp (5 $\times$ 2) LEED pattern in less than one minute. Upon further dosing this adsorbate layer does not remain stable but reacts further and the (5 $\times$ 2) LEED pattern can be seen in

coexistence with a  $(2 \times 1)$  oxygen reconstructions. Obviously oxygen can still adsorb in coexistence with the  $(5 \times 2)$  methoxy layer.

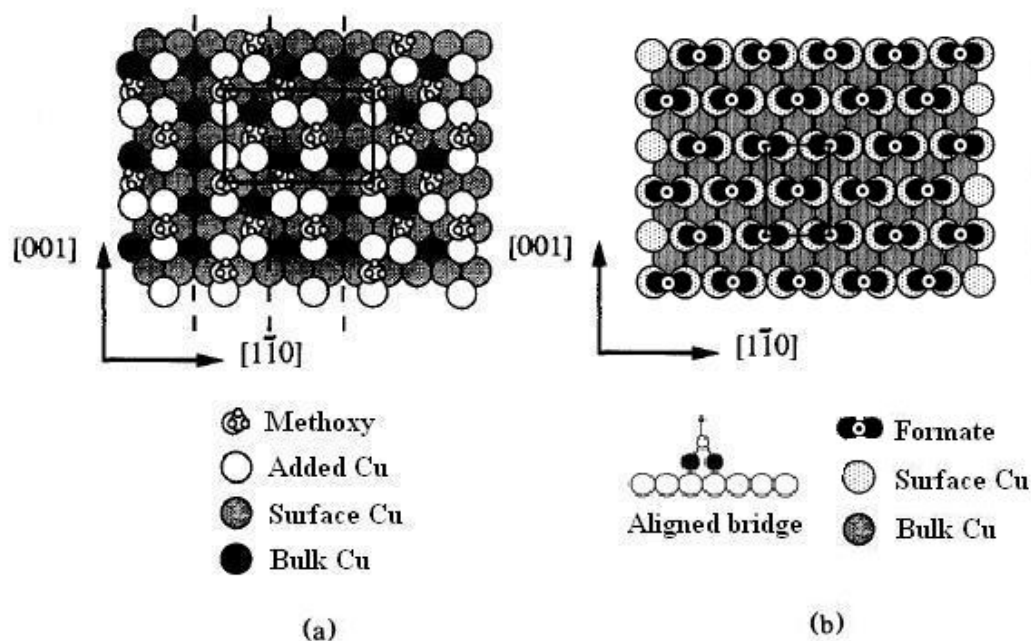


**Figure 4.3** The models for (a) the  $\text{Cu}(110)\text{-}(5 \times 2)\text{-methoxy}$  structures [41] and (b) the  $\text{Cu}(110)\text{-}c(2 \times 2)\text{-formate}$  structures [87, 92] proposed by the group of M. Bowker.

Co-dosing at room temperature but with the partial pressures increased by two orders of magnitude ( $p(\text{CH}_3\text{OH}) = 1 \times 10^{-5}$  mbar,  $p(\text{O}_2) = 0.5 \times 10^{-5}$  mbar) causes the appearance of a  $c(2 \times 2)$  LEED pattern. Extending the co-dosing experiments to longer exposure time also leads to the development of a  $(2 \times 1)$  pattern which coexists with the diffuse  $c(2 \times 2)$  pattern.

The  $c(2 \times 2)$  intermediate structure was only observed by STM in the former studies of methanol oxidation on  $\text{Cu}(110)$ . It was shown [28, 29, 41] that this structure always coexists with  $(5 \times 2)$  or  $(2 \times 1)$  structures on the surface while co-dosing with methanol and oxygen. Due to the difficulties in identifying the adsorbate species by STM, it is still under debate whether the  $c(2 \times 2)$  consists of formate species or it is a methoxy structure. Adsorption experiments with formic acid produced a  $c(2 \times 2)$  and  $(n \times 1)$  ( $n = 3 \sim 4$ ) layer on  $\text{Cu}(110)$  thus supporting the former suggestion [87, 91, 92]. However, recent STM experiments in which a  $c(2 \times 2)$  was generated by co-dosing



with methanol and oxygen are in favor of the methoxy interpretation [28, 29]. Here, since we can create a  $c(2\times 2)$  layer on top of the Cu(110) substrate under high pressure co-dosing condition with methanol and oxygen, *in situ* XPS was used to determine the adsorbate component of the structure and it was found that the  $c(2\times 2)$  structure is related to a formate intermediate on the surface. Fig. 4.3 (b) shows a model for the Cu(110)- $c(2\times 2)$ -formate structures proposed by the group of M. Bowker [87], according to their high resolution STM images after sequential dosing with oxygen and formic acid. In contrast to other structures, the Cu(110)- $c(2\times 2)$ -formate structure contains no added copper atoms in the adlayer. A unit cell contains 1/2 ML adsorbed formate whose geometry is an aligned bridge as indicated at the bottom of Fig. 4.3 (b).

In co-dosing experiments under both low and high pressure conditions, it was found that the mixing ratio of oxygen and methanol strongly affects the LEED patterns. As stated previously, the methanol-rich mixtures have the highest tendency to  $(5\times 2)$ -methoxy or  $c(2\times 2)$ -formate formation, most of the time coexisting with a  $(2\times 1)$ -O structure. The oxygen-rich mixtures do not produce methoxy or formate structures due to the preferential growth of  $(2\times 1)$ -O islands. In this case LEED always shows a sharp  $(2\times 1)$  pattern.

It should be emphasized that the  $c(2\times 2)$  LEED pattern appears only during co-dosing conditions, meaning that the  $c(2\times 2)$  LEED pattern disappears while stopping the inlet of methanol or oxygen. This could be due to the sensitivity of the formate adlayer to the electron beam and the high formate mobility on the surface which have already been shown in the former LEED and STM studies [91, 92]. It was reported [27] that the methoxy-covered surface is also extremely sensitive to the electron beam. In their LEED experiments, the  $(5\times 2)$  methoxy-induced LEED patterns lasted only about 20 s while the sample was maintained at 250 K and this effect had to be overcome by using the manipulator to slowly move the sample so that the electron beam was constantly striking new areas of the sample. Our *in situ* XPS experiments also proved the beam-induced desorption and dissociation effect on the methoxy and formate adlayers. It was found that in half an hour a methoxy and formate mixed adlayer was cleaned by the X-ray photon beam.

### 4.3 PEEM

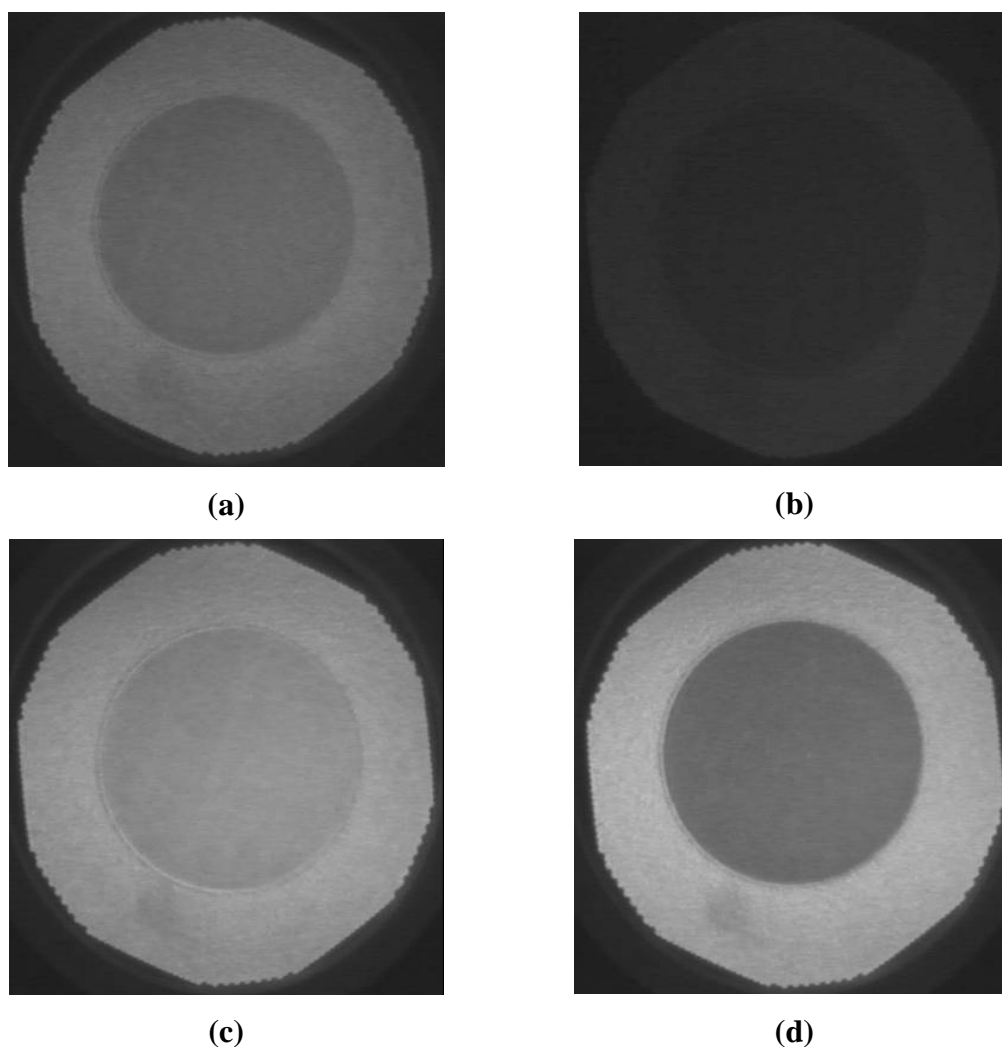


**Figure 4.4** PEEM images of a Pd/Cu(110) microstructured bimetallic surface with different adsorbate structures on top of the Cu(110) surface which is the area inside the circle. (a) Clean surface; (b) Cu(110)-(2×1)-O ( $\theta_o = 0.5$  ML); (c) Cu(110)-(5×2)-methoxy created by co-dosing with  $p(\text{CH}_3\text{OH}) = 1 \times 10^{-7}$  mbar and  $p(\text{O}_2) = 0.5 \times 10^{-7}$  mbar at room temperature; (d) Cu(110)-c(2×2)-formate created by co-dosing with  $p(\text{CH}_3\text{OH}) = 1 \times 10^{-5}$  mbar and  $p(\text{O}_2) = 0.5 \times 10^{-5}$  mbar at room temperature.

As mentioned in chapter 2, the problem of beam damaging effects can be avoided by using PEEM to monitor the state of the surface since PEEM uses a UV-light source with the photon energy below 6.5 eV, which is close to the work function of the surface, and therefore constitutes the softest probe capable of sampling the

electronic structure of the surface. PEEM images primarily the local work function with a typical spatial resolution of 1  $\mu\text{m}$ . Since the different adsorbates normally lead to a different work function of the surface, it is possible to distinguish the different adsorbate structures using PEEM.

Here, we repeated all the gas dosing processes mentioned in last section on a microstructured bimetallic Pd/Cu(110) surface and recorded the PEEM images (Fig. 4.4) which can be related to the known adsorbate structures by LEED. In the images, the area inside the circle is the Cu(110) surface and the area outside the circle is the Pd surface. It is obvious that the images of the Cu(110) surface with different adsorbate structures on top have different PEEM intensities. As has been mentioned in chapter 2, high work function areas are imaged as dark, low work function areas as bright in PEEM. According to this rule, the sequence of the work function of the surfaces from high to low is b) Cu(110)-(2 $\times$ 1)-O ( $\theta_{\text{O}} = 0.5 \text{ ML}$ ) > (d) Cu(110)-c(2 $\times$ 2)-formate > (a) Clean surface > (c) Cu(110)-(5 $\times$ 2)-methoxy.

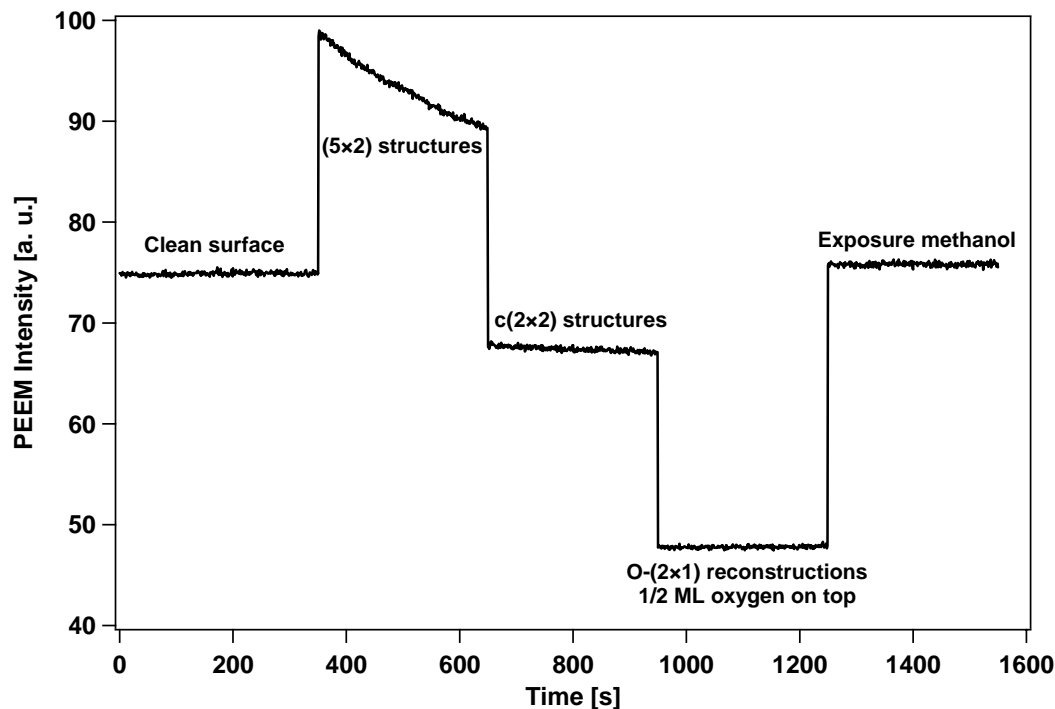


**Figure 4.5** Reference of the PEEM intensities to the different adsorbate structures on Cu(110). The PEEM intensities were determined via digitization of the PEEM images shown in Fig. 4.4.

The PEEM intensity in the chosen area can be determined via digitization of the recorded PEEM images. Fig. 4.5 shows the PEEM intensities of the different adsorbate structures on the Cu(110) surface area as a function of time during dosing of the different gases. It is shown that the PEEM intensity is very sensitive to the change of the adlayer with time.

In Fig. 4.5 it is well visible that the  $(5 \times 2)$  adlayer is very unstable during co-dosing with methanol and oxygen ( $p(\text{CH}_3\text{OH}) = 1 \times 10^{-7}$  mbar,  $p(\text{O}_2) = 0.5 \times 10^{-7}$  mbar). The PEEM intensity of the adlayer slowly decreases, which is in agreement with the LEED observation that under this condition a pure sharp  $(5 \times 2)$  LEED pattern exists less than one minute, and then coexists with  $(2 \times 1)\text{-O}$ . The adsorption of oxygen in the  $(5 \times 2)$  methoxy layer slowly increases the work function of the surface which can be imaged by PEEM. It was also shown that the exposure of methanol on the clean Cu(110) surface does not change the work function of the surface, which again proves the nonreactivity of the clean surface towards methanol.

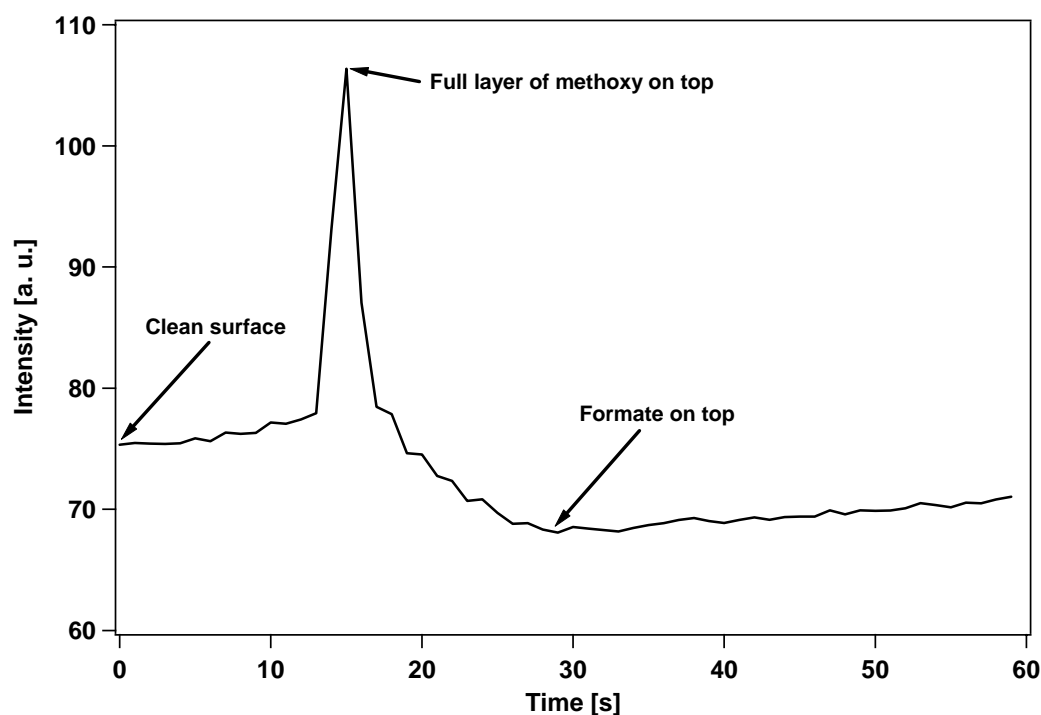


**Figure 4.6** The variation of the PEEM intensity during co-dosing with methanol and oxygen under high pressure ( $p(\text{CH}_3\text{OH}) = 1 \times 10^{-5}$  mbar,  $p(\text{O}_2) = 0.5 \times 10^{-5}$  mbar) at room temperature on Cu(110).

STM studies of methanol oxidation to formate on Cu(110) showed [41] that formate intermediate results from the reaction of adsorbed methoxy and isolated oxygen adatoms generated during dosing. Our LEED experiment co-dosing with methanol and oxygen under high pressure ( $p(\text{CH}_3\text{OH}) = 1 \times 10^{-5}$  mbar,  $p(\text{O}_2) = 0.5 \times 10^{-5}$  mbar) directly showed the appearance of a  $c(2 \times 2)$ -formate structure without the information how this structure was build up. This could be due to the slow ordering process of the adsorbate on the surface. Fig. 4.6 shows the variation of the PEEM intensity during the co-dosing process. It is well visible that a fully covered methoxy layer forms before the build-up of the formate layer on top of the Cu(110) surface. This result clearly indicates that the formate intermediate indeed develops from the methoxy intermediate.

#### 4.4 TPD

Fig. 4.7 shows the TPD spectra following the adsorption of 10 L  $\text{CH}_3\text{OH}$  at 240 K on a Cu(110) surface pre-dosed with 5 L  $\text{O}_2$  at room temperature. The heating rate of a linear ramp is 6 K/min.

Obviously, below room temperature, some methanol and water were desorbed; slightly above room temperature, at about 330 K, formaldehyde, methanol, water and hydrogen were desorbed; at higher temperature, about 430 K,  $\text{CO}_2$  with water and hydrogen were desorbed. The desorbed products evolution is very similar to the first TDS study by Wachs and Madix [23]. It was seen that formaldehyde was the major desorption product at 330 K and methanol desorption was also pronounced at low temperature, whereas only a little  $\text{CO}_2$  desorbed at 430 K. It is obvious that under this sequential dosing condition the methoxy was the most abundant surface intermediate which decomposed to formaldehyde and recombined with hydrogen adatoms to desorb as methanol during heating. This is in agreement with the LEED observation of a sharp  $(5 \times 2)$  structure before the TPD experiment. The formate intermediate on the surface which is desorbed as  $\text{CO}_2$ ,  $\text{H}_2$  or  $\text{H}_2\text{O}$  most possibly formed from the methoxy and the rest oxygen adatoms on the surface during heating, since it was reported [32] that the amount of desorbed  $\text{CO}_2$  strongly depended on the oxygen

exposure time in the sequential dosing process. It should be noted that the H<sub>2</sub>O signal measured in our data set is not good, which could be due to the wall effect of the UHV chamber.

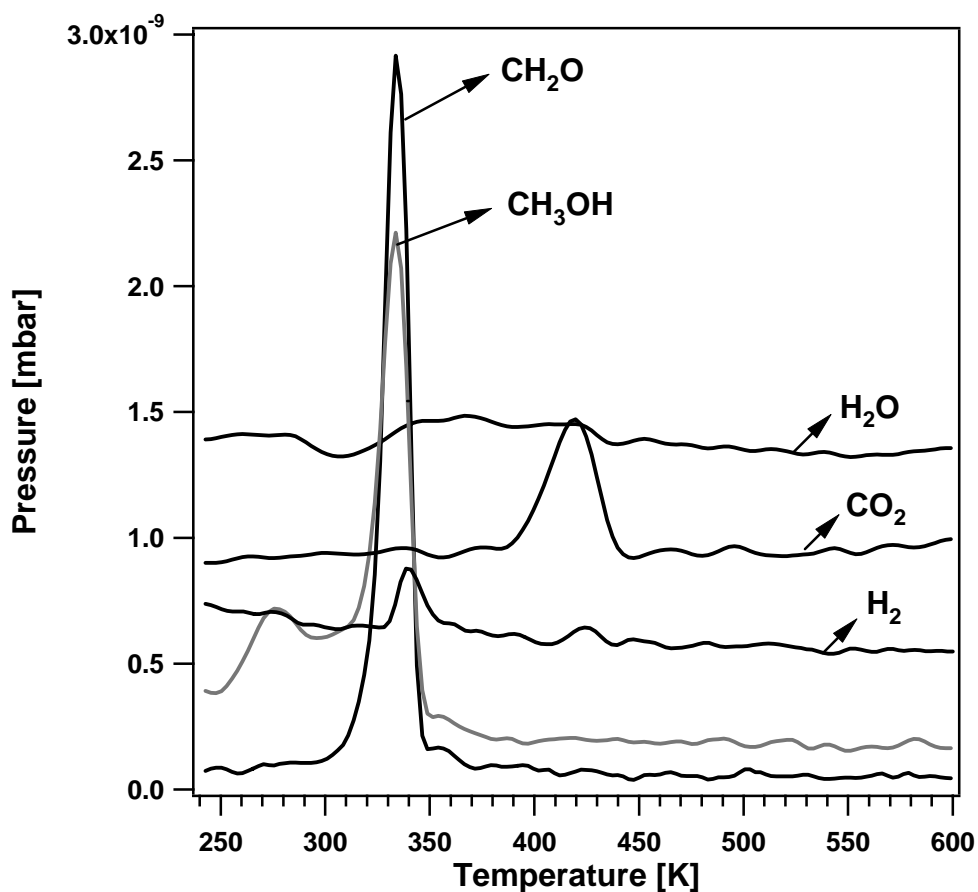
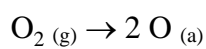
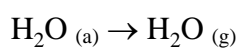
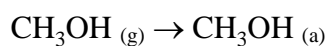
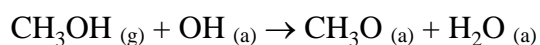
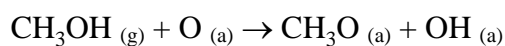


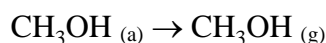
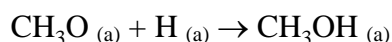
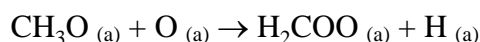
*Figure 4.7* TPD spectra recorded simultaneously from a partially oxidized Cu(110) surface (5 L O<sub>2</sub> at 300 K) after exposure 10 L CH<sub>3</sub>OH at 240 K. The heating rate for the experiment was 6 K/min.

Referring to the former TPD studies [23, 24], we can write out an unstationary reaction scheme to describe above TPD spectra:

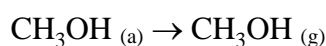
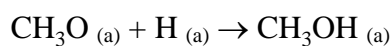
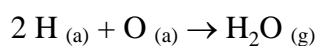
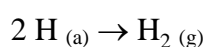
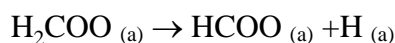
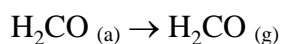
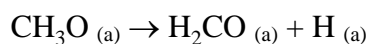


Below room temperature,

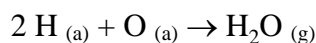
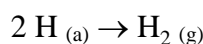
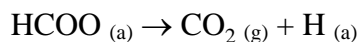




Slightly above room temperature (330 K),



Higher temperature (430 K),



The TPD spectra after the sequential dosing with oxygen and methanol showed that formaldehyde is always the dominant desorption product. In contrast it was reported [40] that when oxygen and methanol gas mixtures were co-dosed on the Cu(110) surface at room temperature, the main product can be switched between formaldehyde and CO<sub>2</sub>. These results concluded that the actual reaction pathway of methanol oxidation on Cu(110) may depend sensitively on the reaction conditions.

Here we compare the TPD spectra (Fig. 4.8) after co-dosing with methanol and oxygen at room temperature under low pressure ( $p(\text{CH}_3\text{OH}) = 1 \times 10^{-7}$  mbar,  $p(\text{O}_2) = 0.5 \times 10^{-7}$  mbar) with that under high pressure ( $p(\text{CH}_3\text{OH}) = 1 \times 10^{-5}$  mbar,  $p(\text{O}_2) = 0.5 \times 10^{-5}$  mbar). Before the TPD experiments, LEED determined that the former surface has a (5×2) + (2×1) mixed adlayer and the latter surface has a c(2×2) + (2×1) mixed adlayer. After the TPD experiments, LEED showed that the former surface still has a (2×1) structure, whereas the latter surface is a sharp (1×1) substrate.

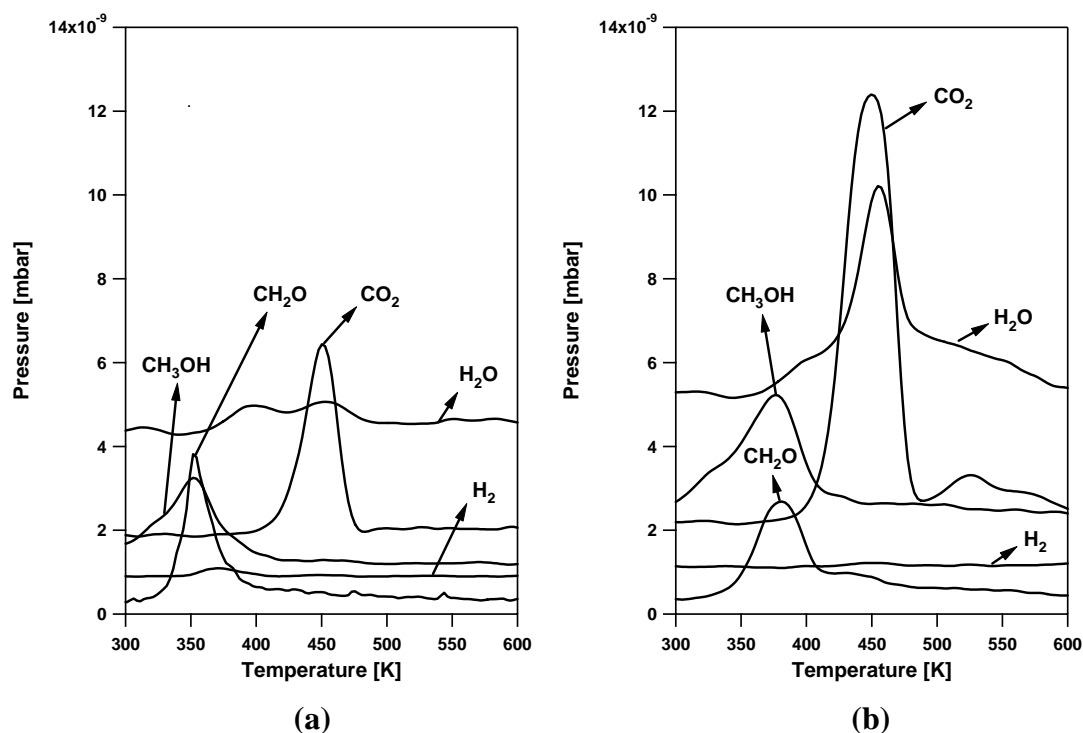


**Figure 4.8** Comparison of TPD spectra after co-dosing with methanol and oxygen at 300 K (a) under low pressure condition ( $p(\text{CH}_3\text{OH}) = 1 \times 10^{-7}$  mbar,  $p(\text{O}_2) = 0.5 \times 10^{-7}$  mbar) and (b) under high pressure condition ( $p(\text{CH}_3\text{OH}) = 1 \times 10^{-5}$  mbar,  $p(\text{O}_2) = 0.5 \times 10^{-5}$  mbar). The heating rate for the experiments was 30 K/min.

In both spectra (a) and (b),  $\text{CO}_2$  becomes a major desorption product, which is different from that in the TPD spectra in Fig. 4.7. Compared with the desorption products from the mixed  $(5 \times 2) + (2 \times 1)$  adlayer, much more  $\text{CO}_2$  was produced from the mixed  $c(2 \times 2) + (2 \times 1)$  adlayer. It indicates that  $c(2 \times 2)$  can be related to the original formate-induced structure on Cu(110). In spectra (b) there are still some methanol and formaldehyde products which could be due to the methoxy intermediate coexisting with the mixed  $c(2 \times 2) + (2 \times 1)$  adlayer, or more possibly due to the reaction between the residual methanol in the gas phase and the surface oxygen since under high pressure co-dosing, after stopping the gas feed, a high background pressure always exists due to the wall effect of the UHV chamber.

## 4.5 Reaction mechanism



The above unstationary reaction experiments with TPD, LEED and PEEM combining with former STM studies give us a lot of information concerning the reaction mechanism of methanol oxidation over Cu(110), for example, the role of the adsorbed oxygen, the active sites for methanol oxidation, the rearrangement of the added copper atoms during the surface reaction, and the possible reaction pathways occurring on the surface.

The strong dependence of the activity of the Cu(110) surface on the oxygen coverage clearly shows that oxygen appears to perform two possible roles: both promoter and poison in the reaction. The clean Cu(110) surface is very unreactive towards methanol at room temperature. The presence of low oxygen coverage ( $< 0.5$  ML) on the surface results in an obvious increase in methanol reactive sticking coefficient so that oxygen at low coverages acts as a promoter forming a strongly bound methoxy intermediate. A high oxygen coverage of  $\sim 0.5$  ML on the surface inhibits the methanol absorption and the surface becomes unreactive again, i.e. oxygen acts as a poison.

It was found that the dual roles of the oxygen on the Cu(110) surface are due to the nature of the  $(2\times 1)$ -O reconstruction, which is a copper-added row structure consisting of Cu-O chains in the  $[001]$  direction. The oxygen atoms at the edges of the chains are much more reactive than those involved in the chains. These terminal oxygen atoms in the O-Cu rows of the  $(2\times 1)$  islands act as the active sites for methanol oxidation [26, 27, 31].

It was reported [93] that the Cu atoms in the  $(2\times 1)$ -O island are unstable at the end of the chains which therefore preferentially terminate in oxygen atoms. When a terminal oxygen atom is removed by the reaction the exposed Cu atom is left with low co-ordination and is free to diffuse away from the chain. It seeks an alternative, stable location during reactions, e.g. associating with the methoxy layer, or bonding to the step of the original surface layer.

With all these information and the reaction scheme proposed in last section, we can summarize the reaction mechanism model as demonstrated in Fig. 4.9.

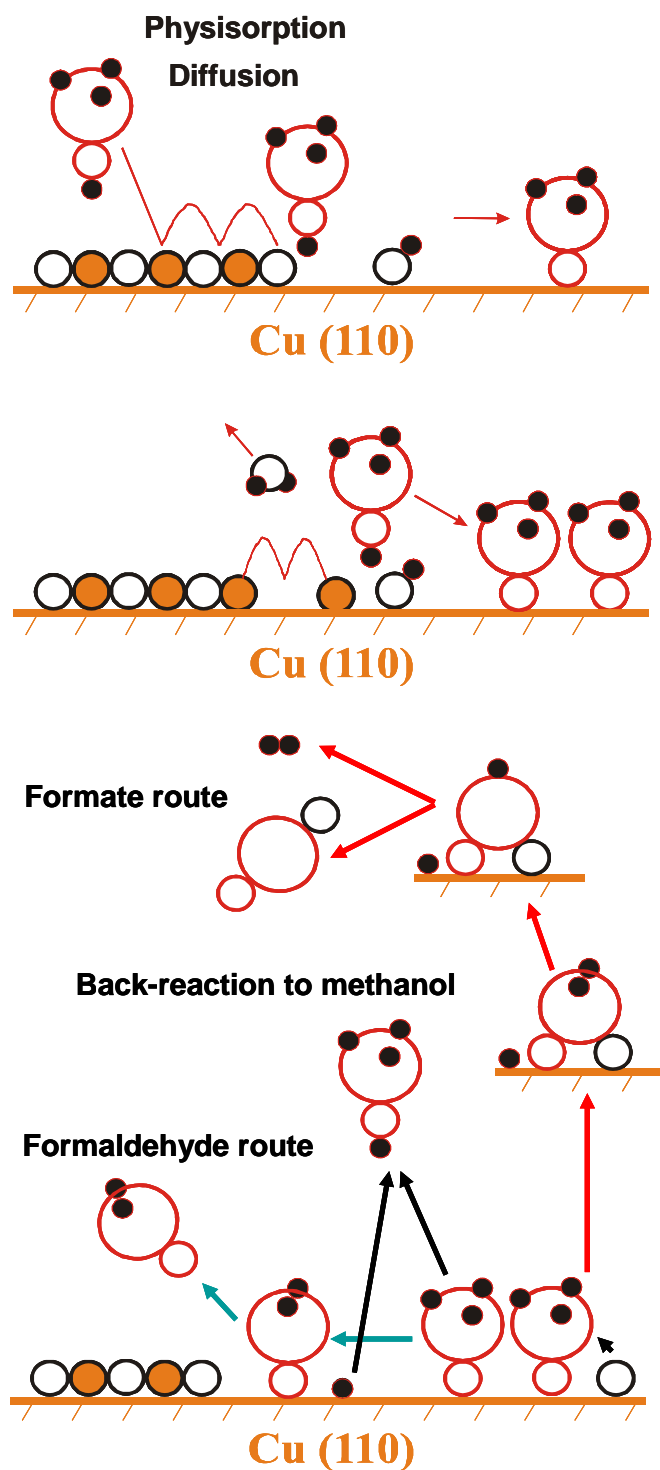


**Figure 4.9** Schematic drawing of the mechanism model for the reaction of methanol with pre-adsorbed oxygen atoms, which adsorb as  $(2 \times 1)$  island on Cu(110). The small yellow circles present added Cu atoms in  $(2 \times 1)$ -O island, the small white circles present O atoms, the very small black circles present H atoms, and the big white circles present C atoms.

The sequence of the reaction of methanol with pre-adsorbed oxygen atoms, which adsorb as  $(2\times 1)$  island on Cu(110), is as follows. First the methanol adsorbs in a weakly held precursor state on the surface, i.e. physisorption, which has a short lifetime, but high diffusivity. It has a high probability during its sojourn of finding one of the reactive terminal oxygen sites in the  $(2\times 1)$ -O islands as long as the oxygen coverage is moderate. This reaction produces methoxy and a terminal OH group. The OH reacts with another incoming methanol molecule to produce a second methoxy and water which desorbs from the surface. The reactive site is regenerated by the diffusion away of the unstable terminal Cu atom. The methoxy groups remain phase separated from the oxygen islands and develop the  $(5\times 2)$  structure.

At temperature slightly above room temperature, methoxy decomposes to formaldehyde and leaves the surface. It also can recombine with a hydrogen adatom to desorb as methanol from the surface. The isolated oxygen adatoms exist on the surface and are highly reactive. This reactive oxygen adatom attacks the neighbouring methoxy group to induce its decomposition and react with it to finally form the stable formate adsorbate. At higher temperature the formate decomposes to  $\text{CO}_2$  and a hydrogen adatom which can either react to  $\text{H}_2$  or  $\text{H}_2\text{O}$ . All of these products leave the surface nearly instantaneously under reaction conditions. It is very clear that three reaction pathways exist on the surface, formaldehyde formation, formate formation and back-reaction to methanol.

## 4.6 Conclusions

Methanol oxidation over a Cu(110) surface was studied under unsteady-state reaction conditions with TPD, LEED and PEEM. It was shown that the surface reactivity with methanol is strongly oxygen coverage dependent. Both the oxygen free surface and the surface fully covered with O- $(2\times 1)$  islands (0.5 ML oxygen coverage) have a very low reactivity for the dissociative adsorption of methanol, whereas a partially O- $(2\times 1)$  islands covered surface (about 0.25 ML oxygen coverage) exhibits a pronounced maximum in oxidation reactivity. Methoxy and formate were determined as the important intermediates during methanol oxidation on Cu(110), methoxy

forming an ordered  $(5 \times 2)$  structure, whereas formate forming an ordered  $c(2 \times 2)$  structure on the surface. The dosing conditions strongly affect the adsorbates formed on the surface. Methoxy is the dominant intermediate after sequential dosing with moderate oxygen and methanol, or co-dosing of methanol and oxygen at low pressure. However, formate can become the dominant intermediate on the surface during co-dosing of methanol and oxygen at high pressure. Combining our observations with the former STM studies mainly conducted by the group of M. Bowker, we conclude that the terminal oxygen atoms in the O-Cu rows of the  $(2 \times 1)$  islands act as the active sites for methanol oxidation. Three possible reaction pathways occur on the Cu(110) surface during methanol oxidation: formaldehyde formation, formate formation and back-reaction to methanol.

## Chapter 5

# Stationary reaction under low pressure conditions

### 5.1 Introduction

Studies of the unstationary reaction kinetics yielded detailed insights into the reaction mechanism of methanol oxidation over Cu(110), for example, the active sites, the adsorbate species, the possible reaction pathways. Especially a number of STM studies mainly conducted by the group of M. Bowker [26, 27, 31, 41] gave plentiful information concerning the adsorbate species existing on Cu(110) during the reaction. Methoxy and formate were determined to be the important adsorbate species. The oxygen coverage was found to strongly affect the activity of the Cu(110) surface. However, it remains unclear to what extent the adsorbates determine the reactivity of the Cu(110) surface. A general problem in relating the findings of STM studies to catalytic activities is that the highly mobile and reactive species are not imaged in STM which means that in the extreme the ordered overlayers nicely imaged with STM may just represent a kind of spectator species with little or no relation to the catalytic reactivity.

One way to tackle this problem is to measure the reaction kinetics under stationary conditions and to utilize *in situ* techniques for probing the adsorbates variation on the surface, because any detailed mechanism has of course to be consistent with the macroscopic kinetics.

For this reason we studied the steady-state kinetics of the reaction in the low pressure range from  $10^{-7} - 10^{-3}$  mbar in the UHV system. Under these conditions the reaction is practically isothermal, and surface reaction steps rather than mass transport through the gas phase limit the reaction. Since the general goal of this thesis is to establish a bridge between the low-pressure single crystal studies and the high-pressure kinetics, we systematically varied the total pressure up to  $10^{-3}$  mbar which is our experimental limitation of the UHV setup. Subsequently we relate the results of the kinetics measurements with that of *in situ* LEED, AES, PEEM, and XPS measurements so that we can establish a connection between the kinetics and the presence of certain adsorbate phases on the Cu(110) surface.

In this chapter we firstly present the results of the stationary reaction kinetics measurements, and then relate the different adsorbate species to the reactivity of the surface. Basing on these results a detailed reaction mechanism is proposed to describe the stationary reaction under low pressure conditions.

## 5.2 Stationary reaction kinetics

### 5.2.1 Temperature Dependence

Fig. 5.1 shows a TPR spectrum obtained at a mixing ratio  $p(\text{CH}_3\text{OH}) : p(\text{O}_2) = 1 : 0.6$  for  $p(\text{CH}_3\text{OH}) = 1.0 \times 10^{-7}$  mbar. The TPR was recorded in a heating/cooling cycle in which a heating/cooling rate of 6 K/min was sufficiently slow to ensure that the reaction was close to steady-state conditions.

The reaction ignites at  $\approx 400$  K as the sample is heated. After passing a first peak, the reactivity drops and approaches a second high temperature peak at  $T \geq 900$  K. Measurements with polycrystalline copper have shown that a maximum in reactivity is found at  $\approx 900$  K, which is slightly outside our accessible temperature range [19]. During cooling the reactivity extends down to  $\approx 320$  K. A pronounced hysteresis is thus present in the low-temperature range of the reaction below 500 K. The hysteresis is reproduced in a second cycle which means that it cannot be caused by irreversible changes in the catalyst but rather has to be caused by differences in the adsorbate coverages and surface structure.

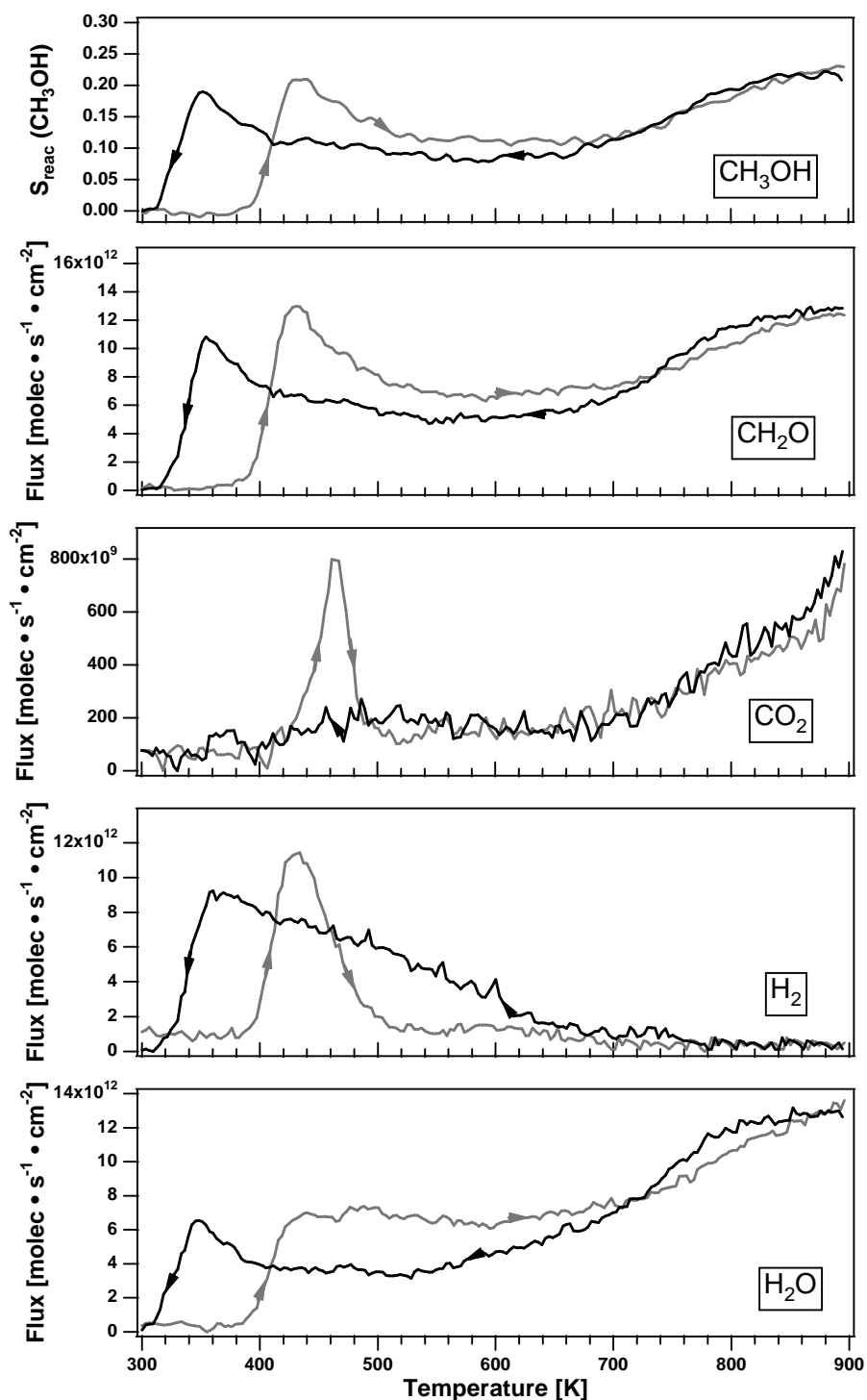


**Figure 5.1** Temperature programmed reaction spectroscopy in the  $10^{-7}$  mbar range with  $p(\text{CH}_3\text{OH}) = 1.0 \cdot 10^{-7}$  mbar,  $p(\text{CH}_3\text{OH}) : p(\text{O}_2) = 1:0.6$ . Temperature up- and down ramping are indicated in each panel. The upper panel represents the reactive sticking coefficient of methanol,  $s_{\text{reac}}(\text{CH}_3\text{OH})$ ; the other panels indicate the production rates of the different products during methanol oxidation.

In Fig. 5.1, the top panel shows the reactive sticking coefficient,  $s_{\text{reac}}$ , of methanol as measured from the variation of the partial pressure of methanol. The reactive sticking coefficient is quite high, reaching 0.2 in the maxima of the catalytic activity. A similarly high sticking coefficient has been found by Bowker et al. in unstationary measurements [26, 31]. The other panels demonstrate that all the products expected from Eqs. (1.1) - (1.3) in chapter 1 are seen in the experiment. The dominant product is formaldehyde, whose production accounts for  $\geq 95\%$  of the reacting methanol. Because of the high selectivity of the reaction for formaldehyde, the reactive sticking coefficient of methanol and the formaldehyde partial pressure are very similar in shape.

It can be seen that the  $\text{CO}_2$  peak is present only during heating but not in the cooling part of the temperature cycle. Although the heating rate of 6 K/min is quite low, at  $10^{-7}$  mbar transients may still contribute to the measured signal. This is the case for the  $\text{CO}_2$  peak measured during heating between 400 and 500 K. A comparison with a TPD spectra of a mixed  $(5\times 2) + (2\times 1)$ -layer shown in chapter 4 reveals that the amount of  $\text{CO}_2$  produced in the  $\text{CH}_3\text{OH}/\text{O}_2$  atmosphere is equal to the  $\text{CO}_2$  desorption signal from the mixed overlayer. The  $\text{CO}_2$  peak can be attributed to the decomposition and desorption of adsorbed formate; its intensity corresponds to a total amount of about half a monolayer. Therefore, we conclude that during the temperature up-ramping experiment formate represents a slowly accumulating adsorbate species which is not restored by the reaction once its decomposition and desorption of  $\text{CO}_2$  sets in. This interpretation is also supported by a separate experiment in which the heating ramp was stopped at 460 K and the  $\text{CO}_2$  signal decayed to zero while the production rates for all other products remained steady.

It is visible in the spectra that  $\text{H}_2$  production is strongly temperature dependent. While temperature up-ramping,  $\text{H}_2$  was produced only in a small temperature range from around 400 K to 500 K, and above 500 K  $\text{H}_2$  is no longer evolved during the stationary reaction. This result can be well linked to the former result of molecular beam reaction at  $10^{-8}$  mbar in ref. [26], where the lack of hydrogen evolution below 320 K and above 470 K was reported. During temperature down ramping the  $\text{H}_2$  production extends over a much wider temperature range of nearly 400 K.



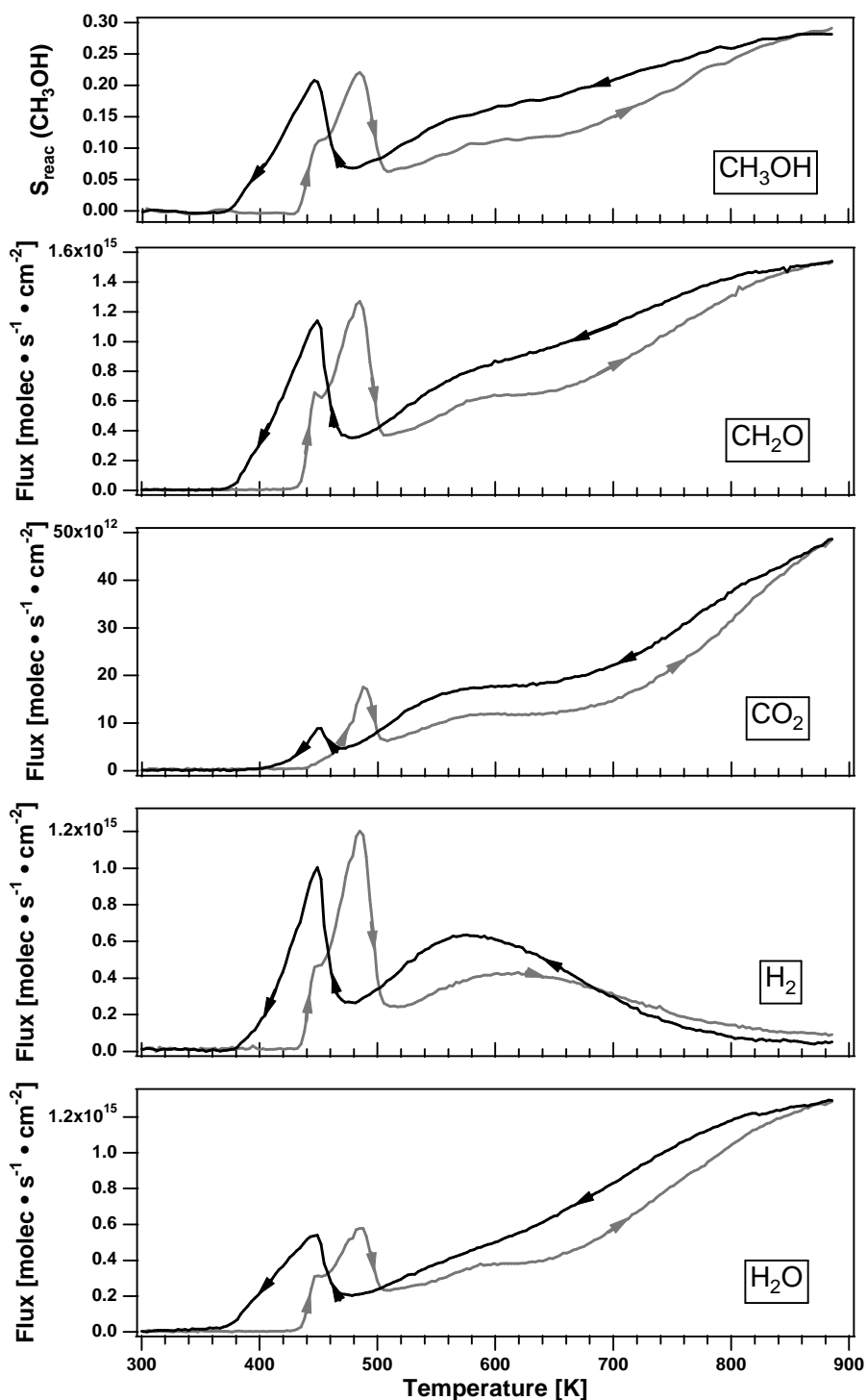


**Figure 5.2** Temperature programmed reaction spectroscopy in the  $10^{-5}$  mbar range with  $p(\text{CH}_3\text{OH}) = 1.0 \cdot 10^{-5}$  mbar,  $p(\text{CH}_3\text{OH}) : p(\text{O}_2) = 1:0.8$ . Temperature up- and down ramping are indicated in each panel. The upper panel represents the reactive sticking coefficient of methanol,  $s_{\text{reac}}(\text{CH}_3\text{OH})$ ; the other panels indicate the production rates of the different products during methanol oxidation.

The TPRS obtained in the  $10^{-5}$  mbar range is displayed in Fig. 5.2. Note that the y-scale in each panel has been scaled to the increase in methanol pressure by two orders of magnitude compared with the experiment in Fig. 5.1. With the exception of the  $\text{CO}_2$  peak, each of the low-temperature reaction peaks of the heating cycle consists of two components, as indicated by shoulders. In contrast to the  $10^{-7}$  mbar range, at higher pressure all peak maxima of the products coincide. The  $\text{CO}_2$  signal around 480 K consists of a shoulder followed by a single peak, which coincides with the higher of the double peaks of the other products. This indicates that the shoulder of the  $\text{CO}_2$  peak coincides with the ignition of the first component of the double peak of the other reacting species, whereas the  $\text{CO}_2$  production maximum and the higher reaction peak proceed in concert. In contrast to the experiment in the  $10^{-7}$  mbar range the  $\text{CO}_2$  peak in the  $10^{-5}$  mbar range represents a stationary production rate and not a transient. This was also supported by a separate experiment, where the heating ramp was stopped at 480 K and the production rates for all products maintained their level with time.

At the  $10^{-5}$  mbar pressure range we can also see a clear structure in the  $\text{H}_2$  production curve forming three distinct regions of the reaction: a narrow low-temperature peak, a broad maximum at intermediate temperatures between roughly 520 and 750 K and a high-temperature region where no  $\text{H}_2$  is produced.

Two competing reaction paths to formaldehyde formation via  $\text{H}_2$  formation and without  $\text{H}_2$  production can be formulated [26, 31]



The different temperature ranges for each reaction path can be visualized with a plot of the ratio of  $\text{CH}_3\text{OH}$  to  $\text{O}_2$  consumption versus the temperature. These results are displayed in Fig. 5.3 for different total pressures. The stoichiometry of the reaction relates the ratio of  $\text{CH}_2\text{O}$  to  $\text{H}_2\text{O}$  and  $\text{H}_2$  to  $\text{H}_2\text{O}$  production, which are also shown. For comparison, the reactive sticking coefficient of methanol, representing the sum of the two pathways is included in the same figure. We note that the peak positions in the TPRS vary strongly with the total pressure.

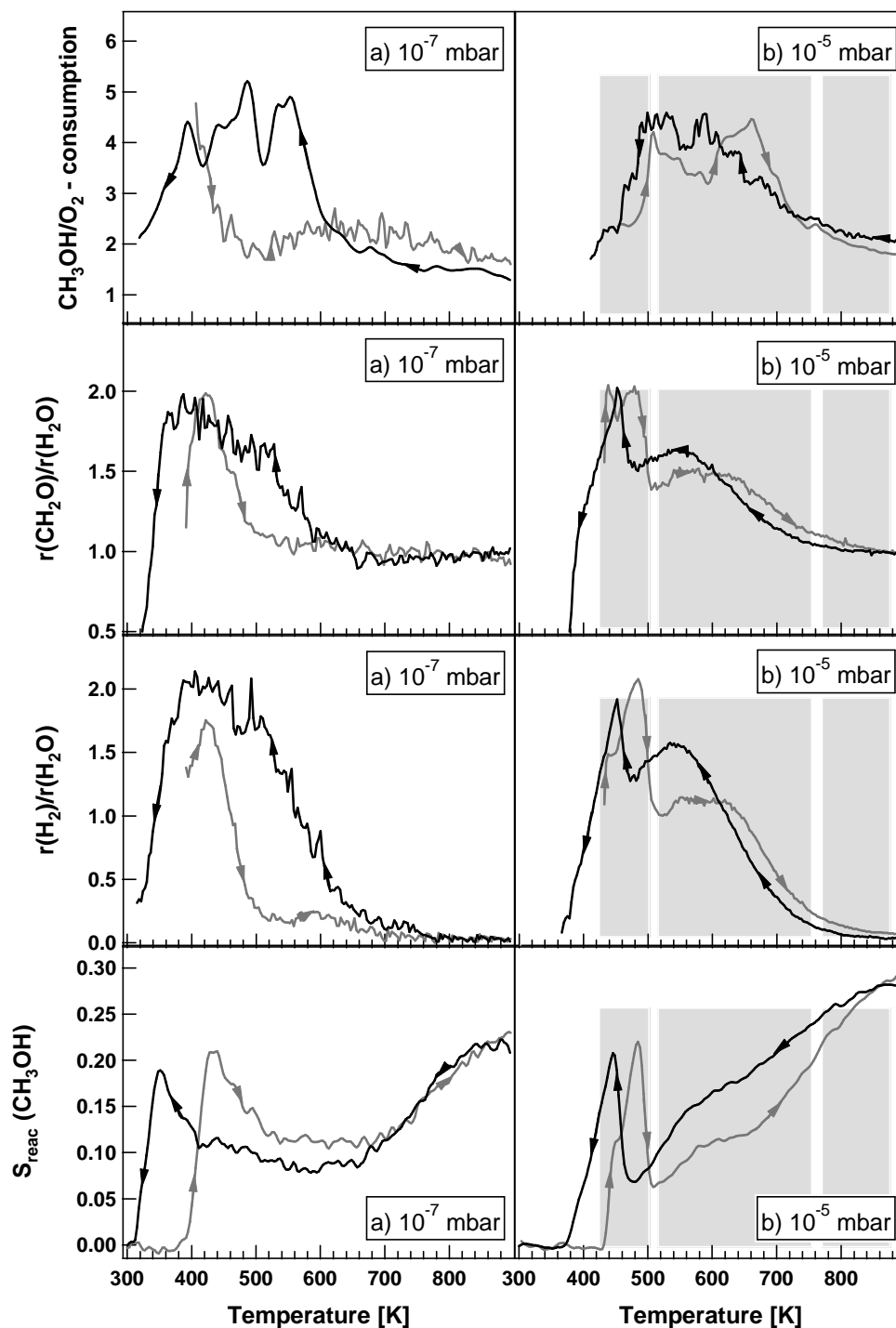


**Figure 5.3** Temperature dependence of the CH<sub>3</sub>OH: O<sub>2</sub> consumption ratio and of the corresponding CH<sub>2</sub>O: H<sub>2</sub>O and H<sub>2</sub>: H<sub>2</sub>O production ratio in the 10<sup>-7</sup> mbar and in the 10<sup>-5</sup> mbar range. Different regimes of the reaction stoichiometry are represented as grey areas in (b). The reactive sticking coefficient of methanol is displayed in the lower panels in order to relate the different regimes to the reactivity of the surface.

In the  $10^{-5}$  mbar range the  $\text{CH}_3\text{OH}/\text{O}_2$  consumption ratio is initially  $\approx 2$ , and then rises to  $\approx 4$ , where it stays with some variation over 150 – 200 K before it drops again to  $\approx 2$ . The ratio thus reflects three regimes of  $\text{H}_2$  production. The three different regimes are indicated by hatched areas in the plot. In the  $10^{-7}$  mbar range the distinction between the different regimes is less pronounced but still exists. In this pressure range we also observe strong hysteresis effects, as indicated in Fig. 5.3.

Under stationary conditions, in agreement with equation (5.1), the  $\text{CH}_3\text{OH}/\text{O}_2$  consumption ratio of  $\approx 4$  corresponds to a substantial hydrogen production in the intermediate temperature range from  $\approx 520$  K to  $\approx 750$  K. In the low temperature range from 400 to 500 K, the ratio  $r(\text{H}_2) / r(\text{H}_2\text{O})$  reaches 2. From equation (5.1) it is clear that this ratio should not exceed 1. This discrepancy, which amounts to a factor of 2, reflects the well-known fact that a reliable calibration of the  $\text{H}_2$  and  $\text{H}_2\text{O}$  signals is rather difficult. Reaction of water at the walls of the QMS chamber and dissociation of water at the QMS filament might be the reason for detecting a too high amount of  $\text{H}_2$  with respect to the  $\text{H}_2\text{O}$  signal. It should be stressed that since all other gases are well calibrated, the overall mass balance, even for H and for O, remains within  $\sim 20\%$  error.

The observation of the hydrogen production in an intermediate-temperature regime, where chemisorbed oxygen was also present on the surface, was attributed by Bowker [26] to two possible causes: (i) a high activation barrier for water formation is present (referred to as an “energetic” reason in Ref. [26]) or (ii) the reactants are organized in spatially separated regimes (referred to as a “structural” reason in Ref. [26]). In our experiments we see a pronounced hysteresis that was several hundred Kelvin wide in product formation, including  $\text{H}_2$  formation. This fact definitely rules out the explanation that the activation barrier is higher for water formation than for  $\text{H}_2$  desorption. Evidently the second explanation (“structural”) holds, and island-forming processes leading to a separation of the reaction partners are responsible for the absence of water formation. This conclusion is corroborated by LEED/Auger data presented in the following section 5.3.

## 5.2.2 Total pressure dependence

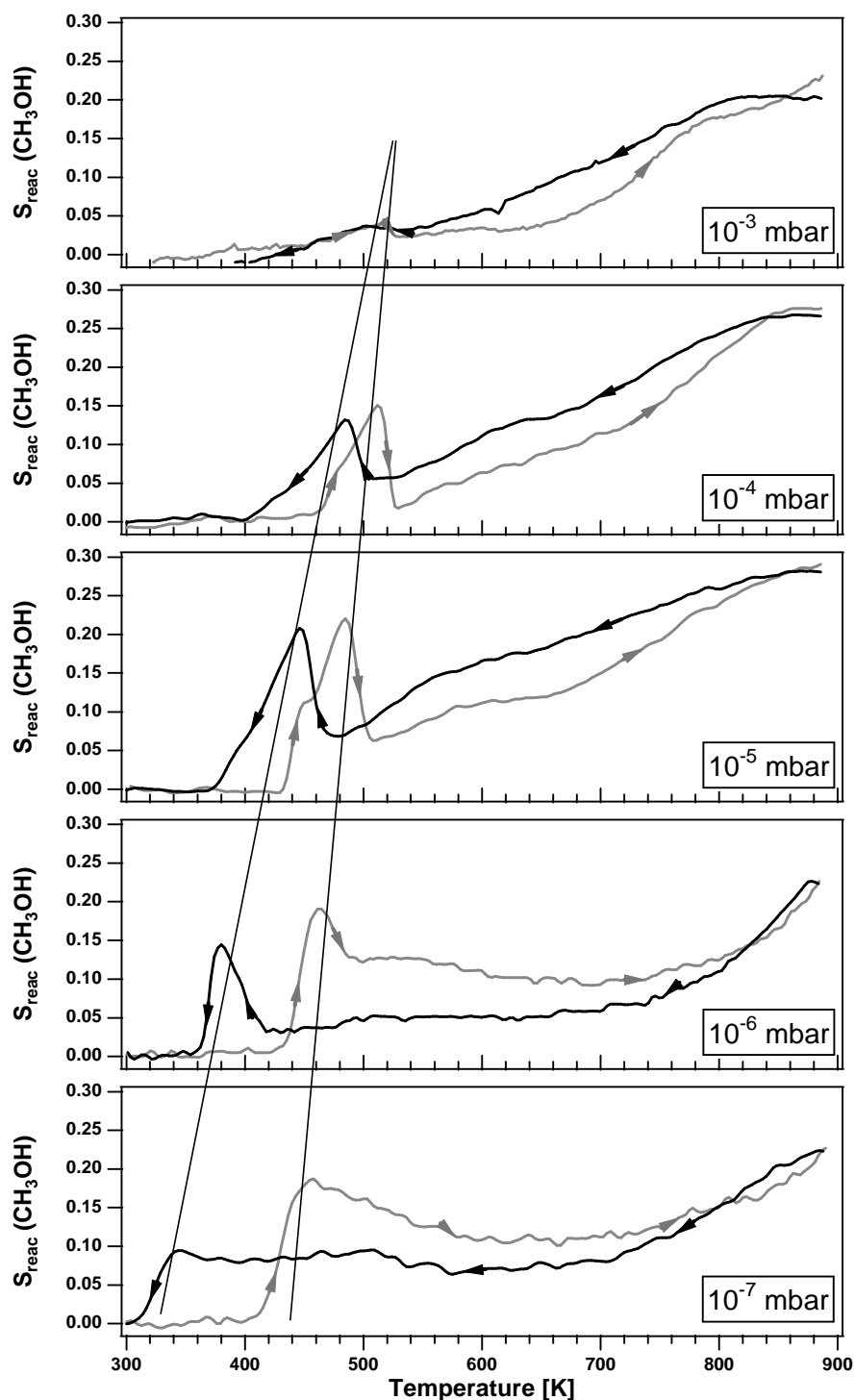


**Figure 5.4** Effect of the total pressure on the low temperature reactivity peaks in temperature cycling experiments. The methanol to oxygen gas mixture was always kept at  $p(\text{CH}_3\text{OH}) : p(\text{O}_2) = 1 : 0.8$  with only the total pressure being varied between  $10^{-7}$  mbar and  $10^{-3}$  mbar. The straight lines indicate systematic shifts in the peak positions with increasing total pressure.

From the steady-state reaction kinetics at the  $10^{-7}$  and  $10^{-5}$  mbar range, we can already observe the differences due to the increase of the total pressure of the reaction. In order to make clear how the total pressure affects the reaction kinetics, we measured the reaction rates with systematically varying the total pressure going up from  $10^{-7}$  to  $10^{-3}$  mbar by each order of magnitude and keeping the constant gas mixing ratio ( $p(\text{CH}_3\text{OH}) : p(\text{O}_2) = 1 : 0.8$ ). The results are shown in Fig. 5.4.

It is visible that, in the upper panels at  $10^{-5}$  and  $10^{-4}$  mbar range, the low temperature reaction peak of the heating cycle consists of two components as indicated by the shoulders. Whereas, in the lower panels at  $10^{-7}$  and  $10^{-6}$  mbar range, only a single low temperature reaction peak is visible.

The other main effect of the pressure increase is that all of the low-temperature peaks between 300 and 520 K are shifted to higher temperature and the separation of the different peaks during heating and cooling becomes smaller with increasing pressures. This is indicated in Fig. 5.4 by two straight lines. The low-temperature reactivity peak shifts to a higher temperature by roughly 20 K per order of magnitude difference in pressure. With decreasing separation of the two reaction peaks, their amplitude becomes smaller until they completely vanish as they coalesce beyond  $10^{-3}$  mbar. In agreement with the vanishing of the low-temperature reactivity peak at higher pressure, no such peak has been observed in studies at atmospheric pressure [21, 22].

Furthermore, it is worth noting that after passing the maximum of the low temperature peak the surface reactivity is more strongly suppressed with the increase of the total pressure. Therefore, the shapes of the low temperature peak are quite different in the each panel.

### 5.2.3 Oxygen partial pressure dependence

The gas mixing ratio has a strong influence on the stationary reaction kinetics as demonstrated in Fig. 5.5, which shows the reaction rates with different ratios of methanol to oxygen,  $p(\text{CH}_3\text{OH})/p(\text{O}_2)$ , during temperature up-ramping in the  $10^{-7}$  mbar (a) and the  $10^{-5}$  mbar pressure (b) range, respectively.

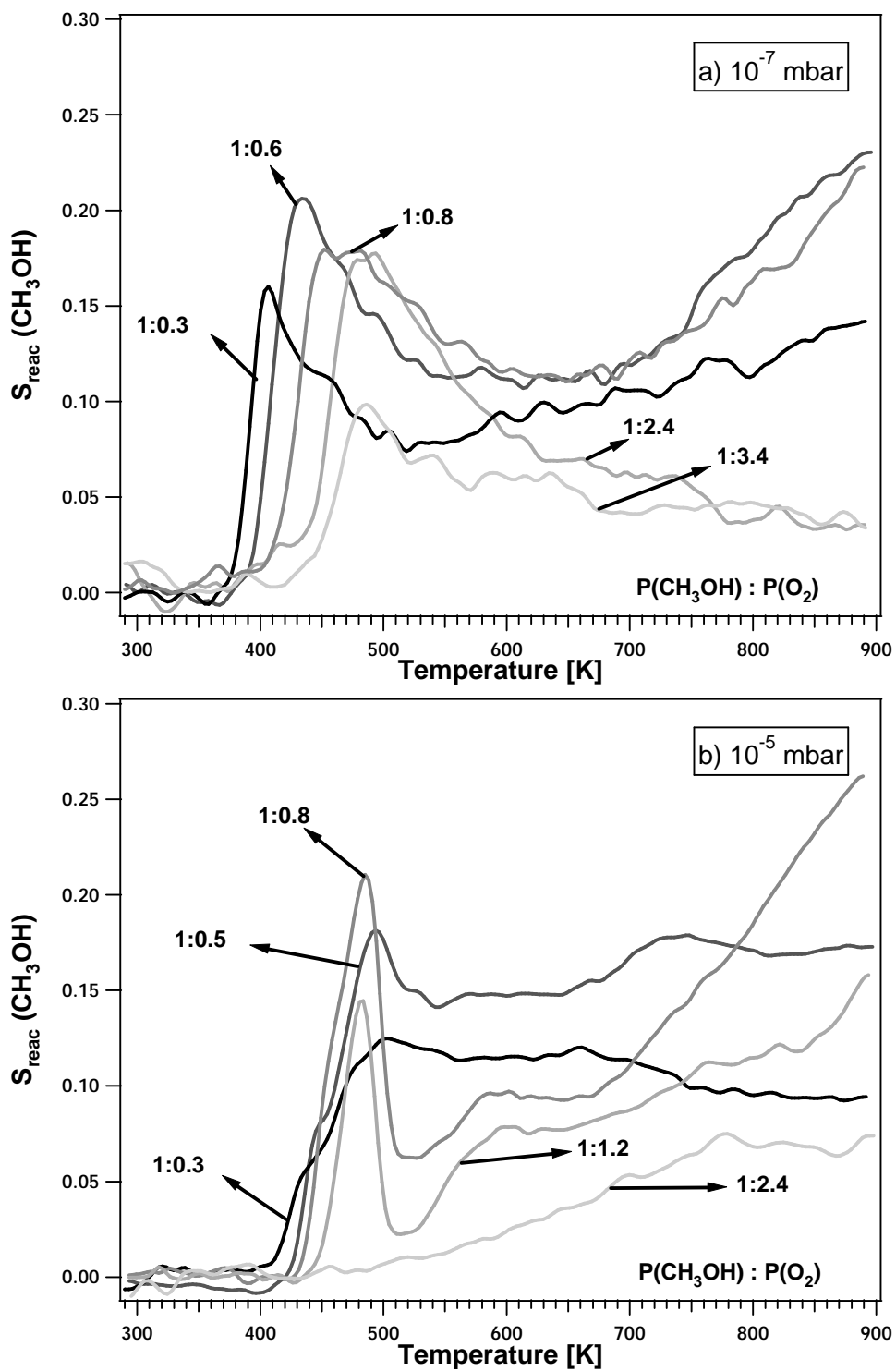


**Figure 5.5** Effect of the gas mixing ratio on methanol conversion over the Cu(110) surface in the  $10^{-7}$  mbar (a) and the  $10^{-5}$  mbar pressure range (b). The methanol conversion is given by the reactive sticking coefficient of methanol. The numbers indicated in the plots are the ratio  $p(\text{CH}_3\text{OH}) : p(\text{O}_2)$ .

In both pressure ranges the relative amount of oxygen in the gas mixture has a similar effect, although there are some differences depending on the total pressure. The optimum ratio for the low temperature conversion as judged from the height of the peak at around 420 K is a 1: 0.6 ratio in the  $10^{-7}$  mbar range, which shifts to a 1: 0.8 ratio at 480 K with  $10^{-5}$  mbar total pressure.

As shown in Fig. 5.5 (a), in the  $10^{-7}$  mbar range, with increasing oxygen content in the gas mixtures, ignition of the reaction shifts to higher temperature, but the conversion becomes low for too high oxygen partial pressures. This latter effect, which is particularly strong at high temperature, is apparently caused by the inhibitory effect of high oxygen coverages.

A similar behaviour can be also found in the reaction rate measurements in the  $10^{-5}$  mbar range as indicated in Fig. 5.5 (b). But the blocking effect of high oxygen content in the gas mixtures is even more dramatic in the higher pressure range. For example, the low temperature reaction peak already disappeared when a mixing ratio of 1: 2.4 was performed. Similarly as we noticed in the last section, it is obvious that after passing the maximum of the low temperature peak the surface reactivity (at around 520 K) has a more pronounced decrease with the increase of the oxygen content in the mixture. This means the suppression phenomena of the surface reactivity after the low temperature peak observed in the effect of the total pressure (Fig. 5.4) is due to the increase of the absolute oxygen partial pressure in the gas phase.

The dependence of the reaction rate on the oxygen partial pressure is more directly shown in Fig. 5.6 for two temperatures, 480 K and 850 K. In this experiment the methanol partial pressure was fixed at  $p(\text{CH}_3\text{OH}) = 1 \times 10^{-5}$  mbar while the oxygen partial pressure was slowly cycled. The reaction is first order with respect to an oxygen partial pressure up to  $\approx 8 \times 10^{-6}$  mbar, where the rate reaches a maximum. The position of the rate maximum varies only very little with the temperature, but the height increases from 480 K to 850 K. Beyond this point the rate decreases with increasing  $p(\text{O}_2)$ , and at high  $p(\text{O}_2)$  the reactivity of the surface becomes quite small. Evidently high oxygen coverage inhibits the reaction. One notes that at 480 K, the complete block of the surface by oxygen sets in earlier than that at 850 K. The



observed inhibitory effect of oxygen supports the reaction mechanism suggested by Bowker [31] that only the edge oxygen adatoms of O-p(2×1) islands are active sites for methoxy formation, whereas the oxygen adatoms in the Cu-O-Cu chains of the O-p(2×1) islands are inactive.

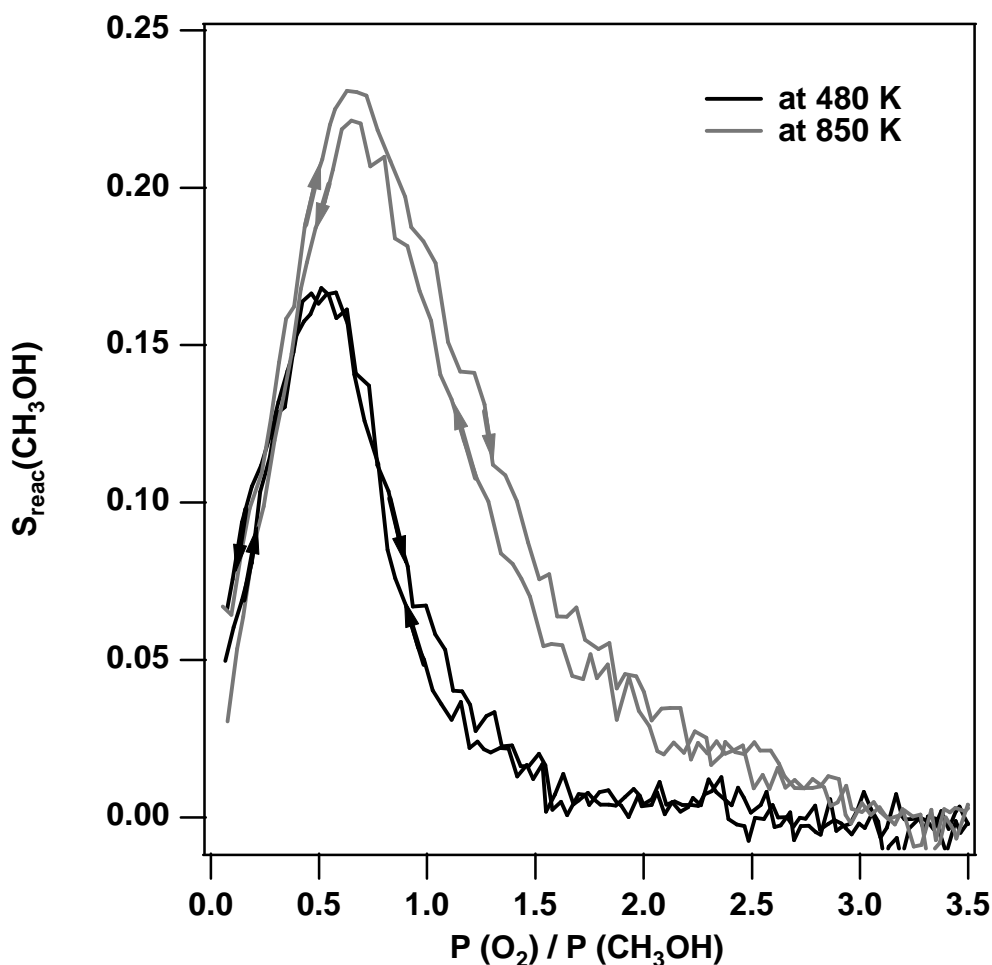


**Figure 5.6** Dependence of the reactive sticking coefficient of methanol,  $s_{\text{reac}}(\text{CH}_3\text{OH})$  on the oxygen partial pressure for  $p(\text{CH}_3\text{OH}) = 1.0 \cdot 10^{-5}$  mbar. Shown are the data for two different temperatures, 480 K and 850 K.

Fig. 5.7 shows the production rates (formaldehyde,  $\text{CO}_2$ ,  $\text{H}_2\text{O}$ ,  $\text{H}_2$ ) in the oxygen-ramping experiments at 480 K and 850 K, respectively. The formation of all the products is first order with respect to oxygen partial pressure while  $p(\text{O}_2) : p(\text{CH}_3\text{OH}) \leq 0.8 : 1$ . All the observations in the oxygen-ramping experiments are in accordance with the results in the TPR experiments in the  $10^{-5}$  mbar range. It is again

visible that at 480 K (the low temperature regime) both  $\text{H}_2\text{O}$  and  $\text{H}_2$  were produced in the reaction, whereas at 850 K (the high temperature regime)  $\text{H}_2\text{O}$  formation was preferred and nearly no  $\text{H}_2$  was produced in the reaction.

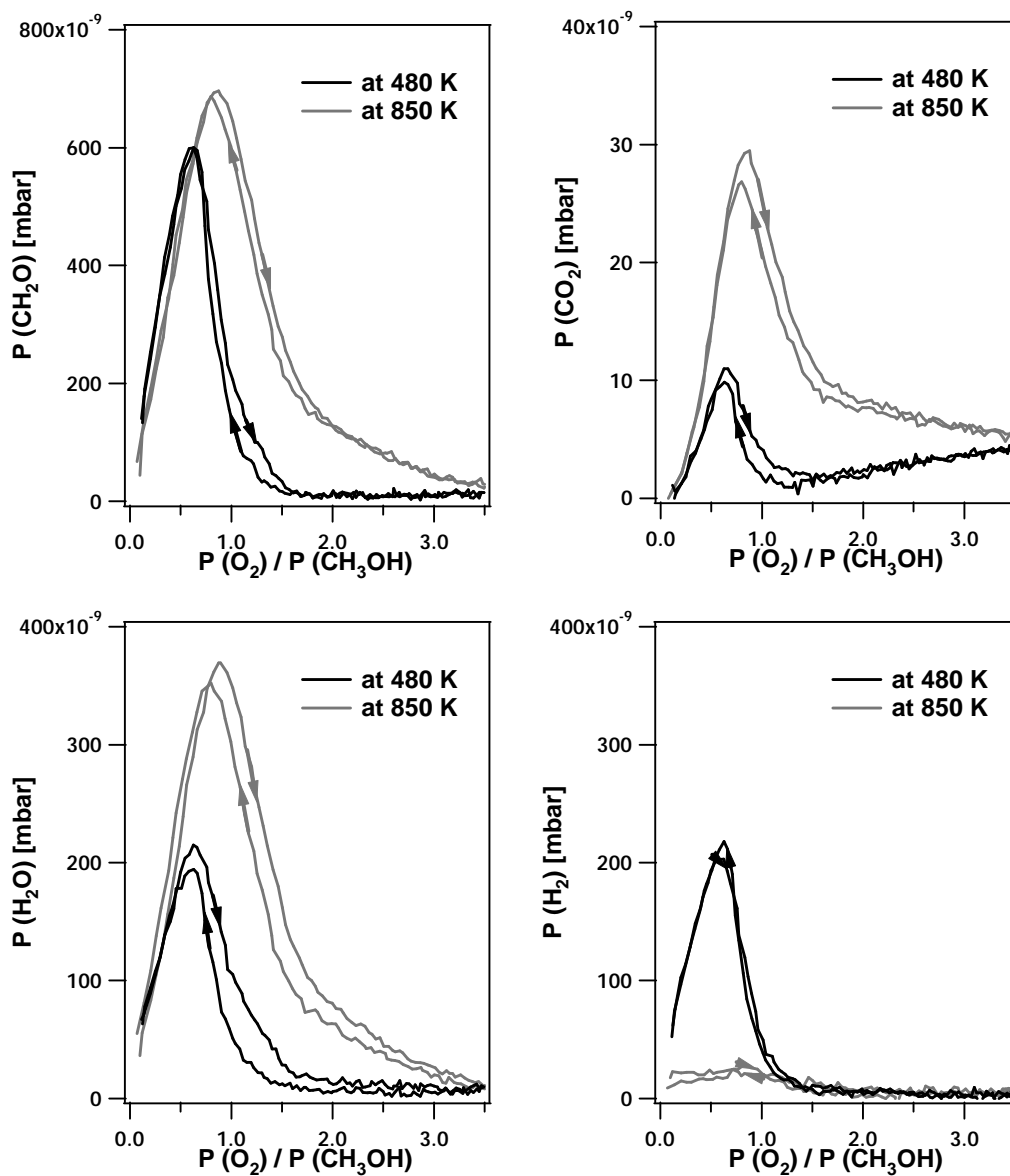


*Figure 5.7* Dependence of the production rates on the oxygen partial pressure for  $p(\text{CH}_3\text{OH}) = 1.0 \cdot 10^{-5}$  mbar. Shown are the data for two different temperatures, 480 K and 850 K.

## 5.3 Adsorbate coverages and reactivity

### 5.3.1 LEED and AES

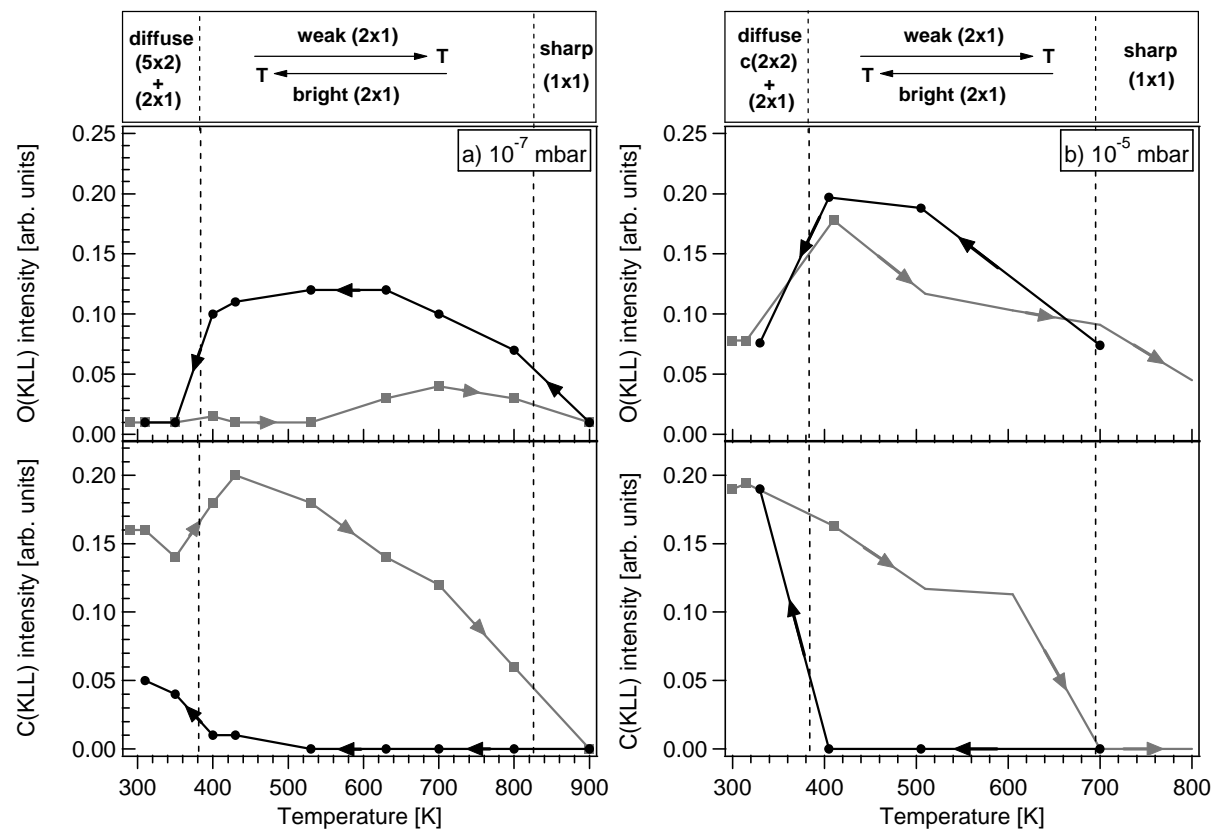


**Figure 5.8** In situ measured Auger data showing a hysteresis in the adsorbate coverages during temperature cycling under stationary reaction conditions. Shown are the  $O_{KLL}/Cu_{KLL}$  and  $C_{KLL}/Cu_{KLL}$  Auger intensity ratios during cycling in two different pressure ranges, at  $10^{-7}$  and  $10^{-5}$  mbar. Experimental conditions: (a)  $p(\text{CH}_3\text{OH}) = 1 \cdot 10^{-7}$  mbar,  $p(\text{O}_2) = 0.6 \cdot 10^{-7}$  mbar (b)  $p(\text{CH}_3\text{OH}) = 1 \cdot 10^{-5}$  mbar,  $p(\text{O}_2) = 0.8 \cdot 10^{-5}$  mbar. The LEED structures observed in situ during the T-cycles are indicated.

In order to characterize the state of the surface under stationary reaction conditions, the Auger peaks of oxygen and carbon and the LEED pattern were monitored during temperature cycling in the  $10^{-7}$  and  $10^{-5}$  mbar range. The results are displayed in Fig. 5.8. The main observation is that during heating the surface is covered by carbon containing species, whereas during cooling the surface is nearly carbon free but exhibits a medium oxygen coverage. At high temperature (above 800 K), the surface exhibits a low adsorbate coverage. The  $(5\times 2)$ -methoxy and the  $c(2\times 2)$ -formate ordered layers are observed only at low temperature.

Clearly, the large hysteresis in the production rates is correlated with an equally large hysteresis in the distributed adsorbate species and their corresponding coverages. The amount of oxygen on the surface can be calibrated to the  $O_{KLL}/Cu_{KLL}$  ratio of 0.22 obtained from a  $(2\times 1)$  oxygen layer with 0.5 ML. Using this reference we can estimate that in the  $10^{-5}$  mbar experiment at high temperatures the surface is covered by  $\approx 0.1$  ML oxygen, whereas at about 400 K,  $\approx 90\%$  of the surface should be covered by a  $(2\times 1)$ -O adlayer.

Unfortunately, calibration of the carbon Auger signal turned out not to be feasible. Since Leibsle et al. [27] have reported the sensitivity of the methoxy layer to the electron beam of their LEED system, beam damaging effects are probably present in our measurements too. In any case, the beam damaging effect should decrease with increasing total pressure, because with higher pressure the turnover frequency of the reaction will increase and with it the probability that dissociation products formed by the electron beam are removed through a clean-off reaction. This effect could be responsible for the small oxygen signal that is seen in the heating part of the  $10^{-7}$  mbar cycle, because at  $10^{-5}$  mbar the oxygen coverage during heating is substantial. This is what one would expect, because if the carbon is present as methoxy or formate species, a correspondingly large oxygen signal has to be found. Thus the absence of such an oxygen signal in the  $10^{-7}$  mbar range might well be due to beam damaging effects. We have no indication that aside from this possible effect any other results are significantly influenced by beam damaging.

### 5.3.2 PEEM

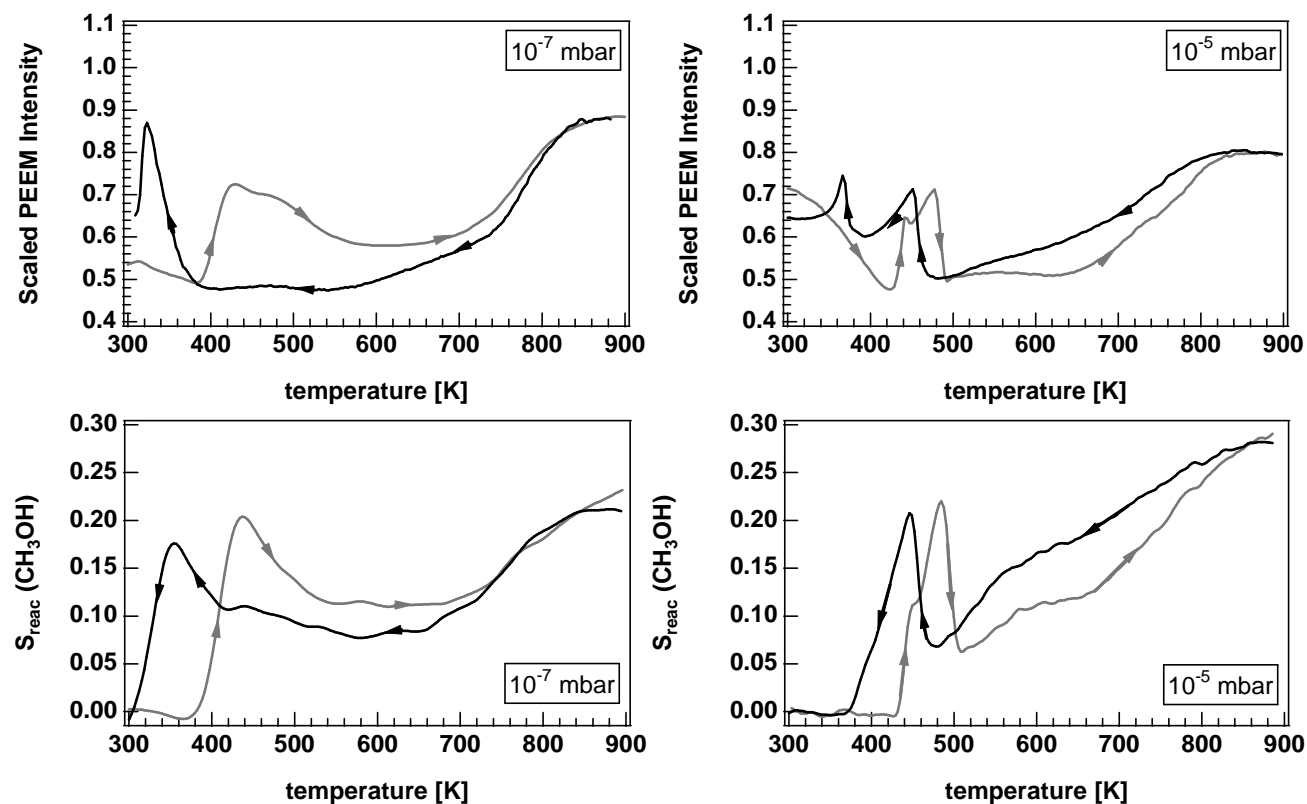


**Figure 5.9** PEEM intensity variations and the corresponding changes in the reactivity of the surface expressed here as reactive sticking coefficient of methanol,  $s_{\text{reac}}(\text{CH}_3\text{OH})$ . Temperature cycles in two different pressure ranges, at  $10^{-7}$  and at  $10^{-5}$  mbar have been conducted. Experimental conditions:  $10^{-7}$  mbar range:  $p(\text{CH}_3\text{OH}) = 1.0 \cdot 10^{-7}$  mbar with  $p(\text{CH}_3\text{OH}) : p(\text{O}_2) = 1 : 0.6$ ;  $10^{-5}$  mbar range:  $p(\text{CH}_3\text{OH}) = 1.0 \cdot 10^{-5}$  mbar with  $p(\text{CH}_3\text{OH}) : p(\text{O}_2) = 1 : 0.8$ . The PEEM data are scaled to the intensity of the clean Cu(110) surface as unity.

The problem of beam damaging effects can be avoided with the use of PEEM to monitor the state of the surface under reaction conditions. The original motivation to use PEEM in this study has been the idea that the ignition and extinction phenomena that occur in the hysteresis experiments might be associated with the spreading of reaction fronts. However, in the investigated parameter range from  $10^{-7}$  mbar to  $10^{-4}$  mbar all surface changes occurred spatially uniformly on the length scales accessible to PEEM. We can nevertheless use the PEEM intensity to monitor the work function (WF) changes of the surface. Since our PEEM intensity was not calibrated by comparison with a Kelvin probe we cannot quantitatively measure the WF. We therefore define a simple arbitrary scale of the PEEM intensity by taking the intensity of the clean Cu(110) as 1.0. With the same settings different structures were prepared and their PEEM intensities were measured. On the same scale the (2×1)-O yields a value of 0.4, the c(5×2)-methoxy a value of 1.4 – 1.6, and the c(2×2)-formate a value of 0.67. All of these values are reproducible within 15%.

The variation in the scaled PEEM intensity during temperature cycles at  $10^{-7}$  and  $10^{-5}$  mbar is displayed in Fig. 5.9, together with the change in catalytic activity expressed here via the reactive sticking coefficient of methanol,  $s_{\text{reac}}$ . As expected the PEEM intensity varies between two extrema, given by the intensity of the (5×2)-methoxy and the (2×1)-O, but over a wide range the intensity is much closer to the oxygen structure than to the methoxy phase.

The double peak structure of the reactivity peak at  $\approx 450$  K during heating, which is hidden as a shoulder in the measurement at  $10^{-5}$  mbar (Fig. 5.2), clearly shows up in the PEEM intensity. The comparison with Fig. 5.2 reveals that the higher-lying of the two reactivity peaks coincides with the CO<sub>2</sub> production maximum, which in contrast to all other products has no clearly discernible second peak, but a slowly increasing onset. The relatively low PEEM intensity is observed in the unreactive range between 300 and 400 K and is consistent with the mixture of oxygen and methoxy or formate islands visible in LEED. The Auger data in Fig. 5.8 show that in the  $10^{-5}$  mbar range the oxygen coverage grows continuously with heating from 300 K until ignition occurs at  $\approx 430$  K. This growth in oxygen coverage is reflected by a corresponding decrease in PEEM intensity in Fig. 5.9.

In an intermediate temperature range between 300 and 700 K the hysteresis effects are substantially larger in the  $10^{-7}$  mbar range than that at  $10^{-5}$  mbar, as far as the oxygen is concerned. This is reflected by the Auger data in Fig. 5.8 and by the PEEM intensity in Fig. 5.9. The oxygen concentration measured by Auger electron spectroscopy is the sum of chemisorbed oxygen and oxygen in organic compounds. The Auger data in the  $10^{-5}$  mbar range show no large hysteresis effect, but since we observe in LEED only weak ( $2\times 1$ ) spots upon heating and sharp, bright ( $2\times 1$ ) spots during cooling, we can conclude that the amount of chemisorbed oxygen has increased strongly on the cooling branch.

At high temperatures, in the range of 800 – 900 K, the PEEM intensity approaches the level of the clean surface, but the difference remains finite and becomes smaller with decreasing total pressure. At  $10^{-5}$  mbar one can estimate a remaining oxygen coverage of 0.1 ML from a linear extrapolation of the PEEM data, which agrees with the Auger measurements in Fig. 5.8.

### 5.3.3 XPS

Since *in situ* AES measurements only yielded the semiquantitative information of the adsorbate coverages during the reaction, we have used *in situ* XPS to investigate the partial oxidation of methanol over Cu(110) in the pressure range between  $10^{-7}$  and  $10^{-5}$  mbar in order to achieve the quantitative analysis of the adsorbate species present on the surface and relate them to the observed catalytic reactivity. The experiments were performed at BESSY in Berlin at the undulator beam line U49/2-PGM1.

Before comparing the catalytic properties with the measured XP spectra, it is necessary to assign the observed spectral features to different surface species. Table 5.1 summarizes the corresponding binding energies of C 1s and O 1s core level for the possible adsorbate species in the former XPS studies of methanol and formic acid oxidation over Cu(110) under UHV conditions [24, 25, 95]. It can be seen that, under low-pressure and unsteady-state conditions, besides oxygen (two different oxygen coverages), two carbon-containing species methoxy and formate are efficiently formed on the surface and can be resolved by XPS.

**Table 5.1** C 1s and O 1s binding energies (eV) for the possible adsorbates in the former XPS studies.

	O 1s	C 1s	Source
O/Cu (110)	530.0 ( $\pm$ 0.2) eV		[24] M. Bowker, R. J. Madix, Surf. Sci., 95 (1980) 190.
CH <sub>3</sub> O/Cu (110)	530.8 eV	286.2 eV	
CH <sub>3</sub> OH/Cu (110)	532.4 eV	286.2 eV	
O/Cu (110)	529.8 eV		[25] A. F. Carley, et al., Catal. Lett., 37 (1996) 79.
CH <sub>3</sub> O/Cu (110)	530.9 eV	285.5 eV	
HCOO/Cu (110)	531.6 eV	288 eV	
O-(2 $\times$ 1)/Cu (110)	530.7 eV		[95] M. Bowker, et al., Surf. Sci. 418 (1998) 71.
O-c(6 $\times$ 2)/Cu (110)	529.5 eV		
HCOO/Cu (110)	531.4 eV	287.9 eV	
HCOOH/Cu (110)	532.7 eV	289.8 eV	
C contamination/Cu		284.5 eV	

It is known in the former studies that co-adsorbing oxygen and methanol under methanol-rich condition favors the formation of methoxy (at  $10^{-7}$  mbar) and formate (at  $10^{-5}$  mbar) species on Cu(110). In order to obtain well resolved methoxy related C 1s and O 1s peaks, an oxygen pre-covered Cu(110) sample was annealed in a methanol rich atmosphere of  $p(\text{CH}_3\text{OH}) = 1.4 \times 10^{-6}$  mbar and  $p(\text{O}_2) = 0.2 \times 10^{-6}$  mbar. Upon cooling the sample, a significant amount of methoxy was temporarily formed on the surface. As demonstrated in Fig. 5.10, the identification of the distinct adsorbate phases was achieved by resolving different components in the C 1s and O 1s core level peaks.

Since the XPS system was originally designed for the high-pressure studies ( $10^{-7}$  – 1 mbar), it was difficult to rule out the effects of contaminations during surface analysis. It was found that, within a day, a SiO<sub>2</sub> contamination below 0.06 ML was slowly accumulated, which could be readily removed by Ar<sup>+</sup> sputtering. A large amount of carbon contamination accumulated when a high methanol and a low oxygen partial pressure were chosen, as visible in Fig. 5.10. One notes that, in the second spectrum at 410 K, with a negligible O 1s signal, a pronounced C 1s peak with



a binding energy of 284.4 eV exists in the spectrum. We assigned it to C(a) contamination. The C(a) contamination (and a very small amount of C(b) contamination at C 1s peak with binding energy of 283.2 eV) occurred probably due to  $C_xH_y$  species possibly generated at the chamber walls. With higher oxygen content in the gas feeding, these carbon contaminations were burned out at elevated temperature. However, at low temperature, these contaminations often existed and occupied nearly 0.5 ML adsorption sites.

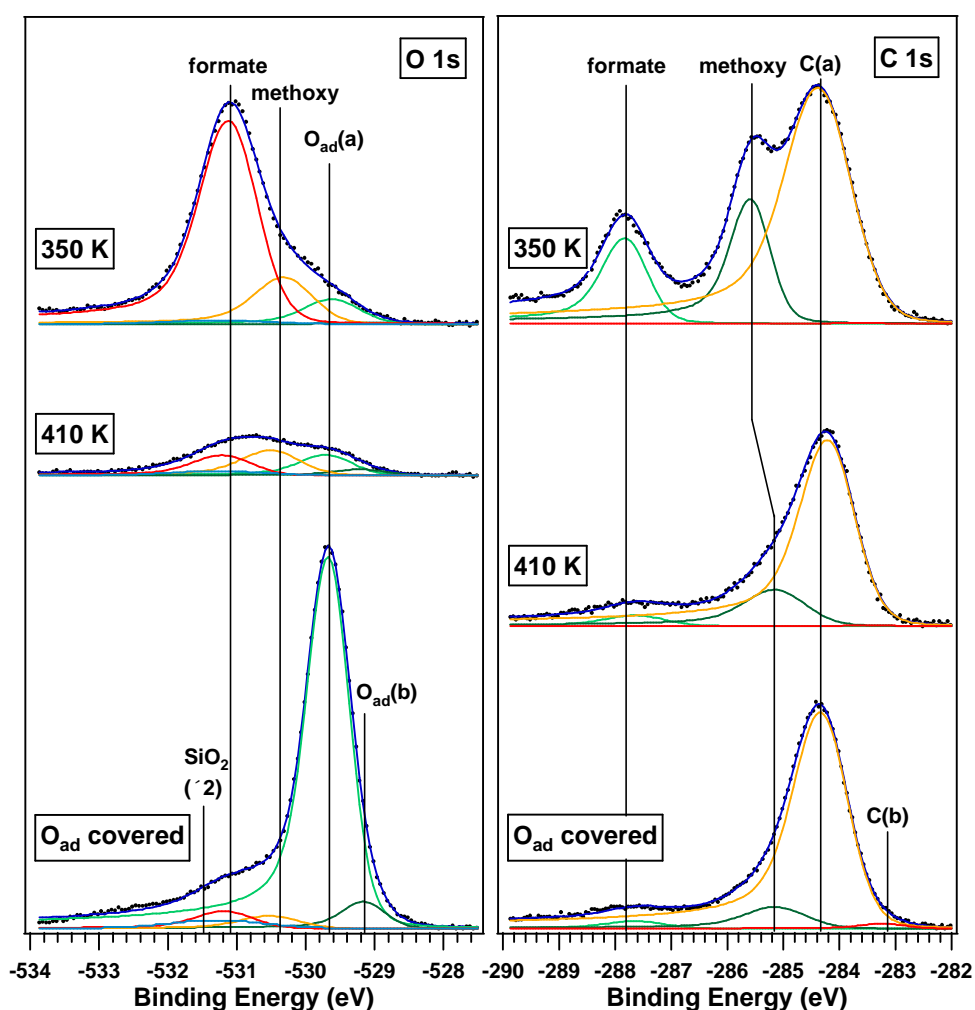


**Figure 5.10** O 1s and C 1s components for different adsorbate species on Cu(110):  $O_{ad}(a)$  (well-ordered  $O(2 \times 1)$ ),  $O_{ad}(b)$  (disordered), methoxy, formate, C(a) and C(b) contaminations, and a small amount of  $SiO_2$  impurity. The spectra were taken on an oxygen pre-covered Cu(110) surface, which was annealed in a methanol rich atmosphere of  $p(CH_3OH) = 1.4 \times 10^{-6}$  mbar and  $p(O_2) = 0.2 \times 10^{-6}$  mbar, and then cooled down at 410 and 350 K.

As shown in Fig. 5.10, on an oxygen pre-covered surface, except the carbon contaminations, a SiO<sub>2</sub> impurity, and a tiny amount of methoxy or formate, two oxygen components with binding energy of 529.7 eV (O<sub>ad</sub>(a)) and 529.2 eV (O<sub>ad</sub>(b)) can be resolved in the O 1s spectrum. The former, O<sub>ad</sub>(a), is abundant and can be assigned to oxygen in well-ordered O-(2×1) islands, which is in agreement with the LEED observation. The identification of the second small O 1s peak, whose binding energy shifts to a little lower value, is a more complex task, since no XPS study reported this oxygen state. However, it has been revealed in a recent STM study [96] of oxygen chemisorbed on Cu(110) that, besides the stable O-(2×1) ordered layer, the isolated disordered metastable states of oxygen present on the surface with evidence for clustering of a small amount of adatoms. Since the amount of the oxygen species, O<sub>ad</sub>(b), is very small, we can nevertheless assign it to a small amount of disordered oxygen adatoms on the surface.

After the sample was annealed in the methanol-rich gas mixture and cooled down to 350 K, C 1s spectrum clearly shows three peaks with binding energies of 284.4 eV, 285.5 eV, and 287.8 eV. The first one is assigned as C(a) contamination, and the other two can be attributed to the methoxy and formate species. O 1s spectrum is accordingly separated to three components with binding energies of 529.7 eV (O<sub>ad</sub>(a)), 530.4 eV, and 531.1 eV. In accordance with the values in the literatures shown in Table 5.1, the values of C 1s and O 1s peaks with binding energies of 285.5 and 530.4 eV are characteristic of methoxy species, whereas the other two peaks at 287.8 and 531.1 eV can be assigned to formate adsorbate.

At 300 K, while co-adsorbing of oxygen and methanol at 10<sup>-5</sup> mbar, e.g. at p(CH<sub>3</sub>OH) = 0.5 × 10<sup>-5</sup> mbar and p(O<sub>2</sub>) = 0.3 × 10<sup>-5</sup> mbar, apart from the C-contamination, formate is exclusively formed on the surface. Since under similar conditions a c(2×2) ordered structure was seen in LEED as indicated in chapter 4, we can conclude that the c(2×2) ordered structure should correspond rather to a formate adlayer than to methoxy, as controversially discussed in [28, 29, 39].

The adsorbate coverages were calibrated using the O 1s intensity of the well known 0.5 ML oxygen coverage of a fully (2×1)-O covered Cu(110) surface. Using the fact that the methoxy molecule consists of C : O = 1 : 1, whereas for formate this

ratio is 1 : 2, the relative sensitivity factor for C 1s and O 1s can be obtained. Within the errors of the experiment the coverage of all adsorbates can be calculated, where the coverage is defined as absolute adsorption sites. It should be noted that one formate molecule is bound to two adsorption sites via its two oxygen atoms as shown in Fig. 4.3(b).

The variation of the adsorbate coverages on the surface during temperature cycles under stationary reaction condition ( $p(\text{CH}_3\text{OH}) = 0.5 \times 10^{-5}$  mbar and  $p(\text{O}_2) = 0.3 \times 10^{-5}$  mbar) is quantitatively displayed in Fig. 5.11, together with the change in formaldehyde production rates. A heating/cooling rate of 5 K/min was sufficiently slow to ensure that the reaction was close to steady-state condition. One notes that, a maximum of 1 ML coverage is reached at low temperature, and at least around 0.5 ML carbon contamination can fill the empty adsorption sites in the ordered adlayers.

It is visible in the upper panel of Fig. 5.11 that, a pronounced hysteresis in the formaldehyde production rates is found during temperature cycles. While temperature up-ramping, the reaction ignites at  $\approx 380$  K; after reaching the maximum of the low-temperature reaction peak at  $\approx 420$  K, the reaction rate drops to nearly zero at 450 K; the surface reactivity resumes again at  $\approx 490$  K and approaches the high temperature peak at  $T > 800$  K. Correspondingly, it is shown by XPS analysis that below 380 K the surface is fully covered by approximate 0.38 ML formate, 0.02 ML methoxy, 0.1 ML oxygen, and 0.5 ML carbon contamination. Starting at 380 K, formate coverage decreases slightly, whereas the coverages of other species remain stable roughly. With the decrease of the formate coverage, a small amount of vacant adsorption sites is produced. From  $\approx 420$  to 490 K, parallel to the decrease of the adsorbed formate coverage, the oxygen coverage on the surface obviously increases reaching about 0.3 ML. During the course, the coverage of the carbon contamination continuously decreases to about 0.2 ML. The oxygen coverage is stable up to  $\approx 490$  K, and decreases significantly above  $\approx 520$  K. With the continuous increase of the temperature to above  $\approx 750$  K, it is shown that only approximately 0.1 ML oxygen exists on the surface, which is in agreement with the estimation from the AES and PEEM measurements. At  $\approx 535$  K, a coverage jump occurs, which is due to the beam injection during the experiment.

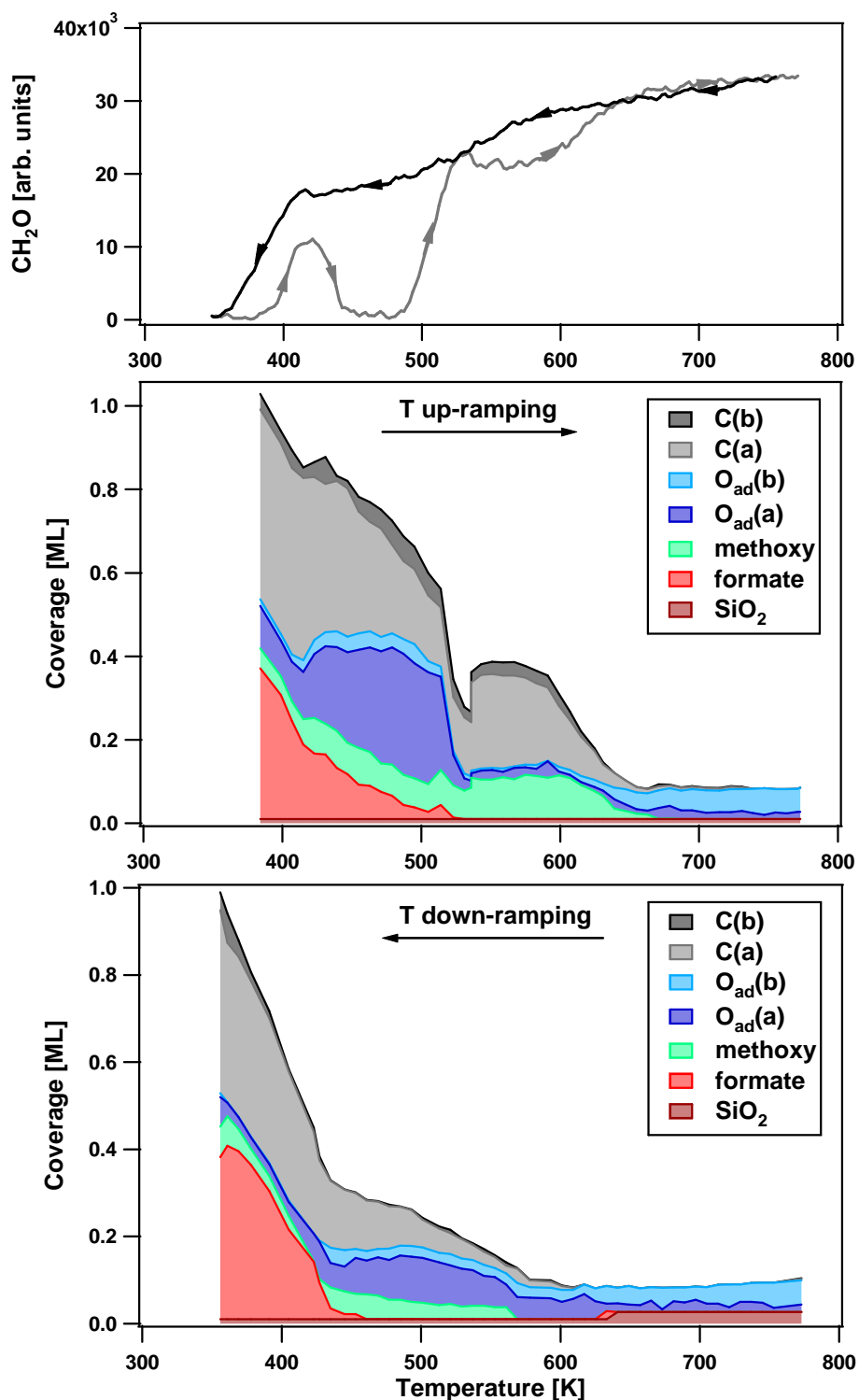


**Figure 5.11** Variation of adsorbate coverages during temperature cycling under stationary reaction condition:  $p(\text{CH}_3\text{OH}) = 0.5 \cdot 10^{-5}$  mbar and  $p(\text{O}_2) = 0.3 \cdot 10^{-5}$  mbar. The upper panel displays the corresponding formaldehyde production rate. The heating/cooling rate for the experiment was 5 K/min.

During cooling the sample, the surface reactivity remained high and extended down to  $\approx 350$  K. As shown in Fig. 5.11, with the exception of the carbon contamination, the surface remains carbon-containing species free in a larger temperature range, which is in concert with the AES measurements. At  $\approx 430$  K, with the obvious decrease of the oxygen coverage, a large amount of formate and carbon contamination starts to accumulate on the surface. Corresponding to the block of the reaction at  $\approx 350$  K, the surface is again completely adsorbates covered.

In Fig. 5.11, it is clearly shown that the hysteresis in the reaction rates is directly connected with a corresponding hysteresis in the adsorbate coverages. Especially the oxygen coverage and the amount of the free surface area strongly affect the surface reactivity. It may be worth mentioning that  $O_{ad}(b)$ , which was assigned to the disordered oxygen species, exists more on the surface at high temperature. This is possibly reasonable, because at high temperature on the one hand the mobility of the oxygen adatoms is high, on the other hand the high reaction probability inhibits the growth of the O-(2 $\times$ 1) islands. Vice versa, more disordered oxygen species (or small oxygen clusters), higher activity can be achieved, since it is well-known that only the terminal oxygen molecules in the O-(2 $\times$ 1) islands are active sites for methanol oxidation. This autocatalytic behaviour may control the oxygen states on the surface, which might cause the high reactivity during temperature down-ramping.

Fig. 5.12 displays the effect of the gas mixing ratio on the formaldehyde production rate and the corresponding adsorbate variation on Cu(110) during the methanol selective oxidation. The methanol partial pressure was kept at  $0.5 \times 10^{-5}$  mbar in the experiments. It is shown that with the low oxygen partial pressure of  $0.15 \times 10^{-5}$  mbar, the formaldehyde production rate is low and slowly increases after the reaction onset at  $\approx 380$  K. It is seen in the corresponding variation of the adsorbates coverage that, the amount of oxygen on the surface is quite low (less than 0.05 ML), whereas the coverage of the carbon contamination remains high. With the higher oxygen partial pressure to  $0.5 \times 10^{-5}$  mbar, the oxygen coverage on the surface increases obviously and promotes the reaction. It can be estimated by relating the oxygen coverage to the surface reactivity that a surface with an oxygen coverage of approximate 0.1 – 0.2 ML exhibits a pronounced maximum in oxidation reactivity.

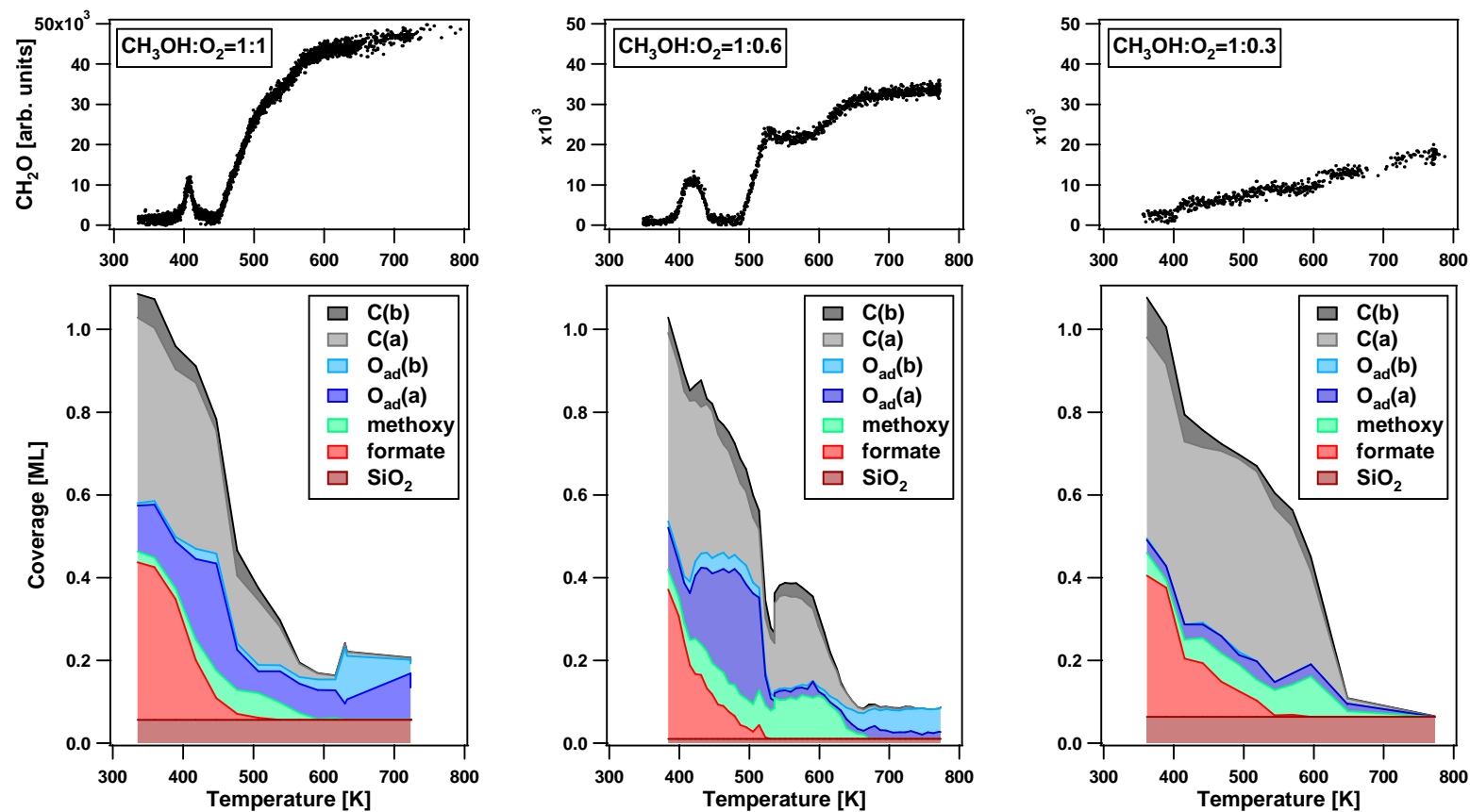


**Figure 5.12** Adsorbates present on Cu(110) during the methanol selective oxidation at  $p(\text{CH}_3\text{OH}) = 0.5 \cdot 10^{-5}$  mbar and different gas mixing ratios. The corresponding upper panel displays the formaldehyde production rate.

It is notable that in contrast to a broad low-temperature peak at  $\text{CH}_3\text{OH} : \text{O}_2 = 1 : 0.6$ , at  $\text{CH}_3\text{OH} : \text{O}_2 = 1 : 1$  a sharp low-temperature peak is visible in the upper panels of Fig. 5.12. This change of the peak shape can be well related to the corresponding accumulation rate of the high oxygen coverage above 0.2 ML which poisons the reaction. In another experiment with an oxygen-rich gas mixture ( $p(\text{CH}_3\text{OH}) = 0.5 \times 10^{-5}$  mbar,  $\text{CH}_3\text{OH} : \text{O}_2 = 1 : 1.8$ ), it was shown that the surface was always covered by about 0.4 ML oxygen besides the carbon contamination, and a negligible reaction rate was detected.

It should be stated that all the values of the absolute adsorbate coverage are only comparable in our own experiments at BEESY due to the presence of a large amount of carbon contamination on the surface. However, the behaviour of the surface still can link to the measurements in the UHV system at PCI, Hannover, which allows us to use the results of the quantitative XPS analysis to explain the observations in the kinetic measurements.

## 5.4 Reaction mechanism

From the above described findings of the stationary reaction kinetics and the different surface adsorbate coverages related to the surface reactivity we can get numerous information concerning the reaction mechanism of methanol oxidation over Cu(110) under low pressure conditions.

The prominent feature of the reaction kinetics in this system is the presence of a very large hysteresis in temperature-dependent measurements. In surface reactions hysteresis typically arises if one of the reactants present in large amounts on the surface inhibits the adsorption of the other reactant. The LEED / PEEM / Auger / XPS measurements conducted here clearly indicate that the hysteresis in the reaction rates is connected with a corresponding hysteresis in the adsorbate coverages. The changes in the brightness of the (2×1) LEED spots (Fig. 5.8) indicate that in addition to the total amount of oxygen, the adlayer ordering may also be different.

The results of the reaction kinetics measurements showed the dramatic changes of the low temperature reaction peak under the different reaction conditions.

Both the ignition temperature and the shape of the reaction peak are strongly dependent on the total pressure of the reaction, as well as the oxygen partial pressure. In the  $10^{-7}$  mbar range the onset of the reaction at  $\approx 400$  K is obviously determined by a structural effect, since during temperature down-ramping the reaction is still active upon down to 330 K. From LEED experiments presented in Chapter 4, we know that, after co-dosing methanol and oxygen at  $10^{-7}$  mbar a perfect  $(5\times 2)$  layer builds up on the Cu(110) surface, and then the layer slowly transforms into a  $(5\times 2) + (2\times 1)$  mixed layer, i.e., oxygen co-adsorbed with methoxy. From the TPD experiments, we know that methoxy decomposes to formaldehyde at low temperature of around 330 K. However, in the TPR experiments, at this temperature no product forms.

The reason why the reaction pathway is blocked could be the high coverage of the adsorbates layer shown in XPS analysis, since in the former STM studies [27] it was suggested that methoxy probably decomposes into formaldehyde and hydrogen on the clean surface. The observation of the ignition temperature delay in the stationary reaction strongly supports the suggestion that the methoxy decomposition needs vacant adsorption sites. In the TPD experiments, due to the back-reaction pathway in which methoxy can recombine with hydrogen adatoms to desorb as methanol even below room temperature, bare surface for methoxy decomposition always exists. In contrast, under stationary conditions if a small amount of vacant adsorption sites is present, they are soon refilled by the molecules from the gas phase. With time and while slowly up-ramping the temperature, formate is produced. In the  $10^{-5}$  mbar range, a  $c(2\times 2) + (2\times 1)$  mixed layer was observed by LEED before the reaction, which indicates a large amount of formate and some oxygen existing on the surface. Since the observed hysteresis of the reaction rate correlates with the adsorbate coverages on the surface as indicated in Fig. 5.8 and 5.12, we conclude that the absence of vacant sites on the surface blocks the occurrence of the reaction at low temperature.

In the  $10^{-7}$  mbar range, starting at  $\approx 420$  K the decomposition of formate takes place leading to the detected  $\text{CO}_2$  desorption peak at 460 K, as shown in Fig. 5.1. This desorption peak coincides with a slight change in the PEEM intensity, indicative of a



change in the adsorbate structure. The correlation with the PEEM intensity is more pronounced in the experiments at  $10^{-5}$  mbar. The two peaks in the PEEM intensity can be well related to the decomposition of the accumulated formate on the surface at 460 K and the real  $\text{CO}_2$  production peak in the reaction at 480 K. One notes that the formate decomposition contributes to the formation of free sites on the surface. Since the decomposition of a formate molecule leads to two free adsorption sites, this reaction pathway plays an important role of maintaining the surface reactive, although the production rate of formate does not have to be high. One more finding supports the proposed scenario of the reaction: the ignition temperature of the reaction at higher total pressures reaches the value at 460 K which is the temperature of formate decomposition. More directly, the XPS analysis during the reaction at  $10^{-5}$  mbar showed the increase of the free surface area proceeds parallel to the decrease of the formate coverage on the surface, which fits the onset of the reaction rate. Therefore we believe that the formate decomposition is an important step in igniting the reaction, although formate is only produced to a minor amount at low temperature.

Following the ignition of the reaction, the free sites generated by the formate decomposition are partially refilled by methoxy and oxygen adsorbates. Methoxy can decompose to formaldehyde and generate a free site as well. Therefore the autocatalytic behaviour directs the reaction pathway of methoxy decomposition, which requires vacant site, and leads to the formation of the dominant product – formaldehyde. The development of the surface adsorbate species is then probably controlled by the composition of the gas mixture, which is reflected in the decay part of the low temperature reaction peak. This could be the reason why the shape of the low temperature reaction peak is strongly oxygen partial pressure dependent. With the increase of the oxygen content in the gas mixture, the accumulation rate of the oxygen-(2×1) island increases and exceeds the reaction rate, so that the amount of the free sites for methoxy decomposition dramatically decreases and the reaction is to some extent blocked again. This regime can be considered as an oxygen poisoning effect, which is supported by the slow decrease at  $10^{-7}$  mbar and the sudden decrease at  $10^{-5}$  mbar of the PEEM intensity in Fig. 5.9, and the accumulation rate of the high oxygen coverage shaping the low-temperature reaction peaks in Fig. 5.12.

Another important finding in the kinetics measurements is that hydrogen formation has a structural reason. If one considers that the methoxy formation can take place only around the perimeter of an oxygen-(2×1) island, it is expected that at low temperature the surface should consist of oxygen-(2×1) islands separated from and probably surrounded by (5×2)-methoxy islands. If the decomposition of the methoxy can take place, the hydrogen adatom released from the decomposing methoxy molecule either diffuses back to an oxygen atom or an OH group finally forming the H<sub>2</sub>O production, or meets another diffusing hydrogen adatom leading to H<sub>2</sub> production. Note that, if the oxygen islands are surrounded by methoxy adatoms the released hydrogen adatoms have more chances to meet each other leading to H<sub>2</sub> production rather than to reach an OH group resulting in desorbing as H<sub>2</sub>O. This mechanism can be regarded as the reason for the H<sub>2</sub> production channel in the intermediate temperature range.

At high temperature above 800 K the adsorbate coverage is fairly low and the mobility of the adsorbed species is high, so that the adsorbed hydrogen released during the formaldehyde formation can always reach an adsorbed oxygen atom. This is why the stoichiometry clearly follows the water formation route, as well as why the poisoning of the reaction with oxygen is less dramatic at high temperature. Since during temperature down ramping the adsorbate coverage is lower and especially the methoxy species are nearly not present on the surface for a much wider temperature range, the reaction extends to a lower temperature and the H<sub>2</sub> production exists for a much wider temperature range as well.

Kinetic measurements have shown that the low temperature reactivity peak around 400 K undergoes a strong upward shift with increasing total pressure, which amounts roughly to a 20 K shift per decade difference in pressure. Quite generally, the increase in pressure will increase the coverage and shift processes to higher temperatures if the number of vacant sites plays an essential role. Here we can be more specific because the increase in total pressure from 10<sup>-7</sup> to 10<sup>-5</sup> mbar proved to be sufficient to cause a change in the structure, from a (5×2)-methoxy at low pressure to a c(2×2)-formate at high pressure. This pressure-induced structural change might be responsible for the shift in the reaction peaks.

To summarize, we can describe the different regimes of the reaction in a temperature-programmed experiment as follows, starting with the preparation of a (5×2)-methoxy structure (in the  $10^{-7}$  mbar range) or a c(2×2)-formate structure (in the  $10^{-5}$  mbar range):

1. Transformation of the adlayer without release of reaction products ( $\approx 300 - 400$  K)

The initially “perfect” (5×2)-methoxy / c(2×2)-formate phase slowly transforms into a mixed diffuse (5×2)-methoxy / c(2×2)-formate + (2×1)-O adlayer, indicating some kind of phase separation. Since the further decomposition of the methoxy species to formaldehyde requires vacant adsorption sites, the surface fully covered with oxygen, methoxy, or formate species would be quite unreactive. This explains why we do not observe any product formation in this regime, even though the methoxy decomposition is thermally activated. Nevertheless, some of the methoxy is transformed into the formate species, which, however, does not lead to the release of products into the gas phase, but to their accumulation on the surface at low temperature.

2. Ignition of the reaction at  $T \approx 400$  K

The ignition of the reaction is presumably initiated by the thermal decomposition of accumulated formate to  $\text{CO}_2$  because the immediate desorption of the  $\text{CO}_2$  creates vacant sites where methoxy can react to formaldehyde, which is also immediately released into the gas phase as product. This autocatalytic process creates additional vacant sites, and thus accelerates the reaction. In addition, formate is generated as a side product, but this pathway becomes significant at high pressure. Apparently, the thermal decomposition of formate does not require vacant sites, because otherwise an autocatalytic behavior would result, generating a steep increase in  $\text{CO}_2$  production, which is not seen in the experiment.

3. Formaldehyde formation via oxidehydrogenation at  $520 \text{ K} < T < 750 \text{ K}$  ( $10^{-5}$  mbar range)

As shown by kinetic measurements, the overall stoichiometry of the reaction in this temperature range follows at low pressure ( $p < 10^{-4}$  mbar) the oxidehydrogenation route (5.1). The fact that the generated hydrogen adatoms were desorbed as  $H_2$  rather than further react with oxygen towards  $H_2O$  indicates that most of the oxygen on the surface is not reactive. This is the case when the oxygen is bound in organic molecules such as methoxy or formate species. The weak ( $2\times 1$ ) spots we observe in LEED seemingly contradict this statement since they demonstrate that chemisorbed oxygen is present. Apparently these oxygen islands can occupy only a relatively small fraction of the surface. Furthermore, since only the edge atoms of the islands are reactive, only a small number of adatoms of large oxygen islands can contribute to the reactivity.

#### 4. Formaldehyde formation via oxidehydrogenation without hydrogen formation at $T > 750$ K ( $10^{-5}$ mbar range)

In the temperature range above 750 K ( $10^{-5}$  mbar) the kinetics of the overall reaction follows the stoichiometry of equation (5.2) without hydrogen release. The adsorbate coverages are small in this range, and the reactivity of the surface is high. Ordered adsorbate phases appear not to play an important role in this range, and the reaction probably proceeds through isolated adsorbate molecules or small clusters.

## 5.5 Conclusions

The steady-state kinetics of methanol oxidation over a Cu(110) surface have been studied under low pressure conditions. A high selectivity for the partial oxidation product formaldehyde was found besides the byproducts  $H_2$ ,  $H_2O$ , and  $CO_2$  in the stationary reactions. The reactivity of the surface at low and intermediate oxygen coverage is quite high, as indicated by a reactive sticking coefficient for methanol, which reaches 0.2. High oxygen coverage inhibits the reaction. The reactivity of the surface exhibits two peaks at low pressure: one at around 400 – 520 K, which disappears when the total pressure exceeds  $10^{-3}$  mbar, and the other at high-temperature of around 900 K that persists at high pressure. Hydrogen production is

observed in an intermediate temperature range, reflecting the presence of a second pathway with less oxygen consumption toward formaldehyde production.

The stationary reaction kinetics is associated with a broad rate hysteresis upon variation of the temperature. The origin of the hysteresis can be attributed to two differently reactive surface phases connected with different carbon-containing species and different oxygen coverages. It can be addressed that the  $c(2\times 2)$  structure whose arrangement has been debated in the literatures is in fact due to a formate species. Ordered overlayers of reaction intermediates, the  $(5\times 2)$ -methoxy and the  $c(2\times 2)$ -formate, occur only in small, roughly 80 K wide T-intervals above 300 K, where the catalytic activity is negligible. Only the low-temperature reactivity peak at  $\approx 400 - 500$  K is associated with a substantial adsorbate coverage, whereas the high-temperature reactivity peak at 900 K correlates with a largely adsorbate-free surface. Apparently high adsorbate coverages have a negative effect on the reactivity of the surface, which can be traced back to a lack of vacant sites required for the methoxy decomposition step to proceed and a limited mobility of the reacting species. Formate species plays an important role to activate the surface since its decomposition creates the vacant sites and therefore ignites the reaction at low temperature.



## Chapter 6

# Methanol oxidation in an intermediate pressure range

### 6.1 Introduction

In the last thirty years, the identification of the active surface phases and of the relevant surface species has been the important aim of various *in situ* studies of methanol oxidation over copper catalysts under both the technical and the UHV conditions. It was shown that engraving contradictions exist due to the variation of measurement conditions.

The UHV studies [23, 31] over the Cu(110) surface showed that oxygen coverage strongly affects the surface reactivity. Both the oxygen free surface and the surface fully covered with O-(2×1) islands (0.5 ML oxygen coverage) have a very low reactivity for the dissociative adsorption of methanol, whereas a partially O-(2×1) islands covered surface (about 0.25 ML oxygen coverage) exhibits a pronounced maximum in oxidation reactivity. It was determined that the active sites in methanol oxidation over Cu(110) are the terminal oxygen atoms in the O-(2×1) islands. The scenario can explain the stationary reaction kinetics measured under low pressure conditions. And a detailed reaction mechanism with methoxy, formate, and surface oxygen species as intermediates has been proposed in chapter 5.

In recent high pressure ( $p \leq 10$  mbar) studies [16-22] on polycrystalline copper sample, a novel subsurface oxygen species, i.e. an oxygen species located in the subsurface region underneath the surface, was detected using *in situ* near-edge X-

ray absorption fine structure (NEXAFS) spectroscopy and X-ray photoelectron spectroscopy (XPS). This new oxygen species which only exists under reaction conditions at high pressure was found to be correlated to a high yield of formaldehyde, whereas both the surface oxygen and the bulk oxide phases inhibited the reaction. Therefore it was suggested that the active catalyst surface is a metallic copper that contains a subsurface oxygen species. The incorporation of subsurface oxygen in the metallic surface most likely leads to a strained copper surface lattice [45, 120]. It has been shown in a number of experimental and theoretical studies [112-115, 162-165] that strain can dramatically change the adsorption properties of metal surfaces and lead to a large increase in reactivity. Consequently, the idea came up that the reactivity of many metal catalysts in real catalysis might be determined by strain effects. To actually verify the factor for a catalytic reaction has been one of the main aims of collaborative efforts in this DFG project [166]. However the mechanism remains speculative since it is still unclear how the strain affects the partial oxidation of methanol on copper surface [167].

In addition to the problem of defining the active state of the catalyst and the role of strain, the reaction system also displays interesting dynamic behavior. Rate oscillations associated with complex temporal variations of different reaction products were discovered at high pressures above  $10^2$  mbar. These oscillations were connected with periodic transitions of the sample surface between metallic copper and copper oxides [19, 94]. Recent Raman studies of methanol partial oxidation over copper at a gas pressure slightly above 1 bar showed both CuO and Cu<sub>2</sub>O present on the surface of the copper catalyst during the reaction. Here, CuO reacted with methanol at lower temperature than Cu<sub>2</sub>O [94].

In this chapter we systematically study the kinetics of methanol oxidation over metallic and oxidized copper surfaces in an intermediate pressure range, mainly at  $10^2$  mbar in a HP-UHV system. During methanol oxidation over an oxidized copper surface, the phase transitions from a deeply oxidized surface (CuO) to a partially oxidized surface (Cu<sub>2</sub>O) and finally a metallic surface were observed by the associated colour changes and by ellipsometry as *in situ* technique. This technique which can be used in the conventional way and also for surface imaging allows



monitoring the degree of oxidation, detecting the spatial inhomogeneities and relating the surface characteristics to the reaction kinetics.

## 6.2 Reaction kinetics

### 6.2.1 Effect of the gas flow and the pump speed

In contrast to the UHV studies, at high pressure heat and mass transport problem can be no longer neglected. The reactivity of the surface might under conditions be limited not only by the kinetics of the surface reaction but by transport through the gas phase. Mixing in the gas phase will be slow at high pressure and strong gradients in concentration and temperature through the gas phase may occur.

As introduced in chapter 3, we designed a high-pressure reaction cell, which was connected to a UHV chamber, for the studies in an intermediate pressure range ( $10^{-3}$  – 1 mbar). It is known [97] that the nature of gas flow through the reactor at high pressures is quite different from that at low pressures. The flow characteristics depend on the flow rate and the geometry of the reactor. Typically three kinds of flow are recognized: turbulent flow which is a viscous flow with mixing motion above a critical Reynolds number (for circular cylindrical pipes  $Re = 2300$ ), laminar flow which is a viscous flow without mixing motion at small Reynolds numbers, and molecular flow which is the passage of a gas through a duct under conditions such that the mean free path of the molecule is very large in comparison with the largest internal dimensions of a cross section of the duct. The Knudsen number  $Kn$ , which is defined as the ratio of the mean free path  $L$  to “a characteristic dimension” of the reactor, helps define the boundary between laminar flow ( $Kn < 0.01$ ) and molecular flow ( $Kn > 1.00$ ). At conditions between the laminar flow and the molecular flow there is a transitional flow region, named the Knudsen flow, where the flow characteristics have properties of both the laminar flow and the molecular flow. Empirically in the vacuum system, below  $10^{-3}$  mbar it is molecular flow, from  $10^{-3}$  to 1 mbar it is Knudsen flow, and above 1 mbar it is viscous (laminar) flow [98].

For example, we can define the flow type for methanol in the reactor. The mean free path of the molecule is given by

$$L = \frac{1}{\sqrt{2}pd^2N}, \quad (6.1)$$

where  $d$  is the molecular diameter and  $N$  is the number of molecules per unit volume.  $N$  is related to the pressure and the temperature of the gas, and can be calculated using the ideal gas equation

$$N = \frac{P}{RT} \times 6.022 \times 10^{23}, \quad (6.2)$$

in which  $R = 62.363 \text{ L} \cdot \text{Torr} \cdot \text{mol}^{-1} \cdot \text{K}^{-1}$ . For methanol, the critical molecular diameter  $d = 4.4 \times 10^{-8} \text{ cm}$  [99]. So the mean free path for methanol at  $25 \text{ }^\circ\text{C}$  is

$$L[\text{cm}] = \frac{0.004}{P[\text{mbar}]}. \quad (6.3)$$

The maximum radius of the reactor is 3 cm. If the methanol pressure in the reactor is  $1 \times 10^{-3} \text{ mbar}$ , the Knudsen number  $\text{Kn} = 1.33$  means the methanol flow in the reactor is still the molecular flow. At methanol pressure above  $1 \times 10^{-1} \text{ mbar}$  the gas flow changes to the laminar flow. And between  $1 \times 10^{-3} \text{ mbar}$  and  $1 \times 10^{-1} \text{ mbar}$ , it is Knudsen flow.

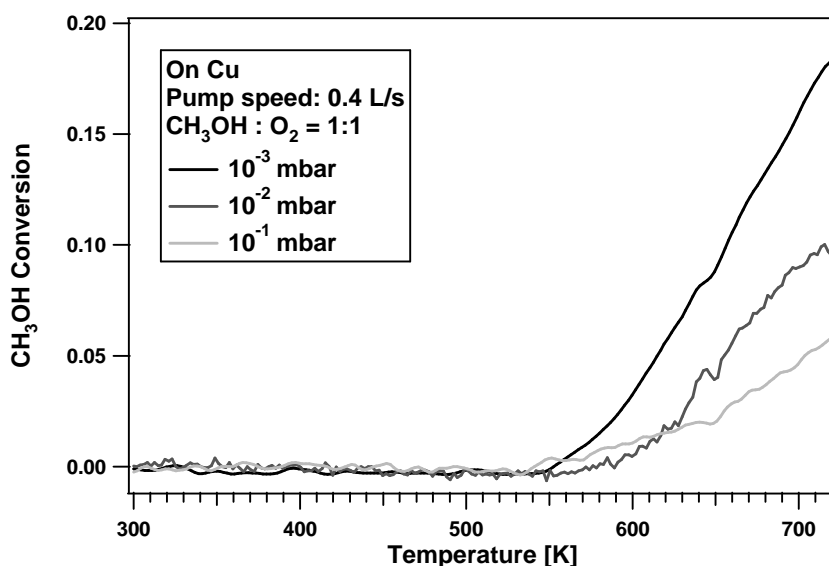


**Figure 6.1** The effect of the total pressure on the reaction rate measurements of methanol oxidation over copper in the high-pressure reaction cell. The pump speed of the system was kept constant at 0.4 L/s. The flow ratio of methanol to oxygen was kept 1:1.

The characteristics of the gas flow strongly affect the results of the kinetics measurements in the high-pressure reaction cell. Fig.6.1 shows the effect of the total

pressure on the rate measurements in methanol oxidation over the copper surface. The methanol to oxygen gas ratio and the pump speed were kept stable and the total pressure increased due to the increase of the gas flow rate in the experiments. It is visible that, while the total pressure in the reaction cell increases from  $10^{-3}$  mbar to  $10^{-1}$  mbar, the methanol conversion decreases from around 0.18 to 0.05. At  $10^{-3}$  mbar range, the gas flow is close to the molecular flow and the result of the rate measurement is very similar to the result at the same pressure range measured in the UHV system (See Fig. 5.4). With the increase of the total pressure, the collision of the gas molecules becomes more frequent and the mean free path of the gas molecules decreases. At  $10^{-1}$  mbar range, the mean free path of the molecules amounts to around 0.4 mm which is already smaller than the distance between the opening of the gas inlet pipe and the sample surface which is indicated as 2 mm in Fig. 3.5. Thus it is clear that at elevated pressures, the diffusion limited conversions of the methanol was measured. Since the mean free path of the molecules is short while the pump speed is constant, meaning the dwell time of the molecules in the reactor remains short, only a part of the reactant molecules can reach and react on the copper surface so that a lower methanol conversion is determined at elevated pressures.

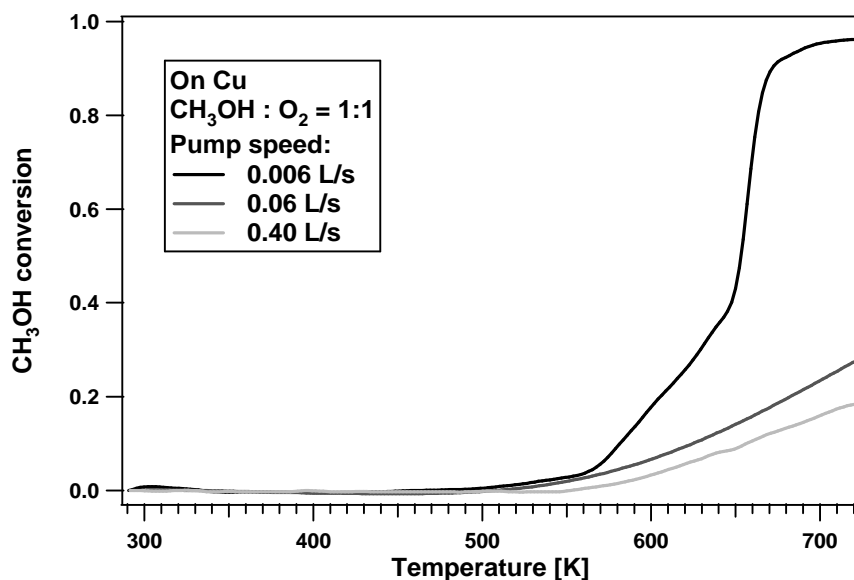


**Figure 6.2** The effect of the pump speed on the reaction rate measurements of methanol oxidation over copper in the high-pressure reaction cell. The flow ratio of methanol to oxygen was kept 1:1.

One has to consider that the pump speed also changes the status of the gas flow in the reactor and affects the result of the rate measurement. This is demonstrated in Fig. 6.2. The methanol to oxygen gas flow ratio was kept 1:1 and the pump speed was varied by using an adjustable needle valve (Pfeiffer EVN116) in front of the turbo molecular pump, as shown in Fig. 3.3. It is visible that, when the pump speed decreased from 0.4 L/s to 0.006 L/s, the methanol conversion increased dramatically. The effective volume of the high-pressure reaction cell is around 0.5 Litres. It means at the pump speed of 0.4 L/s, the dwell time of the molecules in the reactor is around 1 s and the reactor was operated as a continuous flow reactor. Whereas at the very low pump speed of 0.006 L/s, the dwell time of the molecules in the reactor increases to around 100 s. In this case the gas exchange in the reactor is insufficient and very slow so that the reactor behaves rather like a batch reactor where the multiple collisions of both the reactants and the products with the copper surface occur to lead to a very high methanol conversion.

It is noted that, due to the very possible change of the flow characteristics in the high-pressure reaction cell and its dramatic effect on the reaction kinetics under higher pressure conditions, one has to be very careful when comparing the results under these measuring conditions with the kinetics measurements under the UHV conditions. In our case, nevertheless, in order to connect the reaction kinetics under low pressure conditions, the measurements were restricted to the  $10^{-3} - 10^{-2}$  mbar range where the gas flow obeys mainly the properties of the molecular flow. In addition, all the measurements were systematically carried out in the reaction cell, meaning under the same conditions, so that the final results are comparable.

### 6.2.2 Effect of the sample pretreatment

In former high pressure studies [16, 18-21], it was emphasized that the initial copper catalyst had to be activated for the formaldehyde production by a sample pretreatment in which the copper foil was cyclically oxidized by O<sub>2</sub> and then slightly reduced by methanol. It was observed by using atomic force microscopy (AFM) and scanning electron microscopy (SEM) [16] that, after the treatment, the surface morphology changed dramatically from an originally smooth hill-and-valley

morphology to a rough faceted surface terminated with the individual terraces, and the surface area increased up to ten times greater than that before the treatment. The obvious changes of the surface morphology indicated the participation of not only the surface but to a great extent also the bulk in the reactions. Moreover, the formation of copper suboxides  $\text{Cu}_x\text{O}$  ( $2.2 \leq x \leq 2.7$ ) was found *ex situ* by X-ray absorption spectroscopy (XAS) after the pretreatment of the catalyst, and this oxygen species could be related to the selective formaldehyde formation in the reaction [16].

In our system, the original smooth Cu(110) surface initially had a very low reactivity in the  $10^{-2}$  mbar range. With heating/cooling cycles in the reaction atmospheres of the elevated total pressure, the sample surface underwent faceting to the extent that, after the reaction in the 1 mbar range, the changes of the surface colour and morphology could be observed by eye. During the courses the surface reactivity was measured to be enhanced. The dependence of the reactivity on the history of the sample intuitively indicates the importance of the sample pretreatment for the measurements of the reaction kinetics.

Fig. 6.3 shows the comparison of the reactivity over two metallic copper-like samples after the different pretreatment: (a) prepared as usual by reducing in methanol (1 mbar, 673 K, 30 min); (b) prepared by reacting in oxygen-rich gas mixture with  $\text{O}_2$ :  $\text{CH}_3\text{OH} = 6:1$  ( $p_{\text{tot}} = 7 \times 10^{-1}$  mbar) at 673 K, and then slightly reducing in methanol (0.01 mbar, 673 K, 10 min). Two samples seemed similar from the visual impression: yellow colour and shining, except that sample (b) looks like rougher than (a). The TPR experiments were carried out under the same conditions:  $\text{CH}_3\text{OH} : \text{O}_2 = 1 : 1$  with an oxygen flow rate of 0.1 sccm ( $\text{cm}^3/\text{min}$ ). In contrast with the low activity of the sample (a), after the extensive oxygen pretreatment of sample (b) the reactivity is dramatically enhanced, whereas the selectivity to formaldehyde decreases even though it is still the dominant product. It is noted that the ignition temperature of the reactions is not changed obviously, which possibly indicates the common properties of the surfaces. However, the enhanced reactivity suggests the different characteristics in the subsurface or bulk region of the sample due to the different pretreatment. In order to obtain a comparable metallic copper surface, the reduction procedure of the sample in methanol was kept in all measurements.

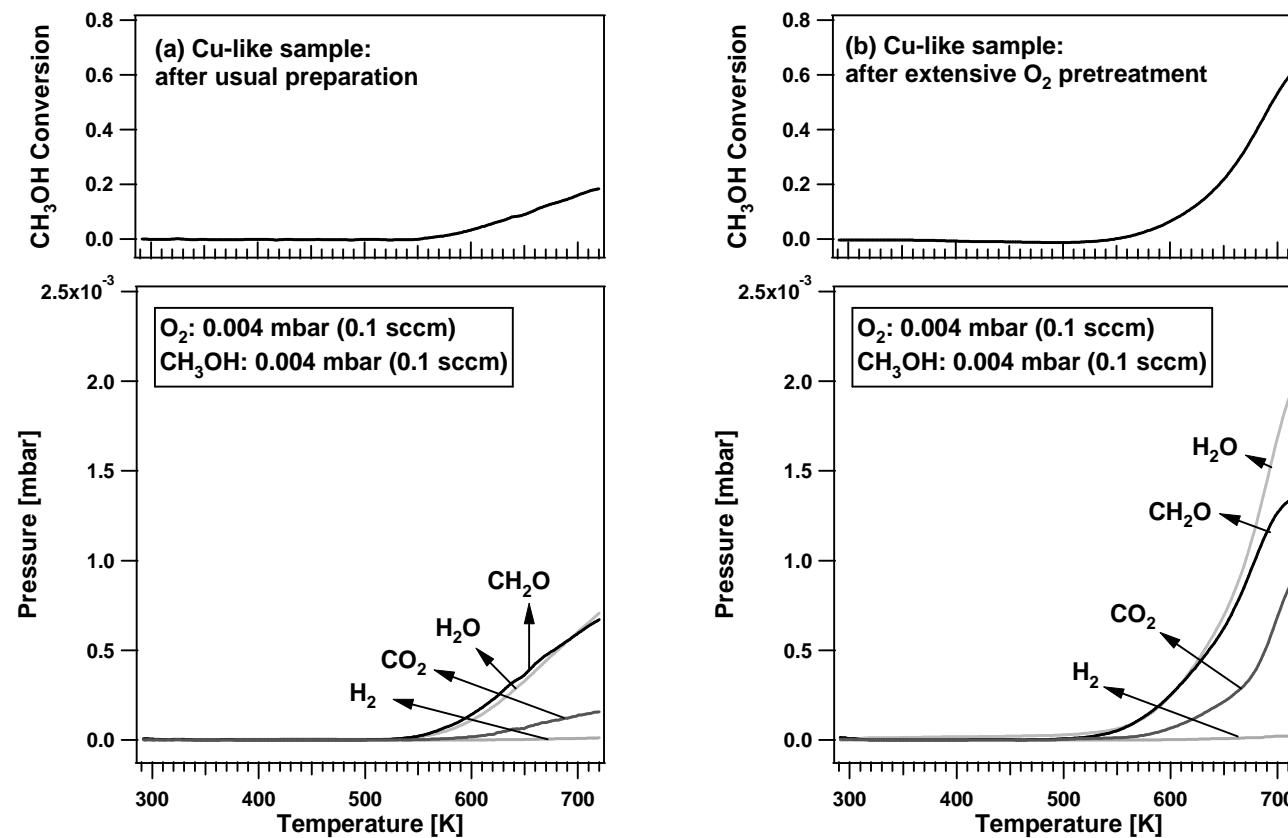


**Figure 6.3** TPRS in the  $10^{-3}$  mbar range with  $\text{CH}_3\text{OH}$  flow rate 0.1 sccm and  $\text{O}_2$  flow rate 0.1 sccm, over two different pretreated sample surfaces: (a) a yellow shining metallic surface prepared usually by reducing in methanol (1 mbar, 673 K, 30 min); (b) a metallic surface prepared by reacting in  $\text{O}_2$ :  $\text{CH}_3\text{OH} = 6:1$  ( $P_{\text{tot}} = 7 \cdot 10^{-1}$  mbar) at 673 K and then slightly reducing in methanol (0.01 mbar, 673 K, 10 min). The heating rate for the experiments was 5 K/min.

### 6.2.3 Dependence on the surface phases

Kinetic measurements were systematically carried out over three differently prepared surfaces of the Cu(110) sample: (a) a metallic surface obtained after the sample had been completely reduced by methanol yielding a yellow shining surface; (b) a partially oxidized surface when the sample had been exposed to oxygen (1 mbar, 423 K, 5 min) until a red Cu<sub>2</sub>O film was formed; and (c) a deeply oxidized surface when the sample had been oxidized by oxygen (1 mbar, 673 K, 30 min) until a black CuO film was observed. Both oxidation processes caused a visible roughening of the initially flat Cu surface.

Fig. 6.4 shows the TPR spectra of the three surfaces obtained with a linear heating rate of 5 K/min under the identical reaction conditions. A mixing ratio of methanol to oxygen of 3:1 was chosen with an oxygen flow of 0.1 sccm. It is obvious that the different surface phases on the copper sample lead to different activities.

On the metallic copper surface, the reaction ignites at  $\approx 500$  K and the surface reactivity slowly increases with temperature up-ramping. The methanol conversion reaches a maximum of  $\sim 20\%$  at 750 K. This value equals approximately the reactive sticking coefficient for methanol oxidation over Cu(110) measured in the UHV experiments shown in chapter 5. Formaldehyde is always the dominant product, whereas the contribution of the total oxidation product CO<sub>2</sub> remains moderate even at elevated temperatures. In the UHV studies described in chapter 5, two rate maxima were found, one at  $\approx 400 - 520$  K and the other at  $\approx 900$  K. The amplitude of the low temperature reactivity peak decreases with increasing total pressure, vanishing beyond  $10^{-3}$  mbar. This low-T reactivity peak therefore should not exist at higher pressure in agreement with the results in Fig. 6.4. Recent *in situ* XPS results of methanol oxidation over a copper foil in the  $10^{-1}$  mbar range showed that at low temperatures the copper surface is covered by adsorbed methoxy and formate species which block the surface reaction [21, 22]. Higher temperatures are required to slowly activate the surface.

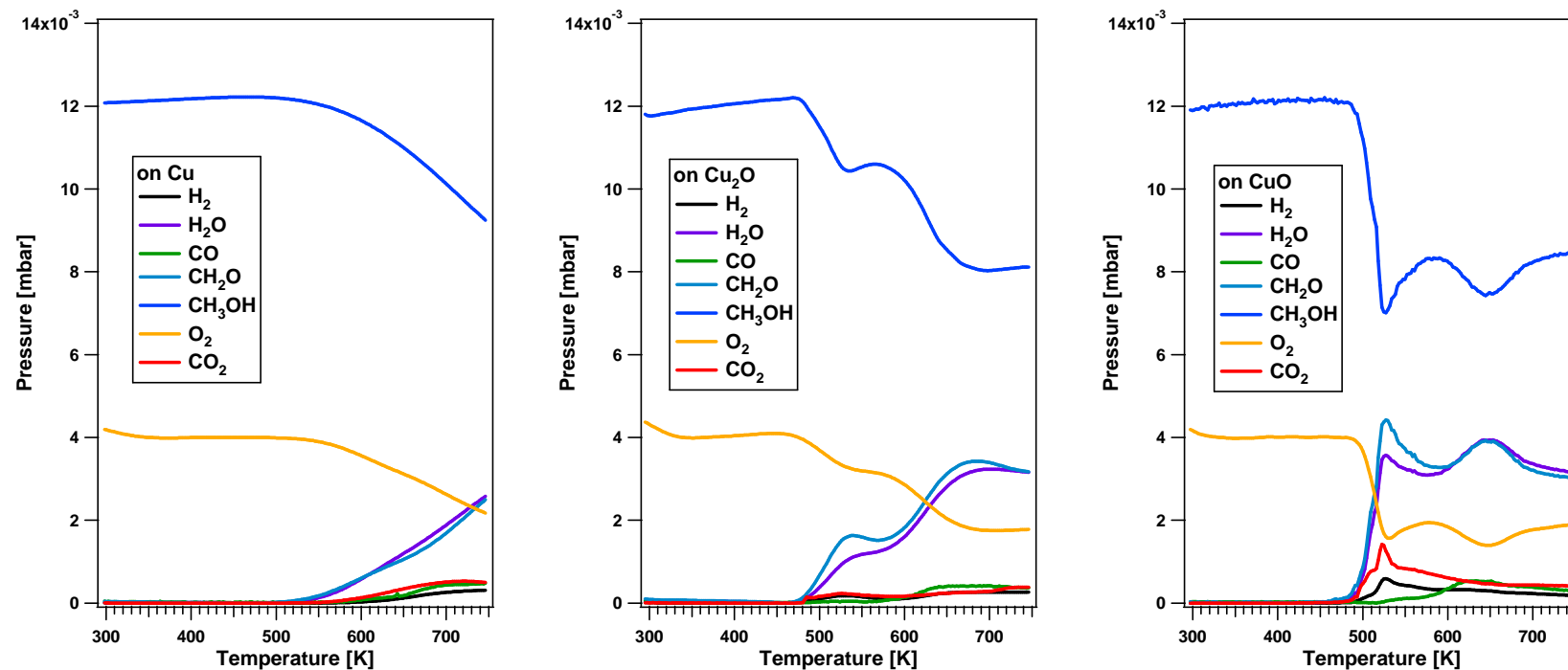


**Figure 6.4** TPRS in the  $10^{-2}$  mbar range with  $\text{CH}_3\text{OH}$  flow rate 0.3 sccm and  $\text{O}_2$  flow rate 0.1 sccm, over three different sample surfaces: a metallic copper surface (yellow, shining), a partially oxidized copper surface where a  $\text{Cu}_2\text{O}$  film was formed (red), and a deeply oxidized copper surface where a  $\text{CuO}$  film was reached (black). The heating rate for the experiments was 5 K/min.



Comparing with the metallic copper surface, both the oxidized surfaces show a higher reactivity. The kinetics exhibit two rate maxima as demonstrated in Fig. 6.3. On the partially oxidized surface ( $\text{Cu}_2\text{O}$ ), the reaction starts at  $\approx 480$  K. After passing a maximum at  $\approx 530$  K, the reactivity increases further reaching a second reactivity peak at  $T \approx 670$  K. The deeply oxidized surface exhibits the highest reactivity while the reaction ignites as well at  $\approx 480$  K. It is noted that with higher reactivity, the partially oxidized surface still keeps the fairly high selectivity to formaldehyde. Whereas the deeply oxidized CuO film shows more total oxidation to  $\text{CO}_2$  although formaldehyde is still the predominant product.

It should be pointed out that only on the metallic copper surface the reaction is in a steady state, whereas the reaction rates of the oxidized surfaces are all unstationary, i.e. the reaction rate changes with time under constant reaction conditions. In separate experiments on the oxidized surface, when the heating ramp was stopped at 520 K and 650 K these surfaces visually slowly changed colour and morphology accompanied by a time-dependent variation of the reaction rate. Apparently a reduction takes place involving not only the surface oxygen but also the bulk oxygen.

#### 6.2.4 Effect of the gas mixing ratio

The gas mixing ratio has almost no influence on the stationary reaction kinetics over the metallic copper surface at  $10^{-2}$  mbar, as demonstrated in Fig. 6.5, which shows the methanol conversion with different flow ratios of methanol to oxygen. This is very different from the stationary reaction kinetics over Cu(110) under low pressure conditions, which show that the methanol conversion-temperature profiles are very sensitive to the gas mixing ratio, especially for the low-temperature reaction peak which does not exist in the profile at  $10^{-2}$  mbar. It was concluded that, under the UHV conditions, the oxygen partial pressure strongly affects the adsorbed oxygen coverage on the surface, which leads to a significantly different surface reactivity. However, at  $10^{-2}$  mbar, it is possible that the oxygen coverage on the surface already remains high due to the high oxygen feed in the gas phase, so that the surface has only a low reactivity and the influence of the gas mixing ratio is weak.

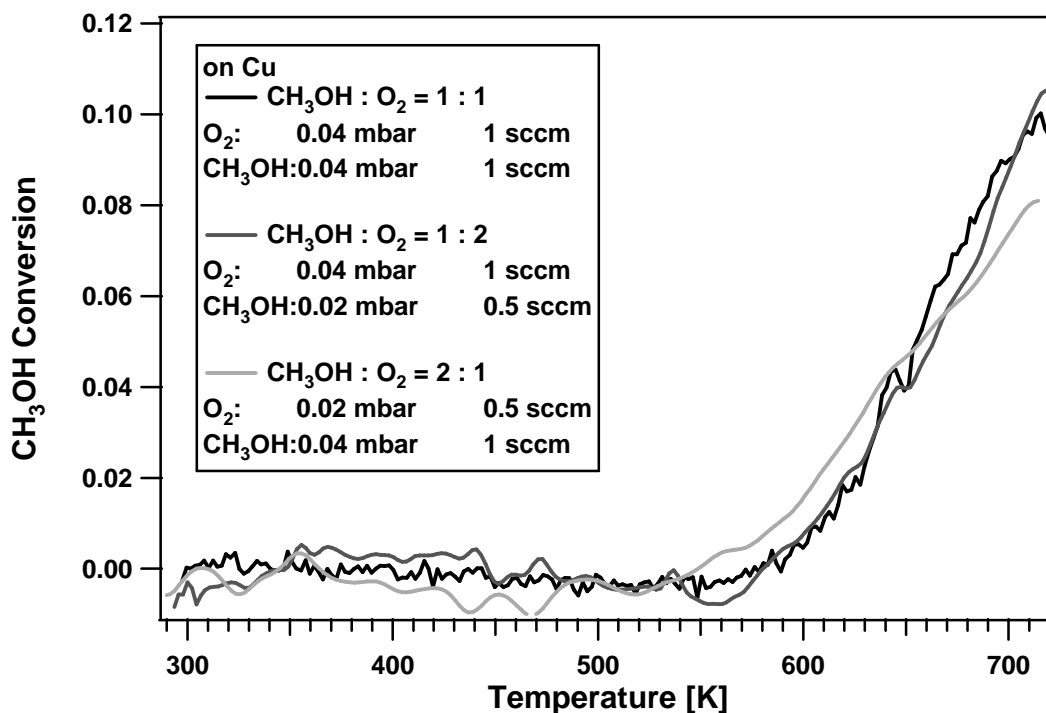


**Figure 6.5** Effect of the gas mixing ratio on methanol conversion over the metallic copper surface in the  $10^{-2}$  mbar range. The heating rate for the experiments was 5 K/min.

In contrast to the metallic copper surface, on the deeply oxidized copper surface, the gas mixing ratio strongly influenced the TPR spectra. This is demonstrated in Fig. 6.6, which shows the methanol conversion and the production rates for different flow ratios of methanol to oxygen. Note that the y-scale in each panel of the production rates has been scaled to the change of the methanol partial pressure. It should be emphasized again that the sample changes its chemical state during heating. It is visible that the methanol conversion decreases with the increase of the methanol content in the gas mixture. Irrespective of the gas mixing ratio the rate curves all exhibit two peaks: one at around 450 – 580 K and the other at 600 – 700 K. However, the shape and the peak maxima shift obviously when varying the gas mixing ratio. With decreasing methanol content in the gas mixture, both the low-temperature and the high-temperature peaks become broader and higher in reactivity, which indicates the slower consumption of bulk oxygen. Under all reaction conditions formaldehyde is the dominant product, whereas CO<sub>2</sub> production varies obviously with the gas mixing ratio especially at around 650 K.

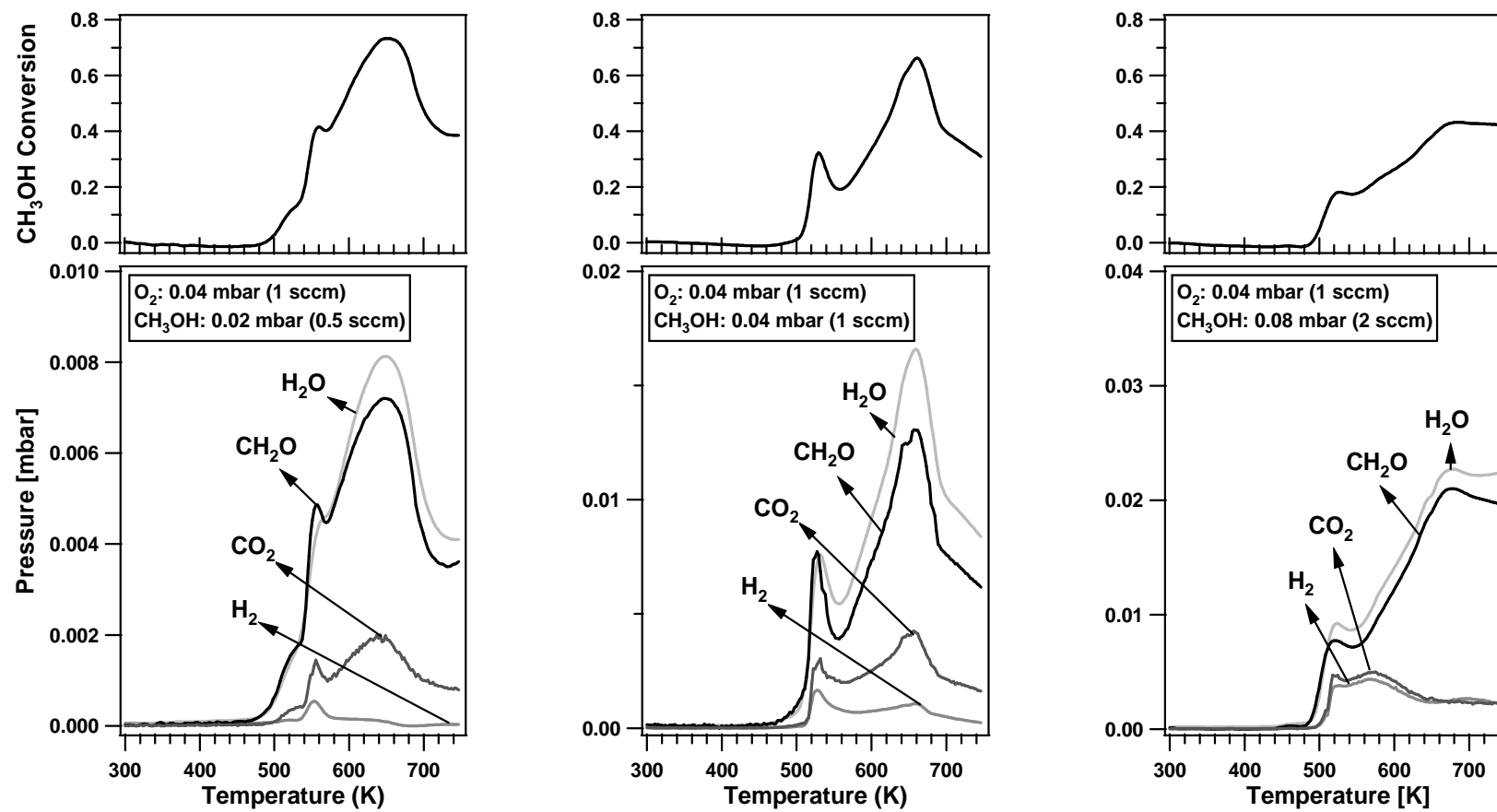


**Figure 6.6** Effect of the gas mixing ratio on methanol conversion and the production rates over the deeply oxidized copper surface ( $p(\text{O}_2) = 1 \text{ mbar}$ , 673 K, 30 min until a black CuO film was observed) in the  $10^2 \text{ mbar}$  range. The sample changed its chemical state during the reaction. The heating rate was 5 K/min.

## 6.3 Reduction of the oxidized copper sample

### 6.3.1 Phase transition observed by optical microscopy

The colour and roughness changes associated with the formation of different Cu oxides make it easy to follow the changes of the surface in the TPR experiments with optical microscopy. Fig. 6.7 shows a set of photographic images of the sample in the reactor during a temperature-programmed reaction starting from a deeply oxidized copper sample. The images are taken using a digital camera with fixed aperture and white balance so that the true sample colour is recorded. The related TPR spectrum is also shown in Fig. 6.7 and the arrows at the top part of the panel indicate the reactivity corresponding to each displayed image. A mixing ratio of methanol to oxygen of 2:1 was chosen with an oxygen flow rate of 0.1 sccm.

In the beginning of the reaction the deeply oxidized sample exhibits a very rough black surface indicative of CuO. Only after ignition of the reaction at  $T \approx 500$  K, the surface starts to change notably. Starting from the center of the sample the copper (II) oxide is converted to the red Cu<sub>2</sub>O oxide associated with a flattening of the surface roughness on a  $\geq 100$   $\mu\text{m}$  length scale. As judged from the images this process is completed around 650 K. At this temperature the reactivity exhibits a pronounced relative maximum which in height is only slightly below the first reactivity peak. Above 650 K the slow change of the surface to a yellow shining state indicates the reduction of the copper (I) oxide to a metallic surface.

One notes that nearly under all conditions formaldehyde is the preferred reaction product. Only directly after ignition on the CuO surface the total oxidation product CO<sub>2</sub> is for a short time higher in intensity than formaldehyde. With progressive reduction of the surface the CO<sub>2</sub> channel decays rapidly in intensity approaching finally the low level characteristic of a metallic surface. The above data show a more or less complete reduction of the deeply oxidized copper sample associated with a drastic change of the surface morphology. In order to obtain more information about the thickness of the oxide layers, we applied ellipsometry as *in situ* technique to study the surface chemistry of the sample during the TPR experiments.

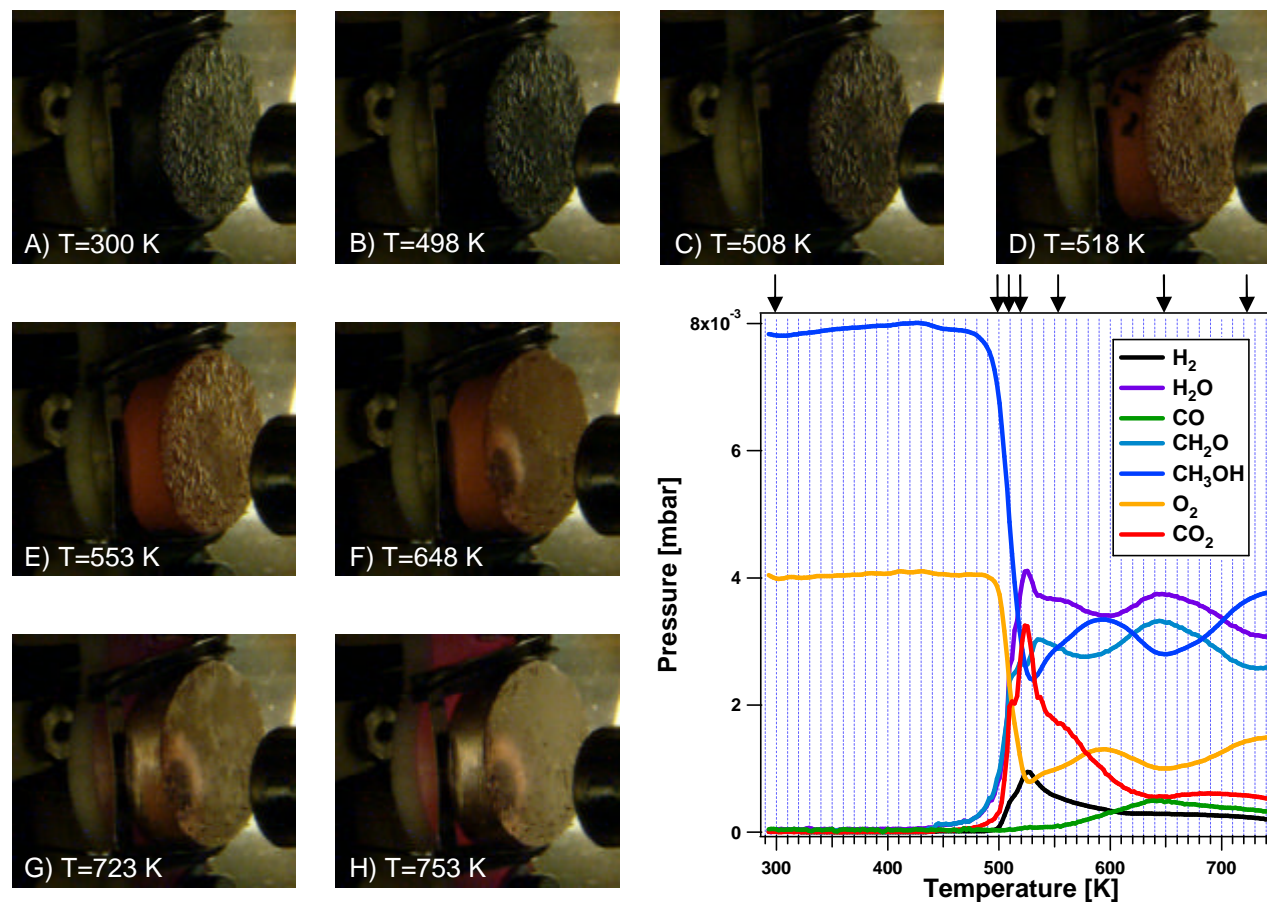


**Figure 6.7** Changes of the oxide phase during the TPR over a deeply oxidized copper sample. The displayed photos of the sample in the reactor were taken using a high quality digital camera with fixed aperture and white balance. The TPR spectrum is also shown and the arrows on top of the panel indicate the reactivity corresponding to each photo. Reaction conditions:  $CH_3OH$  flow rate 0.2 sccm and  $O_2$  flow rate 0.1 sccm.

### 6.3.2 Phase transition determined by ellipsometry

Ellipsometry is a well established technique for the characterization of thin films and surfaces, which allows the determination of optical constants and thickness of a layer system [71]. Ellipsometry uses the fact that the state of polarization of an incident photon beam changes upon reflection at a surface. The change in the state of polarization can be described by two angles,  $\Delta$  and  $\Psi$ , which are obtained by the measurements and which in turn are related to the optical properties and the thickness of the film. From the measured  $\Delta$  and  $\Psi$  values the thickness of the surface layers can be extracted for a multilayer surface model provided that the chemical identity of the different layers has been determined and that the optical constants for these layers are known. The information depth is given by the penetration depth of light (wavelength  $\lambda = 6328 \text{ \AA}$ ) and amounts to 0.1 - 6  $\mu\text{m}$ , with the small value referring to metallic Cu and the large value referring to  $\text{Cu}_2\text{O}$ .

#### 6.3.2.1 Integrating ellipsometry

Fig. 6.8 shows the  $\Delta$  and  $\Psi$  variation measured *in situ* during a TPR experiment on a deeply oxidized copper surface with  $\text{CH}_3\text{OH}$  flow rate of 0.2 sccm and  $\text{O}_2$  flow rate of 0.1 sccm. The corresponding TPR spectrum is included in the same diagram. The change of the  $\Delta$  and  $\Psi$  values reflects the slow conversion from a CuO surface to  $\text{Cu}_2\text{O}$  and at the end to a metallic Cu surface.

For simulating the measured  $\Delta$  and  $\Psi$  values a realistic sequence of model layers had to be found that explains the observed variation of  $\Delta$  and  $\Psi$  in a consistent way. In all simulations the incident beam angle was set to  $70^\circ$ , the optical constants for the gas phase, which has to be included were chosen as  $n = 1$  (refractive index) and  $k = 0$  (extinction coefficient), while for the different Cu and Cu oxide phases of the sample the used values for  $n$ ,  $k$  and the resulting Brewster angle  $\Phi_p$  at the used light wavelength of  $\lambda = 6328 \text{ \AA}$  are listed in Table 6.1 [105].

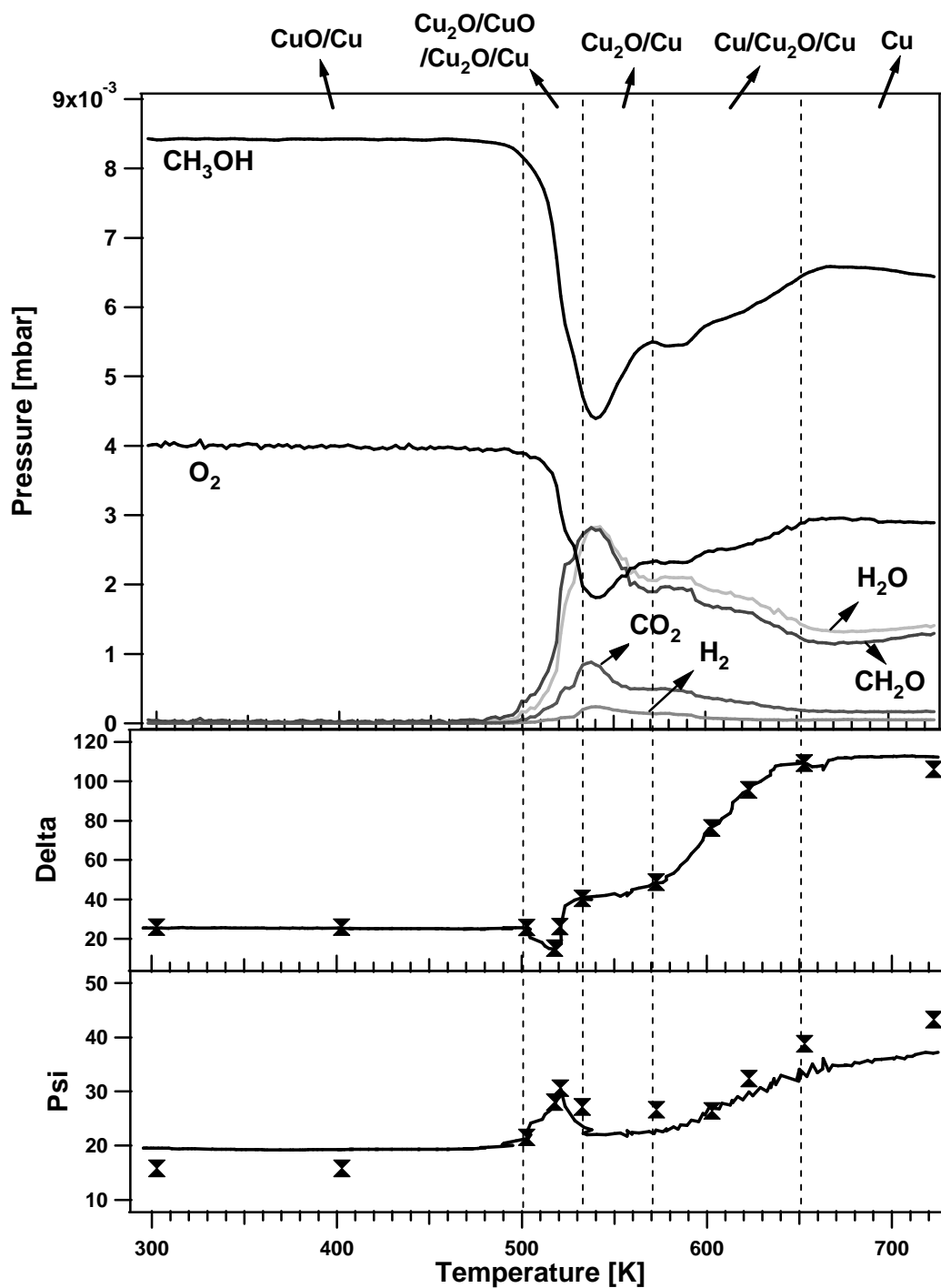


**Figure 6.8** Integrating ellipsometry measurement: the variation of  $\Delta$  and  $\Psi$  values during the TPR over a deeply oxidized copper sample. The simulated  $\Delta$  and  $\Psi$  values were inserted in the variation curves as triangular markers. The lines separated the area for different sample models. Reaction conditions: CH<sub>3</sub>OH flow rate 0.2 sccm and O<sub>2</sub> flow rate 0.1 sccm.

**Table 6.1** The optical constants  $n$  (refractive index),  $k$  (extinction coefficient) and  $\Phi_p$  (Brewster angle) for three different phases, Cu, Cu<sub>2</sub>O, and CuO at a wavelength  $\lambda = 6328 \text{ \AA}$ . The incident angle is  $70^\circ$ .

Phase	$n$	$k$	$\Phi_p$
Cu	0.237	-3.274	$13.33^\circ$
Cu <sub>2</sub> O	2.96	-0.12	$71.33^\circ$
CuO	2.68	-0.45	$69.50^\circ$

Fig. 6.9 shows two examples to simulate the variation of the  $\Delta$  and  $\Psi$  values during the change of the thickness of (a) a CuO film and (b) a Cu<sub>2</sub>O film on top of the Cu substrate with the program Elli which is used for analysis of ellipsometric data and offered by Optrel GBR. It is shown that, for two-layer systems it is easy to determine the thickness of the top layer according to the measured  $\Delta$  and  $\Psi$  values. But for multiple-layer systems, the simulation becomes fairly complex since no unique fit exists for a measured single pair of  $\Delta$  and  $\Psi$  angles [106].

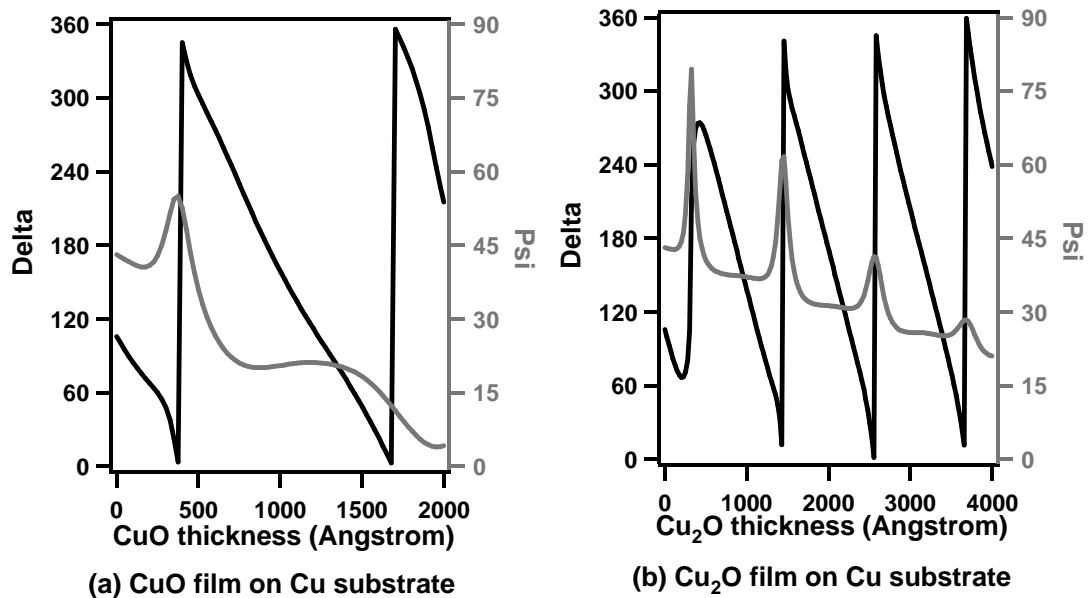


**Figure 6.9** The variation of the  $\Delta$  and  $\Psi$  values during the change of the thickness of (a) a CuO film and (b) a Cu<sub>2</sub>O film on top of the Cu substrate simulated with the program Elli.

However, we found only one layer sequence with which the entire temperature range could be fitted and which does not contradict chemical intuition and the



literature data. The resulting sequence is as follows: The deeply oxidized copper sample with which we start was modeled by a layer of copper (II) oxide on top of metallic bulk Cu, i.e. CuO/Cu. At temperatures above 480 K the sample is partially reduced resulting in a more complicated sequence. Between 490 K and 520 K coexisting oxides with a sequence Cu<sub>2</sub>O/CuO/Cu<sub>2</sub>O/Cu are formed, followed by a Cu<sub>2</sub>O/Cu double layer between 530 K and 600 K when the CuO phase is already consumed. Above 600 K we assume a thin metallic copper layer on top of Cu<sub>2</sub>O, i.e. a Cu/Cu<sub>2</sub>O/Cu sequence. Above 670 K the entire sample approaches a pure metallic state. The formulation of a Cu<sub>2</sub>O/CuO/Cu<sub>2</sub>O/Cu sequence in the range 490 K ≤ T ≤ 520 K is consistent with the results of ref. [121] and it is also in agreement with thermodynamics. The assumption of metallic Cu on top of Cu<sub>2</sub>O at T > 600 K is supported by the XPS study of Bowker et al. showing that vacuum annealing of Cu<sub>2</sub>O at 770 K results in the formation of a thin metallic Cu film on top of Cu<sub>2</sub>O [104].

**Table 6.2** The comparison of the measured ellipsometric data with the simulated  $\Delta$  and  $\Psi$  values according to a reasonable sequence of the layer models of the sample during the TPR experiment.

T	Sample Model (e.g. Å Cu/ Å Cu <sub>2</sub> O/ Å CuO/ Cu)	Simulation		Measurement	
		$\Delta$	$\Psi$	$\Delta$	$\Psi$
303 K	1594 Å CuO/ Cu	25.73	15.70	25.64	19.56
403 K	1594 Å CuO/ Cu	25.73	15.70	25.42	19.26
503 K	2 Å Cu <sub>2</sub> O/ 1275 Å CuO/ 255 Å Cu <sub>2</sub> O/ Cu	25.64	21.45	25.74	21.39
518 K	5 Å Cu <sub>2</sub> O/ 367 Å CuO/ 2240 Å Cu <sub>2</sub> O/ Cu	14.95	27.93	14.92	27.02
521 K	10 Å Cu <sub>2</sub> O/ 220 Å CuO/ 2328 Å Cu <sub>2</sub> O/ Cu	26.06	30.52	26.15	30.46
533 K	3592 Å Cu <sub>2</sub> O/ Cu	40.37	27.02	40.03	22.30
573 K	3570 Å Cu <sub>2</sub> O/ Cu	48.47	26.53	48.39	22.88
603 K	10 Å Cu/ 3496 Å Cu <sub>2</sub> O/ Cu	76.03	26.35	75.95	27.00
623 K	20 Å Cu/ 2300 Å Cu <sub>2</sub> O/ Cu	95.33	32.31	95.68	29.93
653 K	x Å Cu (rough)/ Cu			108.9	32.74
723 K	Cu	105.8	43.16	112.5	37.07

The quality of the fit is demonstrated in Fig. 6.8 and the corresponding layer thicknesses are summarized in Table 6.2. Rather than the individual thickness values the layer sequence should be considered as the essential result of the fitting process. A precise determination of the layer thickness is hampered for several reasons. The simulations which are based upon the Fresnel equations assume strain and defect free chemically homogeneous layers with sharp planar interfaces between them. This is clearly not the case here as already evident from the images in Fig. 6.7 showing a strongly roughened surface. The roughening not only complicates the analysis but it also constitutes an experimental problem. Since the sample roughens dramatically during the reactions a subsequent realignment of the instrument is difficult thus introducing an additional systematic error.

The values listed in Table 6.2 describe the following process: As shown in Fig. 6.8, up to the ignition of the reaction the  $\Delta$  and  $\Psi$  values remain constant corresponding to a CuO film of about 1500 Angstrom thickness on the copper substrate. At around 650 K the  $\Delta$  and  $\Psi$  values of metallic Cu are reached. Between 500 K and 520 K the  $\Delta$  and  $\Psi$  exhibit a pronounced dip and peak, respectively, as demonstrated in Fig. 6.8. For reproducing this dip/peak structure in the simulations we had to assume a layer sequence consisting of a only few Angstrom thick Cu<sub>2</sub>O film on top of a relatively thick CuO layer, which is separated from the metallic Cu substrate again by a Cu<sub>2</sub>O layer. With progressive reduction the CuO layer becomes transformed into Cu<sub>2</sub>O and at the end a Cu<sub>2</sub>O film of several thousand Angstroms thickness remains on top of the metallic Cu substrate. This reduction process of CuO is accompanied by a steep rise of the reactivity. At the rate maximum at T = 540 K still a relatively thick Cu<sub>2</sub>O film exists on the Cu surface. Both angles,  $\Delta$  and  $\Psi$ , change vary little in the following T-interval up to  $\approx$  570 K. Apparently in this T-window a stable and very reactive Cu<sub>2</sub>O film exists on top of the metallic substrate. The following change in angles could only be modeled by a decreasing Cu<sub>2</sub>O thickness accompanied by the formation of a very thin metallic Cu film of a few Angstroms thickness on top of the Cu<sub>2</sub>O layer. The formation of the Cu film terminating the sample surface is associated with a decrease in reactivity by roughly 50%. As the Cu<sub>2</sub>O layer is reduced a rough metallic Cu substrate results with which

progressive annealing flattens until finally at  $\approx 720$  K a metallic shining Cu surface is created.

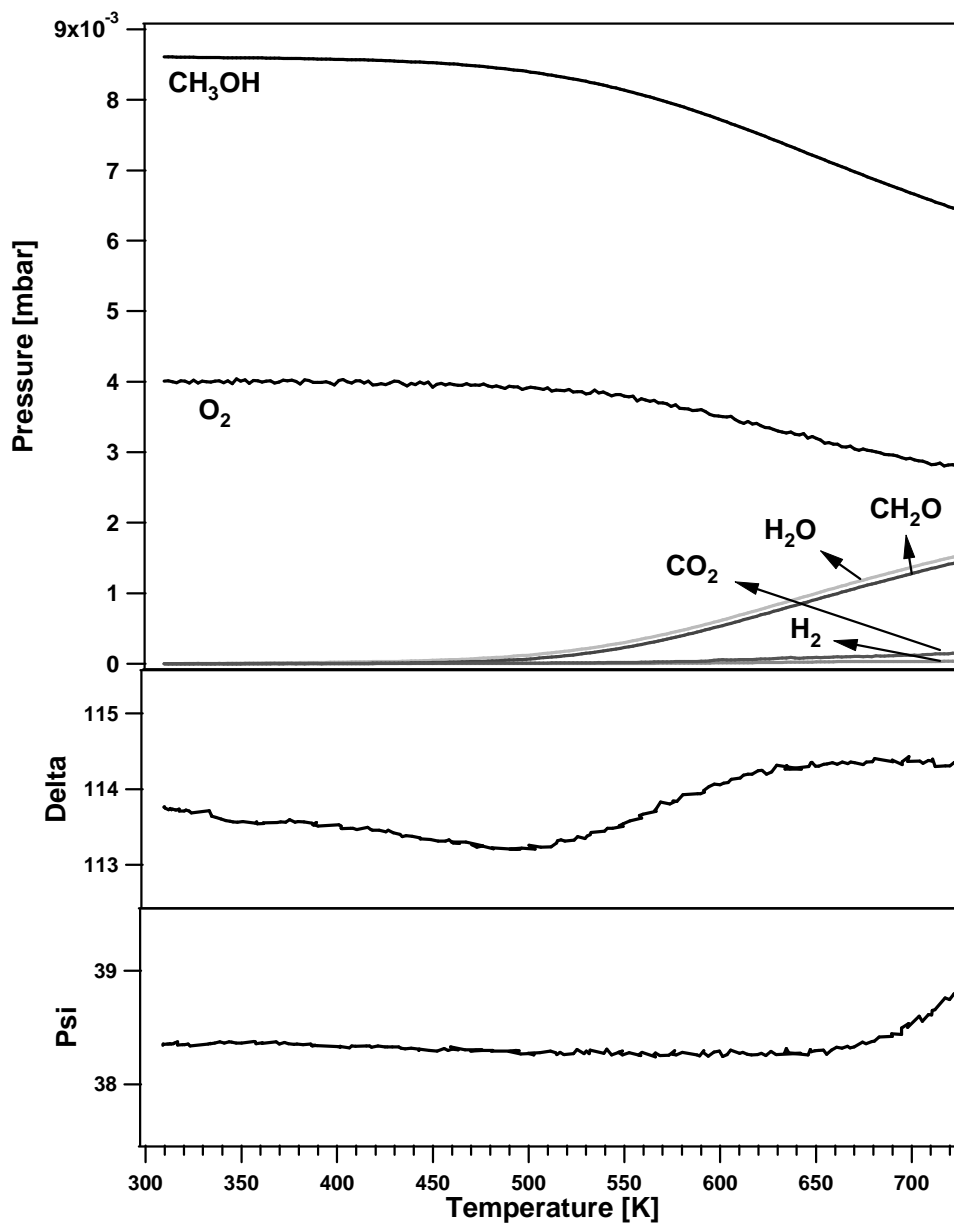


**Figure 6.10** Integrating ellipsometry measurement: the variation of  $\Delta$  and  $\Psi$  values during the TPR over a metallic copper sample. The upper panel is the corresponding TPR spectrum. Reaction conditions:  $\text{CH}_3\text{OH}$  flow rate 0.2 sccm and  $\text{O}_2$  flow rate 0.1 sccm.

Fig. 6.10 shows the TPR spectrum and the *in situ* measured  $\Delta$  and  $\Psi$  variation during the following cooling of the sample after the TPR experiment on

a deeply oxidized copper surface. The cooling rate is same as the heating rate of 5 K/min, and the gas flow rates were kept constant too. The sample is always metallic during the reaction, which is indicated by the measured  $\Delta$  and  $\Psi$  values. It is visible that the  $\Delta$  angle varies only in a few degrees, whereas the value of  $\Psi$  is nearly constant. The variation of the  $\Delta$  angle is pronounced at  $\approx 500$  K. In the meantime the surface loses its reactivity. Therefore the observed change of  $\Delta$  and  $\Psi$  values over the metallic sample during the reaction most likely relates to the change of the surface adsorbate layer, which is in agreement with the former studies of the surface reactions with ellipsometry [107-110]. Again, the metallic surface exhibits a very low reactivity.

### 6.3.2.2 Imaging ellipsometry

The change in the angle  $\Delta$  and  $\Psi$  during the TPR experiment allows imaging the surface with ellipsometric contrast. In the microscope mode the analyzer (A) and the polarizer (P) were adjusted to nullsetting so that only the intensity changes relative to this reference image are visible. Here nullsetting was done for the CuO phase initially present. A severe problem arise with the roughening of the surface because the stray light is unpolarized and therefore a relatively bright background signal exists which cannot be eliminated by nullsetting.

Surprisingly, even with such a rough surface it was possible to obtain images with ellipsometric contrast, which is demonstrated in Fig. 6.11. This figure displays images of the sample during a TPR experiment with a deeply oxidized copper surface. The experiment is thus very similar to Fig. 6.7, but the contrast mechanism of the images is different. The images display a smaller section of only  $1 \times 1.8$  mm<sup>2</sup> compared to the photographic images in Fig. 6.7 which show the complete sample of around  $9 \times 11$  mm<sup>2</sup> dimension. Due to the grazing incidence of the laser beam the images are exactly focused only in a narrow stripe perpendicular to the reflection plane. A completely focused image was constructed by combining a set of nine images where the focus had been shifted stepwise from top to the bottom of the corresponding image.

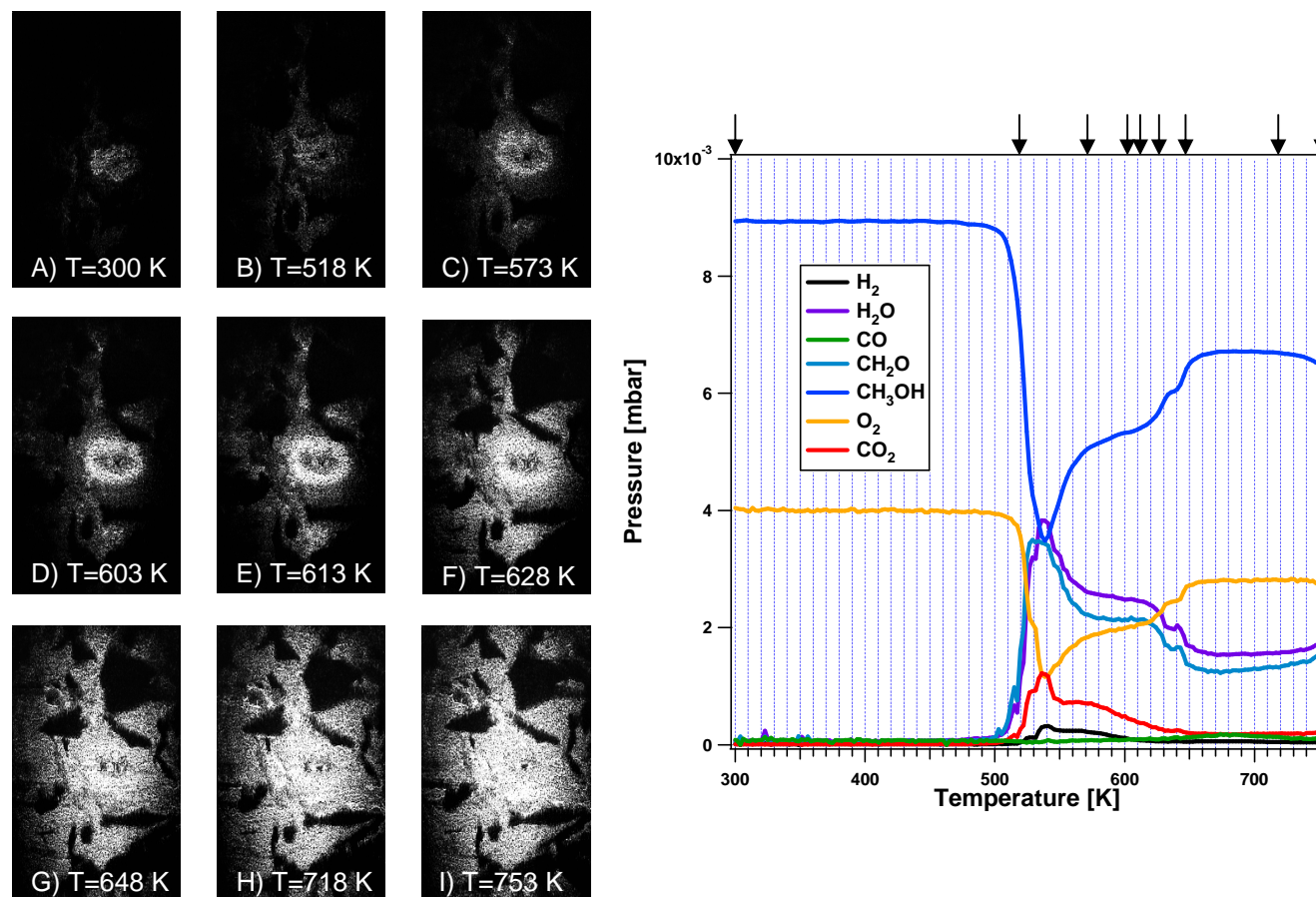


**Figure 6.11** Ellipsometric images during the TPR over a deeply oxidized copper sample. Left: an image series of a  $1 \times 1.8 \text{ mm}^2$  large sample area with ellipsometric contrast; right: the corresponding TPR spectrum. The arrows on top of the panel indicate the reactivity corresponding to each photo. Reaction conditions:  $CH_3OH$  flow rate 0.2 sccm and  $O_2$  flow rate 0.1 sccm.

The images show the reduction process as brightening of the surface. The reduction starts in the center of the sample showing initially a front-like propagation. Above 600 K the area surrounding the reduced part becomes more or less spatially uniform in brightness. The large dark areas which still persist in the images originate from topographical contrast. They represent shadows from protruding parts or deep troughs due to a macroscopic roughness of the surface.

One notes that in the TPR spectra of Fig. 6.8 and 6.11 the reactivity peak at  $T \approx 650$  K which was visible in Fig. 6.4 and 6.7 is absent. This difference reflects the fact that it is difficult to reproduce a CuO film with exactly the same thickness by the preparation of the initial surface. Furthermore, the irreversible morphologic change of the surface maybe also modified the reactivity of the sample. The values of  $\Delta$  and  $\Psi$  in Fig. 6.8 show that the sample at  $T = 650$  K is already close to a completely reduced metallic state. The lower reactivity of the metallic state indicates that the most active state of the surface is not a completely reduced copper surface but a surface which still contains some oxygen.

## 6.4 Surface phases and reactivity

The initial motivation for this study has been to conduct experiments in an intermediate pressure range between the atmospheric pressure and the low pressure conditions of the UHV studies. The rise in pressure from  $10^{-5}$  mbar applied before to  $10^{-2}$  mbar had as consequence a strong modification of the originally single crystalline Cu(110) sample: oxide formation and a strong visible roughening of the surface occurred. Apparently, in the investigated system the pressure gap problem cannot be really separated from the material gap problem because a change in pressure automatically also modifies the substrate.

The kinetics we measured here are qualitatively compatible with the low pressure data obtained with the same Cu(110) sample. According to the previous results measured in the UHV system, the low temperature reactivity peak around 500 K should vanish beyond  $10^{-3}$  mbar and this is the case for the metallic copper surface as evidenced by Fig. 6.4.

A surprising result of this study was the high reactivity of the oxidized surfaces. Over most of the T-range a high selectivity towards formaldehyde was maintained despite the availability of a large oxygen reservoir. This high reactivity of the oxidized samples is not in contradiction to the results of Schlögl et al. which connect the active surface with a metallic state because our experiments are transients, while under the steady state conditions, under which the NEXAFS and XPS experiments were carried out, the surface oxides would not persist [17, 18, 45].

Nevertheless our experiments seem to indicate that oxide surfaces are more reactive than a metallic copper surface as suggested by the correlation between the high rates and the visual impression of a colored surface (see Fig. 6.7). However, we have to be aware that even if the first ten or hundred layers of oxide would be reduced to a metallic state before or during the ignition of the reaction the visual impression would still be that of an oxidized sample. Without surface sensitive techniques we clearly cannot make any definite statement about the reactivity of the oxidized surfaces we prepared. Ellipsometry is in principle a surface sensitive technique which has been shown to be sensitive to adsorbates in the submonolayer range. One has, however, to keep in mind that if simultaneously the bulk properties are modified the signal variations will be dominated by these latter changes and surface modifications will accordingly difficult to detect. The high reactivity we see on the black or red samples could thus be due to a partially reduced surface sitting on top of a thick oxide layer. This would be in line with the general observation that perfect oxide surfaces are typically quite unreactive.

Temperature-programmed desorption (TPD) experiments after methanol adsorption on  $\text{Cu}_2\text{O}$  and  $\text{CuO}$  powder samples gave a quite different product distribution than the one we observed here [104]. Both oxide surfaces yielded  $\text{CO}_2$  and  $\text{H}_2$  as main products in the TPD experiments, a fact attributed to formate formation as intermediate species. It was shown that annealing the  $\text{CuO}$  powder at 800 K in vacuum produced a thick  $\text{Cu}_2\text{O}$  outermost layer. The reduction towards  $\text{Cu}_2\text{O}$  was prevented when the annealing was conducted in an oxygen atmosphere. On both oxide surfaces,  $\text{CuO}$  and  $\text{Cu}_2\text{O}/\text{CuO}$ , mainly total oxidation was observed in the TPD experiments, the total oxidation being more pronounced for the completely

oxidized sample with a CuO surface. Annealing the Cu<sub>2</sub>O powder sample in UHV at 800 K caused the formation of an outermost metallic Cu layer on top of Cu<sub>2</sub>O [103-104]. It is therefore not surprising that such a sample shows nearly the same reactivity in TPD experiments as metallic Cu surfaces.

The thermal stability of the Cu-oxides apparently depends on the preparation conditions [100]. A buffering Cu<sub>2</sub>O layer between the CuO phase on top and the Cu bulk came out of our ellipsometric data for the temperature range between 500 K and 530 K. Here, we assume that the decomposition of CuO mainly takes place via oxygen diffusion into the bulk as is expected from thermodynamical considerations, which show that the reaction  $\text{CuO} + \text{Cu} \rightarrow \text{Cu}_2\text{O}$  is exergonic at 298 K [100].

A CuO film subjected to vacuum annealing was found to transform into Cu<sub>2</sub>O at 470 K and beyond 670 K metallic copper starts to form [100]. These transition temperatures agree roughly with the phase transitions we observe in a MeOH/O<sub>2</sub> atmosphere as demonstrated in Fig. 6.7 and 6.8. This coincidence suggests that the stability of the oxide phases in a reacting MeOH/O<sub>2</sub> environment is essentially given by the thermal stability of the oxides.

From recent *in situ* NEXAFS spectroscopy and XPS experiments with polycrystalline Cu samples in the mbar range it was concluded that the active catalyst surface is a metallic copper that contains a subsurface oxygen species [16-22, 45]. NEXAFS probes the outermost  $\approx 500 \text{ \AA}$  of a solid. In order to be surface sensitive, *in situ* high pressure XPS was also used to characterize the oxygen adsorption states.

At higher pressure, however, a possible contamination of the surface is a severe problem that renders fingerprinting of oxygen species more difficult and may result in contradictory assignments. In fact, in ref. [21, 22] the O 1s component at 531 eV correlated with formaldehyde formation and was accordingly considered as activating species, while in ref. [120] an O 1s species at 530.4 eV exhibited a positive correlation with formaldehyde production. Variation of the exciting photon energy and thus varying the probing depth supported the assignment of this species to subsurface oxygen, i.e. an oxygen species located in the bulk region underneath the surface. In both XPS studies the existence of a Fermi edge [120], and the absence of



features in the Cu LVV Auger spectrum characteristic for Cu<sub>2</sub>O [21, 22], led the authors to conclude that the active Cu catalyst is in its metallic state.

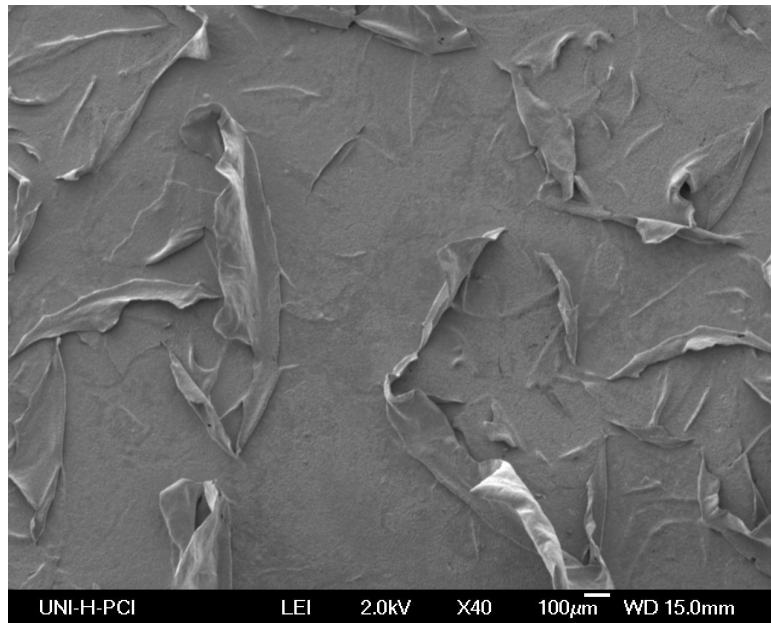
A point which should be considered more closely is the assignment of the O 1s state at 530.4 eV to the subsurface oxygen. Oxygen in Cu<sub>2</sub>O has the same binding energy but on the basis that the copper surface is still metallic and due to the photon variation experiments this state was assigned to subsurface oxygen. In the light of the finding of Bowker et al. [103-104] that a thin metallic Cu layer sits on top of Cu<sub>2</sub>O after annealing beyond 670 K in vacuum a more heterogeneous surface composition could be as well considered. Moreover, a spatially non-uniform surface consisting of metallic Cu and Cu<sub>2</sub>O should perhaps also be taken into account. The clearest evidence for a new oxygen state which was neither Cu<sub>2</sub>O nor chemisorbed oxygen was the appearance of two additional states close to the K-edge of oxygen under reaction conditions which could not be assigned to any of the known oxygen species of the Cu oxide bulk phases [45]. Irrespective of the exact identification of the O-state at 530.4 eV reported in [120], the suboxide species seems to be required in order to optimize the catalytic activity of the copper surface.

## 6.5 Surface morphology and reactivity

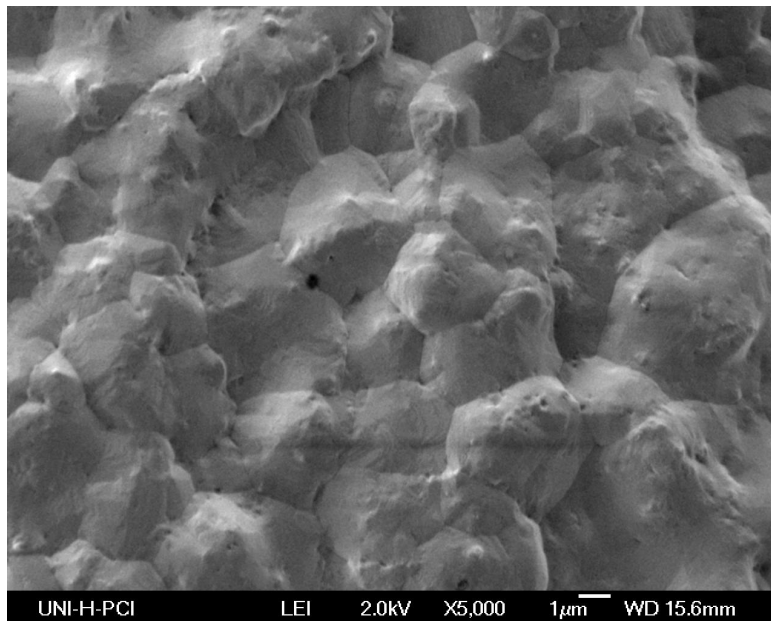
As demonstrated by Fig. 6.7, we observe a quite dramatic effect of the surface morphology on the reactivity. The oxidation of an originally flat surface caused a visible roughening as CuO was formed, but the surface became flat again as the sample was reduced by methanol. After long term reaction treatment, the sample was irreversibly restructured and became completely opaque, which can be observed by means of scanning electron microscopy (SEM) in Fig. 6.12.

In contrast to the original smooth Cu(110) surface, Fig. 6.12(a) shows that the surface was strongly faceted on a macroscale after the oxidation and reduction in oxygen and methanol in a pressure range of  $10^{-2}$  – 1 mbar. An approximate 4-5  $\mu\text{m}$  thick top layer broke and protruded from the substrate, leading to a new surface layer exposed. The resulting increase of the copper surface area is visible. Fig 6.12(b) indicates a morphological restructuring of the top surface layer. Pyramidally

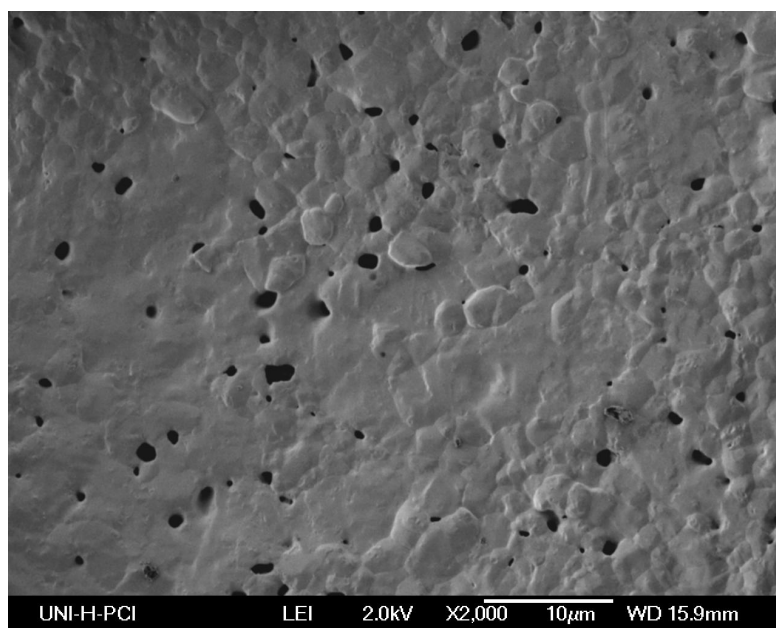
polycrystallites grown onto the copper surface and a network of grain boundaries between the crystallites are the characteristic surface features. On the new surface layer formed during the reaction, some small holes exist with a diameter of approximately several microns. These holes evidently confirm that the reaction not only occurred on the outermost surface but also caused the build-up of deep volumes underneath the metal surface.



(a)



(b)



(c)

**Figure 6.12** Scanning electron microscopy (SEM) pictures of the copper surface after long term catalytic reactions in oxygen and methanol. (a) a  $2.9 \times 2.1 \text{ mm}^2$  large area of the surface; (b) the top surface layer; (c) a new surface layer below the facet formed during the reaction.

Quite generally surfaces are modified by a catalytic reaction with the extent depending on the reaction conditions and the reaction system. As demonstrated by Fig. 6.7, in the case of the selective methanol oxidation we observe a quite dramatic effect. The oxidation of an originally flat surface caused a visible roughening on a  $\approx 100 \mu\text{m}$  length scale as  $\text{CuO}$  is formed, but the surface becomes flat again as the sample is reduced by methanol. Oxide formation on copper surfaces in a tarnishing process is one of the classical problems in solid state chemistry. The basic problem to be solved is that of the mass transport of oxygen and copper as outlined in some paradigmatic papers by C. Wagner [111].

The role of oxides in methanol oxidation over copper has been discussed not only because of their potential contribution to the overall activity but also because the oxide/Cu interface has been made responsible for the strain in the metallic phase which supposedly enhances the catalytic activity [114]. Synergetic effects between metallic Cu and Cu oxides might lie not only in the effect of strain but potentially in the diffusive coupling via mobile adsorbate species. A reaction digging its own bed

might generate potentially a non-uniform surface with a complex spatial or even spatiotemporal organization of the different constituents which are coupled via diffusion or just by strain. Apparently a minor degree of oxidation has a positive effect on the activity of a copper surface but what kind of synergetic effect is behind this enhancement is probably difficult to ascertain without insight into the microscopic organization of the reacting catalyst.

The strong morphological changes we observe evidently reflect a mass transport of copper arising due to the different densities of copper in the metallic phase and in the copper oxides. On a microscale, stepped Cu surfaces were shown to undergo faceting during exposure to oxygen [168]. One might speculate that it is this mass transport of Cu which is responsible for the reactivity peak slightly above 500 K in Fig. 6.7. The mass transport of Cu which occurs as the copper oxide is reduced might generate unstable and reactive configurations and, if stress relief is not fast enough, strain will build up leading to a catalyst with enhanced reactivity as shown in recent quantum chemical calculations [112-115]. A state in which the surface is periodically oxidized and reduced might thus generate the maximum reactivity because a permanent mass transport of copper generates continuously a strained Cu surface with a large amount of disorder present. It would not be necessary to have a system which displays macroscopic rate oscillations. Instead it would suffice to have a local mechanism through which Cu oxide is continuously transformed into Cu metal and vice versa thus keeping the system in an unstable reactive state.

## 6.6 Conclusions

The comparison of the kinetics of methanol oxidation over a metallic, a partially and a deeply oxidized copper surfaces at  $10^{-2}$  mbar indicates that the most active state of the surface is not a completely reduced copper surface but a surface which contains some oxygen in the near surface region. Both the oxidized surfaces exhibit two rate maxima at  $\approx 530$  K and  $\approx 670$  K, whereas the pure metallic copper surface has a high-temperature reactivity beyond 750 K. With its reactivity higher than the metallic copper surface, the partially oxidized surface still keeps the fairly

high selectivity to formaldehyde. The deeply oxidized surface leads to more total oxidation to CO<sub>2</sub>, though it has to some extent high selectivity to formaldehyde as well. The gas mixing ratio of methanol to oxygen has only a weak influence on reactivity as long as the sample stays metallic, whereas the ratio strongly affects the reactions over the deeply oxidized copper sample.

The reaction over the oxidized copper sample at 10<sup>-2</sup> mbar is transient with respect to the oxidized state of the surface. Apparently a reduction takes place involving not only the surface oxygen but also the bulk oxygen. Pronounced transitions of the surface phases from CuO to Cu<sub>2</sub>O and finally to metallic copper during the methanol oxidation reaction were observed by optical microscopy, integrating and imaging ellipsometry. The high reactivity and selectivity to formaldehyde of a sample which contains a thin Cu<sup>1+</sup> oxide film beneath a metallic surface were confirmed by simulating the *in situ* measured ellipsometric data and relating it to the kinetics. The phase transitions from the oxidized to reduced state are accompanied by a surface morphological changes. The strain in the surface and subsurface region, which is caused by the structural transformations, potentially contributes to the catalytic activity of the oxidized surfaces during the reaction.



# Chapter 7

## Pressure and material gap

### 7.1 Introduction

Recently increasing effort has been undertaken in order to answer the question, whether it is justified to transfer results from surface science studies, mostly obtained with single crystal surfaces under UHV conditions, to "real" catalysis, i.e. high pressures and complex materials. A so-called pressure and material gap problem exists for all heterogeneous catalytic processes, and a simply linear extrapolation of the kinetic parameters from the single crystal UHV experiments to the high pressure experiments is not generally relied. Therefore, it is necessary to develop strategies for bridging the pressure and material gap in heterogeneous catalysis. For this purpose, well defined catalytic systems should be investigated over the whole pressure range from UHV conditions up to pressures  $> 1$  mbar.

So far only a small number of reactions were examined under both the low pressure conditions in UHV systems and the high pressure conditions of real catalysis. Methanol selective oxidation to formaldehyde over copper catalysts is an efficient process and has attracted significant scientific interest as model reaction for selective oxidation [116]. A number of high pressure studies [16-22] and low pressure single crystal investigations [23-43] have been published in the last thirty years. However, the pressure and material gap problems are not well understood yet, which is demonstrated in Fig. 7.1. The diagram shows that two different reaction mechanisms were proposed according to single crystal UHV studies and measurements under the conditions of technical catalysis, respectively. A wide unexplored region exists in

pressure and structural complexity, therefore, calls for the effort to bridge the pressure and material gap in this reaction system.

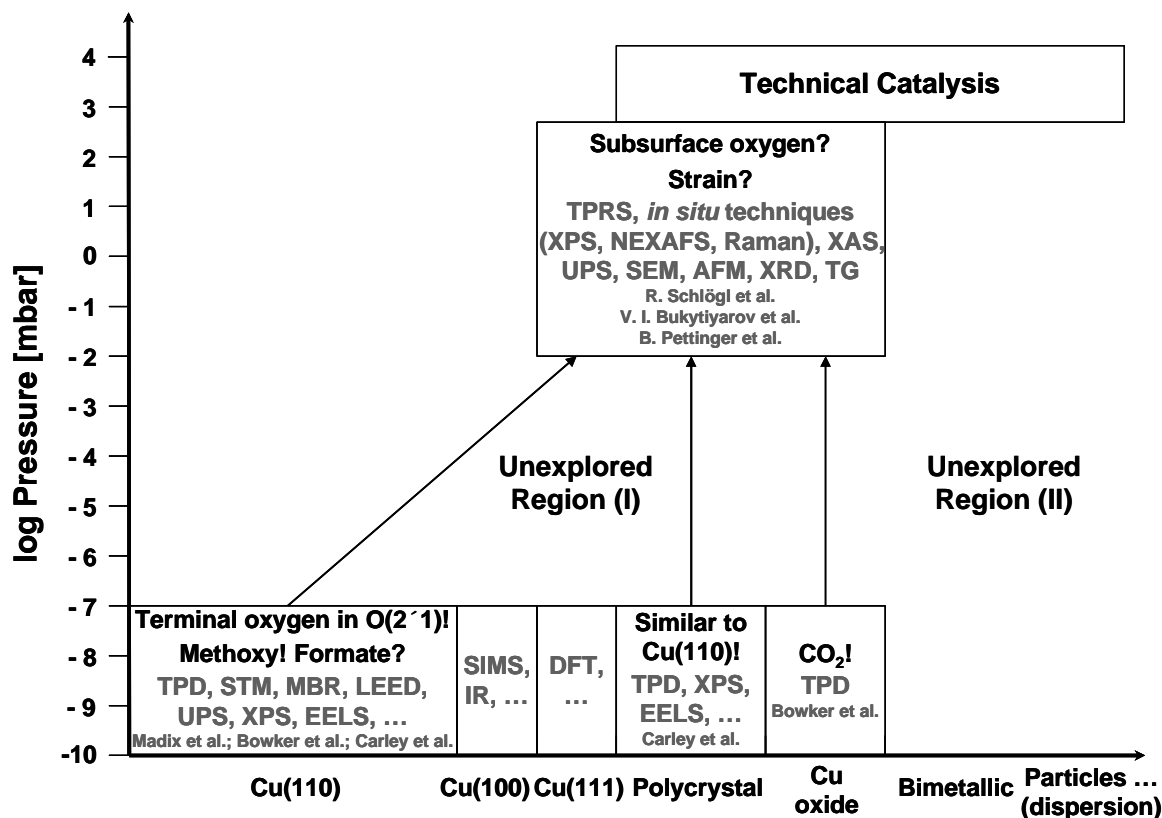


*Figure 7.1 Schematic diagram illustrating the pressure and material gap in methanol selective oxidation over copper catalysts. The content in the each textbox exhibits the main results (black), the applied techniques, and the research groups (grey) in the studies. The question marks indicate that the stated results are still under debate (see text).*

In this chapter, we summarize the current efforts in bridging the pressure and material gap in methanol oxidation over copper. In addition, the methods used in this work for overcoming the pressure and material gap problems are shortly discussed. In the end, an outlook for further studies of the model reaction is proposed.

## 7.2 Pressure gap

In order to resolve the pressure gap problem, several approaches were proposed in comprehensive reviews [6-8]. Typically, numerous experimental systems



have been developed to combine a high-pressure reactor system with an UHV analysis chamber. The high-pressure reactor allows the kinetics of catalytic reactions to be measured on a given surface, while the analysis of the structure and composition of the surface both before and after reaction can be accomplished in the UHV analysis chamber. This approach allows direct comparison of reaction rates measured on single crystal surfaces with those measured on more realistic supported metal catalysts, and also allows detailed study of structure sensitivity, the effects of promoters and inhibitors on catalytic activity, and, in certain cases, identification of reaction intermediates by post-reaction surface analysis. However, the main drawback of a post-reaction analysis is obvious: the evacuation of the reaction mixture results in the disappearance of weakly adsorbed species, but these species might determine the activities of the catalyst samples under reaction conditions.

This drawback can be eliminated if another approach is used. It consists in the application or development of analytical tools that can work at pressures  $> 1$  mbar. Most of these methods use photons instead of electrons as probe, for example, X-ray photoelectron spectroscopy (XPS), X-ray absorption near-edge structure (XANES), polarization modulation infrared absorption spectroscopy (PM-IRAS), sum frequency generation (SFG), and Raman spectroscopy [16-22, 45, 117-121]. The development of the set of techniques makes it possible to *in situ* characterize the catalytic surfaces at high-pressure.

In the following sections, we summarize the investigations of methanol oxidation over copper catalysts in the whole pressure range from UHV conditions up to pressures  $> 1$  mbar. Our recent findings can be used to link the former observations in both the UHV studies below  $10^{-7}$  mbar and the studies under more technical conditions above  $10^{-2}$  mbar.

### 7.2.1 UHV studies below $10^{-7}$ mbar

As shown in Fig. 7.1, methanol oxidation has been extensively studied over copper single crystals [23-44, 122-125], polycrystalline copper [25], and to small extent over copper oxides [104] under UHV conditions below  $10^{-7}$  mbar. Especially the studies over Cu(110), due to the fact that it has high reactivity compared with

other low-index planes of Cu and shows very interesting processes of surface reconstruction in the reaction, yielded detailed insights into the reaction mechanism. The polycrystalline copper surface exhibits a similar reactive behaviour as the Cu(110) surface in the low pressure range [25]. Adsorbed oxygen, depending on its coverage, performs two roles – promoter at low coverage and poison at high coverage – in the reaction. On Cu(110), the terminal oxygen atoms in the (2×1)-O islands act as the active sites for methanol oxidation. Methoxy and formate are found as the important intermediates during the surface reactions. However, while numerous studies have confirmed the prominent role of methoxy in the methanol oxidation mechanism, the role of the formate intermediate has been less clear. Methoxy forms an ordered (5×2) structure on Cu(110), and decomposes to formaldehyde slightly above room temperature. Formate, whose adsorbate structure is still under debate, decomposes to CO<sub>2</sub> at around 460 K. A TPD study of methanol adsorption on copper oxides [104] shows only the total oxidation product CO<sub>2</sub>.

### 7.2.2 Studies under technical conditions

Under more technical conditions between 10<sup>-2</sup> mbar and 1 mbar, a novel subsurface oxygen species was detected over a polycrystalline copper foil with the help of several *in situ* high pressure techniques. Its abundance can be linearly correlated with the amount of formaldehyde produced in the catalytic reaction [45, 120]. In contrast, the conversion of methanol is negatively affected by the abundance of surface oxygen species, which indicates that the pure copper surface is catalytically inactive in the selective oxidation of methanol to formaldehyde [120]. The formation of bulk oxide was found to be detrimental to formaldehyde production as well. On the basis of these observations, it has been proposed that the active catalyst surface is metallic copper that contains a sub-surface oxygen species. It is further assumed that the incorporation of sub-surface oxygen in the metallic surface could increase the catalytic reaction by inducing strain in the copper surface lattice, which could lead to an upward shift of the *d*-states of copper and thereby to a stronger surface-adsorbate interaction [112]. Under *in situ* measuring conditions (400 °C,  $p_{\text{total}} = 0.6$  mbar), the

formation of intermediates like methoxy and formate on the copper surface was not observed [45, 120].

### 7.2.3 Bridging the pressure gap

Obviously, in order to connect the findings of former UHV studies to real catalysis, it is necessary to perform measurements in the unexplored region (I) in Fig. 7.1. For this purpose, we have systematically varied the reaction total pressure from  $10^{-7}$  up to  $10^{-3}$  mbar in the UHV system, where we conducted rate measurements over a Cu(110) surface. The steady-state kinetics have been followed with *in situ* LEED, AES, PEEM, and XPS measurements in order to relate the presence of certain adsorbate phases and their coverages to the catalytic activity of the copper surface. Furthermore, in a high-pressure reaction cell which is connected to a UHV chamber, the kinetics of methanol oxidation over metallic and oxidized copper surfaces have been studied in the  $10^{-2}$  mbar range, and followed with *in situ* ellipsometry measurements used as a new high-pressure method. In Chapter 4-6, the influence of the total pressure on the reactivity of the copper surfaces has been presented in detail. Here, the main findings are summarized and linked to the former studies at both low and high pressures.

1. The coverages and ordering of the surface oxygen species strongly affect the surface reactivity, which supports that the surface oxygen species is directly involved in the methanol selective oxidation to formaldehyde. The reactivity of the surface at low and intermediate oxygen coverage is quite high, as indicated by a reactive sticking coefficient for methanol, which reaches 0.2 in agreement with former molecular beam reaction measurements at  $10^{-8}$  mbar [26, 31]. High oxygen coverage inhibits the reaction, which leads to the disappearance of the low-temperature reaction peak at around 400 – 520 K when the total reaction pressure exceeds  $10^{-3}$  mbar. This fits the observations over polycrystalline copper foils at pressure  $> 10^{-2}$  mbar, which the temperature profile only exhibits the high-temperature reactivity and is weakly sensitive to the total reaction pressure [45]. This inhibition factor can also explain the observation that the conversion of methanol is negatively affected by the abundance of surface oxygen species at high pressure.

2. With the pressure increase from  $10^{-7}$  to  $10^{-5}$  mbar, the dominant intermediate on the surface under reaction conditions shifts from methoxy to formate. Formate forms an ordered  $c(2\times 2)$  structure over Cu(110), and plays an important role in the reaction: its decomposition creates the vacant sites and therefore ignites the reaction at low-temperature. High adsorbate coverages have a negative effect on the reactivity of the surface, because of a lack of vacant sites required for the methoxy decomposition step, which is supported by the former STM results measured at  $10^{-8}$  mbar [27]. Quite generally, the increase in pressure increases the coverage and shifts processes to higher temperatures if the number of vacant sites plays an essential role in the reaction. This might be responsible for the decrease of the activity of the metallic copper surface at high pressure. In addition, we have found that, substantial carbon-containing adsorbates only exist on the surface at low-temperature, whereas at high-temperature the surface remains largely adsorbate-free except of the adsorbed oxygen. This might explain the observation at high pressure that no trace of carbon-containing intermediates was observed at 400 °C [45, 120].

3. Formaldehyde is always the predominant product in the reactions over metallic copper, which supports the idea that the metallic copper is the selective phase for methanol oxidation to formaldehyde. At  $10^{-2}$  mbar, the surface adsorbates still govern the surface reactivity, since no obvious phase transition occurs over metallic copper during the reaction. The oxidized copper surfaces exhibit higher activity compared with the metallic surface under same reaction condition, which indicates that the most active state of the surface is not a completely reduced surface but a surface which contains some oxygen. This is in concert with the findings at high pressures [120]. However, it is hard to determine whether bulk oxygen or some other oxygen species is the selective species to produce formaldehyde, since the reaction over the oxidized copper sample at  $10^{-2}$  mbar is transient. Moreover, the oxidation of the copper surface not only changes the surface phases, but also modifies the surface morphology, which makes the issue quite complex. In next section, we will continue to discuss the point since it is obviously involved in the material gap problem.

All in all, we have successfully bridged the pressure gap between  $10^{-7}$  and  $10^{-2}$  mbar over a Cu(110) surface. Some remaining questions call for the further

investigations over Cu(110): (1) to extend the *in situ* XPS study into the higher pressure range from  $10^{-2}$  to 1 mbar; (2) to improve the HP-UHV system so that we can use ellipsometry to determine *in situ* the possible phase transition during the steady-state reaction at  $10^{-2}$  – 1 mbar.

### 7.3 Material gap

The catalysts used in real catalytic procedures are usually substantial mixtures, which are typically not well defined and too complex to be analyzed. Therefore, as a first step to bridge the material gap, simple model systems shall be investigated. These model systems rank from single crystal, polycrystal, bimetallic surfaces, and planar metal/oxide systems up to defined, dispersed metal/oxide systems. With increasing structural complexity, the model systems approach increasingly the technical catalysts. For this purpose, the preparation and complete characterization of these model systems are required.

Technically, elemental copper is used as unsupported catalyst for the oxidative dehydrogenation of alcohols with air to their respective aldehydes. As a model reaction, methanol oxidation has been extensively studied over copper single crystals [23-44, 122-125] and polycrystalline copper [16-22, 25, 45, 120]. However, it is known that copper has a high affinity for oxygen, and accordingly, it is expected that during the reaction the surface of the copper catalyst forms various oxides changing in time if there is a high feed of oxygen, e.g. during the reaction at high pressures. This was observed in the studies at pressure above  $10^{-2}$  mbar [19, 94]. Obviously, the pressure gap problem cannot be separated from the material gap problem, because a change in pressure also modifies the catalyst. In the following section, we continue to discuss the effect of the formation of copper oxides on the sample reactivity.

The special efficiency of real catalysts made typically of several components is based on favorable cooperation of the individual components on reaction conditions. Apart from the modification of the electronic and geometrical structure of the active phase with the transition from ideal to real reaction conditions, dynamic coupling processes of material transfer, e.g. surface diffusion, in these assembled catalysts also

play an important role. As an attempt to bridge the material gap (unexplored region (II) in Fig. 7.1), in this work two microstructured bimetallic copper model catalysts, Pd/Cu(110) and Cu/ZnO/Al<sub>2</sub>O<sub>3</sub>, were used to study the spatiotemporal dynamics of the reaction.

### 7.3.1 Copper

As shown in Fig. 7.1, several low-index planes (110), (100) and (111) of copper have been used to investigate the oxidation of methanol [23-44, 122-125]. Most of the experimental work was carried out over Cu(110) [23-44] and Cu(100) [38, 122], whereas few studies report the reactivity on Cu(111), because the Cu(111) surface is considered to be the most stable in terms of surface coordination [126]. The three surfaces exhibit different reactivity, which might be traced back to the different oxygen reconstructions over the surfaces. At low coverage ( $\leq 0.5$  ML), oxygen forms (2 $\times$ 1)-O reconstructions over Cu(110) and (2 $\sqrt{2}$  $\times$  $\sqrt{2}$ ) R45 $^\circ$ -O reconstructions over Cu(100), respectively [79]. Adsorption of oxygen over Cu(111) is rather complex, leading to formation of a surface oxide [126]. According to the models of the oxygen reconstructions, they all consist of the so-called “copper-added row” structures, i.e. O-Cu-O chains. But the (2 $\times$ 1)-O structures over Cu(110) expose the most low-coordinate, terminal oxygen atoms which have been determined as the active sites for methanol oxidation. Therefore, the Cu(110) surface exhibits the highest reactivity at low oxygen coverages. A comparison of the reactivities over Cu(110), Cu(111) and polycrystalline copper surfaces at low pressure [25] showed that the reactive behaviour of the polycrystalline copper surface is similar to that of Cu(110) surface.

### 7.3.2 Copper oxides

TPD studies of methanol adsorption on bulk powders of CuO and Cu<sub>2</sub>O [104] have showed that methanol decomposes to CO<sub>2</sub>, H<sub>2</sub> and H<sub>2</sub>O on copper oxide surfaces, indicating that copper oxides lead to the total oxidation of methanol. In recent high-pressure studies over a copper foil [19] a rate oscillation has been discovered at pressure above 10<sup>-2</sup> mbar and related to periodic phase transitions between metallic

copper and copper oxides. Even though it was reported [16] that the oxidized copper surface exhibits higher activity than the metallic copper surface with the high formaldehyde selectivity, it is believed that the formation of the bulk oxides is detrimental to formaldehyde production. Consequently, a subsurface oxygen species was proposed to be responsible for the enhanced reactivity. Obviously, the system becomes complex due to the formation of various forms of (sub)-oxides changing in time during the high-pressure reaction.

In order to understand the effect of copper oxides on the sample reactivity, we have produced a  $\text{CuO}_x$ -like sample in the UHV system by sputtering a Cu(110) surface (600 eV, sample temperature 400 °C, sample current 1.2 – 1.5  $\mu\text{A}$ ) in oxygen atmosphere ( $P_{\text{O}_2} = 5 \times 10^{-5}$  mbar) for 4 hours. After the preparation, a red opaque sample surface was observed. AES showed a large amount of oxygen on the surface, where the oxygen to copper peak-to-peak intensity exceeds that of the high coverage  $c(6 \times 2)\text{-O}$  phase. Fig. 7.2 shows a comparison of the TPR spectra over the oxygen-sputtered Cu(110) surface with that over a clean Cu(110) surface. The reactions were conducted at  $10^{-5}$  mbar with a methanol to oxygen gas ratio of 1:0.8. The heating rate was 6 K/min. The reactivity of the  $\text{CuO}_x$ -like sample is lower than that over Cu(110), whereas more  $\text{CO}_2$  and  $\text{H}_2\text{O}$  were produced in the intermediate-temperature range. However, there are still some common properties in the spectra, e.g. the same ignition temperature, two reaction peaks at low- and high-temperatures, and the high selectivity to formaldehyde.

A CuO film subjected to vacuum annealing was found to transform into  $\text{Cu}_2\text{O}$  at  $\approx 470$  K and beyond 670 K metallic copper started to form on top [100]. Therefore, it is supposed that the  $\text{CuO}_x$ -like sample produced by oxygen-sputtering at 673 K consists of a thin copper film on top. Such a structure explains the similar behaviour of the  $\text{CuO}_x$ -like sample and Cu(110). More  $\text{CO}_2$  and  $\text{H}_2\text{O}$  productions in the intermediate-temperature range might be due to the reduction of the bulk oxide since after the reaction, AES showed a pronounced decrease of oxygen content in the sample. Furthermore, after completely reducing the sample, it is seen that the single crystalline structure of Cu(110) was largely destroyed.

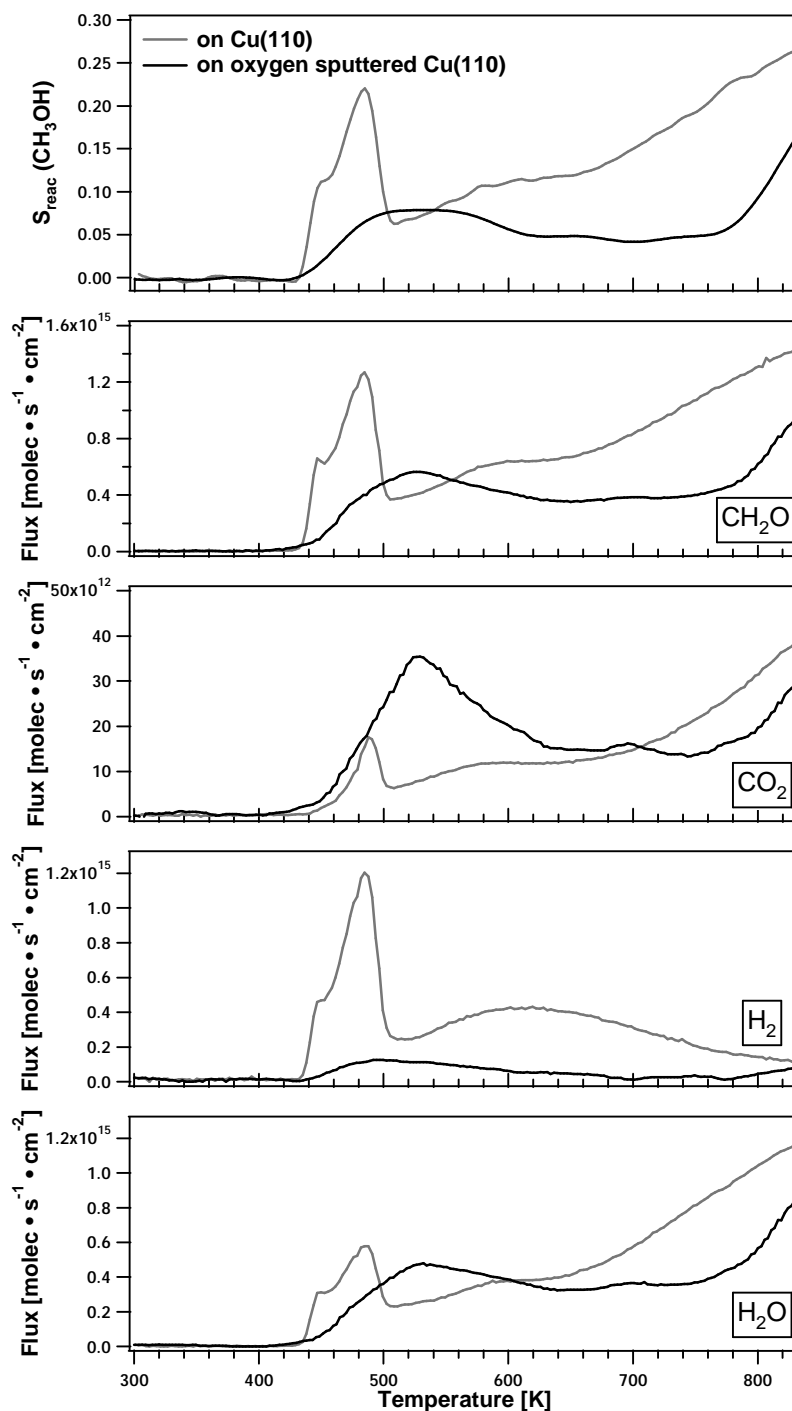


**Figure 7.2** The comparison of temperature programmed reaction spectroscopy over a Cu(110) surface and an oxygen-sputtered Cu(110) surface in the  $10^{-5}$  mbar range with  $p(\text{CH}_3\text{OH}) = 1.0 \cdot 10^{-5}$  mbar,  $p(\text{CH}_3\text{OH}) : p(\text{O}_2) = 1:0.8$ . The upper panel represents the reactive sticking coefficient of methanol,  $s_{\text{reac}}(\text{CH}_3\text{OH})$ ; the other panels indicate the production rates of the different products during methanol oxidation.



In the HP-UHV system, we have compared the kinetics of methanol oxidation over a metallic, a partially and a deeply oxidized copper surfaces at  $10^{-2}$  mbar. Both the oxidized copper surfaces exhibit higher activity than the metallic copper surface. However, the reactions over the oxidized copper surfaces are transient, that is to say, a reduction takes place involving not only the surface oxygen but also the bulk oxygen. Therefore, it is difficult to directly determine the active phase for producing formaldehyde. With the help of *in situ* ellipsometry measurements and the following simulation of the measured ellipsometric data, a sample model was constructed. This model which contains a thin  $\text{Cu}^{1+}$  oxide film beneath a metallic copper surface could be associated with the high reactivity and selectivity to formaldehyde. This conclusion agrees with the findings in other high-pressure studies [16-22, 45, 120].

Ellipsometry is considered as a new *in situ* high-pressure method in this work, since it is a light in / light out technique and thereby has not pressure limitation. It is a powerful technique for the characterization of thin films on surfaces, e.g. in determining the optical constants and thickness of the thin films. Therefore, it provides the information not only of the surface region but also of the subsurface layer. In our work, we have successfully used the technique to monitor the degree of oxidation (i.e. phase transitions) of the sample, and to detect the spatial inhomogeneities of the surface during the reaction. However, the lack of the chemical information of the detected layer systems limits the explanation of the measured data. Other *in situ* high-pressure techniques are required to fill out this gap. Moreover, a precise measurement is hampered by the morphology changes, e.g. the roughening and the spatial inhomogeneities, which often occur in the high-pressure reactions. Therefore, more careful control of the reaction conditions might be necessary to separate the effect of the phases and the morphology.

### 7.3.3 Microstructured bimetallic copper catalysts

Microstructured bimetallic surfaces prepared by optical lithography allow us to study dynamic effects under low pressure conditions with spatially resolving *in situ* techniques such as photoelectron emission microscopy (PEEM) and scanning photoelectron microscopy (SPEM). By varying the geometry and dimension of the

structures, one can control the diffusional flow between the differently active metals. The following effects have been observed [127]: macroscopic size effects in reactivity due to diffusional coupling, front nucleation at domain boundaries and the formation of stationary concentration patterns due to reversible adsorbate-induced segregation in bimetallic alloyed films. These studies can provide the important information of synergetic effects present in composite catalysts.

### 7.3.3.1 Pd/Cu(110)

Similar to copper, palladium has received great interest with regard to catalytic methanol oxidation, due partly to environmental concerns regarding control of volatile organic compound formation from industrial processes as well as automobile emissions standards [128-130]. The oxidation of methanol on Pd single crystals under UHV conditions has been extensively studied [131-139], whereas a few studies have been conducted under high-pressure conditions too [140-143]. It is generally accepted that methanol decomposes readily on Pd at room temperature via the formation of a methoxy intermediate to form adsorbed CO and H. In contrast with the high selectivity to formaldehyde on Cu(110), under steady-state conditions, only CO<sub>2</sub> and H<sub>2</sub>O were identified as oxidation products on Pd(110) [131]. Thus, in considering the modification of a copper catalyst with Pd, it was planned to investigate how this affects the interplay and interconversion between the important surface intermediates, e.g. O-Cu(110), O-Pd, methoxy-Cu(110), formate-Cu(110), and methoxy-Pd.

The PEEM images in Fig. 7.3 show the titration of an oxygen saturated Pd/Cu(110) microstructure with methanol at 470 K. Dark areas represent oxygen covered surface, whereas bright areas mark a low concentration of oxygen. Inside the circle, the substrate is a Cu(110) surface and the surrounding area is covered with a 1500 Å-thick Pd film. It is shown that, initially both the Pd and Cu(110) surfaces are covered with oxygen; after around 4 minutes, the Cu (110) surface is firstly reduced homogenously, whereas no visible change occurs on Pd; After 6 minutes, the Cu(110) surface is completely reduced; at around 8 minutes after titration, the Pd surface starts to be homogenously reduced. During this process, no reaction fronts appear.

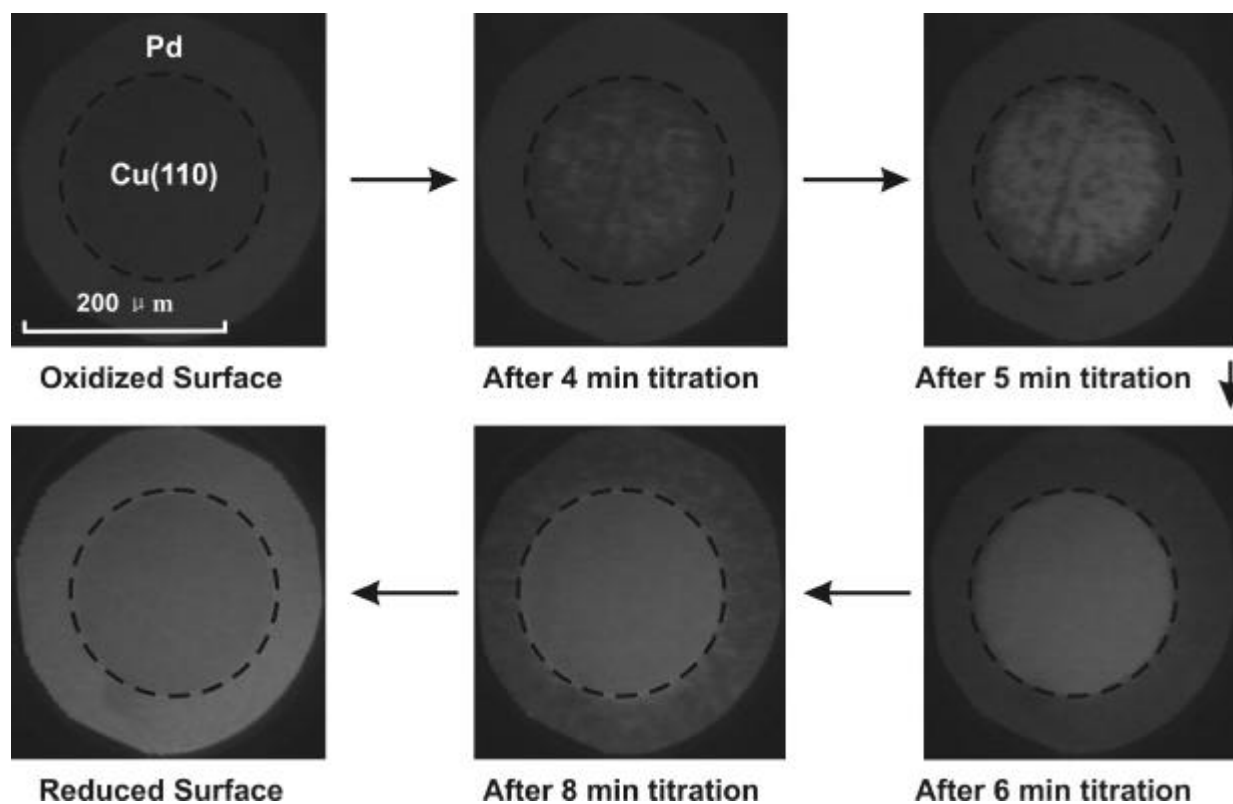


**Figure 7.3** PEEM images showing different stages in the titration of an oxygen saturated Pd/Cu(110) microstructure with methanol at  $p(\text{CH}_3\text{OH}) = 1 \cdot 10^{-7}$  mbar and  $T = 470$  K. Inside the circle, the substrate is a Cu(110) surface and the surrounding area is covered with a 1500 Å-thick Pd film.

The PEEM experiments have been also carried out on the Pd/Cu(110) surface under steady-state reaction conditions. In the investigated parameter range from  $10^{-7}$  to  $10^{-5}$  mbar, no reaction fronts or stationary patterns were found. The reaction proceeds spatially homogenous on Cu and Pd, respectively. No pattern forming effects were observed at the Pd/Cu interface on a length scales accessible to PEEM.

To our great surprise, even though AES showed that palladium existed on the surface, SPEM measurements in ELETTRA (Synchrotron light source in Trieste, Italy) have revealed that a thin copper film totally covered the palladium structures. This is demonstrated in Fig. 7.4, which shows the Cu 3p intensity on Cu(110) and Pd/Cu(110) regions, as well as the SPEM Pd 3d and Cu 3p images of the same surface region.

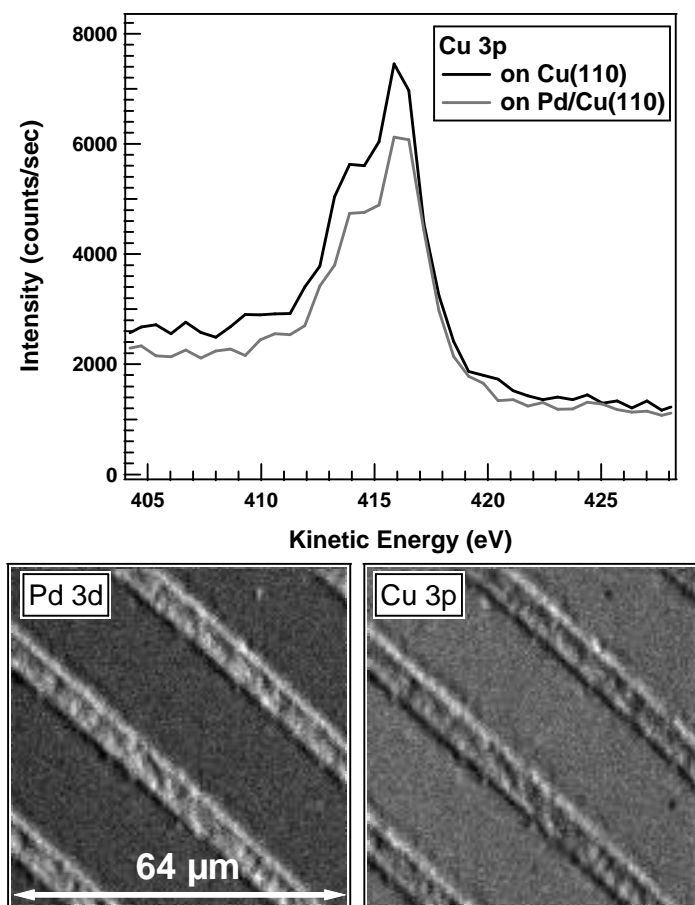


**Figure 7.4** A thin copper film totally covers the palladium structures of a Pd/Cu(110) microstructured sample. Top: Cu 3p intensity obtained over Cu(110) and Pd/Cu(110), respectively. Below: SPEM Pd 3d and Cu 3p images of the surface in the same structure region.

Obviously, the microstructured Pd/Cu(110) sample was completely modified during the former treatments and the reactions. A CuPd[85:15](110) alloy surface has been studied by M. A. Newton et al. [144-151] for the oxidative dehydrogenation of methanol. It was reported that this alloy surface exhibited a very similar reactive behaviour to Cu(110), whereas no tendency towards a Pd-like behaviour was observed. The “Cu-like” behaviour of the Cu-Pd alloy surface has been attributed to the surface structure of the alloy. It was found that the alloy surface layer itself is depleted in Pd. On the basis of the relative strengths of the CuCu, CuPd, and PdPd bonds, and surface free energy terms, the equilibrium surface layer is predicted to be

essentially devoid of Pd [150]. A study of ultrathin Pd films on Cu(100) with positron-annihilation-introduced Auger electron spectroscopy (PAES) [152] showed that the top-layer composition is temperature-dependent. In contrast with the traditional electron-induced AES, PAES obtains information selectively from the topmost layer. As a Pd film deposited on Cu(100) at 173 K is warmed to 423 K, a copper overlayer forms and Pd moves one atomic layer down. Furthermore, it is well known that, copper atoms are very mobile during methanol oxidation [93]. Therefore, it is very likely that copper atoms diffuse to and sit on the Pd structures in the reaction.

### 7.3.3.2 Cu/ZnO/Al<sub>2</sub>O<sub>3</sub>

The scientific interest in the interaction of methanol with copper surfaces arises from not only the relevant synthesis of formaldehyde over pure copper catalyst, but also that it is a key mechanistic step in several technologically important catalytic processes using the supported copper catalysts, e.g. methanol synthesis from syngas over Cu/ZnO catalysts and methanol steam reforming over Al<sub>2</sub>O<sub>3</sub> supported Cu/ZnO [11-13]. It is widely accepted that the use of ZnO as a support material leads to a highly dispersed and active Cu catalyst, whereas Cu and ZnO alone exhibit only negligible activity. The proposed synergetic role of ZnO in the catalytic system can be classified into three categories: (i) spillover model by Burch et al. and Spencer [153, 154] in which ZnO acts as a reservoir of hydrogen for the hydrogenation of CO over Cu surfaces; (ii) the morphology effect proposed by Yoshihara et al. [155], Ovesen et al. [156], Hadden et al. [157], and Topsøe et al. [14, 158], in which the morphology of copper particles on a ZnO support is responsible for the effect of ZnO upon the methanol synthesis on Cu; and (iii) the active site model on Cu surfaces proposed by Fujitani et al. [159–160], in which the creation of the Cu-Zn active site in surface alloy enhances the catalytic activity. Recently, it was also proposed [15] that the turnover frequency for methanol production has a positive correlation with the observed microstrain of copper in the Cu/ZnO system.

Due to the strong interaction between Cu and ZnO in the system, it is expected that dynamic processes during the reaction can be observed by PEEM over a microstructured Cu/ZnO film deposited on sapphire. For instance, spillover model can be

observed by size effects in reactivity due to diffusional coupling of hydrogen, or if the strain exists in copper due to ZnO, the influence of boundaries on the catalytic reactivity can be observed.

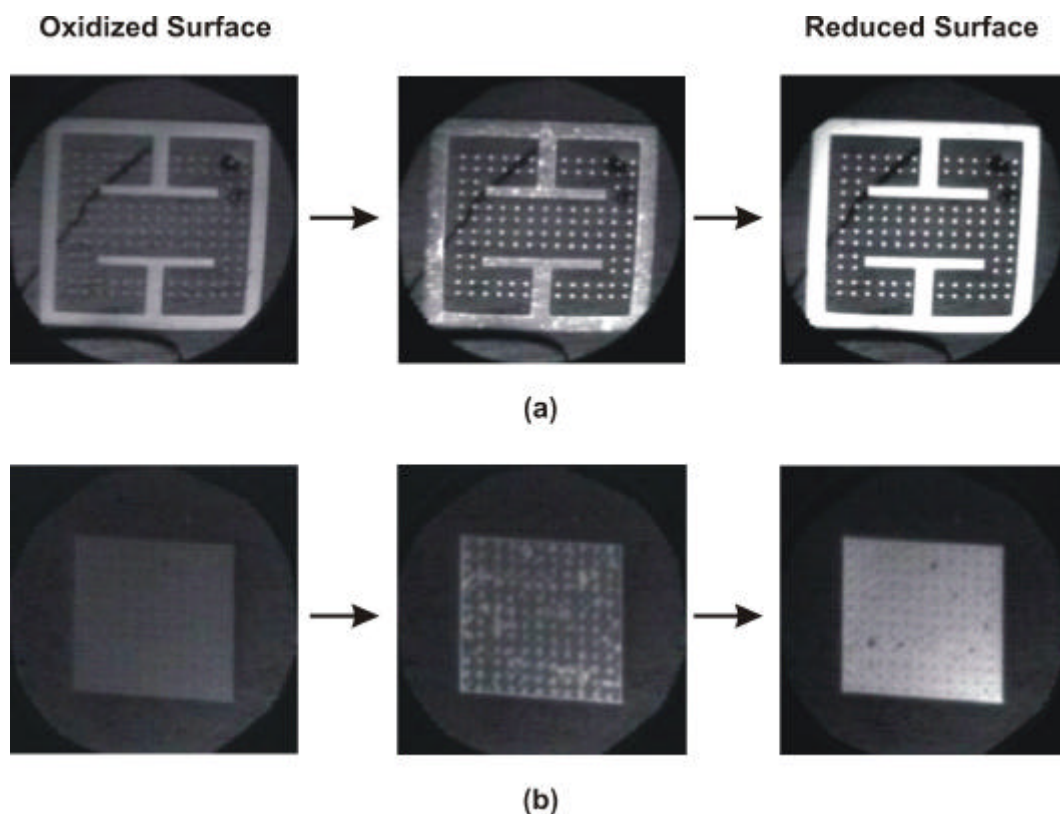


**Figure 7.5** PEEM images ( $500 \times 500 \mu\text{m}^2$ ) showing the titration of oxygen saturated Cu/ZnO/Al<sub>2</sub>O<sub>3</sub> microstructures with methanol at  $p(\text{CH}_3\text{OH}) = 1 \times 10^{-6}$  mbar and  $T = 420$  K. Cu structures are imaged brighter, whereas ZnO film is imaged darker. (a) Reaction starts from small size Cu-domain; (b) Reaction starts from small size ZnO-domain.

Both size effects and boundary effects can be observed in Fig. 7.5, which shows the PEEM images during the titration of two oxygen saturated Cu/ZnO microstructures with methanol at 420 K. According to the work function contrast, the Cu structures are imaged brighter, whereas the ZnO film is imaged darker. It is visible that only the copper surface is reduced after titration, whereas no obvious contrast change occurs on the ZnO film. As shown in Fig. 7.5(a), during the titration, the reaction starts from the small sized Cu-domains on the ZnO film (center parts in the structure). The reduction of the large area of the structure takes longer time, and

obviously ignites from the boundary of the Cu structure and the ZnO film. Fig. 7.5(b) shows an inverse structure in which the small sized ZnO domains exist on a copper square. Clearly the reaction is initiated at the boundaries of the small sized ZnO domains. Obviously, the interaction between ZnO and Cu is essential for the reaction to proceed. Since PEEM yields no direct information about the chemical state and the composition of the catalyst surface [127], it is necessary to use SPEM which can provide the missing chemical information, to identify the synergetic effect of ZnO on Cu *in situ*. Therefore, it is planned to conduct experiments using the synchrotron light source at ELETTRA.

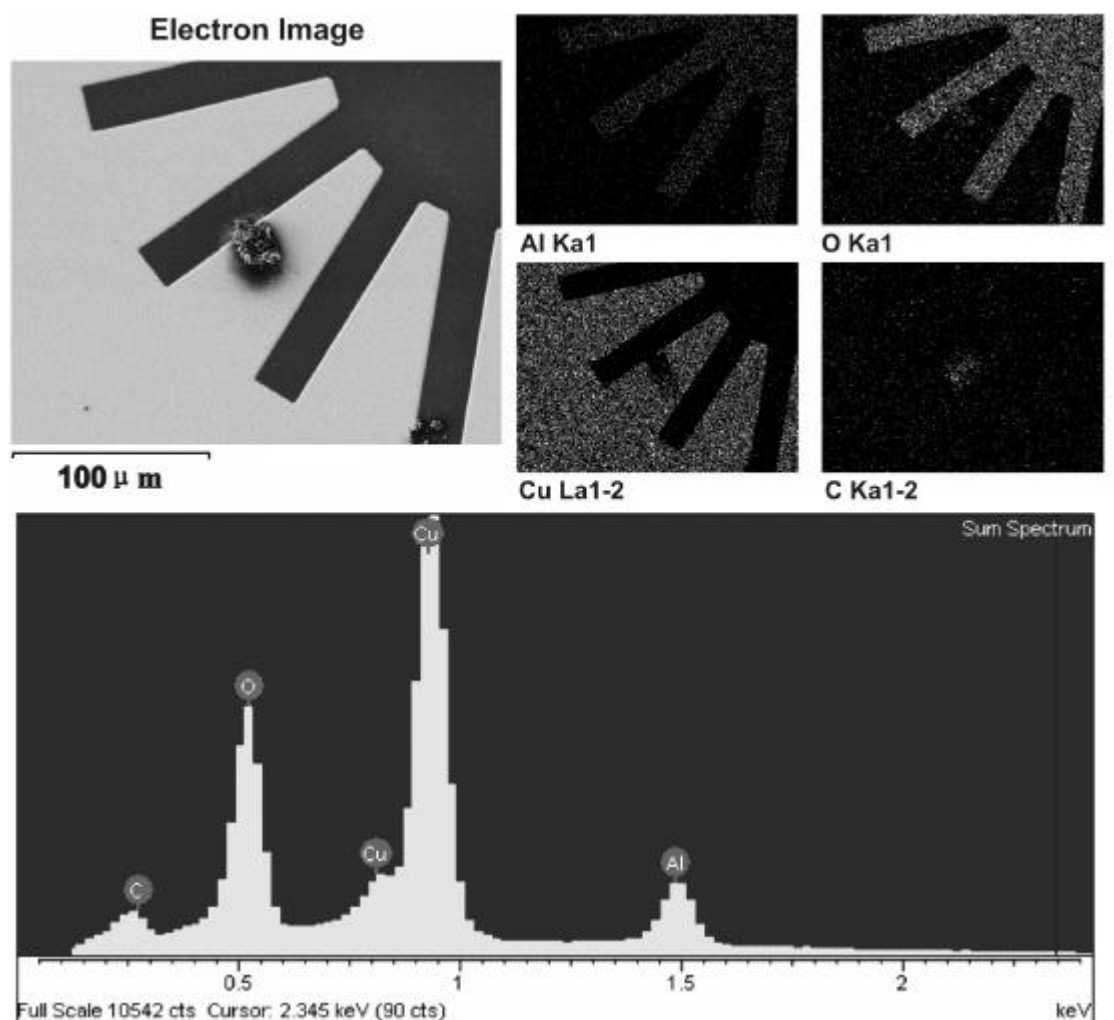


**Figure 7.6** SEM image of a Cu/ZnO microstructure, the EDX spectrum of the Cu/ZnO/Al<sub>2</sub>O<sub>3</sub> film, and the corresponding EDX mappings of Al, O, Cu, and C, after the sample was used for kinetic measurements at high temperature.

The steady-state reaction kinetics of methanol oxidation and methanol synthesis from  $\text{CO} + \text{H}_2$  have been measured over microstructured  $\text{Cu}/\text{ZnO}/\text{Al}_2\text{O}_3$  model catalyst in the  $10^{-7} - 10^{-5}$  mbar range. No reaction rate could be detected at low temperature ( $< 450$  K). Therefore, the measurements have been continued at higher temperatures up to 670 K. Soon, it was found by PEEM that clusters formed on the surface. It became very difficult to image the surface due to a weak surface conductivity. AES measurements showed that the Zn signal had steeply decreased. Efforts to reproduce the observations in Fig 7.5 were unsuccessful, and instead, the copper surface was reduced homogeneously. Most likely, the model catalyst surface was modified by increasing the measurement temperature. After the sample had been moved out from the UHV system, it was investigated by scanning electron microscopy (SEM) measurement and energy dispersive X-ray (EDX) analysis. Fig. 7.6 shows the SEM image of a  $\text{Cu}/\text{ZnO}$  microstructure, the EDX spectrum, and the corresponding EDX mappings of Al, O, Cu, and C. It is quite surprising that no trace of ZnO exists on the surface. Therefore, it can be concluded that the ZnO film was evaporated in the vacuum due to high temperature. This conclusion is supported by ref. [161] which reports that a ZnO film can be prepared only when the substrate temperature does not exceed 473 K.

Both described studies over microstructured bimetallic model catalysts show that, the effort to bridge the material gap is hampered by the sample stability (composition, morphology, and reproduction of chemical defects) during the reaction. This requires developing the new *in situ* methods and producing more advanced model catalysts.

## 7.4 Conclusions and outlook

We have attempted to bridge the pressure and material gap in methanol selective oxidation over copper catalysts. The pressure gap problem can be solved by a continuous increase in the pressure of the reaction mixture, and carrying out *in situ* studies. The solution to the material gap problem is to step by step increase the structure complexity of the model catalysts.



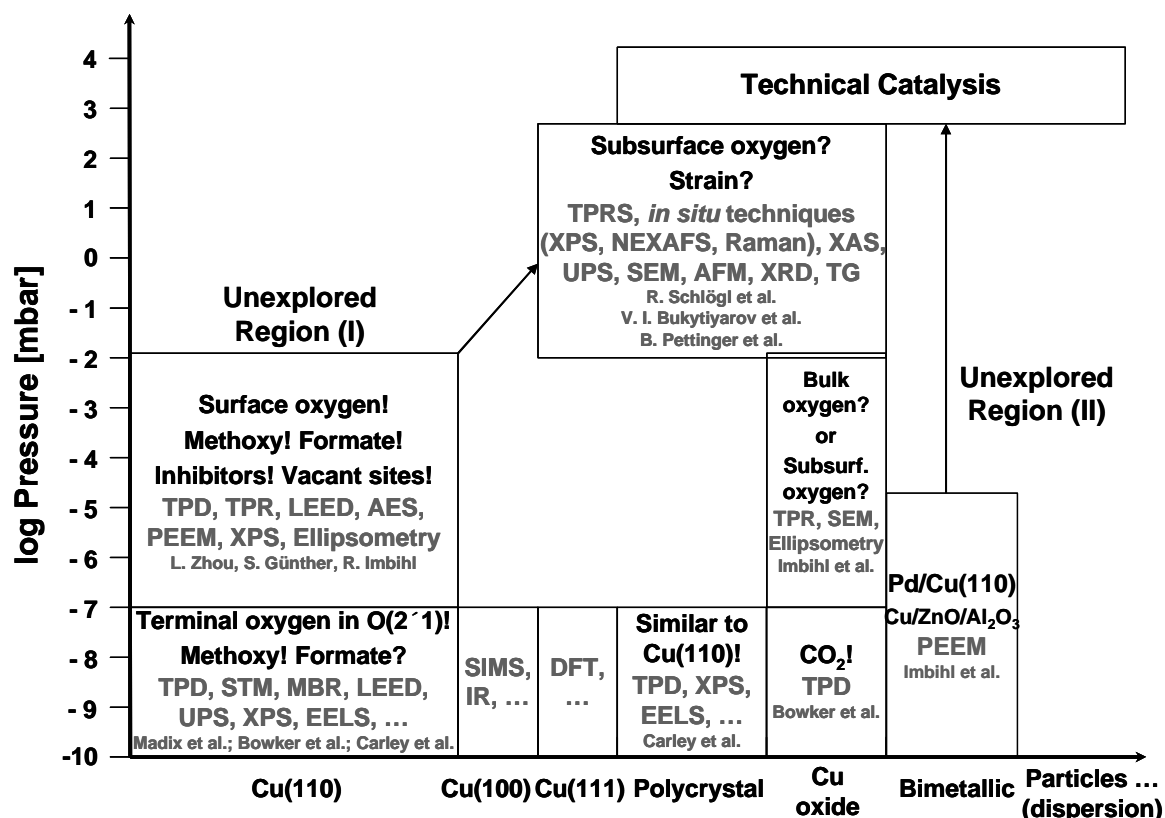


**Figure 7.7** Schematic diagram illustrating the current status of the pressure and material gap in methanol selective oxidation over copper catalysts. The content in the each textbox exhibits the main results (black), the applied techniques, and the research groups (grey) in the studies. The question marks indicate that the stated results are still under debate.

As summarized in Fig. 7.7, in this work, the pressure gap between  $10^{-7}$  and  $10^{-2}$  mbar over a Cu(110) surface has been successfully bridged, whereas the attempt to bridge the material gap is still difficult due to the difficulties in avoiding the strong modification of the well-defined model catalysts by the reaction. Our findings can well link the former UHV results to the high-pressure observations. However, even though some findings seem to support the reaction mechanism proposed by Schlögl et al., we have no direct evidence to prove participation of the so-called subsurface oxygen species and to establish the effect of strain on the reactivity.

Therefore, the continuous increase of the total reaction pressure from  $10^{-2}$  to 1 mbar is suggested, which is demonstrated in Fig. 7.7 as “unexplored region (I)”. *In situ* XPS and ellipsometry studies on Cu(110) might be useful to solve the pressure

---

gap problem. In order to disclose the “unexplored region (II)” in Fig. 7.7, i.e. to bridge the material gap, two bimetallic model catalysts, Cu/ZnO/Al<sub>2</sub>O<sub>3</sub> and Cu/Pd film on Ru(0001), are planned to be studied under controlled reaction conditions.

## Chapter 8

### Summary

In general, processes on realistic catalysts are far too complex to allow the identification of the microscopic reaction steps. This problem calls for idealization of the experimental conditions such as the use of single crystalline surfaces and the investigations under well-controlled vacuum conditions (UHV conditions). The price to pay for this so-called surface science approach is the introduction of a pressure and material gap by which catalytic properties (elementary reaction steps, reaction intermediates, etc.) determined under well-defined conditions may not be transferable to realistic reaction conditions. Therefore, the relevance of surface science studies to realistic catalytic systems requires the development of methodologies for bridging the pressure and material gap in heterogeneous catalysis. As a part of the effort for the purpose, in this work, methanol selective oxidation to formaldehyde over various model copper catalysts has been thoroughly studied, following the strategy of systematically increasing the total pressure during the measurements of the reaction kinetics and utilizing *in situ* techniques to monitor the variation of the surface species and phases during the reactions.

First of all, methanol oxidation over a Cu(110) surface has been studied under unsteady-state reaction conditions in the  $10^{-7}$  and  $10^{-5}$  mbar ranges with temperature-programmed desorption (TPD), low energy electron diffraction (LEED) and photoelectron emission microscopy (PEEM). Two oxygen-induced reconstructions of the surface, Cu(110)-(2×1)-O ( $\mathbf{q}_O = 0.5$  ML) and Cu(110)-c(6×2)-O ( $\mathbf{q}_O = 0.67$  ML), have been observed by LEED after exposure of 10 L oxygen at room temperature and

extensive exposure of  $10^4$  L oxygen at 100 °C, respectively. It is shown that the surface reactivity with methanol is strongly oxygen coverage dependent. Both the clean surface and the surface with an oxygen coverage upon 0.5 ML have a very low reactivity for the oxidative adsorption of methanol, whereas a partially  $(2\times 1)$ -O islands covered surface ( $\theta_{\text{O}} \approx 0.25$  ML) exhibits a pronounced maximum in reactivity.

Methoxy and formate species have been determined as important intermediates of the surface reaction. Methoxy forms an ordered  $(5\times 2)$  structure, whereas formate forms an ordered  $c(2\times 2)$  structure on the Cu(110) surface. The dosing conditions strongly affect the composition and the ordering of the adsorbate layer on the surface. Methoxy is the dominant intermediate after sequential dosing with moderate oxygen and methanol, or after co-dosing of methanol and oxygen at  $10^{-7}$  mbar under methanol-rich conditions. Formate becomes the predominant intermediate during co-dosing of methanol and oxygen at  $10^{-5}$  mbar under methanol-rich conditions. An extended co-dosing of methanol-rich gas mixture leads to the coexistence of separate oxygen, methoxy and formate islands.

Oxygen-rich gas mixtures do not produce methoxy or formate on the surface due to the preferential growth of  $(2\times 1)$ -O islands. Depending on the coverage, oxygen performs two roles – both promoter and poison – in the reaction. It can be concluded that the terminal oxygen atoms in the O-Cu rows of the  $(2\times 1)$ -O islands act as the active sites for methanol oxidation.

Three possible reaction pathways have been identified by TPD: methoxy decomposition to formaldehyde at 360 K (selective oxidation), formate formation and decomposition to  $\text{CO}_2$  at 460 K (total oxidation), and methoxy recombination with hydrogen adatoms to methanol below room temperature and at 360 K (back-reaction).

The steady-state kinetics of methanol oxidation over Cu(110) have been studied under low pressure conditions from  $10^{-7}$  to  $10^{-3}$  mbar in a UHV system. *In situ* investigations with low energy electron diffraction (LEED), Auger electron spectroscopy (AES), and photoelectron emission microscopy (PEEM) allow relating the presence of certain adsorbate phases to the catalytic activity. Moreover, with the

help of the *in situ* high-pressure X-ray photoelectron spectroscopy (XPS) facility at BESSY, the variation of the adsorbate coverages during the reaction has been quantitatively investigated. These results help to confirm the reaction mechanism.

A high selectivity for the partial oxidation product formaldehyde is found besides the byproducts  $H_2$ ,  $H_2O$ , and  $CO_2$  in the stationary reactions. The reactivity of the surface at low and intermediate oxygen coverage is quite high, as indicated by a reactive sticking coefficient for methanol, which reaches 0.2. High oxygen coverages inhibit the reaction. The reactivity of the surface exhibits two peaks at low pressure: one at around 400 – 520 K, which disappears when the total pressure exceeds  $10^{-3}$  mbar, and the other at high-temperature of around 900 K that persists at high pressure. Hydrogen production is observed in an intermediate temperature range, reflecting the presence of a second pathway with less oxygen consumption towards formaldehyde production. In the  $10^{-5}$  –  $10^{-4}$  mbar range, with the exception of the  $CO_2$  peak, each of the low-temperature reaction peaks consists of two components: one coincides with the onset of the  $CO_2$  production, and the other coincides with the maximum of the  $CO_2$  peak.

The stationary reaction kinetics are associated with a broad rate hysteresis upon cycling of the temperature. The origin of the hysteresis can be attributed to two differently reactive surface phases connected with different carbon-containing species and different oxygen coverages. Ordered overlayers of reaction intermediates, the  $(5\times 2)$ -methoxy and the  $c(2\times 2)$ -formate, occur only in small, roughly 80 K wide T-intervals above 300 K, where the catalytic activity is negligible. The surface exhibits substantial carbon coverage upon heating, but on the cooling branch the surface is largely carbon free down to  $\approx 400$  K, where the surface becomes covered by carbon-containing adsorbates again. Furthermore, only the low-temperature reactivity peak at  $\approx 400$  – 500 K is associated with a substantial adsorbate coverage, whereas the high-temperature reactivity peak at 900 K correlates with a largely adsorbate-free surface. Apparently, high adsorbate coverages have a negative effect on the reactivity of the surface, which can be traced back to a lack of vacant sites required for the methoxy decomposition step to proceed and a limited mobility of the reacting species. Formate

species plays an important role to activate the surface since its decomposition creates the vacant sites and therefore ignites the reaction at low temperature.

Kinetic measurements have shown that, with increasing the total reaction pressure, the low-temperature reactivity peak shifts to higher temperatures by roughly 20 K per order of magnitude difference in pressure. In addition, the separation of the different reactivity peaks during heating and cooling (hysteresis) becomes smaller. Quite generally, the increase in pressure increases the coverage and shifts processes to higher temperatures if the number of vacant sites plays an essential role. In addition, the pressure-induced structural change, from a (5×2)-methoxy at low pressure to a c(2×2)-formate at high pressure, might also be responsible for the shift in the reaction peaks.

The spatiotemporal dynamics of methanol oxidation over Cu(110) and two microstructured bimetallic model catalysts, Pd/Cu(110) and Cu/ZnO/Al<sub>2</sub>O<sub>3</sub>, have been studied with PEEM in the UHV system. At low pressures, the reaction proceeds spatially homogeneously on Cu(110) and Pd/Cu(110), whereas both size effects and boundary effects have been observed over Cu/ZnO/Al<sub>2</sub>O<sub>3</sub>, which indicates a possible synergetic effect of ZnO on Cu. Both microstructured samples are not chemically stable during the reactions. On Pd/Cu(110), copper atoms are very mobile under reaction conditions, and finally form a thin copper film on top of the palladium structures. The ZnO film has a low evaporation temperature and disappears from the sapphire substrate after the reaction temperature exceeds 470 K.

The kinetics of methanol oxidation over metallic and oxidized copper surfaces have been studied in the 10<sup>-2</sup> mbar range in a high-pressure reaction cell which is connected to a UHV chamber. Both oxidized surfaces exhibit two rate maxima at ≈ 530 K and ≈ 670 K, whereas the metallic copper surface only has its high temperature reactivity beyond 750 K. Despite its reactivity being higher than that of the metallic copper surface, the partially oxidized surface still keeps the fairly high selectivity to formaldehyde. The deeply oxidized surface causes more total oxidation to CO<sub>2</sub>, although the high selectivity to formaldehyde maintains over most of the temperature range. The comparison of the kinetics indicates that the most active state

of the surface is not a completely reduced copper surface but a surface which contains some oxygen in the near surface region. The gas mixing ratio of methanol to oxygen has only a weak influence on reactivity as long as the sample stays metallic, whereas it strongly affects the reactions over the deeply oxidized copper sample.

The reaction over the oxidized copper sample at  $10^{-2}$  mbar is transient. A reduction takes place involving not only the surface oxygen but also the bulk oxygen. Pronounced transitions of the surface phases from CuO to Cu<sub>2</sub>O and finally to metallic copper during the methanol oxidation reaction have been observed by optical microscopy, laterally integrating and imaging ellipsometry. The high reactivity and selectivity to formaldehyde of a sample, which contains a thin Cu<sub>2</sub>O film beneath a metallic surface, have been confirmed by simulating the *in situ* measured ellipsometric data and relating them to the reaction kinetics. The reduction of the oxidized surface is accompanied by drastic surface morphological changes.





## Bibliography

- [1] G. A. Somorjai, *Chemistry in Two Dimensions: Surfaces*, Cornell Univ. Press, Ithaca, NY, 1981.
- [2] A. Zangwill, *Physics at Surfaces*, Cambridge Univ. Press, New York, 1988.
- [3] G. Ertl and J. Kiippers, *Low Energy Electrons and Surface Chemistry*, VCH, Weinheim, 1985.
- [4] D. P. Woodruff and T. A. Delchar, *Modern Techniques of Surface Science*, Cambridge Univ. Press, New York, 1986.
- [5] M. R. Albert and J. T. Yates, *The Surface Scientist's Guide to Organometallic Chemistry*, American Chemical Society, Washington, DC, 1987.
- [6] K. Christmann, *Introduction to Surface Physical Chemistry*, Steinkopff Verlag, Darmstadt, Springer-Verlag, New York, 1991.
- [7] V. I. Bukhtiyarov, *Kinet. Catal.* 44 (2003) 420.
- [8] J. A. Rodriguez, D. W. Goodman, *Surf. Sci. Rep.* 14 (1991) 1.
- [9] C. N. Satterfield, *Heterogeneous Catalysis in Practice*, McGraw Hill, New York, 1980.
- [10] C. L. Thomas, *Catalytic Processes and Proven Catalysts*, Academic Press, New York, 1970.
- [11] J. Walker, *Formaldehyde*, Reinhold, Amsterdam, 1964.

- [12] Ullmann, Encyclopedia of Industrial Chemistry, Verlag Chemie, Weinheim, 1982.
- [13] E. Jones, G. Fowle, *J. Appl. Chem.* 3 (1953) 206.
- [14] P. L. Hansen, J. B. Wagner, S. Helveg, J. R. Rostrup-Nielsen, B. S. Clausen, H. Topsøe, *Science* 295 (2002) 2053.
- [15] M. M. Günter, T. Ressler, B. Bems, C. Büscher, T. Genger, O. Hinrichsen, M. Muhler, R. Schlögl, *Catal. Lett.* 71 (2001) 37.
- [16] T. Schedel-Niedrig, T. Neisius, I. Böttger, E. Kitzelmann, G. Weinberg, D. Demuth, R. Schlögl, *Phys. Chem. Chem. Phys.* 2 (2000) 2407.
- [17] A. Knop-Gericke, M. Hävecker, T. Schedel-Niedrig, R. Schlögl, *Catal. Lett.* 66 (2000) 215.
- [18] A. Knop-Gericke, M. Hävecker, T. Schedel-Niedrig, R. Schlögl, *Top. Catal.* 10 (2000) 187.
- [19] H. Werner, D. Herein, G. Schulz, U. Wild, R. Schlögl, *Catal. Lett.* 49 (1997) 109.
- [20] I. Böttger, T. Schedel-Niedrig, O. Timpe, R. Gottschall, M. Hävecker, T. Ressler, R. Schlögl, *Chem. Eur. J.* 6 (2000) 1870.
- [21] V. I. Bukhtiyarov, I. P. Prosvirin, E. P. Tikhomirov, V. V. Kaichev, A. M. Sorokin, V. V. Evstigneev, *React. Kinet. Catal. Lett.* 79 (2003) 181.
- [22] I. P. Prosvirin, E. P. Tikhomirov, A. M. Sorokin, V. V. Kaichev, V. I. Bukhtiyarov, *Kinet. Catal.* 44 (2003) 662.
- [23] I. E. Wachs, R. J. Madix, *J. Catal.* 53 (1978) 208.
- [24] M. Bowker, R. J. Madix, *Surf. Sci.* 95 (1980) 190.
- [25] A. F. Carley, A. W. Owens, M. K. Rajumon, M. W. Roberts, *Catal. Lett.* 37 (1996) 79.

- 
- [26] S. M. Francis, F. M. Leibsle, S. Haq, N. Xiang, M. Bowker, *Surf. Sci.* 315 (1994) 284.
- [27] F. M. Leibsle, S. M. Francis, S. Haq, M. Bowker, *Surf. Sci.* 318 (1994) 46.
- [28] S. L. Silva, R. M. Lemor, F. M. Leibsle, *Surf. Sci.* 421 (1999) 135.
- [29] S. L. Silva, R. M. Lemor, F. M. Leibsle, *Surf. Sci.* 421 (1999) 146.
- [30] A. F. Carley, P. R. Davies, G. G. Mariotti, S. Read, *Surf. Sci.* 364 (1996) 525.
- [31] M. Bowker, *Top. Catal.* 3 (1996) 461.
- [32] P. R. Davies, G. G. Mariotti, *J. Phys. Chem.* 100 (1996) 19975.
- [33] R. J. Madix, S. G. Telford, *Surf. Sci.* 328 (1995) 576.
- [34] J. Nakamura, Y. Kushida, Y. Choi, T. Uchijima, T. Fujitani, *J. Vac. Sci. Technol., A* 15 (1997) 1568.
- [35] Z.-M. Hu, K. Takahashi, H. Nakatsuji, *Surf. Sci.* 442 (1999) 90.
- [36] A. Sotiropoulos, P. K. Milligan, B. C. C. Cowie, M. Kadodwala, *Surf. Sci.* 444 (2000) 52.
- [37] M. A. Karolewski, R. G. Cavell, *Appl. Surf. Sci.* 173 (2001) 151.
- [38] K. Mudalige, M. Trenary, *Surf. Sci.* 504 (2002) 208.
- [39] F. M. Leibsle, *Surf. Sci.* 401 (1998) 153.
- [40] P. R. Davies, G. G. Mariotti, *Catal. Lett.* 43 (1997) 261.
- [41] A. H. Jones, S. Poulston, R. A. Bennett, M. Bowker, *Surf. Sci.* 380 (1997) 31.
- [42] B. A. Sexton, A. E. Hughes, N. R. Avery, *Surf. Sci.* 155 (1985) 366.
- [43] J. N. Russell Jr., S. M. Gates, J. T. Yates Jr., *Surf. Sci.* 163 (1985) 516.
- [44] J. R. B. Gomes, J. A. N. F. Gomes, *Surf. Sci.* 471 (2001) 59.

- [45] A. Knop-Gericke, M. Hävecker, T. Schedel-Niedrig, R. Schlögl, *Top. Catal.* 15 (2001) 27.
- [46] N. Ashcroft, N. Mermin, *Solid State Physics*, Holt-Sounders, 1976.
- [47] E. A. Wood, *Appl. Phys.* 35 (1964) 1306.
- [48] <http://www.chem.qmw.ac.uk/surfaces/>
- [49] M. J. Pilling, P. W. Seakins, *Reaction Kinetics*, Oxford Univ. Press, New York, 1995.
- [50] M. Boudart, G. D-Mariadassou, *Kinetics of Heterogeneous Catalytic Reactions*, Princeton Univ. Press, Princeton, 1984.
- [51] A. W. Czanderna, *Methods of Surface Analysis*, Vol. 1, Elsevier Scientific Publishing Company, Amsterdam, 1975.
- [52] M. P. Seah, W. A. Dench, *Surf. Interface Anal.* 1 (1979) 1.
- [53] H. Ibach, *Electron Spectroscopy for Surface Analysis*, Springer-Verlag, Berlin, 1977.
- [54] M. A. Hove, W. H. Weinberg, C. M. Chan, *Low-Energy Electron Diffraction*, Springer-Verlag, Berlin, 1986.
- [55] E. Brüche, *Z. Phys.* 86 (1933) 448.
- [56] J. Pohl, *Z. Tech. Phys.* 15 (1934) 579.
- [57] H. Mahl, J. Pohl, *Z. Tech. Phys.* 16 (1935) 219.
- [58] S. Günther, B. Kaulich, L. Gregoratti, M. Kiskinova, *Prog. Surf. Sci.* 70 (2002) 187.
- [59] H. H. Rotermund, *Surf. Sci. Rep.* 29 (1997) 265.
- [60] W. Engel, M. E. Kordesh, H. H. Rotermund, S. Kubala, A. Von Oertzen, *Ultramicroscopy* 36 (1991) 148.

- [61] Focus PEEM, Product Information, Focus GmbH, Omicron Vakuumphysik GmbH, Idsteiner Str. 78, D-65232 Taunusstein, Germany.
- [62] A. von Oertzen, H. H. Rotermund, S. Jakubith, G. Ertl, *Ultramicroscopy* 36 (1991) 107.
- [63] R. H. Fowler, *Phys. Rev.* 38 (1931) 45.
- [64] H. H. Rotermund, W. Engel, M. E. Kordesh, S. Jakubith, A. Von Oertzen, G. Ertl, *Ultramicroscopy* 36 (1991) 164.
- [65] K. Siegbahn, et al, *Nova Acta Regiae Soc. Sci., Ser. IV, Vol. 20, 1967.*
- [66] The Multiskop manual, Optrel GBR, Guerickestr. 11, D-10587 Berlin, Germany.
- [67] M. Born, *Optics*, Springer-Verlag, New York, Heidelberg, 1998.
- [68] R. M. A. Azzam, N. M. Bashara, *Ellipsometry and Polarized Light*, Elsevier Science B. V., Amsterdam, 1999.
- [69] R. Reiter, H. Motschmann, H. Orendi, A. Nemetz, W. Knoll, *Langmuir* 8 (1992) 1784.
- [70] S. Henon, J. Meunier, *Rev. Sci. Instrum.* 62 (1991) 936.
- [71] M. Harke, R. Teppner, O. Schulz, H. Orendi, H. Motschmann, *Rev. Sci. Instrum.* 68 (1997) 3130.
- [72] H. Riesenberger, *Handbook of Microscopy*, VEB Verlag Technik, Berlin, 1988.
- [73] H. Lüth, *Surfaces and Interfaces of Solid Materials*, Springer-Verlag, Berlin, Heidelberg, 1998.
- [74] F. Besenbacher, J. K. Nørskov, *Prog. Surf. Sci.* 44 (1993) 5.
- [75] R. Feidenhans'l, F. Grey, R. L. Johnson, S. G. J. Mochrie, J. Bohr, M. Nielsen, *Phys. Rev. B: Condens. Matter* 41 (1990) 5420.

- [76] R. Feidenhans'l, F. Grey, M. Nielsen, F. Besenbacher, F. Jensen, E. Laegsgaard, I. Stensgaard, K. W. Jacobsen, J. K. Nørskov, R. L. Johnson, *Phys. Rev. Lett.* 65 (1990) 2027.
- [77] S. R. Parkin, H. C. Zeng, M. Y. Zhou, K. A. R. Mitchell, *Phys. Rev. B: Condens. Matter* 41 (1990) 5432.
- [78] A. P. Baddorf, J. F. Wendelken, *Surf. Sci.* 256 (1991) 264.
- [79] W. Liu, K. C. Wong, H. C. Zeng, K. A. R. Mitchell, *Prog. Surf. Sci.* 50 (1995) 247.
- [80] W. Liu, K. C. Wong, K. A. R. Mitchell, *Surf. Sci.* 339 (1995) 151.
- [81] F. Frechard, R. A. v. Santen, *Surf. Sci.* 407 (1998) 200.
- [82] P. Liu, Y. Wang, *Surf. Sci.* 440 (1999) 81.
- [83] A. F. Carley, P. R. Davies, R. V. Jones, K. R. Harikumar, G. U. Kulkarni, M. W. Roberts, *Top. Catal.* 11/12 (2000) 299.
- [84] S. Y. Liem, J. H. R. Clarke, G. Kresse, *Surf. Sci.* 459 (2000) 104.
- [85] P. Liu, Y. Wang, *Surf. Sci.* 468 (2000) 122.
- [86] N. Hartmann, R. J. Madix, *Surf. Sci.* 488 (2001) 107.
- [87] M. Bowker, S. Poulston, R. A. Bennett, P. Stone, A. H. Jones, S. Haq, P. Hollins, *J. Mol. Catal. A: Chem.* 131 (1998) 185.
- [88] X. C. Guo, R. J. Madix, *Surf. Sci.* 367 (1996) L95.
- [89] W. W. Crew, R. J. Madix, *Surf. Sci.* 349 (1996) 275.
- [90] C. Barnes, P. Pudney, Q. Guo, M. Bowker, *J. Chem. Soc., Faraday Trans.* 86 (1990) 2693.
- [91] R. A. Bennet, S. Poulston, M. Bowker, *J. Chem. Phys.* 108 (1998) 6916.
- [92] S. Haq, F. M. Leibsle, *Surf. Sci.* 375 (1997) 81.

- [93] M. Bowker, S. Poulston, R. A. Bennett, P. Stone, *J. Phys.: Condens. Matter* 10 (1998) 7713.
- [94] Andrzej Kudelski, Bruno Pettinger, *Surf. Sci.* 566-568 (2004) 1007.
- [95] P. Stone, S. Poulston, R. A. Bennett, N. J. Price, M. Bowker, *Surf. Sci.* 418 (1998) 71.
- [96] A. F. Carley, P. R. Davies, R. V. Jones, K. R. Harikumar, G. U. Kulkarni, M. W. Roberts, *Top. Catal.* 11 (2000) 299.
- [97] [http://www.tau.ac.il/~phchlab/experiments/vacuum/sime\\_vacuum.html](http://www.tau.ac.il/~phchlab/experiments/vacuum/sime_vacuum.html)
- [98] Grundlagen der Vakuumtechnik, Berechnungen und Tabellen, Leybold-Heraeus GmbH, 2004.
- [99] [http://www.sigmaaldrich.com/Brands/Aldrich/Tech\\_Bulletins/AL\\_143/Molecular\\_sieves.html](http://www.sigmaaldrich.com/Brands/Aldrich/Tech_Bulletins/AL_143/Molecular_sieves.html)
- [100] S. Y. Lee, N. Mettlach, N. Nguyen, Y.M. Sun, J. M. White, *Appl. Surf. Sci.* 206 (2003) 102.
- [101] Y. Iijima, N. Niimura, K. Hiraoka, *Surf. Interface Anal.* 24 (1996) 193.
- [102] P. D. Kirsch, J. G. Ekerdt, *J. Appl. Phys.* 90 (2001) 4256.
- [103] S. Poulston, P.M. Parlett, P. Stone and M. Bowker, *Surf. Interface Anal.* 24 (1996) 811.
- [104] S. Poulston, E. Rowbotham, P. Stone, P. Parlett, M. Bowker, *Catal. Lett.* 52 (1998) 63.
- [105] E. D. Palik, *Handbook of Optical Constants of Solids*, Academic Press, Boston, 1985.
- [106] H. Derin, K. Kantarli, *Appl. Phys. A* 75 (2002) 391.
- [107] F. H. P. M. Habraken, G. A. Bootsma, *Surf. Sci.* 87 (1979) 333.

- [108] F. H. P. M. Habraken, C. M. A. M. Mesters, G. A. Bootsma, *Surf. Sci.* 97 (1980) 264.
- [109] W. E. J. v. Kooten, O. L. J. Gijzeman, J. W. Geus, *Surf. Sci.* 280 (1993) 243.
- [110] W. E. J. v. Kooten, D. D. Kragten, O. L. J. Gijzeman, J. W. Geus, *Surf. Sci.* 290 (1993) 302.
- [111] C. Wagner, K. Grünwald, *Z. Phys. Chem. B* 40 (1938) 455.
- [112] M. Mavrikakis; B. Hammer; J. K. Nørskov, *Phys. Rev. Lett.* 81 (1998) 2819.
- [113] Y. Xu; M. Mavrikakis, *Surf. Sci.* 494 (2001) 131.
- [114] S. Sakong; A. Groß, *Surf. Sci.* 525 (2003) 107.
- [115] A. Roudgar; A. Groß, *Phys. Rev. B: Condens. Matter* 67 (2003) 033409.
- [116] K. H. Schulz, D. F. Cox, *J. Catal.* 143 (1993) 464.
- [117] R. W. Joyner, M. W. Roberts, *Chem. Phys. Lett.* 60 (1979) 459.
- [118] E. Ozensoy, D. C. Meier, D. W. Goodman, *J. Phys. Chem. B* 106 (2002) 9367.
- [119] G. Rupprechter, H. Unterhalt, M. Morkel, P. Galletto, L. Hu, H.-J. Freund, *Surf. Sci.*, 502–503 (2002) 109.
- [120] H. Bluhm, M. Hävecker, A. Knop-Gericke, E. Kleimenov, R. Schlögl, D. Teschner, V. I. Bukhtiyarov, D. F. Ogletree, M. Salmeron, *J. Phys. Chem. B* 108 (2004) 14340.
- [121] A. Kudelski, B. Pettinger, *Surf. Sci.* 566-568 (2004) 1007.
- [122] M. A. Karolewski, R. G. Cavell, *Appl. Surf. Sci.* 173 (2001) 151.
- [123] J. R. B. Gomes, J. A. N. F. Gomes, F. Illas, *Surf. Sci.* 443 (1999) 165.
- [124] J. R. B. Gomes, J. A. N. F. Gomes, *Surf. Sci.* 446 (2000) 283.



- [125] J. R. B. Gomes, J. A. N. F. Gomes, F. Illas, *J. Mol. Catal. A: Chem.* 170 (2001) 187.
- [126] T. Matsumoto, R. A. Bennett, P. Stone, T. Yamada, K. Domen, M. Bowker, *Surf. Sci.* 471 (2001) 225.
- [127] R. Imbihl, *J. Mol. Catal. A: Chem.* 158 (2000) 101.
- [128] H. Y. H. Chan, C. T. Williams, M. J. Weaver, C. G. Takoudis, *J. Catal.* 174 (1998) 191.
- [129] R. W. McCabe, P. J. Mitchell, *J. Catal.* 103 (1987) 419.
- [130] O. Fujita, K. Ito, *J. Soc. Met. Eng., Int. J. Ser. II* 31 (1988) 314.
- [131] N. Hartmann, F. Esch, R. Imbihl, *Surf. Sci.* 297 (1993) 175.
- [132] J. L. Davis, M. A. Barteau, *Surf. Sci.* 235 (1995) 235.
- [133] J. J. Chen, Z. C. Jiang, Y. Zhou, B. R. Chakraborty, N. Winograd, *Surf. Sci.* 328 (1995) 248.
- [134] M. Rebholz, N. Kruse, *J. Chem. Phys.* 95 (1991) 7745.
- [135] K. Christmann, J. E. Demuth, *J. Chem. Phys.* 76 (1982) 6308.
- [136] K. Christmann, J. E. Demuth, *J. Chem. Phys.* 76 (1982) 6318.
- [137] J. L. Davis, M. A. Barteau, *Surf. Sci.* 197 (1988) 123.
- [138] M. Rebholz, V. Matolin, R. Prins, N. Kruse, *Surf. Sci.* 251/252 (1991) 1117.
- [139] J. A. Gates, L. L. Kesmodel, *J. Catal.* 83 (1983) 437.
- [140] R. K. Sharma, B. Zhou, S. Tong, K. T. Chuang, *Ind. Eng. Chem. Res.* 34 (1995) 4310.
- [141] E. M. Cordi, J. L. Falconer, *J. Catal.* 162 (1996) 104.
- [142] J. Rasko, J. Bontovics, F. Solymosi, *J. Catal.* 146 (1994) 22.

- [143] R.W. McCabe, P. J. Mitchell, *Appl. Catal., A* 27 (1986) 83.
- [144] M. A. Newton, *J. Catal.* 182 (1999) 357.
- [145] C. Cottrell, M. Bowker, A. Hodgson, G. Worthy, *Surf. Sci.* 325 (1995) 57.
- [146] M. A. Newton, M. Bowker, *Surf. Sci.* 307–309 (1994) 445.
- [147] M. A. Newton, M. Bowker, *Catal. Lett.* 21 (1993) 139.
- [148] M. A. Newton, S. M. Francis, M. Bowker, *Phys. Rev. B: Condens. Matter* 45 (1992) 9451.
- [149] M. A. Newton, S. M. Francis, M. Bowker, *Surf. Sci.* 269-270 (1992) 41.
- [150] M. A. Newton, S. M. Francis, M. Bowker, *Surf. Sci.* 259 (1991) 55.
- [151] M. A. Newton, S. M. Francis, Y. Li, D. Law, M. Bowker, *Surf. Sci.* 259 (1991) 45.
- [152] A. R. Koymen, K. H. Lee, G. Yang, K. O. Jensen, A. H. Weiss, *Phys. Rev. B: Condens. Matter* 48 (1993) 2020.
- [153] R. Burch, S. E. Golunski, M. S. Spencer, *J. Chem. Soc., Faraday Trans.* 86 (1990) 2683.
- [154] M. S. Spencer, *Catal. Lett.* 50 (1998) 37.
- [155] J. Yoshihara, C. T. Campbell, *J. Catal.* 161 (1996) 776.
- [156] C. V. Ovesen, B. S. Clausen, J. Schiøtz, P. Stoltze, H. Topsøe, J. K. Nørskov, *J. Catal.* 168 (1997) 133.
- [157] R. A. Hadden, B. Sakakini, J. Tabatabaei, K.C. Waugh, *Catal. Lett.* 44 (1997) 145.
- [158] N. Y. Topsøe, H. Topsøe, *J. Mol. Catal. A: Chem.* 141 (1999) 95.
- [159] T. Fujitani, J. Nakamura, *Appl. Catal. A* 191 (2000) 111.

- 
- [160] Y. Choi, K. Futagami, T. Fujitani, J. Nakamura, *Appl. Catal. A* 208 (2001) 163.
- [161] Z. M. Jarzebski, *Oxide Semiconductors*, Pergamon Press Ltd., Oxford, 1973.
- [162] M. Gsell, P. Jakob, D. Menzel, *Science* 280 (1998) 717.
- [163] P. Jacob, M. Gsell, D. Menzel, *J. Chem. Phys.* 114 (2001) 10075.
- [164] A. Schlapka, M. Lischka, A. Groß, U. Käsberger, P. Jakob, *Phys. Rev. Lett.* 91 (2003) 016101.
- [165] S. Y. Ohno, K. Yagyu, K. Nakatsuji, F. Komori, *Surf. Sci.* 554 (2004) 183.
- [166] F. Girgsdies, T. Ressler, U. Wild, T. Wübber, T. J. Balk, G. Dehm, L. Zhou, S. Günther, E. Arzt, R. Imbihl, R. Schlögl, *Catal. Lett.* 102 (2005) 91.
- [167] S. Sakong, A. Groß, *J. Catal.* 231 (2005) 420.
- [168] N. Reinecke, S. Reiter, S. Vetter, E. Taglauer, *Appl. Phys. A* 75 (2002) 1.



## List of abbreviations

AES	Auger Electron Spectroscopy
AFM	Atomic Force Microscopy
BESSY	Berlin Electron Storage Ring Company for Synchrotron Radiation
DFG	Deutsche Forschungsgemeinschaft (German Research Foundation)
DFT	Density Function Theory
EDX	Energy Dispersive X-ray analysis
EELS	Electron Energy Loss Spectroscopy
ELETTRA	Synchrotron light source in Trieste, Italy
HP-XPS	The high-pressure XPS experimental setup at BESSY, Berlin
HP-UHV	The experimental setup of a high-pressure reaction cell connected to a UHV chamber at the lab in Hannover
IR	Infrared Spectroscopy
L	Langmuir, $1 \text{ L} = 1 \times 10^{-6} \text{ Torr} \cdot \text{s}$
LEED	Low Energy Electron Microscopy
MBR	Molecular Beam Reaction
ML	Monolayer, $1 \text{ ML} = 1.08 \times 10^{15} \text{ atoms/cm}^2$
NEXAFS	Near-Edge X-ray Absorption Fine Structure spectroscopy
PAES	Positron-annihilation-introduced Auger electron spectroscopy
PEEM	Photoelectron Emission Microscopy
PM-IRAS	Polarization Modulation Infrared Absorption Spectroscopy
QMS	Quadrupole Mass Spectrometer
sccm	The unit of the flow rate, $\text{cm}^3/\text{min}$
SEM	Scanning Electron Microscopy
SFG	Sum Frequency Generation

---

SIMS	Secondary Ion Mass Spectrometer
SPEM	Scanning Photoelectron Microscopy
STM	Scanning Tunnelling Microscopy
TDS	Thermal Desorption Spectroscopy
TG	Thermogravimetry
TPD	Temperature-programmed Desorption
TPRS	Temperature-programmed Reaction Spectrum
XANES	X-ray Absorption Near-Edge Structure spectroscopy
XAS	X-ray Absorption Spectroscopy
XPS	X-ray Photoelectron Spectroscopy
XRD	X-ray Diffraction
UHV	Ultrahigh Vacuum
UPS	Ultraviolet Photoelectron Spectroscopy
UV	Ultraviolet

## List of Figures

2.1	Scheme of the experimental setup for temperature-programmed techniques.	9
2.2	Energy-level diagram illustrating the two possible filling mechanisms of a K-shell core hole generated by electron-impact ionization.	11
2.3	Operation of the cylindrical mirror analyzer as an Auger Electron Spectrometer.	13
2.4	Scheme of the experimental setup for LEED.	15
2.5	Scheme of the diffraction process.	16
2.6	Schematic drawing of the Photoelectron Emission Microscope.	19
2.7	The basic elements of an X-ray photoelectron spectrometer.	24
2.8	The Jones representation of polarized light represents any state of polarization as a linear combination of two orthogonal linearly polarized light waves.	26
2.9	Schematic drawing of the principle components of the electric field vector involved in a reflection experiment using linearly polarized light.	27
2.10	Ellipsometer in a PCSA-configuration.	29
3.1	Schematic drawing of the UHV system equipped with AES, LEED, QMS, and PEEM.	34

- 
- 3.2 Schematic drawing of the photolithography processes to prepare the microstructured Pd/Cu(110) sample (a), which has an approximate 1500 Å palladium layer on Cu(110); and Cu/ZnO/Al<sub>2</sub>O<sub>3</sub> sample (b), which has an approximate 1500 Å copper layer and a few micrometers ZnO layer on top of sapphire (Al<sub>2</sub>O<sub>3</sub>). 36
- 3.3 Schematic drawing of the HP-UHV system equipped with ellipsometer. 40
- 3.4 The home-built sample holder for ellipsometer application. 41
- 3.5 Schematic drawing of the high pressure reaction cell for ellipsometer application. 42
- 3.6 Arrangement of the Multiskop Ellipsometer and the reaction cell. 43
- 3.7 Schematic drawings of the in situ HP-XPS setup at BESSY. 45
- 4.1 LEED structures observed in methanol oxidation over Cu(110) (see text). 48
- 4.2 Schematic drawings for two equilibrium oxygen reconstructions: (a) Cu(110)-(2×1)-O [79], (b) Cu(110)-c(6×2)-O [76]. The small black circles represent the O atoms, whereas the grey and white circles represent super Cu atoms and Cu atoms in the layers below, respectively. Unit cells are shown. 49
- 4.3 The models for (a) the Cu(110)-(5×2)-methoxy structures [41] and (b) the Cu(110)-c(2×2)-formate structures [87, 92] proposed by the group of M. Bowker. 52
- 4.4 PEEM images of a Pd/Cu(110) microstructured bimetallic surface with different adsorbate structures on top of the Cu(110) surface which is the area inside the circle. (a) Clean surface; (b) Cu(110)-(2×1)-O ( $q_{\text{O}} = 0.5 \text{ ML}$ ); (c) Cu(110)-(5×2)-methoxy created by co-dosing with



- $p(\text{CH}_3\text{OH}) = 1 \times 10^{-7}$  mbar and  $p(\text{O}_2) = 0.5 \times 10^{-7}$  mbar at room temperature; (d) Cu(110)-c(2×2)-formate created by co-dosing with  $p(\text{CH}_3\text{OH}) = 1 \times 10^{-5}$  mbar and  $p(\text{O}_2) = 0.5 \times 10^{-5}$  mbar at room temperature. 54
- 4.5 Reference of the PEEM intensities to the different adsorbate structures on Cu(110). The PEEM intensities were determined via digitization of the PEEM images shown in Fig. 4.4. 55
- 4.6 The variation of the PEEM intensity during co-dosing with methanol and oxygen under high pressure ( $p(\text{CH}_3\text{OH}) = 1 \times 10^{-5}$  mbar,  $p(\text{O}_2) = 0.5 \times 10^{-5}$  mbar) at room temperature on Cu(110). 56
- 4.7 TPD spectra recorded simultaneously from a partially oxidized Cu(110) surface (5 L O<sub>2</sub> at 300 K) after exposure 10 L CH<sub>3</sub>OH at 240 K. The heating rate for the experiment was 6 K/min. 58
- 4.8 Comparison of TPD spectra after co-dosing with methanol and oxygen at 300 K (a) under low pressure condition ( $p(\text{CH}_3\text{OH}) = 1 \times 10^{-7}$  mbar,  $p(\text{O}_2) = 0.5 \times 10^{-7}$  mbar) and (b) under high pressure condition ( $p(\text{CH}_3\text{OH}) = 1 \times 10^{-5}$  mbar,  $p(\text{O}_2) = 0.5 \times 10^{-5}$  mbar). The heating rate for the experiments was 30 K/min. 60
- 4.9 Schematic drawing of the mechanism model for the reaction of methanol with pre-adsorbed oxygen atoms, which adsorb as (2×1) island on Cu(110). The small yellow circles present added Cu atoms in (2×1)-O island, the small white circles present O atoms, the very small black circles present H atoms, and the big white circles present C atoms. 62
- 5.1 Temperature programmed reaction spectroscopy in the  $10^{-7}$  mbar range with  $p(\text{CH}_3\text{OH}) = 1.0 \times 10^{-7}$  mbar,  $p(\text{CH}_3\text{OH}): p(\text{O}_2) = 1: 0.6$ . Temperature up- and down ramping are indicated in each panel. The

- upper panel represents the reactive sticking coefficient of methanol,  $s_{\text{reac}}(\text{CH}_3\text{OH})$ ; the other panels indicate the production rates of the different products during methanol oxidation. 67
- 5.2 Temperature programmed reaction spectroscopy in the  $10^{-5}$  mbar range with  $p(\text{CH}_3\text{OH}) = 1.0 \times 10^{-5}$  mbar,  $p(\text{CH}_3\text{OH}): p(\text{O}_2) = 1: 0.8$ . Temperature up- and down ramping are indicated in each panel. The upper panel represents the reactive sticking coefficient of methanol,  $s_{\text{reac}}(\text{CH}_3\text{OH})$ ; the other panels indicate the production rates of the different products during methanol oxidation. 69
- 5.3 Temperature dependence of the  $\text{CH}_3\text{OH}: \text{O}_2$  consumption ratio and of the corresponding  $\text{CH}_2\text{O}: \text{H}_2\text{O}$  and  $\text{H}_2: \text{H}_2\text{O}$  production ratio in the  $10^{-7}$  mbar and in the  $10^{-5}$  mbar range. Different regimes of the reaction stoichiometry are represented as grey areas in (b). The reactive sticking coefficient of methanol is displayed in the lower panels in order to relate the different regimes to the reactivity of the surface. 71
- 5.4 Effect of the total pressure on the low temperature reactivity peaks in temperature cycling experiments. The methanol to oxygen gas mixture was always kept at  $p(\text{CH}_3\text{OH}): p(\text{O}_2) = 1: 0.8$  with only the total pressure being varied between  $10^{-7}$  mbar and  $10^{-3}$  mbar. The straight lines indicate systematic shifts in the peak positions with increasing total pressure. 73
- 5.5 Effect of the gas mixing ratio on methanol conversion over the Cu(110) surface in the  $10^{-7}$  mbar (a) and the  $10^{-5}$  mbar pressure range (b). The methanol conversion is given by the reactive sticking coefficient of methanol. The numbers indicated in the plots are the ratio  $p(\text{CH}_3\text{OH}): p(\text{O}_2)$ . 75
- 5.6 Dependence of the reactive sticking coefficient of methanol,  $s_{\text{reac}}(\text{CH}_3\text{OH})$  on the oxygen partial pressure for  $p(\text{CH}_3\text{OH}) = 1.0 \times 10^{-5}$

- mbar. Shown are the data for two different temperatures, 480 K and 850 K. 77
- 5.7 Dependence of the production rates on the oxygen partial pressure for  $p(\text{CH}_3\text{OH}) = 1.0 \times 10^{-5}$  mbar. Shown are the data for two different temperatures, 480 K and 850 K. 78
- 5.8 In situ measured Auger data showing a hysteresis in the adsorbate coverages during temperature cycling under stationary reaction conditions. Shown are the  $\text{O}_{\text{KLL}}/\text{Cu}_{\text{KLL}}$  and  $\text{C}_{\text{KLL}}/\text{Cu}_{\text{KLL}}$  Auger intensity ratios during cycling in two different pressure ranges, at  $10^{-7}$  and  $10^{-5}$  mbar. Experimental conditions: (a)  $p(\text{CH}_3\text{OH}) = 1 \times 10^{-7}$  mbar,  $p(\text{O}_2) = 0.6 \times 10^{-7}$  mbar (b)  $p(\text{CH}_3\text{OH}) = 1 \times 10^{-5}$  mbar,  $p(\text{O}_2) = 0.8 \times 10^{-5}$  mbar. The LEED structures observed in situ during the T-cycles are indicated. 79
- 5.9 PEEM intensity variations and the corresponding changes in the reactivity of the surface expressed here as reactive sticking coefficient of methanol,  $s_{\text{reac}}(\text{CH}_3\text{OH})$ . Temperature cycles in two different pressure ranges, at  $10^{-7}$  and at  $10^{-5}$  mbar have been conducted. Experimental conditions:  $10^{-7}$  mbar range:  $p(\text{CH}_3\text{OH}) = 1.0 \times 10^{-7}$  mbar with  $p(\text{CH}_3\text{OH}): p(\text{O}_2) = 1: 0.6$ ;  $10^{-5}$  mbar range:  $p(\text{CH}_3\text{OH}) = 1.0 \times 10^{-5}$  mbar with  $p(\text{CH}_3\text{OH}): p(\text{O}_2) = 1: 0.8$ . The PEEM data are scaled to the intensity of the clean Cu(110) surface as unity. 81
- 5.10 O 1s and C 1s components for different adsorbate species on Cu(110):  $\text{O}_{\text{ad}}(\text{a})$  (well-ordered O(2×1)),  $\text{O}_{\text{ad}}(\text{b})$  (disordered), methoxy, formate, C(a) and C(b) contaminations, and a small amount of  $\text{SiO}_2$  impurity. The spectra were taken on an oxygen pre-covered Cu(110) surface, which was annealed in a methanol rich atmosphere of  $p(\text{CH}_3\text{OH}) = 1.4 \times 10^{-6}$  mbar and  $p(\text{O}_2) = 0.2 \times 10^{-6}$  mbar, and then cooled down at 410 and 350 K. 85

- 
- 5.11 Variation of adsorbate coverages during temperature cycling under stationary reaction condition:  $p(\text{CH}_3\text{OH}) = 0.5 \times 10^{-5}$  mbar and  $p(\text{O}_2) = 0.3 \times 10^{-5}$  mbar. The upper panel displays the corresponding formaldehyde production rate. The heating/cooling rate for the experiment was 5 K/min. 88
- 5.12 Adsorbates present on Cu(110) during the methanol selective oxidation at  $p(\text{CH}_3\text{OH}) = 0.5 \times 10^{-5}$  mbar and different gas mixing ratios. The corresponding upper panel displays the formaldehyde production rate. 90
- 6.1 The effect of the total pressure on the reaction rate measurements of methanol oxidation over copper in the high-pressure reaction cell. The pump speed of the system was kept constant at 0.4 L/s. The flow ratio of methanol to oxygen was kept 1:1. 102
- 6.2 The effect of the pump speed on the reaction rate measurements of methanol oxidation over copper in the high-pressure reaction cell. The flow ratio of methanol to oxygen was kept 1:1. 103
- 6.3 TPRS in the  $10^{-3}$  mbar range with  $\text{CH}_3\text{OH}$  flow rate 0.1 sccm and  $\text{O}_2$  flow rate 0.1 sccm, over two different pretreated sample surfaces: (a) a yellow shining metallic surface prepared usually by reducing in methanol (1 mbar, 673 K, 30 min); (b) a metallic surface prepared by reacting in  $\text{O}_2$ :  $\text{CH}_3\text{OH} = 6:1$  ( $P_{\text{tot}} = 7 \times 10^{-1}$  mbar) at 673 K and then slightly reducing in methanol (0.01 mbar, 673 K, 10 min). The heating rate for the experiments was 5 K/min. 106
- 6.4 TPRS in the  $10^{-2}$  mbar range with  $\text{CH}_3\text{OH}$  flow rate 0.3 sccm and  $\text{O}_2$  flow rate 0.1 sccm, over three different sample surfaces: a metallic copper surface (yellow, shining), a partially oxidized copper surface where a  $\text{Cu}_2\text{O}$  film was formed (red), and a deeply oxidized copper surface where a  $\text{CuO}$  film was reached (black). The heating rate for the experiments was 5 K/min. 108

- 
- 6.5 Effect of the gas mixing ratio on methanol conversion over the metallic copper surface in the  $10^{-2}$  mbar range. The heating rate for the experiments was 5 K/min. 110
- 6.6 Effect of the gas mixing ratio on methanol conversion and the production rates over the deeply oxidized copper surface ( $p(\text{O}_2) = 1$  mbar, 673 K, 30 min until a black CuO film was observed) in the  $10^{-2}$  mbar range. The sample changed its chemical state during the reaction. The heating rate was 5 K/min. 111
- 6.7 Changes of the oxide phase during the TPR over a deeply oxidized copper sample. The displayed photos of the sample in the reactor were taken using a high quality digital camera with fixed aperture and white balance. The TPR spectrum is also shown and the arrows on top of the panel indicate the reactivity corresponding to each photo. Reaction conditions:  $\text{CH}_3\text{OH}$  flow rate 0.2 sccm and  $\text{O}_2$  flow rate 0.1 sccm. 113
- 6.8 Integrating ellipsometry measurement: the variation of  $\Delta$  and  $\Psi$  values during the TPR over a deeply oxidized copper sample. The simulated  $\Delta$  and  $\Psi$  values were inserted in the variation curves as triangular markers. The lines separated the area for different sample models. Reaction conditions:  $\text{CH}_3\text{OH}$  flow rate 0.2 sccm and  $\text{O}_2$  flow rate 0.1 sccm. 115
- 6.9 The variation of the  $\Delta$  and  $\Psi$  values during the change of the thickness of (a) a CuO film and (b) a  $\text{Cu}_2\text{O}$  film on top of the Cu substrate simulated with the program Elli. 116
- 6.10 Integrating ellipsometry measurement: the variation of  $\Delta$  and  $\Psi$  values during the TPR over a metallic copper sample. The upper panel is the corresponding TPR spectrum. Reaction conditions:  $\text{CH}_3\text{OH}$  flow rate 0.2 sccm and  $\text{O}_2$  flow rate 0.1 sccm. 119

- 6.11 Ellipsometric images during the TPR over a deeply oxidized copper sample. Left: an image series of a  $1 \times 1.8 \text{ mm}^2$  large sample area with ellipsometric contrast; right: the corresponding TPR spectrum. The arrows on top of the panel indicate the reactivity corresponding to each photo. Reaction conditions:  $\text{CH}_3\text{OH}$  flow rate 0.2 sccm and  $\text{O}_2$  flow rate 0.1 sccm. 121
- 6.12 Scanning electron microscopy (SEM) pictures of the copper surface after long term catalytic reactions in oxygen and methanol. (a) a  $2.9 \times 2.1 \text{ mm}^2$  large area of the surface; (b) the top surface layer; (c) a new surface layer below the facet formed during the reaction. 126
- 7.1 Schematic diagram illustrating the pressure and material gap in methanol selective oxidation over copper catalysts. The content in the each textbox exhibits the main results (black), the applied techniques, and the research groups (grey) in the studies. The question marks indicate that the stated results are still under debate (see text). 132
- 7.2 The comparison of temperature programmed reaction spectroscopy over a Cu(110) surface and an oxygen-sputtered Cu(110) surface in the  $10^{-5}$  mbar range with  $p(\text{CH}_3\text{OH}) = 1.0 \times 10^{-5}$  mbar,  $p(\text{CH}_3\text{OH}) : p(\text{O}_2) = 1 : 0.8$ . The upper panel represents the reactive sticking coefficient of methanol,  $s_{\text{reac}}(\text{CH}_3\text{OH})$ ; the other panels indicate the production rates of the different products during methanol oxidation. 140
- 7.3 PEEM images showing different stages in the titration of an oxygen saturated Pd/Cu(110) microstructure with methanol at  $p(\text{CH}_3\text{OH}) = 1 \times 10^{-7}$  mbar and  $T = 470 \text{ K}$ . Inside the circle, the substrate is a Cu(110) surface and the surrounding area is covered with a 1500 Å-thick Pd film. 143
- 7.4 A thin copper film totally covers the palladium structures of a Pd/Cu(110) microstructured sample. Top: Cu 3p intensity obtained

- 
- over Cu(110) and Pd/Cu(110), respectively. Below: SPEM Pd 3d and Cu 3p images of the surface in the same structure region. 144
- 7.5 PEEM images ( $500 \times 500 \mu\text{m}^2$ ) showing the titration of oxygen saturated Cu/ZnO/Al<sub>2</sub>O<sub>3</sub> microstructures with methanol at  $p(\text{CH}_3\text{OH}) = 1 \times 10^{-6}$  mbar and  $T = 420$  K. Cu structures are imaged brighter, whereas ZnO film is imaged darker. (a) Reaction starts from small size Cu-domain; (b) Reaction starts from small size ZnO-domain. 146
- 7.6 SEM image of a Cu/ZnO microstructure, the EDX spectrum of the Cu/ZnO/Al<sub>2</sub>O<sub>3</sub> film, and the corresponding EDX mappings of Al, O, Cu, and C, after the sample was used for kinetic measurements at high temperature. 147
- 7.7 Schematic diagram illustrating the current status of the pressure and material gap in methanol selective oxidation over copper catalysts. The content in the each textbox exhibits the main results (black), the applied techniques, and the research groups (grey) in the studies. The question marks indicate that the stated results are still under debate. 149

## List of Tables

- |     |   |     |
|-----|---|-----|
| 5.1 | C 1s and O 1s binding energies (eV) for the possible adsorbates in the former XPS studies.  | 84  |
| 6.1 | The optical constants $n$ (refractive index), $k$ (extinction coefficient) and $\phi_p$ (Brewster angle) for three different phases, Cu, Cu <sub>2</sub> O, and CuO at a wavelength $\lambda = 6328 \text{ \AA}$ . The incident angle is $70^\circ$ . | 116 |
| 6.2 | The comparison of the measured ellipsometric data with the simulated $\Delta$ and $\Psi$ values according to a reasonable sequence of the layer models of the sample during the TPR experiment.   | 117 |



# List of publications

Parts of this thesis have been or will be published in due course:

- Low pressure methanol oxidation over a Cu(110) surface under stationary conditions: (I) Reaction kinetics  
**Ling Zhou**, Sebastian Günther, and Ronald Imbihl  
Journal of Catalysis 230 (2005) 166
- Low pressure methanol oxidation over a Cu(110) surface under stationary conditions: (II) Adsorbates coverage and reactivity  
**Ling Zhou**, Sebastian Günther, and Ronald Imbihl  
Journal of Catalysis 232 (2005) 295
- Methanol oxidation over oxidized copper surfaces: Reaction kinetics and ellipsometry  
**Ling Zhou**, Sebastian Günther, Dariusz Moszynski, and Ronald Imbihl  
Submitted to Journal of Catalysis
- Adsorbates present during the partial methanol oxidation over Cu(110): An *in situ* XPS study  
S. Günther, **L. Zhou**, R. Imbihl, M. Hävecker, A. Knop-Gericke, E. Kleimenov, and R. Schlögl  
In preparation
- Strained thin copper films as model catalysts in the materials gap  
F. Girgsdies, T. Ressler, U. Wild, T. Wübber, T. J. Balk, G. Dehm, **L. Zhou**, S. Günther, E. Arzt, R. Imbihl, and R. Schlögl  
Catalysis Letters 102 (2005) 91



# Curriculum Vitae

## Personal

Birth	July 16, 1974 in Hubei, China
Nationality	Chinese
Marital Status	Married

## Education

7.2001 – present	Ph.D. in Prof. Dr. R. Imbihl's group, Institute of physical chemistry and electrochemistry, University of Hannover, Germany
6.2001	Master Degree in Engineering University of Petroleum, Beijing (China)
9.1998 – 6.2001	Prof. Dr. Shen Shikong's Group, CNPC Key Laboratory of Catalysis, Faculty of Chemical Engineering, University of Petroleum, Beijing (China)
6.1995	Bachelor Degree in Engineering Hubei Institute of Technology
9.1991 – 6.1995	Department of Chemical Engineering, Hubei Institute of Technology

## Professional Experience

10.2003 – 1.2004	Visiting scientist in Prof. Dr. Giovanni Comelli's group, National Laboratory TASC-INFN, Trieste, Italy Project: Imaging CeO <sub>2</sub> (111) surface with STM
7.1995 – 8.1998	Engineer in Wuhan Paper Mill, Hubei, China



# Acknowledgements

The thesis work was carried out at the Institute of Physical Chemistry and Electrochemistry, University of Hannover from August 2001 to March 2005. Here, I would like to express my gratitude to all those who gave me the possibility to complete this thesis.

First of all I would like to thank my supervisor Prof. Dr. Ronald Imbihl for providing a wonderful work atmosphere and giving me the opportunity to do my PhD work in his group. His scientific insights, supports and his numerous discussions on the project and my thesis writing are especially valuable for the implement of this work. I thank him for his constant assistance of my scientific work.

I am deeply indebted to Dr. Sebastian Günther, currently working in LUM, whose help, stimulating suggestions, numerous discussions and encouragement helped me in all the time of research for and writing of this thesis. Especially, His always-ready-to-help attitude facilitated my work very much. I am impressed with his plentiful research work experience and his serious, diligent work attitude which will be of great benefit to me for my future research work.

I would like to thank all my current and some former colleagues in the working group of Prof. Imbihl, not only for their help, scientific support, and valuable hints, but also for the fun we had together. I am much obliged to Tobias Neubrand, Dr. Monika Hinz, Dr. Dariusz Moszynski, Dr. Hubertus Marbach, Dr. Axel Scheibe, Yingfeng Zeng, Hong Liu, and Miguel Pineda. A special thank goes to Mrs. Carmen Gatzen, the secretary of the group, who helped and taught me a lot both in the work and in the life.

I also want to sincerely thank other colleagues at the institute: Dr. Armin Feldhoff and Ms. Kerstin Janze for their kind help on the electron microscopy, Dr. Xiaobo Yang for his valuable comments on the manuscript of this thesis.

I wish to convey my warmest thanks to Prof. Dr. Giovanni Comelli, Dr. Friedrich Esch, and Dr. Cristina Africh at INFM-TASC, Trieste, Italy. During my stay at their laboratory as a visiting scientist in 2003, they gave me a lot of help on STM

studies. I wish to thank Prof. Dr. Robert Schlögl, Dr. T. Ressler, Dr. A. Knop-Gericke, Dr. Michael Hävecker, Dr. Spiros Zafeiratos, Dipl. Phys. Evgueni Kleimenov at FHI, Berlin, for their valuable cooperation of the DFG project and the full support of our beamtime at BESSY. My thanks also go to Prof. Maya Kiskinova, Dr. Luca Gregoratti, Dr. Andrea Locatelli, and Dr. Alexei Barinov at Elettra, Trieste, Italy, for their powerful support of our beamtimes with Nanospectroscopy and ESCA Microscopy facilities.

As for the financial support, I appreciate the Georg Christoph Lichtenberg-fellowship which supported me from 8.2001 - 7.2004 and DFG (German Research Foundation) for the further support from 8.2004 till now. Here I have to mention, as a graduate student participating in the Graduate Program "New materials with tailored properties", I benefit a lot from the wonderful organization of the program: I learnt a lot of basic knowledge, and discussed with other graduates in the different research fields. All these finally broaden my vision in science. Here, I specially thank Prof. Dr. Peter Behrens, Prof. Dr. Josef-Christian Buhl, Prof. Dr. Paul Heitjans, Dr. Thomas Bredow, and all other professors who contribute their unselfish work to the program.

A special acknowledgement flies back China to my former supervisor Prof. Shikong Shen and his wife Prof. Xuejia Ding, who introduced me to step into the door of science, and whose inculcation is of great benefit to my research work. I would also like to thank all my friends, especially the friends in Hannover, Berlin and Munich, for their support and friendship.

Lastly, I want to thank my parents, who taught me the value of hard work by their own example. I would like to share this moment of happiness with my parents, brothers and sisters. They rendered me enormous support during the whole tenure of my research. Particularly, I am grateful to my wife Jing for the substantial and moral support she provided throughout my research work. Without her patient love and understanding I would never have completed my present work.

Finally, again, I would like to thank all whose direct and indirect support helped me completing my thesis in time.